



HAL
open science

Taking into account of the discontinuous nature of the solvent in the mechanical modeling of swelling clays

van Duy Tran

► **To cite this version:**

van Duy Tran. Taking into account of the discontinuous nature of the solvent in the mechanical modeling of swelling clays. Mechanics [physics.med-ph]. Université de Lorraine, 2017. English. NNT : 2017LORR0036 . tel-01661513

HAL Id: tel-01661513

<https://theses.hal.science/tel-01661513>

Submitted on 12 Dec 2017

HAL is a multi-disciplinary open access archive for the deposit and dissemination of scientific research documents, whether they are published or not. The documents may come from teaching and research institutions in France or abroad, or from public or private research centers.

L'archive ouverte pluridisciplinaire **HAL**, est destinée au dépôt et à la diffusion de documents scientifiques de niveau recherche, publiés ou non, émanant des établissements d'enseignement et de recherche français ou étrangers, des laboratoires publics ou privés.



AVERTISSEMENT

Ce document est le fruit d'un long travail approuvé par le jury de soutenance et mis à disposition de l'ensemble de la communauté universitaire élargie.

Il est soumis à la propriété intellectuelle de l'auteur. Ceci implique une obligation de citation et de référencement lors de l'utilisation de ce document.

D'autre part, toute contrefaçon, plagiat, reproduction illicite encourt une poursuite pénale.

Contact : ddoc-theses-contact@univ-lorraine.fr

LIENS

Code de la Propriété Intellectuelle. articles L 122. 4

Code de la Propriété Intellectuelle. articles L 335.2- L 335.10

http://www.cfcopies.com/V2/leg/leg_droi.php

<http://www.culture.gouv.fr/culture/infos-pratiques/droits/protection.htm>

Prise en compte du caractère discontinu du solvant dans la modélisation mécanique des argiles gonflantes

THÈSE

présentée et soutenue publiquement le 26 Avril 2017
pour l'obtention du

Doctorat de l'Université de Lorraine
Spécialité Mécanique-Énergétique

par

Van Duy TRAN

Ingénieur en Construction de l'Université de Liège, Belgique

Membres du Jury

M. Claude BOUTIN	Professeur, ENTPE, Vaulx-en-Velin (<i>Rapporteur</i>)
M. Jean-François DUFREÛCHE	Professeur, Université de Montpellier (<i>Rapporteur</i>)
M. Olivier MILLET	Professeur, Université de La Rochelle (<i>Membre</i>)
M. Márcio A. MURAD	Professeur, Laboratório Nacional de Computação Científica Petrópolis, RJ, Brésil (<i>Membre</i>)
Mme. Julia MAINKA	Maître de Conférence, Université de Lorraine (<i>Membre</i>)
M. Christian MOYNE	Directeur de Recherche, CNRS, Université de Lorraine (<i>Directeur de thèse</i>)

Acknowledgment

First of all, I would like to express my sincerest gratitude to my supervisors Mr. Christian MOYNE, Research Director at CNRS and Mrs. Julia MAINKA, Associate Professor of Université de Lorraine for having supervised me during the thesis, especially for their patience, motivation, enthusiasm, and massive knowledge. Their guidance helped me in all the time of research and writing of this thesis. I could not have imagined having better supervisors and mentor for my Ph.D work. I had a great pleasure to work with them.

I am very grateful to my two reviewers Mr. Claude BOUTIN, Professor of École Nationale des Travaux Publics de l'État (ENTPE) and Mr Jean-François DUFRÊCHE, Professor of Université de Montpellier for their encouragement, insightful comments, and hard questions. My sincere thanks also goes to Mr. Mácio A. MURAD, Professor of Laboratório Nacional de Computação Científica in Brazil and Mr. Olivier MILLET, Professor of Université de La Rochelle for agreeing to participate to my thesis committee.

I would like to thank the secretaries of LEMTA, Fatiha Boumendjel, Irène Leonard, Valérie Reichhart for facilitating my doctoral procedure.

I would like to thank my French friends in LEMTA Lionel, Thomas, William, Sofiane for providing amazing work environment during my thesis study.

Additionally, and much importantly, I am greatly thankful the funding source that helped my PhD work possible: CNRS/University of Lorraine grant.

I offer my gratitude to my Vietnamese friends who work and study in Nancy Lam, Tung, Hoan, Tuyen, Mai, Hung, Giang, Le, Quyen, Thang, Hoa, Trung, Nguyet, M. My, Mme. Nga, Diem, Hiep and many others for sharing with me the living experiences that could not learn at school.

I would like to thank my family, my in-laws for their valuable supports through my work and life.

Last but definitely not the least, I would like to thank my wife Huong for her continuous support and especially her love which is the biggest motivation for me to complete the PhD requirements.

Contents

Nomenclature	15
Introduction	17
1 Introduction to the modeling of expansive clays	21
1.1 Clay mineralogy	21
1.1.1 Basic structures and classification of clay minerals	21
1.1.2 Isomorphous substitution	23
1.2 Swelling mechanisms of clays	23
1.2.1 Crystalline swelling and cation hydration	23
1.2.2 Osmotic swelling and electrical double layer	24
1.3 Electrical double layer theory	25
1.3.1 Classical Poisson-Boltzmann Theory	25
1.3.2 Disjoining pressure	29
1.4 Multi-scale structure of clayey soils	31
1.5 Previous works and thesis scope	32
1.5.1 Literature review	32
1.5.2 Thesis scope	33
2 Introduction to Density Functional Theory and application to Hard-Sphere fluids	35
2.1 Classical Density Functional Theory	35
2.2 Radial Distribution Function	36
2.2.1 Definition	37
2.2.2 Ornstein-Zernike equation	38
2.2.3 Closures	39
2.3 Density functional perturbation theory	41
2.4 Fundamental Measure Theory	42
2.4.1 Percus-Yevick direct correlation function of hard spheres	42
2.4.2 Excess free energy functional	44
2.5 Application of the hard sphere fluid in EDL model approaches	48
2.5.1 FMT applied to planar geometry cases	49
2.5.2 Bulk hard sphere fluid equations	49
2.5.3 Results and discussion	50
2.6 Conclusion	53
Appendix A	55
A.1 Fourier transform of $\Theta(d - \mathbf{r})$	55
A.2 Development of the Fundamental Measure Theory	56
A.2.1 Determination of the constants c_1 - c_4	56
A.2.2 "White Bear" version	59
A.3 One-dimensional weight functions $\omega_\alpha(z)$	61

3	Lennard-Jones fluid	65
3.1	Introduction	65
3.2	DFPT applied to Lennard-Jones fluids	66
3.3	Determination of the RDF using integral equation theory	67
3.3.1	Homogeneous Lennard-Jones fluids	67
3.3.2	Inhomogeneous LJ fluids	69
3.4	Results and discussions	70
3.4.1	Effective intermolecular potential	70
3.4.2	Density profiles of inhomogeneous Lennard-Jones fluids	71
3.4.3	Radial distribution function of inhomogeneous LJ fluids	75
3.5	Application to Electrical Double Layer	75
3.5.1	Density profile of the pure solvent	81
3.5.2	Density profiles of the constituents of the electrolyte solution	82
3.6	Conclusion	83
	Appendix B	85
B.1	Fourier 1D transform	85
B.2	3D transform	86
B.3	Hankel transform	87
B.4	Numerical Hankel transform	88
4	Dipolar Hard-Sphere fluid	91
4.1	Introduction	91
4.2	Mean spherical approximation for homogeneous DHS fluid	95
4.3	Dielectric permittivity	99
4.4	Density Functional Perturbation Theory (DFPT) approach for the DHS fluid	102
4.4.1	Introduction	103
4.4.2	Behavior of the bulk DHS fluid	106
4.4.3	Behavior of HS dipolar fluids confined between two walls	108
4.5	Towards a “civilized” model of the Electrical Double Layer	115
4.5.1	Interaction potentials	115
4.5.2	DFPT applied to electrolyte solutions	116
4.5.3	Poisson equation	121
4.5.4	Results and discussions	122
4.6	Conclusion	123
	Appendix C	125
C.1	Legendre polynomials	125
C.2	Calculation details in modeling dipolar hard sphere fluids	126
C.2.1	In the homogeneous bulk fluid	126
C.2.2	Dipole-dipole excess chemical potential of an inhomogeneous DHS fluid	132
C.3	Clausius-Mossotti formula	135
5	Modeling the hydro-mechanical behavior of unsaturated swelling clays	137
5.1	Introduction	137
5.2	Multi-scale model equations in an isotropic medium approximation	140
5.2.1	Elastic contact stress	140
5.2.2	Effective disjoining pressure	141
5.2.3	Equivalent fluid pressure	142
5.2.4	Porosities	143
5.3	Application to an oedometric swelling pressure test	146
5.3.1	Initial “dry state”	147

5.3.2	Final fully saturated state	148
5.3.3	Intermediate saturations	149
5.4	Results and discussion	153
5.4.1	Swelling and disjoining pressure	153
5.4.2	Deformation and porosities	156
5.5	Conclusion	158
	Conclusion and future work	161
	Résumé en français	163

List of Figures

1.1	(a) Silica tetrahedron unit; (b) Silica tetrahedra arranged in a hexagonal network [1].	22
1.2	(a) Octahedral unit; (b) Sheet structure built by octahedral units [1].	22
1.3	Schematic representation of several clay mineral groups [1].	22
1.4	Structure diagram of montmorillonite [1].	23
1.5	Conceptual model of the sequential crystalline swelling process for smectites [2].	24
1.6	Evolution of basal distance with relative water pressure for Na-Montmorillonites, where P/P_0 designates the relative pressure of the adsorbed water. The formation of 0,1 and 2 layers of water is also observed [3].	25
1.7	Scheme of the Electrical Double Layer between two adjacent clay platelets [4]. .	26
1.8	Electrical Double Layer scheme.	26
1.9	Profile of the electric potential inside the EDL in the case of a 1:1 electrolyte solution, $c_b = 0.1$ mol/l; $\Sigma = -0.1\text{C.m}^{-2}$; $H=1\text{nm}$	28
1.10	Ion distributions in the EDL space for the case of a 1:1 electrolyte solution, $c_b = 0.1\text{mol/l}$; $\Sigma = -0.1\text{C.m}^{-2}$; $H=1\text{nm}$	29
1.11	Mechanical equilibrium in the EDL.	30
1.12	Disjoining pressure of a 1:1 electrolyte solution with $\Sigma = -0.1\text{ C.m}^{-2}$ predicted by the Poisson-Boltzmann model.	31
1.13	High resolution SEM images of clay texture at different length scales [5].	32
1.14	Three-scale representation of expansive clay media.	32
1.15	34
2.1	Radial Distribution Function of the uniform hard-sphere fluid at the reduced particle density $\rho d^3 = 0.813$	38
2.2	Geometric quantities of two interpenetrating spheres.	43
2.3	HS model for the water solvent in an Electrical Double Layer.	48
2.4	Contact value of the hard-sphere fluid near a hard wall versus the grid point number $d/\Delta z$ for a reduced bulk density $\rho d^3 = 0.7$	50
2.5	Density profiles of inhomogeneous hard sphere fluids at different reduced bulk densities near a hard wall in comparison with Monte Carlo simulation taken from [6].	51
2.6	Density profiles of a hard sphere fluid confined between two hard walls for different separation distances between the walls for the reduced bulk density $\rho_b d^3 = 0.813$	52
2.7	Disjoining pressure profile of a hard-sphere fluid confined between two planar hard walls as a function of the separation distance $2H$ at the reduced bulk density $\rho_b d^3 = 0.73$	52
3.1	WCA separation of the intermolecular LJ potential.	66
3.2	Radial Distribution Function $g(r)$ of bulk Lennard-Jones fluids obtained with two closures: HNC + B(r) and HNC and comparison with simulation results. .	68

3.3	Radial distribution function of a homogeneous LJ fluid at high density and low temperature: $\rho\sigma^3 = 0.85$, $\frac{k_B T}{\epsilon} = 0.88$. The circles are MC results taken from [7].	68
3.4	Two-dimensional geometry of Lennard-Jones fluids confined between two walls.	69
3.5	Influence of λ on the radial distribution function of a bulk Lennard-Jones fluid at $\rho\sigma^3 = 0.5$ and $T^* = 1.35$.	71
3.6	λ -dependency of the radial distribution function for various densities at $T^* = 1$. The red, blue and sky blue curves correspond to $\rho\sigma^3 = 0.2$, $\rho\sigma^3 = 0.4$ and $\rho\sigma^3 = 0.6$, respectively. The solid curves are calculated with $\lambda = 0.5$ and the dashed curves are the averaged curves in terms of λ .	71
3.7	Density distribution profile of an inhomogeneous LJ fluid near a hard wall: $\rho_b\sigma^3 = 0.5$, $T^* = 1.2$. The MC simulation results are reported in the work of Lutsko [8].	72
3.8	As Fig.3.7 for $\rho_b\sigma^3 = 0.65$.	73
3.9	As Fig.3.7 for $\rho_b\sigma^3 = 0.82$.	73
3.10	Density profiles of an inhomogeneous Lennard-Jones fluid confined between two hard walls: $\rho_b\sigma^3 = 0.75$; $T^* = 1.304$, and $2H = 5\sigma$. The open circles represent the MC simulation results [9].	74
3.11	Solid-fluid LJ 10-4-3 potential at $2H = 7.5\sigma$.	74
3.12	Density profiles of a Lennard-Jones fluid confined between two LJ walls: $\rho_b\sigma^3 = 0.5925$; $T^* = 1.2$, and $2H = 7.5\sigma$. The open circles represent the MC simulation results of [10].	75
3.13	Radial distribution functions of an inhomogeneous LJ fluid near a hard wall at $\rho_b\sigma^3 = 0.5$ and $T^* = 1.35$. The corresponding density profile is presented in Fig.3.7.	76
3.14	As Fig.3.13 for $\rho_b\sigma^3 = 0.65$. The corresponding density profile is presented in Fig.3.8.	76
3.15	As Fig.3.13 for $\rho_b\sigma^3 = 0.82$. The corresponding density profile is presented in Fig.3.9.	77
3.16	Fluid-solid LJ potential $V_\alpha^{LJ}(z) + V_\alpha^{LJ}(2H - z)$ between two clay surfaces placed at $\pm H$ and species α of an electrolyte solution for $L = 7 \times 10^{-10}$ m, $\rho_O^s d^3 = 0.052$, $\beta\epsilon_{O-\alpha} = 0.2669$ and $2H = 10d$.	79
3.17	Density profile of water considered as a LJ fluid confined between two clay lamellae represented by rigid LJ walls separated by a distance of $2H = 3d$ at: $\rho_b d^3 = 0.7344$, $\beta\epsilon = 1.077$.	81
3.18	Density profile of water LJ fluid confined between two extremely attractive clay lamellae at: $\rho_b d^3 = 0.7344$, $\beta\epsilon = 1.077$, $2H = 15d$.	82
3.19	Density profiles of the different components for an electrolyte solution 1:1; $c_b = 0.1M$, $\rho_0 d^3 = 0.7344$, $\beta\epsilon = 0.7407$ confined between two clay lamellae separated by a distance $2H = 4d$.	83
3.20	Density profiles of different components for a 1:1 electrolyte solution: $\rho_0 d^3 = 0.7344$, $\beta\epsilon_{water-water} = 1.077$, $2H = 5d$, $\beta\epsilon_{water-ion;ion-ion} = 0.6667$.	84
4.1	Modeling the water molecule as a dipolar hard sphere.	91
4.2	Keesom interaction between permanent dipoles.	92
4.3	Debye interaction between permanent and induced dipoles.	92
4.4	London dispersion force between fluctuating and induced dipoles.	93
4.5	Geometrical configuration of dipole-dipole interactions.	93
4.6	Representation of a vector in spherical coordinates: θ and ϕ are respectively the polar and the azimuth angles.	94

4.7	Projections of total correlation function $h(1,2)$ for a dipolar hard spheres fluid with $\rho d^3 = 0.7$ and $m^{*2} = \frac{\beta}{4\pi\epsilon_0 d^3} m^2 = 2$	99
4.8	Fröhlich approach for the determination of the dielectric constant ϵ : an infinite dielectric medium of dielectric permittivity $\epsilon\epsilon_0$ is submitted to an electric field E ; inside this medium there is a void spherical cavity of volume V (dielectric permittivity ϵ_0) occupied by N dipoles. \mathbf{E}' is the electric field inside the cavity prior to the introduction of the N dipoles.	100
4.9	Relation between the relative permittivity of a homogeneous DHS fluid of a density $\rho d^3 = 0.7$ and the molecular parameter $y = \beta\rho m^2/(9\epsilon_0)$	102
4.10	Dipole position and orientation.	105
4.11	Dipole orientation profiles of a bulk fluid for different uniform electric fields: $E_0 = \Sigma/\epsilon_0$ and $\alpha(\theta) = \sqrt{\alpha_x^2 + \alpha_y^2}$	108
4.12	Evolution of the permittivity of a bulk DHS fluid submitted to an electric field $E_0 = \Sigma/\epsilon_0$, where Σ is the surface charge of the walls (bulk density $\rho_b d^3 = 0.734$ and reduced dipole moment strength $m^{*2} = 0.75$).	109
4.13	Density profile of a DHS fluid confined between two hard walls with $\rho_b d^3 = 0.7$ and $m^{*2} = 2$	111
4.14	Dipole orientation distribution of the DHS fluid confined between two hard walls with $\rho_b d^3 = 0.7$, $m^* = 2$, $2H = 15d$	112
4.15	Density profile of a DHS fluid in comparison with that of the corresponding HS fluid: $\rho_b d^3 = 0.7$ and $m^{*2} = 2$	112
4.16	Density profiles of HS and DHS fluids ($2H = 2d$, $\rho_b d^3 = 0.7$ and $m^{*2} = 2$). The density profiles are depicted on the left and the dipole orientation distribution is presented on the right.	113
4.17	Same configuration as in Fig. 4.16 with $2H = 2.5d$	114
4.18	Same configuration as in Fig. 4.16 with $2H = 3d$	114
4.19	Disjoining pressure profile of the DHS fluid in comparison with that of the HS fluid: $\rho_b d^3 = 0.7$ and $m^{*2} = 2$	115
4.20	Density profiles of ions in the EDL space with $2H = 4d$, $\rho_d^b d^3 = 0.734$, $d = 2.8\text{\AA}$, $m^{*2} = 0.02$, $\Sigma = -0.0135\text{ C/m}^2$ and $c_b = 10^{-3}\text{ mol/L}$	123
4.21	As in Fig. 4.20 for the dipole density profile and that of the corresponding hard sphere fluid.	123
4.22	The evolution of the different electric fields in the EDL space.	124
5.1	Experimental setup of the swelling pressure tests performed by Imbert and Villar [11].	138
5.2	Evolution of the swelling pressure and the saturation degree during water infiltration of the pellets/bentonite powder mixture of the experiment MGR7 in [11].	138
5.3	Multi-scale structure of swelling clays.	139
5.4	Distribution of (a) the water molecule density and (b) solvation pressure as a function of the interlayer space [12].	142
5.5	Disjoining pressure profiles of a PB fluid ($c_b = 10^{-4}\text{ mol/l}$) and a HS fluid ($\rho_b d^3 = 0.73$) as a function of normalized inter platelet distance $2H/d$ ($d_{H_2O} = 2.8\text{\AA}$).	143
5.6	Disjoining pressure profiles obtained with a PB law Eq.(5.7) for $c_b = 10^{-4}\text{ mol/l}$ and with a HS fluid Eq.(5.8). The red point indicates the value at the initial state of the imbibition experiment equal to the capillary pressure.	148

5.7	Representation of the sample at intermediate saturations as composed of two parts: the bottom being fully saturated and the top at the initial saturation. The overall saturation is obtained by the volume ratio of the two parts. On the left: configuration without local deformation; on the right: with local deformation Δ due to different water contents	150
5.8	(a) Numerical results of the swelling pressure as a function of the overall saturation of the medium and comparison to the experimental data from [11]; (b) Disjoining pressure in the bottom (saturated \rightarrow PB law) and in the top part (initial state \rightarrow HS law). The curves are obtained with with $K_s = 5$ MPa.	154
5.9	(a) External pressure as a function of the total saturation of the medium for different values of K_s . (b) Evolution of the swelling pressure at the final (saturated) state as a function of the microscopic bulk modulus K_s	155
5.10	Deformation in the bottom (at full saturation) and top (at initial saturation) parts as a function of the total saturation of the medium for $K_s = 5$ MPa.	156
5.11	Volumetric strain of (a) the micropores and (b) the clay particles in the bottom (saturated) and top (initial state) parts as a function of the total saturation of the medium for $K_s = 5$ MPa.	157
5.12	Volumetric strain of (a) the micropores and (b) the clay particles at the fully saturated state as a function of the microscopic bulk modulus K_s	158
5.13	Variation of the disjoining pressure between the initial ($S_w^i = 0.26$) and the final fully saturated state as a function of the microscopic bulk modulus K_s	159

List of Tables

B.1	Hankel transform.	89
4.1	Evaluation of angular convolutions of the basic functions.	96

Nomenclature

Latin symbol

D	: electric displacement field
E	: electric field
I	: identity tensor
M	: total electric moment
m	: dipole moment
n	: normal vector
P	: medium polarization
\mathbf{r}	: spatial particle position
B	: Bridge function
c	: direct correlation function
c_-	: anion concentration
c_+	: cation concentration
d	: particle diameter
\mathcal{F}	: intrinsic free energy
g	: radial distribution function
h	: total correlation function
H	: half of separation distance between two parallel walls
K_s	: microscopic bulk modulus
	: macroscopic bulk modulus
k_B	: Boltzmann constant
m^*	: reduce dipole moment
N	: number of particles
n_α	: weighted density
n_f	: micro-porosity
P	: polarization
P_f	: capillary pressure
p	: fluid pressure
q	: volumetric ion charge density
S	: sphere surface
r_c	: cut-off radius
T	: absolute temperature
T^*	: reduced temperature
u	: interparticle potential
s	: normalization of indirect correlation function
V	: volume
V_{ext}	: external potential
y	: cavity distribution function

Greek symbol

α	: dipole orientation distribution
β	: inverse temperature
ϵ_0	: vacuum permittivity constant
ϵ_0	: relative permittivity constant
Σ	: surface charge
μ	: chemical potential
$\tilde{\mu}$: electrochemical potential
ψ	: electric potential relative to the bulk value
λ_D	: Debye length
τ_M	: Maxwell stress tensor
Π_d	: disjoining pressure
Ω	: grand potential
ρ	: particle density
Λ	: thermal de Broglie
γ	: indirect correlation function
λ	: coupling parameter
Θ	: Heaviside function
ω	: weight function
ξ	: Scaled Particle Theory variable
δ	: Dirac function
Φ	: reduced excess free energy
η	: packing fraction
σ	: Lennard-Jones interaction range
σ_T	: total stress
σ_E	: effective contact stress
μ_s	: microscopic shear modulus
ν_s	: Poisson coefficient of clay particle
χ^{eff}	: effective Bishop tensor

Subscript and superscript

+	: cation
-	: anion
<i>b</i>	: bulk
0	: reference system
$\hat{}$: Fourier transform
$\tilde{}$: Hankel transform
<i>HS</i>	Hard Sphere
<i>LJ</i>	Lennard-Jones
<i>id</i>	ideal
<i>ex</i>	excess
<i>corr</i>	correlation
<i>dd</i>	dipole-dipole
<i>el</i>	electric
<i>CS</i>	Carnahan-Starling

Introduction

Swelling hydrated clays are encountered in various aspects of life ranging from agricultural activities, environmental protection and industry processes to civil engineering. They are used for example as water barriers, clay liners for high-level radioactive waste management or drying mud for petroleum exploitation [13]. An important feature is the swell-shrink behavior which can be troublesome: it is able to cause the collapse of buildings, bridges, roads, rails and tunnels constructed on swelling clay sites. In the petroleum industry, the stability of boreholes drilled through clay-rich shales is strongly dependent on their swelling capacity. Resolving such problems requires a deep understanding of the physical phenomena underlying the swell-shrink behavior of expansive clayey soils.

In this framework, the present work focuses on modeling the mechanical behavior of smectites which are the main mineral component of expansive clays. At the nanoscopic scale they are composed of an assembly of electrically charged phyllosilicate layers called platelets. Their negative charge stems from isomorphous substitutions of structural cations of higher valence by others with lower valence and the presence of defects in the smectite crystal lattice. In order to achieve global electroneutrality, exchangeable cations are present in the interlayer space [14]. This negative charge is primarily responsible for a variety of coupled hydro-mechanical electrochemical phenomena such as swelling when imbibing the interlayer space with water or polar organic solvents. The understanding of the physical phenomena at the origin of the swelling of hydrated smectites is therefore a central task in modeling expansive clayey soils.

A crucial feature for modeling clayey soils is a reasonable geometrical representation. Expansive clays exhibit a hierarchy of structures which are characterized at least by three distinct length scales (nano, micro and macro) and two porosity levels (nano and micro-pores) [15]. The finest scale is the nanoscale, wherein the charged clay platelets are separated by a nanoporous network saturated by an aqueous electrolyte solution. The negative surface charge of the platelets attracts the cations of the electrolyte solution in order to ensure global electroneutrality. Because of this attraction, the cation concentration in the vicinity of the clay surface exceeds that of the equilibrium solution far away from the clay surface referred to as “bulk” solution. The positively charged cations close to the negatively charged clay platelet surface form a diffuse “Electrical Double Layer” (EDL). The characteristic length of the EDL is the Debye’s length $\mathcal{O}(10^{-9} \text{ m})$ which gives the length over which the charged particles interact. At the intermediate microscale of characteristic length $\mathcal{O}(10^{-6} \text{ m})$, the clay platelets assemble to swollen clay clusters which constitute the solid phase at that length scale. The latter are separated by a network of micropores filled either by pure bulk water at full saturation or by a mixture of water and air in the unsaturated case. Regarding their size the micropores are completely free of EDL effects.

Based on this local configuration, the purpose is to make predictions about the mechanical behavior of these media at the observable macroscale. One of the most rigorous techniques to upscale the coupled hydro-mechanical electrochemical phenomena occurring at the nano- and microscales to the observable macroscale is periodic homogenization [16]. That is why this procedure is used in the frame of this Ph.D thesis to derive the macroscopic constitutive laws which are relevant for civil engineers. In this scope, studying the phenomena occurring at the local scales and more precisely at the nanoscale plays a crucial role in modeling expansive

clays.

The classical approach for modeling the physical phenomena occurring at the nanoscale is the EDL theory, initially proposed by Gouy and Chapman [17], in which the water solvent is considered as a dielectric continuum and the ions as point charges. The swelling pressure is the repulsion resulting from the combined effects of the electrostatic attraction between the negative surface charge of the clay platelets with the dissolved cation cloud of the electrolyte solution and the predominant role of the osmotic pressure. It can be obtained by solving the classical Poisson-Boltzmann (PB) problem. Despite its simplicity, this approach is able to describe quantitatively the EDL behavior at high hydration levels, in the so-called osmotic swelling regime [18]. However, the PB model predicts only swelling and fails at low hydration in the so-called crystalline swelling regime. Thus, many extensions of the PB theory have been proposed to improve the nanoscale description [19]. In order to account for both swelling and shrinkage in the crystalline swelling regime, most of them include the finite size and correlation effects between ions only, while keeping the assumption of a continuous water solvent [20]. Although the water solvent does not contribute to the formation of the EDL, it plays an utmost important role in the nanoscale behavior because of its dominant density compared to that of ions. However, the complexity in modeling water makes the full understanding of the nanoscale behavior of expansive clays a huge challenge. Today, along with the development of computer performance, the behavior inside the EDL can be predicted correctly by Molecular Dynamics (MD) and Monte Carlo (MC) simulations if the interparticle interactions are exactly known. Nevertheless, these techniques are so far computationally expensive and almost impossible to include into upscaling methods to propagate the physical phenomena from the nano- to the macroscale. Hence, less detailed physical approaches are more convenient but yield inherently less satisfying results in comparison with simulation data.

The present work aims at filling this gap. The main task is to propose an improved description of the nanoscale behavior of clayey soils by accounting for the molecular nature of the water solvent. Different phenomena of increasing complexity are consecutively taken into account such as the finite size and polar nature of the water solvent through interparticle correlations in the electrolyte solution in order to reproduce experimental observations at low interplatelet distances (crystalline swelling). To this end, this thesis treats firstly the pure solvent only, because of its crucial role, as i) a simple Hard Sphere (HS) fluid accounting for particle size effects only; ii) a Lennard-Jones (LJ) fluid averaging over the different dipolar interactions ; and iii) a Dipolar Hard Sphere (DHS) fluid to account more precisely for dipolar interactions. Ions are finally added to complete the EDL model. According to the general plan discussed above, this thesis is organized in five chapters.

Chapter 1 presents firstly the multiscale structure of expansive clays with an emphasize on the nanoscale structure. The particular physical characteristics at that length scale which governs the swelling behavior during hydration are discussed. A three-scale scheme of swelling clays is then proposed which serves as basis in the present model approach for transferring the coupled hydro-mechanical electrochemical phenomena from the nano- to the macroscale. The Poisson-Boltzmann theory is briefly recalled to give an idea of the classical nanoscale portrait. An overview of several existing improvements of the Poisson-Boltzmann model are then presented which allow to account for the molecular nature of the ions in the electrolyte solution. Their limitations in comparison with experimental results are the starting point of the present approach.

To model the nanoscale behavior the Density Functional Theory (DFT) approach is chosen in the present work. In this context, chapter 2 firstly presents the basic features of this method. Interparticle correlation effects play a significant role in the fluid behavior and are studied in the frame of this theory through the Radial Distribution Function (RDF). The RDF and its determination are thus presented using an approach of statistical mechanics. As hard sphere fluids are the fundamental reference systems of all kinds of discontinuous fluids, the principle

ideas of Fundamental Measure Theory (FMT), the most efficient approach of the DFT for studying such fluid systems, are finally recalled in this chapter.

In chapter 3, the water solvent is treated as an inhomogeneous Lennard-Jones fluid which is the simplest way to account for its polar nature. In contrast to HS fluids which account only for repulsive interparticle interactions, the LJ interaction potential consists of a short-range repulsive and a long-range attractive part. The repulsive part can be treated by FMT by considering an equivalent hard sphere potential while the attractive part is here explicitly studied by using an exact DFT approach called Density-Functional Perturbation Theory (DFPT). In the present DFPT approach, interparticle correlations are determined by solving the Ornstein-Zernike equation supplemented by the HyperNetted-Chain (HNC) closure including an appropriate bridge function. Ions are finally added to an appropriate Lennard-Jones fluid in order to give a first estimate of the EDL behavior.

Chapter 4 considers explicitly the finite size and polar nature of the water solvent by a representation as a Dipolar Hard Sphere (DHS) fluid whose behavior depends on both the spatial positions and the dipole orientation of the molecules. Similar to the LJ fluid, the DHS fluid comprises a short-range hard sphere interaction potential which is treated by FMT. The complex long-range dipolar interaction part is modeled by a modified DFPT approach in which intermolecular dipole-dipole correlation effects are calculated using the Mean Spherical Approximation (MSA) as initially proposed by Wertheim [21]. Ions are then added to complete the DHS water model in the EDL.

Chapter 5 presents finally an application example of the work of this thesis towards civil engineering. The idea is to incorporate the improved nanoscale portrait developed in the framework of this thesis in the double-porosity model of the modified effective stress principle of unsaturated swelling clays recently derived by our group using periodic homogenization [22]. The resulting model is then applied to simulate numerically the swelling pressure evolution during hydration at fixed volume. Starting from a formulation of the mechanical equilibrium at both the nanoscale of the electrical-double layer and the microscale where capillary effects take place, the coupling between these two effects is incorporated in the overall stress over the entire saturation range. The numerical results indicate that considerable improvements of the model predictions at the macroscale can be obtained with a more accurate formulation of the nanoscale phenomena by accounting for intermolecular correlation effects in the electrolyte solution.

Chapter 1

Introduction to the modeling of expansive clays

Smectites are the main component of expansive clays which are widespread in nature. The shrink-swell behavior is a particular physical characteristic of such media, which is at the origin of many serious challenges in civil engineering. Understanding of the coupled hydro-mechanical electrochemical phenomena underlying the swelling is therefore a crucial requirement.

To this end, this chapter starts by presenting the typical structure of smectite clays which underlies their physical properties. Several important characteristics of smectites such as their hydration behavior, exchangeable cation capacity and the swelling mechanism are then presented. In the last part of this chapter, a typical multi-scale model of swelling clays is presented which will be applied in the last chapter of this Ph.D. thesis to transpose the mechanical behavior from the nanoscopic clay platelet scale to the observable macro scale using a periodic homogenization method.

1.1 Clay mineralogy

Clays are probably the most active constituent of soils. With a grain size of less than 2μ , the influence of clay minerals on the soil properties depends not only on their quantity in the soil, but essentially on their nature. In order to understand the coupled hydro-mechanical electrochemical phenomena of expansive clayey soils, it is thus necessary to know the crystal structure and composition of clay minerals in general and of smectites in particular, as they are the clay group that exhibits swelling.

1.1.1 Basic structures and classification of clay minerals

The most commonly layered lattice structure of clay minerals is made up of two basic structural units: a silica tetrahedron (T) and an aluminum octahedron (O). The silica tetrahedron is formed by a silicon cation SiO^{4+} with four surrounding oxygen anions O^{2-} arranged in a way to define the corners of a tetrahedron. Each tetrahedron shares its three corners with its neighbors to form a hexagonal network called the tetrahedral sheet (Fig.1.1). The aluminum octahedron is composed of an aluminium Al^{3+} (or magnesium Mg^{2+}) cation surrounded by six hydroxyl groups OH^- . Multiple edge-sharing octahedra build up the octahedral sheet (Fig.1.2).

These two basic sheets are arranged into layers which are called *phyllosilicates* and often described as 2:1 if they consist of two tetrahedral and one octahedral sheet (TOT) or 1:1 if they involve units of alternating tetrahedral and octahedral sheets (TO). The kaolinite and halloysite groups are build by 1:1 phyllosilicates whose basic structural unit is asymmetric. In contrast, the basic structural unit of 2:1 clays (TOT) is symmetric. The TOT unit can be found

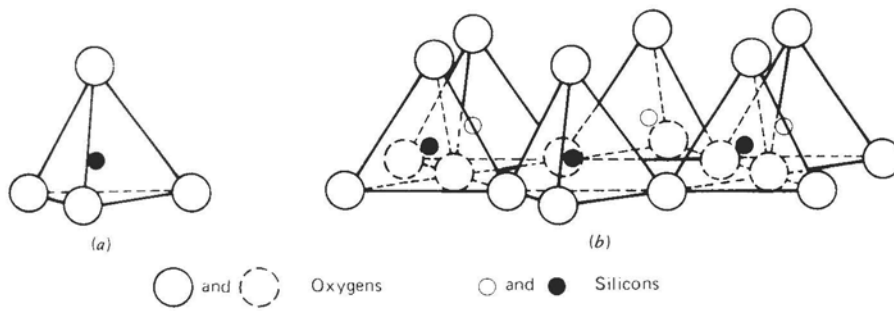


Figure 1.1: (a) Silica tetrahedron unit; (b) Silica tetrahedra arranged in a hexagonal network [1].

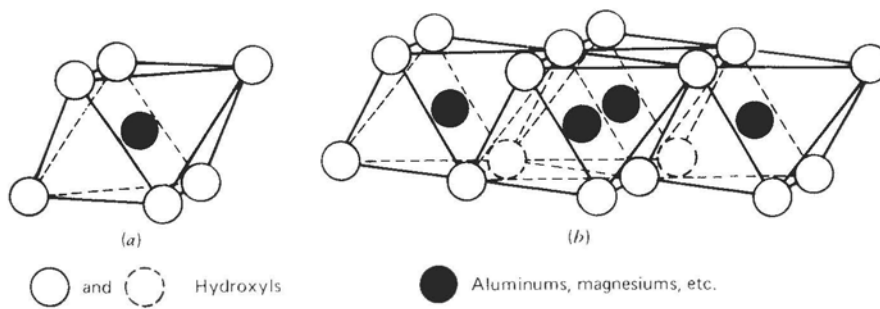


Figure 1.2: (a) Octahedral unit; (b) Sheet structure built by octahedral units [1].

in many groups such as the mica, smectite and vermiculite groups which can be distinguished according to their mineral structure and physical properties (Fig.1.3).

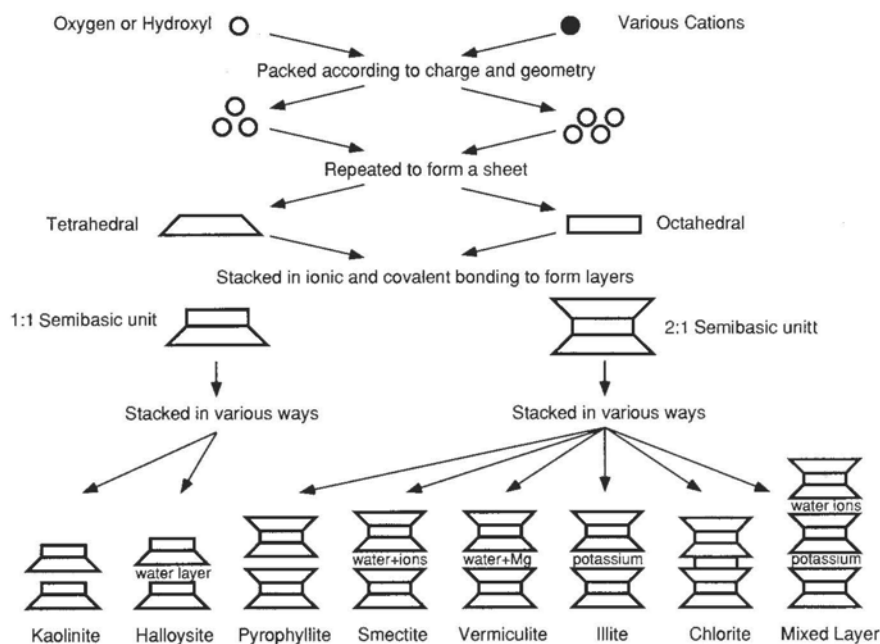


Figure 1.3: Schematic representation of several clay mineral groups [1].

1.1.2 Isomorphous substitution

In practice, the structural composition of the phyllosilicate layers is often modified through the substitution of one cation in the clay sheet by another cation of lower valence and of the same size without changing the basic structure of the crystal. Common examples include the substitution of Si^{4+} by Al^{3+} in the tetrahedra sheet, and Al^{3+} by Mg^{2+} , Fe^{2+} in the octahedral sheet. Such process is referred to as *isomorphous substitution* which is the primary source of the negative surface charge of the phyllosilicate layer of the smectite group which is compensated by cations in the electrolyte solution filling the interlayer space. It is this process that is responsible for many particular physical phenomena of clay soils such as swelling and shrinkage.

As an example Fig.1.4 presents the basic crystal structure of montmorillonite, the most common member of the smectite group which is the main component of most expansive soils. The interlayer space between the clay sheets contains water and free ions in order to ensure the overall electroneutrality of the system (clay sheets + interlayer fluid). The clay sheets are weakly linked to each other, which allows the smectites to swell.

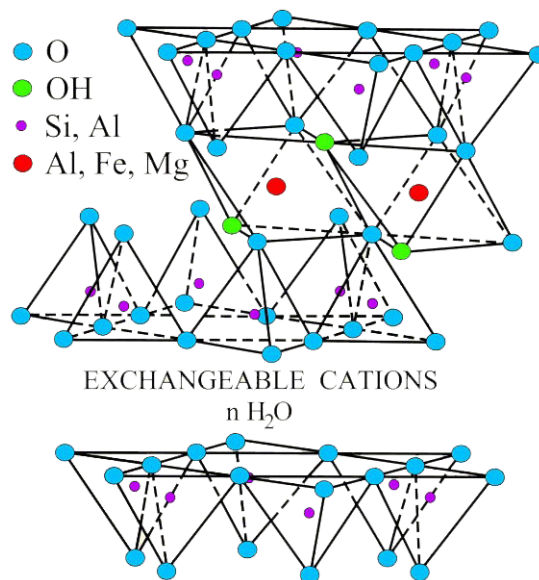


Figure 1.4: Structure diagram of montmorillonite [1].

1.2 Swelling mechanisms of clays

The swelling behavior is a complex mechanism of hydrated expansive clays which stems from water-clay interactions at the clay platelet scale. This process is commonly distinguished into two regimes: crystalline and osmotic swelling corresponding to low and high hydration state of clays. Crystalline swelling takes place when dry expansive clays are in contact with water and then sequentially intercalate one, two, three, or four discrete layers of water in the interlayer space. This process occurs firstly and is controlled by hydration energy forces while osmotic swelling is associated with longer-range electrical double layer effects.

1.2.1 Crystalline swelling and cation hydration

Because of their negative surface charge, two adjacent 2:1 smectite layers tend *a priori* to repel each other. In contrast, the presence of exchangeable cations located near the platelet surface in the interlayer space or in the hexagonal holes of the tetrahedral sheets to ensure global

electroneutrality, adds an attractive interaction, and decreases the interlayer distance. When the dry smectite is in contact with water, the interlayer cations will be hydrated and polar molecules such as ethylene glycol or glycerol can be introduced into the interlayer space which leads to a widening of the interlayer space referred to as *swelling*. At very low hydration, the so-called “crystalline swelling” is a discrete process which corresponds to the intercalation of 0 to 4 layers of water molecules [13] (Fig.1.5). During the cation hydration mechanism, the water molecules are more or less ordered because of the orientation of their negative pole toward the hydrated cation which reduces the intermolecular attraction force between the clay platelet surface and the interlayer cations. X-ray diffraction analyses confirm that the expansion of

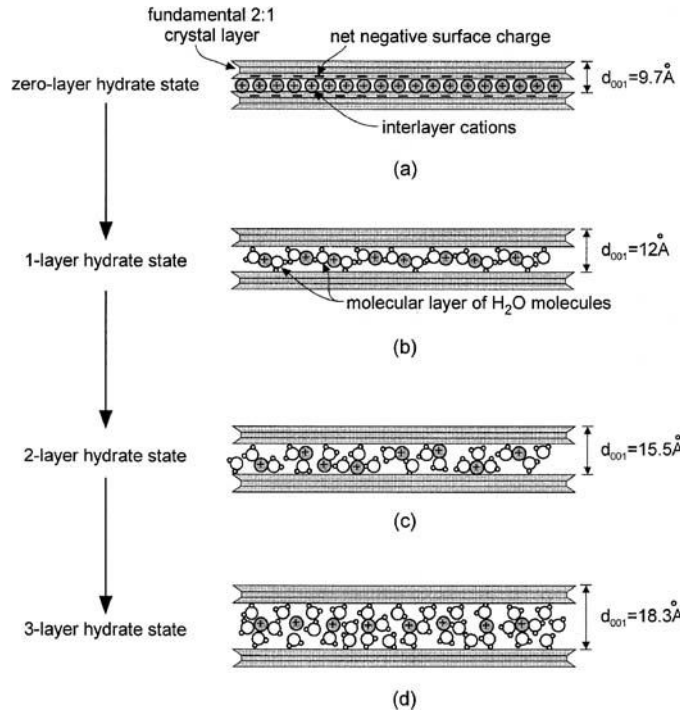


FIG. 1—Conceptual model of the sequential crystalline swelling process for smectite

Figure 1.5: Conceptual model of the sequential crystalline swelling process for smectite

smectites during the crystalline swelling regime is a discrete process [23, 24]. It can be observed in the water vapor adsorption isotherm [3]. Figure 1.6 presents an evolution of the interlayer distance of Na-Montmorillonites with the relative water pressure during the water adsorption isotherm, which allows to determine the swelling pressure for the crystalline swelling. For a pure montmorillonite, this pressure is of about 1.1×10^8 and 0.27×10^8 Pa, corresponding to the formation of one, two and three water layers, respectively [25].

1.2.2 Osmotic swelling and electrical double layer

When the interlayer distance exceeds 4 water layers, the solvation forces between the cations and the clay layers become negligible in comparison with the electrostatic forces between the adjacent layers. This second swelling regime is referred to as *osmotic swelling*.

To ensure global electroneutrality, highly charged clay sheets attract dissolved anions close to the solid surface in the interlayer space. The cation concentration adjacent to the surface is therefore extremely high compared that of the bulk electrolyte solution, while that of anions in the vicinity of the clay particles is very low. In this region, the cation concentration decreases with the distance away from the clay platelets while that of anions increases

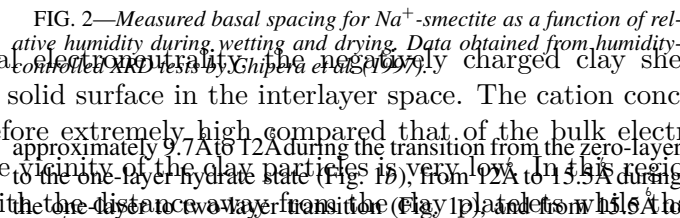


FIG. 2—Measured basal spacing for Na⁺-smectite as a function of relative humidity during wetting and drying. Data obtained from humidity-controlled XRD tests by Chipera et al. (1997).

For Na⁺-smectite undergoing a wetting (adsorption) process, the relative humidity (RH) regimes corresponding to stable hydrate states are approximately 30 % RH–60 % RH for stability of the one-layer state and greater than 75 % RH for stability of the two-layer state.

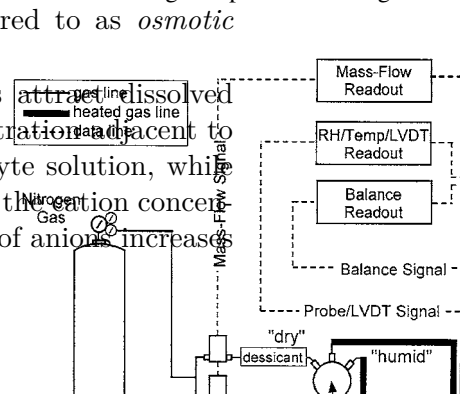
relative humidity. Computer simulations of Chipera et al. (1996) suggest that gravimetric water adsorption for smectite at the one-layer, two-layer, and three-layer states are approximately 10, 19, and 22 %, respectively.

Depending on the effective charge properties of the clay surface and the type and valency of predominant cations (e.g., Na⁺ or Ca²⁺), crystalline swelling either involves one to four layers of water or additional interlayer water. Osmotic swelling proceeds within the interlayer space beyond the third or fourth layer of water, a process that fills the pore space, resulting in bulk volume changes of several hundred percent for smectite under free swelling conditions (Norrish 1954). Volume changes associated with the crystalline swelling process, however, remain positive.

Direct measurements of deformations associated with osmotic swelling have historically been limited to the micrometer (layer) scale. Humidity-controlled XRD studies have afforded measurements of transitions in basal spacing during the crystalline swelling process and are prevalent in the geotechnical literature (e.g., Gillery 1959; Del Pennino et al. 1994; Chipera et al. 1997). These studies have provided a wealth of information regarding the swelling mechanism at the molecular level, but are unable to provide evidence regarding the macroscopic volume change behavior of bulk specimens. The experimental system described in the following section was developed to investigate this issue.

Experimental System

A humidity-controlled experimental system was developed to study the relationship between ambient relative humidity and the swelling behavior of expansive clay materials (see section 1.2.2). This system was adapted from the experimental system described in a previous article (Loko and Lu 2003). Simple modifications have been made such that the system can accommodate a large strain of compacted clay specimens, in addition to the measurement of relative humidity content, may also be continuously measured. Figure 3 shows a schematic of the current experimental system. Relative humidity is controlled in a closed environmental chamber by independent flow of vapor-saturated (“wet”) and desiccated (“dry”) air using two mass-flow controllers (MKS Instrumentation) and a specimen-testing chamber.



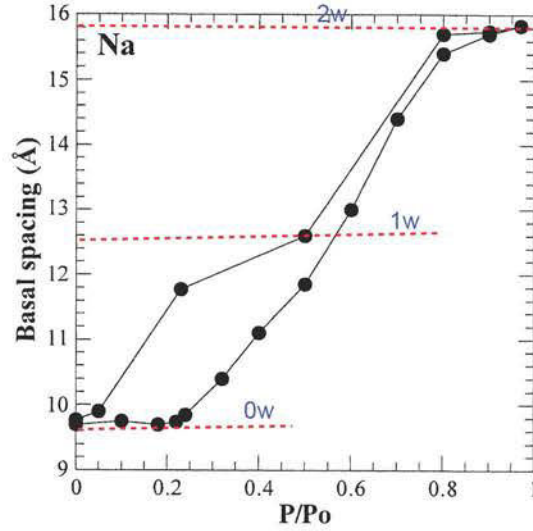


Figure 1.6: Evolution of basal distance with relative water pressure for Na-Montmorillonites, where P/P_0 designates the relative pressure of the adsorbed water. The formation of 0,1 and 2 layers of water is also observed [3].

until reaching the bulk values. Its length is characterized by the Debye's length. Together with the negatively charged clay platelet surface it builds the so-termed *Diffuse Double Layer* or *Electrical Double Layer* (EDL) [26]. The excess of the cation concentration inside the EDL is at the origin of an osmotic water flow from the bulk solution to the inter-platelet space to restore equilibrium [25]. The equilibrium state of the clay platelet configuration results from the competition between electrostatic attraction and osmotic repulsion forces.

When two clay platelets approach, their respective double layers begin to overlap. The repulsion resulting from this overlap is responsible for the osmotic swelling which is, contrarily to the crystalline swelling, a continuous process (Fig.1.7).

1.3 Electrical double layer theory

In the classical EDL theory, the nanoscale clay portrait is composed of two parallel incompressible solid platelets with a negative surface charge separated by a distance $2H$. The inter-platelet space is filled by an aqueous binary electrolyte solution with completely dissolved monovalent ions being in thermodynamic equilibrium with an external reservoir (called *bulk*) containing the same electrolyte solution. In order to ensure global electroneutrality, the negative surface charge of the clay platelets is compensated by an excess of cations close to the interface building the EDL (Fig.1.8). In this section, the ion concentration profiles will be studied in the framework of Poisson-Boltzmann theory in order to describe qualitatively physical phenomena occurring at the nanoscale such as the disjoining pressure.

1.3.1 Classical Poisson-Boltzmann Theory

The Poisson-Boltzmann theory is the classical continuous approach to describe qualitatively EDL phenomena. It is based on the following assumptions:

1. Ions are considered as point charges without any interparticle interactions.
2. The negative charge of the clay sheets is supposed to be uniformly distributed over their surface.

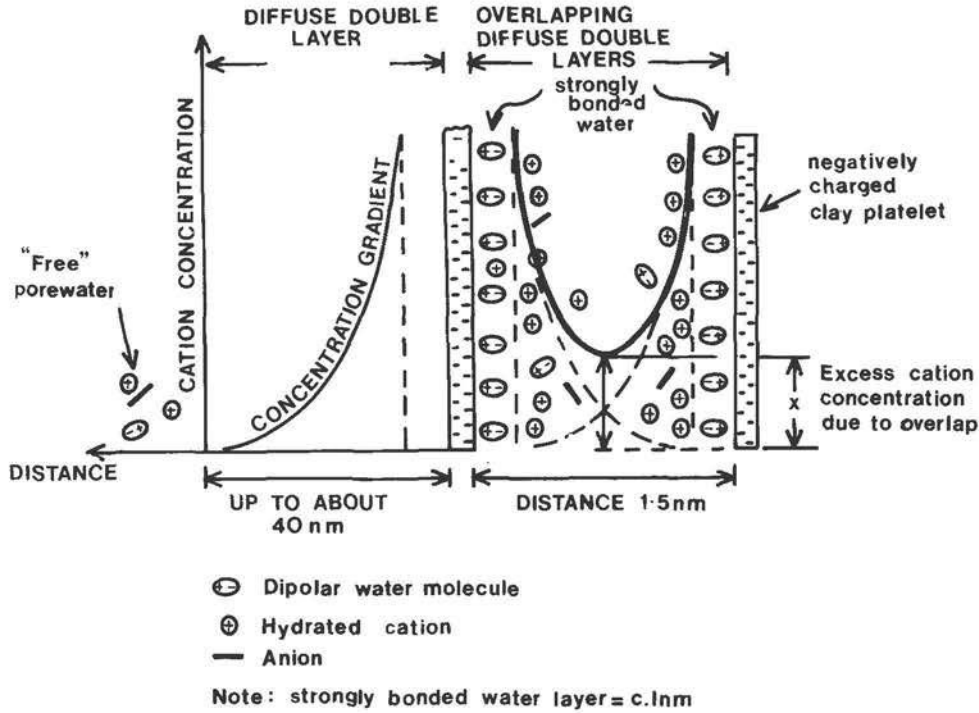


FIG. 5. Model of double-layer (osmotic) swelling of two clay mineral platelets. Double-layer

Figure 1.7: Scheme of the Electrical Double Layer between two adjacent clay platelets [4].

Molecular Nature of the Solvent

Scale Clay Models



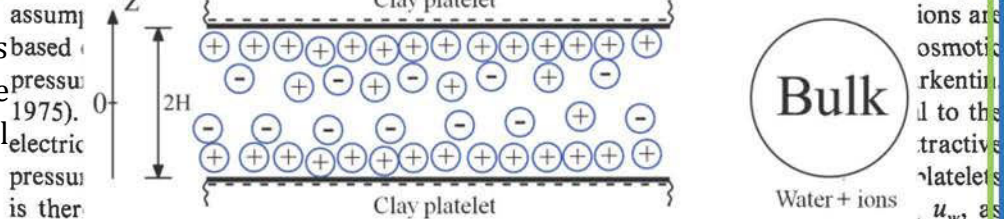
ia MAINKA, Christian MOYNE

inique Théorique et Appliquée), Vandoeuvre-les-Nancy, France

Introduction

swelling since an 'out of balance' cation condition will be created and water will be drawn into the system to restore equilibrium.

Swelling pressures can be calculated from double-layer theory if a number of simplifying



Electrical Double Layer scheme

Electrolyte concentration, cation valency, temperature and dielectric constant all play their part in pl... low concentration generate

Computational methods

❖ Density Functional Theory (DFT)

Grand potential $\Omega[\rho] = F[\rho] + \int dr [V(r) - \mu]$

Equilibrium state $\frac{\delta \Omega[\rho]}{\delta \rho(\mathbf{r})} \Big|_{V,T,\mu} = 0 \rightarrow \rho(\mathbf{r}) = \rho_b \exp \left\{ \beta \left(\mu_b^{ex} - \frac{\delta F^{ex}}{\delta \rho(\mathbf{r})} - V(\mathbf{r}) \right) \right\}$

3. The water solvent is simulated by a dielectric continuous medium with a constant permittivity.

A binary 1:1 electrolyte solution (e.g. Na^+ and Cl^-) is selected to study the ion concentration distributions (c_+ and c_-) inside the EDL. Note that the ion densities are identical in the neutral bulk fluid ($c_+^b = c_-^b = c_b$).

Denoting by \mathbf{E} , Φ and q , the electric field, potential and volumetric ion charge density in the EDL space, respectively, the governing equations of the system are given by

$$\nabla \cdot (\epsilon \epsilon_0 \mathbf{E}) = q, \quad (1.1)$$

$$\mathbf{E} = -\nabla \Phi, \quad (1.2)$$

$$q = F(c_+ - c_-), \quad (1.3)$$

where F is the Farady constant, ϵ_0 the vacuum permittivity and ϵ the relative dielectric constant of the solvent.

In the one-dimensional case, Φ depends only on the spatial coordinate perpendicular to the plates denoted by z (Fig.1.8). As a result, the 1D Poisson equation is directly obtained from the above equations

$$\epsilon \epsilon_0 \frac{d^2 \Phi}{dz^2} = -F(c_+ - c_-). \quad (1.4)$$

It is completed by the Neumann boundary condition resulting from the electroneutrality condition

$$\mathbf{E} \cdot \mathbf{n} = -\frac{d\Phi}{dn} = -\frac{\Sigma}{\epsilon \epsilon_0}, \quad (1.5)$$

where \mathbf{n} is the normal vector outward to the solid phase and Σ the surface charge.

In what follows, the Boltzmann distribution is derived for the ions inside the EDL. The concentration of ion i (Na^+ and Cl^- in this case) of an ideal mixture is related to the chemical potential μ_i by

$$\mu_i = \mu_i^0 + RT \ln \frac{c_i}{c_i^0}, \quad (1.6)$$

where R is the ideal gas constant, μ_i^0 the reference chemical potential of ion i at the concentration c_i^0 . The electrochemical potential $\tilde{\mu}_i$ is then introduced, which is, in this case, the mechanical work being necessary to bring the ion i from a reference state (where the electrical potential is defined as zero) to a specified concentration and electrical potential

$$\begin{aligned} \tilde{\mu}_i &= \mu_i + Fz_i \Phi \\ &= \mu_i^0 + RT \ln \frac{c_i}{c_i^0} + Fz_i \Phi, \end{aligned} \quad (1.7)$$

with z_i denoting the ion valence. In the bulk fluid, the electrochemical potential is given by

$$\tilde{\mu}_i^b = \mu_i^0 + RT \ln \frac{c_b}{c_i^0} + Fz_i \Phi_b. \quad (1.8)$$

At the thermodynamic equilibrium, the electrochemical potential is uniform $\tilde{\mu}_i = \tilde{\mu}_i^b$, so that the combination of Eqs. (1.7) and (1.8) leads to the Boltzmann distribution

$$c_i = c_b \exp\left(-\frac{Fz_i \psi}{RT}\right), \quad (1.9)$$

where $\psi = \Phi - \Phi_b$ is the electric potential relative to the bulk value. The combination of Eq.(1.4) and Eq.(1.9) builds the classical Poisson-Boltzmann (PB) theory. Applied to the

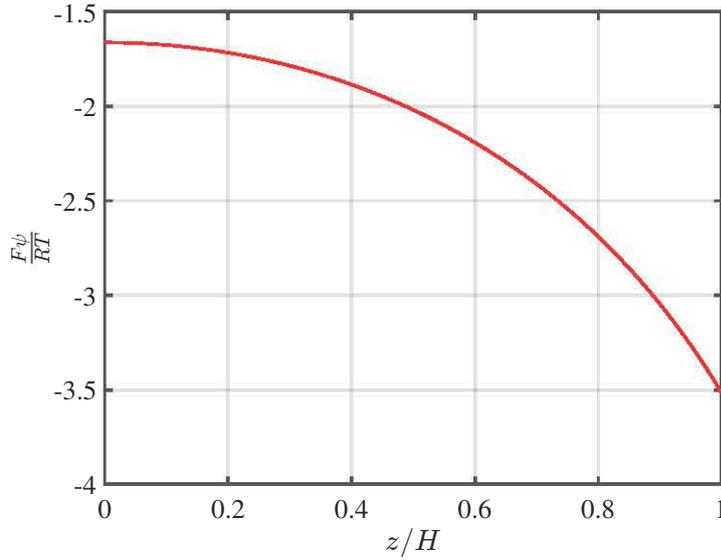


Figure 1.9: Profile of the electric potential inside the EDL in the case of a 1:1 electrolyte solution, $c_b = 0.1 \text{ mol/l}$; $\Sigma = -0.1 \text{ C.m}^{-2}$; $H=1 \text{ nm}$.

planar geometry in Fig.1.8 with $-H \leq z \leq H$, this theory allows to numerically calculate the 1D profile of the relative electric potential $\psi(z)$ inside the EDL from

$$\begin{aligned} \epsilon\epsilon_0 \frac{d^2\psi}{dz^2} &= -Fc_b \left[\exp\left(-\frac{F\psi}{RT}\right) - \exp\left(\frac{F\psi}{RT}\right) \right] \\ &= 2Fc_b \sinh\left(\frac{F\psi}{RT}\right), \end{aligned} \quad (1.10)$$

or

$$\frac{d^2\psi}{dz^2} = \frac{2Fc_b}{\epsilon\epsilon_0} \sinh\left(\frac{F\psi}{RT}\right), \quad (1.11)$$

supplemented by the boundary condition (1.5) which is rewritten as

$$\left. \frac{d\psi}{dz} \right|_{z=H} = -\frac{\Sigma}{\epsilon\epsilon_0}. \quad (1.12)$$

The ion concentration distributions are finally obtained with Eq.(1.9).

In this ionic liquid theory, it is useful to introduce a characteristic length scale named the Debye length which is defined as

$$\lambda_D = \sqrt{\frac{\epsilon\epsilon_0 RT}{\sum_i q_i^2 c_i}}. \quad (1.13)$$

It determines the scale over which the electric potential and the ion concentrations vary inside the electrolyte solution away from the charged clay platelet surface. That is an order of magnitude of the EDL thickness.

Numerical results for the electric potential and the ion concentration profiles are illustrated in Fig.1.9 and Fig.1.10, respectively. The cation concentration increases monotonously from the center to the solid surface and is dominant compared to that of anions which evolves inversely.

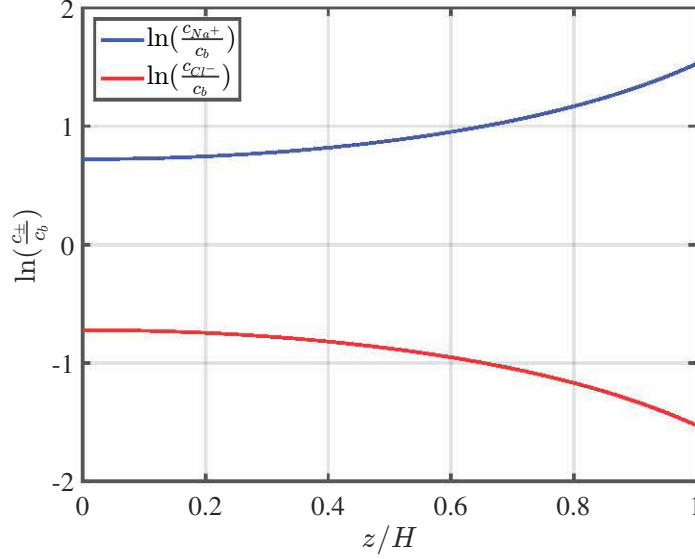


Figure 1.10: Ion distributions in the EDL space for the case of a 1:1 electrolyte solution, $c_b = 0.1\text{mol/l}$; $\Sigma = -0.1\text{C.m}^{-2}$; $H=1\text{nm}$.

1.3.2 Disjoining pressure

Macroscopic expansion is an important characteristic property of smectites, which arises among other phenomena from electrochemical repulsion in the clay-water system at the nanoscopic clay platelet scale. In the classical EDL theory, only the interactions between cations and the negatively charged clay platelets are considered to be at the origin of the so-called disjoining pressure at the nanoscale and of the resulting swelling pressure of the overall medium at the macroscale. In what follows the disjoining pressure is derived for an EDL system by using the Poisson-Boltzmann model.

Designating by p the fluid pressure, the mechanical equilibrium equation for the 1D case of the EDL is written as [27]

$$-\frac{dp}{dz} + qE = 0. \quad (1.14)$$

In combination with Eqs.(1.2), (1.3) and (1.9), the above equation becomes

$$-\frac{dp}{dz} + 2Fc_b \sinh\left(\frac{F\psi}{RT}\right) \frac{d\psi}{dz} = 0, \quad (1.15)$$

$$-\frac{d}{dz} \left[p - 2RTc_b \cosh\left(\frac{F\psi}{RT}\right) \right] = 0, \quad (1.16)$$

which means that the term $p - 2RTc_b \cosh\left(\frac{F\psi}{RT}\right)$ is independent of z . In the case of large separation distances, the bulk behavior is found at the center between the two plates with $\psi = 0$ and $p = p_b$ (p_b designates the bulk pressure), which allows to write

$$p - 2RTc_b \cosh\left(\frac{F\psi}{RT}\right) = p_b - 2RTc_b. \quad (1.17)$$

Rearranging the terms of the above equation and using Eq.(1.9) the pressure of the fluid phase is then given by

$$p = p_b + 2RTc_b \left[\cosh\left(\frac{F\psi}{RT}\right) - 1 \right]$$

$$\begin{aligned}
 &= p_b + RT [c_+ + c_- - 2c_b] \\
 &= p_b + \pi,
 \end{aligned} \tag{1.18}$$

where the Donnan osmotic pressure is introduced as [28]

$$\pi = RT [c_+ + c_- - 2c_b]. \tag{1.19}$$

Eq.(1.14) can be rewritten as

$$-\nabla p + \nabla \cdot \tau_M = 0, \tag{1.20}$$

where the Maxwell stress tensor is defined by

$$\tau_M = \epsilon\epsilon_0 \left(\mathbf{E} \otimes \mathbf{E} - \frac{E^2}{2} \mathbf{I} \right). \tag{1.21}$$

It is straightforward to verify that $\nabla \cdot \tau_M = qE$. The exerted stress is $\boldsymbol{\sigma} = -p\mathbf{I} + \tau_M$. The disjoining stress tensor is introduced by referring to the bulk situation

$$\mathbf{\Pi}_d = -\boldsymbol{\sigma} - p_b\mathbf{I} = \pi\mathbf{I} - \tau_M. \tag{1.22}$$

In the 1D case of the double layer $\mathbf{\Pi}_d$ is constant in the z direction

$$\Pi_d = RT [c_+ + c_- - 2c_b] - \frac{\epsilon\epsilon_0}{2} E^2. \tag{1.23}$$

It can be calculated using the EDL properties in the middle of the interlayer spacing ($z = 0$) where $\mathbf{E} = 0$ or at the solid surface ($z = H$) where $\mathbf{E}(z = H) = -\Sigma/\epsilon\epsilon_0$, it comes

$$\Pi_d = RT [c_+ + c_- - 2c_b] - \frac{\epsilon\epsilon_0}{2} \left(\frac{\Sigma}{\epsilon\epsilon_0} \right)^2. \tag{1.24}$$

$$\tag{1.25}$$

is always
according to
inter distance

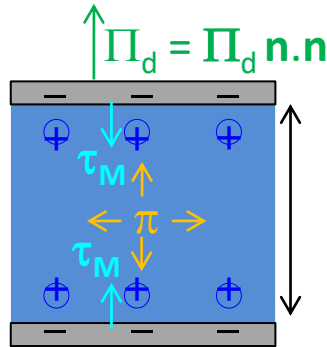


Figure 1.11: Mechanical equilibrium in the EDL.

in Fig.1.12 for different bulk ion concentrations. Obviously, the disjoining pressure resulting from the PB model is always repulsive and decreases monotonously when the interlayer distance increases.

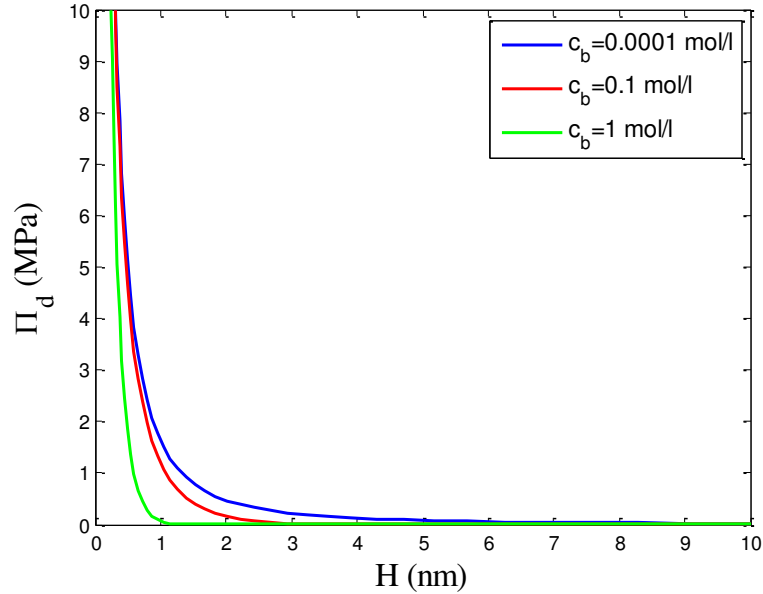


Figure 1.12: Disjoining pressure of a 1:1 electrolyte solution with $\Sigma = -0.1 \text{ C.m}^{-2}$ predicted by the Poisson-Boltzmann model.

1.4 Multi-scale structure of clayey soils

Clay minerals exhibit distinct structural arrangements depending on the considered length scale. Three different structural length scales (nano-, micro- and macroscale) are typically distinguished and the associated fundamental structural components are clay platelets and particles for the solid phase and pores and cracks for the fluid phase.

The determination of the structure at the different length scales is the aim of a multitude of experimental investigations [29, 5]. For example, Scanning Electron Microscopy (SEM) and Transmission Electron Microscopy (TEM) are typical experimental tool used to provide insight into the structure of clay minerals at the nano- and the micro-scale. Fig.1.13 shows a high resolution SEM image of the structural organization of smectites at different length scales as given by [5]. Obviously, at the smallest scale (10 nm), we can see an assembly of parallel clay platelets which is surrounded by a solution. At larger scales, the clay structure is composed of clay clusters and a pore network.

From these experimental observations, a typical three-scale representation is proposed as shown in Fig.1.14 which is used to describe electro-chemo-mechanical phenomena occurring in saturated [15] and unsaturated [22] swelling clayey soils. This model representation is characterized by two porosity levels (nano- and micro-pores) and three separate length scales (nano-, micro- and macroscale). The nanoscale representation is composed of incompressible, linear-elastic parallel clay platelets exhibiting a negative surface charge. The platelets are separated by a nanoporous network which is saturated by an aqueous binary electrolyte solution. At the intermediate microscale, the clay platelets form swollen clay clusters constituting the solid particles. At this length scale, they are separated from each other by a micropore network filled with bulk water (saturated case) or with a mixture of bulk water and air (unsaturated case). Regarding their size, the micropores are completely free from EDL effects. Such local representation allows to model the hydro-mechanical behavior of a swelling clay system from the nanoscale to the macroscale by using for example periodic homogenization methods [30].

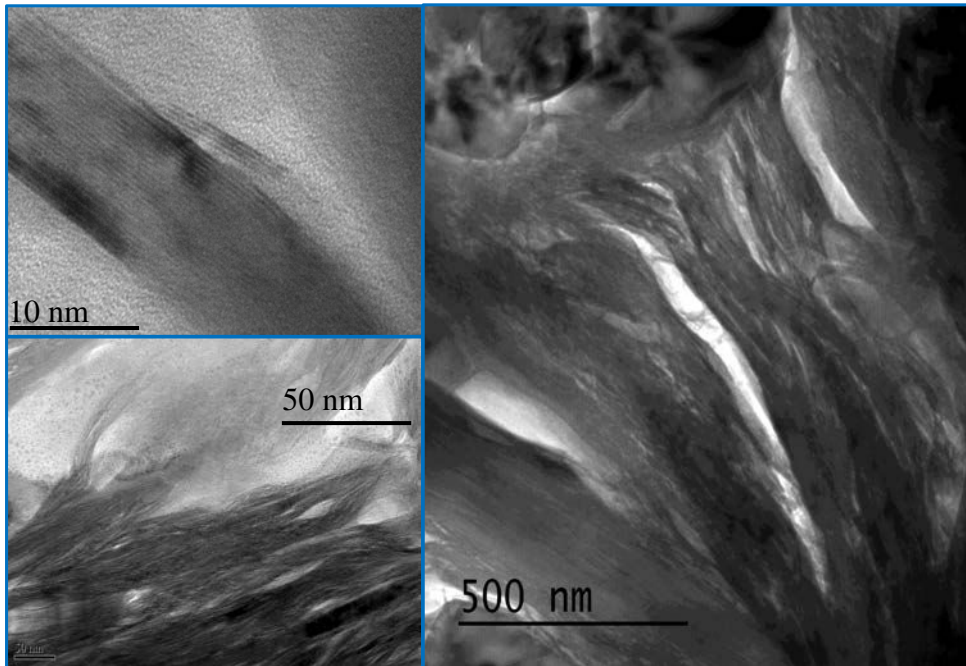


Figure 1.13: High resolution SEM images of clay texture at different length scales [5].

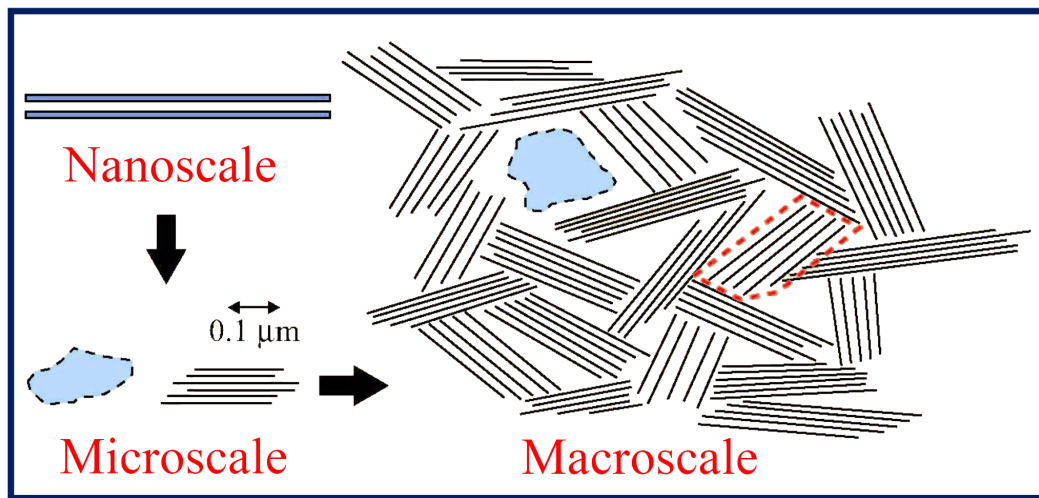


Figure 1.14: Three-scale representation of expansive clay media.

1.5 Previous works and thesis scope

1.5.1 Literature review

Based on their multi-scale structure, several two- and three-scale models have been developed by Moyne and Murad [16, 31, 32, 33, 15] for saturated expansive clays which are rigorously derived by micromechanical analyses using periodic homogenization [30] to propagate the coupled electro-chemico-mechanical phenomena from the nano- to the macro-scale. This allows to obtain macroscopic constitutive laws where the effective medium properties account for the local clay matrix structure and composition. The three-scale model has further been extended to unsaturated swelling clays [22] resulting in a novel macroscopic effective stress principle which is able to describe the hydro-mechanical behavior of swelling clays during oedometric water infiltration [34].

The limitation of these works is to use the classical Poisson-Boltzmann theory to capture the physics at the nanoscale, which neglects completely the molecular nature of the water solvent and ion size effects. These approaches describe therefore only accurately the osmotic swelling regime, where only swelling is observed and fails in the crystalline swelling regime. With the aim of improving the nanoscale description, Tien Dung Le [35] has accounted for the finite size and interparticle correlation effects of ions for both the two- and three-scale model of saturated swelling media in his Ph.D thesis using classical Density Functional Theory coupled with the Mean Spherical Approximation (MSA) and the anisotropic HyperNetted-Chain (HNC) approach to compute the ion distributions in the interlayer space. Such model is able to predict swelling and shrinking in the crystalline swelling regime, but it completely neglects the molecular nature of the water solvent.

A variety of experimental and modeling efforts have been undertaken aiming to understand the primary role of the water solvent in the nanoscopic behavior of hydrated expansive clayey soils. Ferrage et al. [24, 36] highlight the discrete evolution of the swelling pressure from zero to two molecular water layers in smectite clays during the crystalline swelling regime (small interplatelet distances) using X-ray and neutron diffraction techniques. These observations are confirmed by Monte Carlo (MC) simulations using the CLAYFF model proposed by Cygan et al. [37]. The related oscillatory form of the water molecule distribution in the inter-platelet pores that means the existence of discrete water layers is also obtained by Delville [38, 39] from MC simulations which uses the classical SPCE (Extended Single Point Charge) model of water [40]. The evolution of the related swelling pressure that results at the macroscale has been studied in the frame of experimental oedometric water infiltration tests performed by Imbert and Villar [11]. They showed an increase of the swelling pressure during the water uptake process which is related to the water transfert between the different pore types (micro- and nanopores). In addition, their studies highlighted that final value of the swelling pressure at complete saturation depends on the initial dry density and the initial water content.

Accounting for the molecular nature of the water solvent in the electrolyte solution is thus indispensable for small interplatelet distances or in the crystalline swelling regime in order to correctly predict the hydro-mechanical behavior of hydrated clays. This task is highly difficult because of the complexity of the coupled intermolecular interactions in the water solvent, but it should be undertaken in a realistic theoretical model of expansive clayey soils.

1.5.2 Thesis scope

This thesis aims at improving the nanoscale description of expansive clayey soils initially developed in the work of Tien Dung Le [35] by considering water no longer as a continuous solvent but as individual polar molecules. The final objective is to reconcile with existing experimental and computational modeling results such as the presence of discrete water layers in the inter-platelet space and the resulting oscillatory form of the disjoining pressure evolution during the hydration process of expansive clays in the crystalline swelling (low water content).

To this end, different model approaches of increasing complexity are proposed to account for the molecular nature of water aiming at determining the physical phenomena that govern the mechanical behavior at low interplatelet distances. The water solvent is firstly modeled as a hard sphere fluid which is successfully treated using the Fundamental Measure Theory (FMT) (chapter 2). Such a model allows to account for the finite size of the water molecules. The polar nature of the water solvent can be considered in a first approach through an interparticle Lennard-Jones (LJ) potential which averages over the different types of Van der Waals interactions (chapter 3). The interparticle LJ potential is composed a short-range soft repulsive and a long-range attractive part. The soft repulsive part is considered as an equivalent hard sphere reference system which is treated by FMT. An exact Density Functional Perturbation Theory (DFPT) approach accounting for interparticle correlation effects of the inhomogeneous LJ fluid is proposed in this chapter to study the attractive part. In Chapter 4 the dipolar nature of the

water solvent is considered explicitly by modeling water as a Dipolar Hard Sphere (DHS) fluid being hard spheres with a permanent dipole moment embedded at their center. This complex fluid is treated by a modified DFPT approach incorporating the dipole-dipole correlation effects which can be approximately calculated from the Ornstein-Zernike equation supplemented by the MSA closure proposed by Wertheim [21]. Ions are finally added to the pure solvent to complete the EDL model as it is shown in Fig.1.15. Such an EDL model is commonly referred to as *civilized* model.

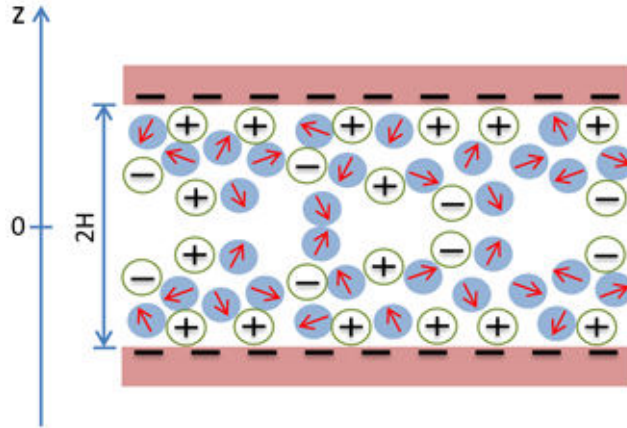


Figure 1.15:

Towards an application of the present work, in Chapter 5 an improved expression of the disjoining pressure at the nanoscale accounting for the molecular nature of the water solvent is included in our recently developed modified form of Terzaghi's effective stress principle of unsaturated expansive clays [22] in order to numerically simulate the hydro-mechanical behavior of expansive clays during water infiltration tests. The aim is to highlight the domain of validity and the limits of the classical PB theory and the possible improvements that can be obtained by considering the molecular nature of water which is a highly interesting topic in civil engineering.

Chapter 2

Introduction to Density Functional Theory and application to Hard-Sphere fluids

Classical Density Functional Theory (DFT) is probably the most powerful tool for theoretical analyses of inhomogeneous fluids. For this reason, this approach is chosen for modeling the water solvent in the inter-platelet space of smectite clays. The present chapter resumes thus the fundamental principles underlying all model approaches developed in the frame of this Ph.D thesis.

To start, a brief introduction to DFT is presented resulting in the fundamental general equation that is used to determine the water molecule (and ion) distribution at the nanoscopic clay platelet scale. The correlations between the constituents which play a crucial role in determining the thermodynamic properties of fluids are herein taken into account by the Radial Distribution Function (RDF) [41]. The later is determined by the resolution of the Ornstein-Zernike equation splitting intermolecular interactions into a direct and an indirect part.

The simplest case of a discontinuous fluid is the Hard-Sphere (HS) fluid with a purely repulsive intermolecular potential accounting exclusively for particle size effects. The HS fluid is generally considered as a reference case for more complex fluids and it is successfully treated by the Fundamental Measure Theory (FMT) [42]. This chapter summarizes thus the main ideas of the derivation of FMT from classical DFT.

2.1 Classical Density Functional Theory

Established in the mid 1970s, the DFT was originally derived for quantum mechanical systems and has further been extended to classical statistical mechanics [43]. Since then, DFT has turned out to be a powerful tool for theoretical analyses of inhomogeneous systems in different configurations such as drying and wetting, interfacial phenomena (e.g. surface adsorption and desorption) and capillary condensation. DFT is formulated starting from a density functional definition of the thermodynamic potentials. In the case where the temperature, the volume and the chemical potential (assuming an equilibrium situation) are held fixed, the thermodynamic function to minimize is the grand potential, $\Omega[\rho]$ which is defined as a functional of the density distribution $\rho(\mathbf{r})$ by

$$\Omega[\rho] = \mathcal{F}[\rho] + \int \rho(\mathbf{r}) [V_{\text{ext}}(\mathbf{r}) - \mu] d\mathbf{r}, \quad (2.1)$$

where $\mathcal{F}[\rho]$ is the intrinsic free energy functional, $V_{\text{ext}}(\mathbf{r})$ the external potential acting on the particles, and μ the chemical potential. At the equilibrium state, the grand potential is

minimum. The density profile $\rho(\mathbf{r})$ can therefore be determined from the variational principle

$$\frac{\delta\Omega[\rho]}{\delta\rho(\mathbf{r})} = 0. \quad (2.2)$$

where $\frac{\delta\Omega[\rho]}{\delta\rho(\mathbf{r})}$ designates the functional derivative of the grand potential Ω relative to the distribution function $\rho(\mathbf{r})$. The reader is referred to the book of Hansen and McDonald (§ 3.2) [44] for a short and simple introduction to functional differentiation.

The intrinsic free energy \mathcal{F} can be split into an ideal and an excess part

$$\mathcal{F}[\rho] = \mathcal{F}^{id}[\rho] + \mathcal{F}^{ex}[\rho], \quad (2.3)$$

in which the later is generally not known exactly while the ideal term is given by

$$\mathcal{F}^{id}[\rho] = k_B T \int \rho(\mathbf{r}) \left(\ln [\rho(\mathbf{r})\Lambda^3] - 1 \right) d\mathbf{r}, \quad (2.4)$$

where k_B is the Boltzmann constant, T the absolute temperature and Λ the thermal de Broglie wavelength (this length plays no role in the following developments). The functional derivative of this ideal part relative to $\rho(\mathbf{r})$ gives the ideal chemical potential

$$\frac{\delta\mathcal{F}^{id}}{\delta\rho(\mathbf{r})} = k_B T \ln [\rho(\mathbf{r})\Lambda^3]. \quad (2.5)$$

The variational principle (2.2) can therefore be written as

$$0 = k_B T \ln [\rho(\mathbf{r})\Lambda^3] + \frac{\delta\mathcal{F}^{ex}}{\delta\rho(\mathbf{r})} + V_{\text{ext}}(\mathbf{r}) - \mu. \quad (2.6)$$

With $\beta = 1/k_B T$, it follows directly

$$\rho(\mathbf{r})\Lambda^3 = \exp \left[\beta \left(\mu - \frac{\delta\mathcal{F}^{ex}[\rho]}{\delta\rho(\mathbf{r})} - V_{\text{ext}}(\mathbf{r}) \right) \right]. \quad (2.7)$$

At thermodynamic equilibrium in a homogeneous fluid (bulk fluid), the chemical potential admits the decomposition

$$\mu = \mu_b = \mu_b^{id} + \mu_b^{ex} = k_B T \ln (\rho_b \Lambda^3) + \mu_b^{ex}, \quad (2.8)$$

where ρ_b designates the bulk particle density. Combined with Eq.(2.7), the following expression is finally obtained for the density distribution $\rho(\mathbf{r})$

$$\rho(\mathbf{r}) = \rho_b \exp \left[\beta \left(\mu_b^{ex} - \frac{\delta\mathcal{F}^{ex}[\rho]}{\delta\rho(\mathbf{r})} - V_{\text{ext}}(\mathbf{r}) \right) \right]. \quad (2.9)$$

The above relation is the fundamental equation underlying all developments of DFT. It remains to find an expression of the excess free energy functional $\mathcal{F}^{ex}[\rho]$, which is the key ingredient of the various DFT approaches [45].

2.2 Radial Distribution Function

The excess free energy functional $\mathcal{F}^{ex}[\rho]$ includes interparticle interactions, in which correlation effects plays a significant role. In order to account for these effects, it is convenient to introduce the Radial Distribution Function (RDF) (or pair correlation function) $g(r)$ which describes how the density of a fluid varies with distance from a reference particle.

2.2.1 Definition

Preliminary remark: all calculations are presented here in the canonical ensemble in which the number of particles N , the volume V and the absolute temperature T are fixed. The extension to the grand canonical ensemble (fixed chemical potential μ , volume V and temperature T) can be found, for example in the textbook of Hill [46] for more details.

Consider a closed system of N particles without any external field in a volume V (with the average number density $\rho = N/V$) and at the temperature T (the inverse temperature is defined by $\beta = 1/k_B T$), in which the interaction between particles is characterized by the potential energy $U_N(\mathbf{r}_1, \dots, \mathbf{r}_N)$ with \mathbf{r}_i denoting the spatial position of particle i ($i = 1, \dots, N$). The probability of finding particle 1 at $\mathbf{r}_1 + d\mathbf{r}_1$, particle 2 at $\mathbf{r}_2 + d\mathbf{r}_2$, etc is given by [41]

$$P^{(N)}(\mathbf{r}_1, \dots, \mathbf{r}_N) d\mathbf{r}_1 \dots d\mathbf{r}_N = \frac{e^{-\beta U_N}}{Z_N} d\mathbf{r}_1 \dots d\mathbf{r}_N, \quad (2.10)$$

where $Z_N = \int \dots \int e^{-\beta U_N} d\mathbf{r}_1 \dots d\mathbf{r}_N$ is the configurational integral averaging over all possible combinations of particle positions. Since $P^{(N)}$ is a probability density function, it normalizes to unity

$$\int \dots \int P^{(N)}(\mathbf{r}_1, \dots, \mathbf{r}_N) d\mathbf{r}_1 \dots d\mathbf{r}_N = 1. \quad (2.11)$$

In order to obtain the probability of a reduced configuration, in which only the positions of the first 1 to n particles ($n < N$) are fixed at $\mathbf{r}_1, \dots, \mathbf{r}_n$ irrespective of the remaining $N - n$ particle positions, Eq.(2.10) is integrated over the configuration of the $N - n$ remaining particles

$$P^{(N)}(\mathbf{r}_1, \dots, \mathbf{r}_n) = \frac{1}{Z_N} \int \dots \int e^{-\beta U_N} d\mathbf{r}_{n+1} \dots d\mathbf{r}_N. \quad (2.12)$$

The particles being identical, the probability of finding any particle in $d\mathbf{r}_1$ at \mathbf{r}_1, \dots , and any particle in $d\mathbf{r}_n$ at \mathbf{r}_n is defined by the n -particle density defined as

$$\rho^{(n)}(\mathbf{r}_1, \dots, \mathbf{r}_n) = \frac{N!}{(N - n)!} P^{(n)}(\mathbf{r}_1, \dots, \mathbf{r}_n). \quad (2.13)$$

The prefactor $N!/(N - n)!$ can be explained by the fact that there are N possible choices for the first particle, $N - 1$ for the second, etc.

In the simplest case of a homogeneous fluid with $n = 1$, $\rho^{(1)}$ gives the one-particle density which is independent of the position \mathbf{r}_1 and equal to the macroscopic density

$$\frac{1}{V} \int \rho^{(1)}(\mathbf{r}_1) d\mathbf{r}_1 = \rho^{(1)} = \frac{N}{V} = \rho. \quad (2.14)$$

If the particles are independent of each other, $\rho^{(n)}$ is simply equal to ρ^n . It is now convenient to introduce the n -particle correlation function $g^{(n)}$ of an arbitrary fluid by

$$\rho^{(n)}(\mathbf{r}_1, \dots, \mathbf{r}_n) = \rho^n g^{(n)}(\mathbf{r}_1, \dots, \mathbf{r}_n). \quad (2.15)$$

From Eqs.(2.13) and (2.15), $g^{(n)}$ is defined by

$$g^{(n)}(\mathbf{r}_1, \dots, \mathbf{r}_n) = \frac{V^n N!}{N^n (N - n)!} P^{(n)}(\mathbf{r}_1, \dots, \mathbf{r}_n). \quad (2.16)$$

In statistical mechanics, the pair correlation function $g^{(2)}(\mathbf{r}_1, \mathbf{r}_2)$, also known as the Radial Distribution Function (RDF) plays a crucial role for determining the thermodynamic properties of a fluid. If the system is isotropic, $g^{(2)}(\mathbf{r}_1, \mathbf{r}_2)$ depends only on the relative distance $r = |\mathbf{r}_1 - \mathbf{r}_2|$ between two particles and $g^{(2)}(\mathbf{r}_1, \mathbf{r}_2) = g^{(2)}(r) \equiv g(r)$. It follows

$$\rho^{(2)}(\mathbf{r}_1, \mathbf{r}_2) = \rho^2 g^{(2)}(\mathbf{r}_1, \mathbf{r}_2) = \rho^{(2)}(\mathbf{r}_1, \mathbf{r}_2) = N(N - 1) P^{(2)}(\mathbf{r}_1, \mathbf{r}_2). \quad (2.17)$$

Integrating over the entire volume by noting that $\int \int P^{(2)}(\mathbf{r}_1, \mathbf{r}_2) d\mathbf{r}_1 d\mathbf{r}_2 = 1$ results then in

$$N(N-1) = \rho^2 \int \int g^{(2)}(\mathbf{r}_1, \mathbf{r}_2) d\mathbf{r}_1 d\mathbf{r}_2 \quad (2.18)$$

$$= \frac{N^2}{V} \int g^{(2)}(\mathbf{r}) d\mathbf{r} = \frac{N^2}{V} \int_0^\infty g(r) 4\pi r^2 dr. \quad (2.19)$$

It follows

$$\int \rho g(\mathbf{r}) d\mathbf{r} = \int_0^\infty \rho g(r) 4\pi r^2 dr = N - 1 \approx N, \quad (2.20)$$

where the quantity $\rho g(r) 4\pi r^2$ represents hence the number of molecules lying within the spherical shell centered at a reference particle and between the two radii r and $r + dr$.

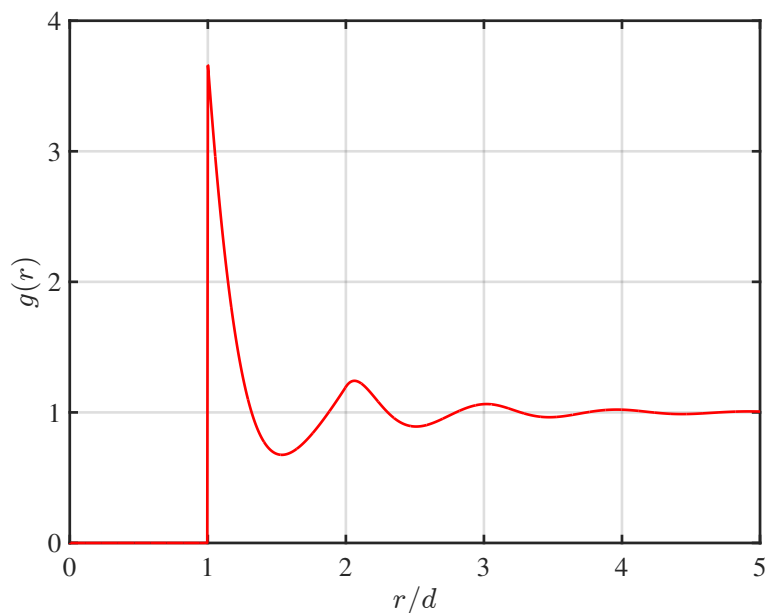


Figure 2.1: Radial Distribution Function of the uniform hard-sphere fluid at the reduced particle density $\rho d^3 = 0.813$.

Fig.2.1 shows an example of a typical profile of the radial distribution function $g(r)$ of a hard sphere fluid of diameter d , in the example of an isotropic HS fluid of reduced density $\rho d^3 = 0.813$. It is characterized by an oscillatory behavior as a function of the reduced distance r/d from the reference particle placed at the origin. Because of the exclusion volume due to the finite size of hard spheres, $g(r/d < 1) = 0$ and the maxima of $g(r)$ are placed nearly at entire multiples of the sphere diameter $r/d = 1, 2, \dots$ with an average value tending asymptotically towards 1.

2.2.2 Ornstein-Zernike equation

From the asymptotic behavior of $g(r)$ which tends towards 1 as $r \rightarrow \infty$, it is convenient to define the total correlation function $h(r)$ as

$$h(r) = g(r) - 1, \quad (2.21)$$

which measures the total influence of molecule 1 on molecule 2 at a separation distance r . Ornstein and Zernike proposed in 1914 [47] to split this influence into two contributions, a direct and an indirect part. The direct contribution is resumed by the direct correlation function, denoted $c(r)$. For the indirect contribution, the authors propose to consider the

direct interaction between particle 1 and a third particle (labeled 3), which in turn interacts with particle 2, directly or indirectly. The indirect part is weighted by the density distribution of particle 3 and averaged over all its possible positions. This decomposition for the case of a uniform and isotropic fluid of density ρ is described mathematically by the Ornstein-Zernike (OZ) equation [47]

$$h(r_{12}) = c(r_{12}) + \rho \int d\mathbf{r}_3 c(r_{13})h(r_{23}), \quad (2.22)$$

where $\mathbf{r}_{ij} = \mathbf{r}_i - \mathbf{r}_j$ ($i, j = 1, 2, 3$) denotes the distance between two particles i and j ($i, j = 1, 2, 3$). For an infinite fluid, Eq.(2.22) can be rewritten as a spatial convolution

$$h(\mathbf{r}_{12}) = c(\mathbf{r}_{12}) + \rho \int d\mathbf{r}_3 c(\mathbf{r}_{12} - \mathbf{r}_{32})h(\mathbf{r}_{32}) = c(\mathbf{r}_{12}) + \rho(c \otimes h)(\mathbf{r}_{12}). \quad (2.23)$$

2.2.3 Closures

It is evident that the Ornstein-Zernike relation Eq.(2.22) contains two unknowns (i.e $h(r)$ and $c(r)$). Therefore, it needs to be supplemented by an auxiliary closure relation. Using a diagrammatic expansions of the pair correlation functions as shown in [44] the following exact relation can be obtained

$$h(r) + 1 = \exp[-\beta u(r) + \gamma(r) + B(r)], \quad (2.24)$$

where $u(r)$ is the interparticle potential, $\gamma(r)$ the indirect correlation function defined as $\gamma(r) \equiv h(r) - c(r)$ and $B(r)$ is the so-called "bridge" function. The bridge function $B(r)$ is not known exactly, that is why Eq.(2.24) may be regarded as the definition of $B(r)$. Finding an appropriate approximation of $B(r)$ called "closure", plays the essential role of Integral Equation Theories (IET). Among the various existing approximations [48], one has to cite the Hyper-Netted Chain (HNC) which is obtained by setting $B(r) = 0$

$$h(r) + 1 = \exp[-\beta u(r) + h(r) - c(r)]. \quad (2.25)$$

Another typical approximation is the Percus-Yevick (PY) closure which is derived from the linearization of the HNC closure Eq.(2.25), $\exp \gamma(r) \simeq 1 + \gamma(r)$

$$g(r) = \exp[-\beta u(r)][1 + \gamma(r)]. \quad (2.26)$$

The PY closure Eq.(2.26) plays a particular role because it yields an analytic solution for the direct correlation function in the fundamental case of a hard sphere fluid [49]

$$c(r) = \begin{cases} 0 & \text{for } r > d, \\ -\lambda_1 - 6\eta\lambda_2 \frac{r}{d} - \frac{\eta}{2}\lambda_1 \frac{r^3}{d^3} & \text{for } r < d, \end{cases} \quad (2.27)$$

where d is the particle diameter, $\eta = \frac{\pi}{6}\rho d^3$ the particle volume fraction and λ_1, λ_2 are defined by

$$\begin{aligned} \lambda_1 &= \frac{(1 + 2\eta)^2}{(1 - \eta)^4}, \\ \lambda_2 &= -\frac{(1 + \eta/2)^2}{(1 - \eta)^4}. \end{aligned}$$

In general, the PY closure relation turns out to be more successful than the HNC closure when the intermolecular potential is strongly repulsive and short-ranged. In contrast, the HNC approximation is more accurate than PY for systems governed by long-range attractive potentials (e.g. electrolyte solutions) [44]. An extension of the PY approximation for common

fluid models consisting of a hard-sphere interaction plus an isotropic attractive tail due to the intermolecular potential $u_1(r)$ is the Mean Spherical Approximation (MSA) [50]. For a given spherically symmetric potential

$$u(r) = \begin{cases} \infty & \text{for } r < d, \\ u_1(r) & \text{for } r > d, \end{cases} \quad (2.28)$$

the MSA is defined in terms of the radial distribution function $g(r)$ and the direct correlation function $c(r)$ by

$$\begin{cases} g(r) = 0, & r < d \\ c(r) = -\beta u_1(r), & r > d. \end{cases} \quad (2.29)$$

The first relation in Eq.(2.29) is exact, while the second one is an extension of the asymptotic long-range behavior of $c(r)$ ($r \gg d$), which is obviously an approximation.

The most attractive feature of MSA is to provide an analytic solution for ionic [51, 52] and dipolar hard sphere fluids [21]. For ionic fluids, the analytical MSA solution for the direct correlation function $c_{ij}^{MSA}(r)$ between two particle i and j is split into a short-range term $\tilde{c}_{ij}(r)$ being the direct correlation function of a system of uncharged hard spheres and an electrical long-range term

$$c_{ij}^{MSA}(r) = \begin{cases} \tilde{c}_{ij}(r) - \frac{\beta}{4\pi\epsilon\epsilon_0} \frac{q_i q_j}{d} \left(2B - \frac{B^2 r}{d} \right) & \text{for } r < d \\ -\frac{\beta}{4\pi\epsilon\epsilon_0} \frac{q_i q_j}{r} & \text{for } r > d, \end{cases} \quad (2.30)$$

where q_i, q_j are the electric charges and ϵ_0, ϵ designate the vacuum permittivity and the relative permittivity of the solvent, respectively. The parameter B is given by

$$B = \frac{x + 1 - \sqrt{1 + 2x}}{x}, \quad x = \lambda_D d, \quad (2.31)$$

with λ_D the Debye length which can be written as

$$\lambda_D^2 = \frac{\beta}{\epsilon\epsilon_0} \sum_{i=1}^N \rho_i q_i^2, \quad (2.32)$$

where ρ_i designates the density of ion i .

Because of their simplicity, the PY, HNC and MSA closures are commonly selected to study simple fluids. However, the absence of the bridge function $B(r)$ can cause poor performances of these approximations even in the case of simple fluids. In order to overcome these shortcomings, various assumptions of the bridge function $B(r)$ have been proposed [53]. Typical examples are the Percus-Yevick (PY), Verlet (V) bridge functions.

$$B^{PY}(r) = B^{PY}[(\gamma(r))] = \ln[1 + \gamma(r)] - \gamma(r), \quad (2.33)$$

$$B^V(r) = B^V[(\gamma(r))] = \frac{-\gamma(r)^2}{2[1 + \alpha\gamma(r)]}, \quad (2.34)$$

with $\alpha = 0.8$ in the original Verlet bridge function [54]. Another usual approximation is the Martynov-Sarkisov (MS) bridge function [55]

$$B^{MS}(r) = B^{MS}[\gamma(r)] = [1 + 2\gamma(r)]^{1/2} - \gamma(r) - 1. \quad (2.35)$$

In the case of more complex fluids such as Lennard-Jones fluids, the role of the bridge function $B(r)$ becomes predominant. Some appropriate bridge functions for such fluids will be presented and discussed in chapter 3.

2.3 Density functional perturbation theory

Recalling the fundamental equation of DFT (2.9) for solving the density distribution of an inhomogeneous fluid

$$\rho(\mathbf{r}) = \rho_b \exp \left[\beta \left(\mu_b^{ex} - \frac{\delta \mathcal{F}^{ex}[\rho]}{\delta \rho(\mathbf{r})} - V_{ext}(\mathbf{r}) \right) \right]. \quad (2.36)$$

It remains to find an expression of the excess free energy functional $\mathcal{F}^{ex}[\rho]$ which can be done by using a perturbation method starting from the exact relation (see [44] for a derivation):

$$\rho^{(2)}(\mathbf{r}_1, \mathbf{r}_2) = 2 \frac{\delta \mathcal{F}^{ex}[\rho]}{\delta u(\mathbf{r}_1, \mathbf{r}_2)}, \quad (2.37)$$

where $u(\mathbf{r}_1, \mathbf{r}_2)$ is the pair potential between two particles located at \mathbf{r}_1 and \mathbf{r}_2 , respectively. In the framework of Density Functional Perturbation Theory (DFPT), the later can be expressed as the sum of a repulsive part $u_0(\mathbf{r}_1, \mathbf{r}_2)$ being the reference term, and a weak attractive part $u_a(\mathbf{r}_1, \mathbf{r}_2)$ considered as the perturbation term. Introducing a coupling parameter λ , allows then to continuously vary the intermolecular potential from the initial reference state ($\lambda = 0$) to the final state ($\lambda = 1$). The complete intermolecular potential is then written as

$$u_\lambda(\mathbf{r}_1, \mathbf{r}_2) = u_0(\mathbf{r}_1, \mathbf{r}_2) + \lambda u_a(\mathbf{r}_1, \mathbf{r}_2), \quad 0 \leq \lambda \leq 1. \quad (2.38)$$

In combination with Eq.(2.37), it comes

$$\rho^{(2)}(\mathbf{r}_1, \mathbf{r}_2; \lambda) = 2 \frac{\delta \mathcal{F}^{ex}[\rho; \lambda]}{\delta u_\lambda(\mathbf{r}_1, \mathbf{r}_2)} = 2 \frac{\delta \mathcal{F}^{ex}[\rho; \lambda]}{\delta [\lambda u_a(\mathbf{r}_1, \mathbf{r}_2)]}. \quad (2.39)$$

The change in the Helmholtz free energy with respect to λ is then given by

$$\delta \mathcal{F}^{ex}[\rho; \lambda] = \frac{1}{2} d\lambda \iint \rho^{(2)}(\mathbf{r}_1, \mathbf{r}_2; \lambda) u_a(\mathbf{r}_1, \mathbf{r}_2) d\mathbf{r}_1 d\mathbf{r}_2. \quad (2.40)$$

Integrating the above relation between $\lambda = 0$ (reference system) and $\lambda = 1$ gives hence an exact expression of the excess free energy

$$\mathcal{F}^{ex}[\rho] = \mathcal{F}^0[\rho] + \frac{1}{2} \int_0^1 d\lambda \iint \rho^{(2)}(\mathbf{r}_1, \mathbf{r}_2; \lambda) u_a(\mathbf{r}_1, \mathbf{r}_2) d\mathbf{r}_1 d\mathbf{r}_2, \quad (2.41)$$

where $\mathcal{F}^0[\rho]$ is the excess free energy functional of the reference fluid of density $\rho(\mathbf{r})$ with the pair potential $u_0(\mathbf{r}_1, \mathbf{r}_2)$. The pair density with the potential $u_\lambda(\mathbf{r}_1, \mathbf{r}_2)$ is now defined by

$$\rho^{(2)}(\mathbf{r}_1, \mathbf{r}_2; \lambda) = \rho(\mathbf{r}_1)\rho(\mathbf{r}_2) [1 + h(\mathbf{r}_1, \mathbf{r}_2; \lambda)], \quad (2.42)$$

with $h(\mathbf{r}_1, \mathbf{r}_2; \lambda)$ the total correlation function. Eq.(2.41) becomes then

$$\mathcal{F}^{ex}[\rho] = \mathcal{F}^0[\rho] + \frac{1}{2} \iint \rho(\mathbf{r}_1)\rho(\mathbf{r}_2) u_a(\mathbf{r}_1, \mathbf{r}_2) d\mathbf{r}_1 d\mathbf{r}_2 + \mathcal{F}^{corr}[\rho], \quad (2.43)$$

where $\mathcal{F}^{corr}[\rho]$ denotes the contribution to the excess free energy \mathcal{F}^{ex} due to interparticle correlations induced by the perturbation part of the interparticle potential

$$\mathcal{F}^{corr}[\rho] = \frac{1}{2} \int_0^1 d\lambda \iint \rho(\mathbf{r}_1)\rho(\mathbf{r}_2) h(\mathbf{r}_1, \mathbf{r}_2; \lambda) u_a(\mathbf{r}_1, \mathbf{r}_2) d\mathbf{r}_1 d\mathbf{r}_2. \quad (2.44)$$

Note that the density profiles $\rho(\mathbf{r}_1)$ and $\rho(\mathbf{r}_2)$ are maintained constant while increasing λ . To do this, the external potential $V_{ext}(\mathbf{r})$ has to be adjusted as explained in Sullivan [56] and

Evans [57]. The density distribution expression Eq.(2.36) for an inhomogeneous fluid is finally written as

$$\rho(\mathbf{r}_1) = \rho_b \exp \left[\beta \left(\mu_b^{ex} - \frac{\delta \mathcal{F}^0[\rho]}{\delta \rho(\mathbf{r}_1)} - \int \rho(\mathbf{r}_2) u_a(\mathbf{r}_1, \mathbf{r}_2) d\mathbf{r}_2 - \int_0^1 d\lambda \int \rho(\mathbf{r}_2) h(\mathbf{r}_1, \mathbf{r}_2; \rho; \lambda) u_a(\mathbf{r}_1, \mathbf{r}_2) d\mathbf{r}_2 - V_{\text{ext}}(\mathbf{r}_1) \right) \right]. \quad (2.45)$$

Eq.(2.45) is the expression underlying all perturbation theories for both bulk and inhomogeneous fluids using various approximations for the excess free energy of the reference system $\mathcal{F}^0[\rho]$ and for the total correlation function of the inhomogeneous system $h(\mathbf{r}_1, \mathbf{r}_2; \rho; \lambda)$ [58]. Such DFT approach allows to obtain an exact expression for the particle density profiles of inhomogeneous fluids starting from the determination of the total correlation function $h(\mathbf{r}_1, \mathbf{r}_2; \rho; \lambda)$ of the inhomogeneous fluids. DFPT is the main theory in the present work, which treats the different fluid models such as Lennard-Jones and Dipolar Hard-Sphere fluids presented in the following chapters.

2.4 Fundamental Measure Theory

Hard Sphere fluid is the most simple particle fluid and is the fundamental reference system of the different fluid models used in this work. With the aim of calculating the density distribution $\rho(\mathbf{r})$ of hard sphere fluids in any geometry using Eq.(2.9), the Fundamental Measure Theory was suggested in its original form by Rosenfeld [42, 59], and further developed by Kierlik and Rosinberg [60, 61]. It is noteworthy that Cuesta applied the FMT formalism to another geometry, namely parallel hard cubes instead of hard spheres [62]. The latest developments of FMT can be found in two review articles published by Roth et al. [63, 64]. For the sake of simplicity, in this thesis, the FMT formalism is applied to one-component hard sphere fluids (but can be extended to the cases of mixtures) based on the synthetic introduction of Hansen and McDonald [44].

2.4.1 Percus-Yevick direct correlation function of hard spheres

The starting point of FMT is the fact that the PY direct correlation function Eq.(2.27) of a hard sphere fluid may be expressed in terms of geometric quantities produced by the intersection of two spheres of radius R ($2R = d$) and separated by a distance $r > R$ (see Fig.2.2) such as the overlap volume $\Delta V(r)$, the overlap surface $\Delta S(r)$ and the overlap radius $\Delta R(r) = 2R - \bar{R}$, where $\bar{R} = R + r/4$ is the mean radius of the convex envelope surrounding the spheres. The idea is here that these geometric quantities can be expressed in terms of convolutions of the characteristic volume function $\omega_3(\mathbf{r})$ and surface function $\omega_2(\mathbf{r})$ of individual spheres

$$\omega_3(\mathbf{r}) = \Theta(R - |\mathbf{r}|), \quad \omega_2(\mathbf{r}) = \delta(R - |\mathbf{r}|), \quad (2.46)$$

where Θ denotes the Heaviside function, δ the Dirac function and $r = |\mathbf{r}|$. It comes

$$\begin{aligned} \Delta V(r) &= \omega_3 \otimes \omega_3 = \int \omega_3(\mathbf{r} - \mathbf{r}') \omega_3(\mathbf{r}') d\mathbf{r}' = 2 \int_{r/2}^R \pi(R^2 - r'^2) dr' \Theta(d - r) \\ &= \frac{4}{3} \pi R^3 \left(1 - \frac{3}{2}x + \frac{x^3}{2} \right) \Theta(d - r), \end{aligned} \quad (2.47)$$

$$\begin{aligned} \Delta S(r) &= 2\omega_3 \otimes \omega_2 = 2 \int \omega_3(\mathbf{r} - \mathbf{r}') \omega_2(\mathbf{r}') d\mathbf{r}' = 4\pi R \left(R - \frac{r}{2} \right) \Theta(d - r) \\ &= 4\pi R^2 \left(1 - \frac{r}{d} \right) \Theta(d - r), \end{aligned} \quad (2.48)$$

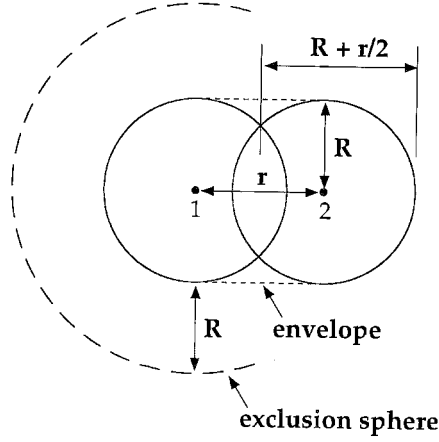


Figure 2.2: Geometric quantities of two interpenetrating spheres.

$$\Delta R(r) = \frac{\Delta S}{8\pi R} + \frac{R}{2}\Theta(d-r) = \left(R - \frac{r}{4}\right)\Theta(d-r), \quad (2.49)$$

where \otimes is the spatial convolution and $x = r/d$. The direct correlation function $c(r)$ of hard spheres given by the Percus-Yevick Eq.(2.27) can be rewritten with some algebra as

$$-c(r) = \chi^{(3)}\Delta V(r) + \chi^{(2)}\Delta S(r) + \chi^{(1)}\Delta R(r) + \chi^{(0)}\Theta(d-r), \quad (2.50)$$

where the coefficients $\chi^{(\alpha)}$ ($\alpha = 0, 1, 2, 3$) are given by

$$\begin{aligned} \chi^{(0)} &= \frac{1}{1 - \xi_3}, & \chi^{(1)} &= \frac{\xi_2}{(1 - \xi_3)^2}, \\ \chi^{(2)} &= \frac{\xi_1}{(1 - \xi_3)^2} + \frac{\xi_2^2}{4\pi(1 - \xi_3)^3}, \\ \chi^{(3)} &= \frac{\xi_0}{(1 - \xi_3)^2} + \frac{2\xi_1\xi_2}{(1 - \xi_3)^3} + \frac{\xi_2^3}{4\pi(1 - \xi_3)^4}, \end{aligned} \quad (2.51)$$

where $\xi_\alpha = \rho\mathcal{R}^{(\alpha)}$ are the so-called SPT (Scaled Particle Theory) variables [65] related to the fundamental geometric measures of a sphere $\mathcal{R}^{(\alpha)}$ as follows

$$\begin{aligned} \mathcal{R}^{(3)} &= \frac{4}{3}\pi R^3 \quad (\text{volume}), & \mathcal{R}^{(2)} &= 4\pi R^2 \quad (\text{surface}) \\ \mathcal{R}^{(1)} &= R \quad (\text{rayon}), & \mathcal{R}^{(0)} &= 1. \end{aligned} \quad (2.52)$$

To write $c(r)$ in Eq.(2.50) solely in terms of the characteristic functions of an individual sphere, the Heaviside function $\Theta(d-r)$ has to be decomposed in a sum of convolutions of single sphere functions

$$\Theta(d - |\mathbf{r}|) = 2(\omega_3 \otimes \omega_0 + \omega_2 \otimes \omega_1 + \omega_2 \otimes \omega_1), \quad (2.53)$$

where the scalar functions (ω_α) with ($\alpha \in 0, 1, 2, 3$) and the vector functions ω_α with ($\alpha \in 1, 2$) are all expressed in terms of the two basic functions of Eq.(2.46) as given by

$$\omega_3(\mathbf{r}) = \Theta(R - |\mathbf{r}|), \quad (2.54)$$

$$\omega_2(\mathbf{r}) = \delta(R - |\mathbf{r}|), \quad (2.55)$$

$$\omega_1(\mathbf{r}) = \frac{\omega_2(\mathbf{r})}{4\pi R}, \quad (2.56)$$

$$\omega_0(\mathbf{r}) = \frac{\omega_2(\mathbf{r})}{4\pi R^2}, \quad (2.57)$$

$$\omega_2 = \nabla\omega_3 = \delta(|\mathbf{r}|-R)\frac{\mathbf{r}}{r}, \quad (2.58)$$

$$\omega_1 = \frac{\omega_2}{4\pi R}. \quad (2.59)$$

In the case of the vector function, the convolution product \otimes includes a scalar product. Note that the representation of $\Theta(d-|\mathbf{r}|)$ in Eq.(2.53) can be easily verified in the Fourier space (see Appendix A.1). As a result, the PY direct correlation function in Eq.(2.50) can be rewritten as

$$\begin{aligned} -c(r) &= \chi^{(3)}\omega_3 \otimes \omega_3 + 2\chi^{(2)}\omega_2 \otimes \omega_3 \\ &+ \chi^{(1)} \left[\frac{1}{4\pi R}\omega_2 \otimes \omega_3 + R(\omega_0 \otimes \omega_3 + \omega_1 \otimes \omega_2 + \omega_1 \otimes \omega_2) \right] \\ &+ 2\chi^{(0)}[\omega_0 \otimes \omega_3 + \omega_1 \otimes \omega_2 + \omega_1 \otimes \omega_2], \\ &= \chi^{(3)}\omega_3 \otimes \omega_3 + 2\chi^{(2)}\omega_2 \otimes \omega_3 + \chi^{(1)} \left[2\omega_1 \otimes \omega_3 + \frac{1}{4\pi}(\omega_2 \otimes \omega_2 + \omega_2 \otimes \omega_2) \right] \\ &+ 2\chi^{(0)}[\omega_3 \otimes \omega_0 + \omega_1 \otimes \omega_2 + \omega_1 \otimes \omega_2], \end{aligned} \quad (2.60)$$

or in a more compact form

$$c(r) = \sum_{\alpha,\beta} c_{\alpha\beta} \omega_\alpha \otimes \omega_\beta. \quad (2.61)$$

2.4.2 Excess free energy functional

The fundamental hypothesis of FMT is to assume that the excess free energy functional of a hard sphere fluid, \mathcal{F}^{ex} , can be expressed in the form of a weighted density functional

$$\beta\mathcal{F}^{ex}[\rho] = \int \Phi[\{n_\alpha(\mathbf{r}')\}]d\mathbf{r}', \quad (2.62)$$

where Φ is the reduced excess free energy density which is a function of spatially weighted densities $n_\alpha(\mathbf{r})$ defined by

$$n_\alpha(\mathbf{r}) = \int \rho(\mathbf{r}')w_\alpha(\mathbf{r}-\mathbf{r}')d\mathbf{r}'. \quad (2.63)$$

The next step is to identify the weight functions $w_\alpha(\mathbf{r})$ in Eq.(2.63). The idea is to decompose the direct correlation function $c(|\mathbf{r}-\mathbf{r}'|)$ in terms of the weight functions $w_\alpha(\mathbf{r})$. Starting from the following definition [44]

$$-c(|\mathbf{r}-\mathbf{r}'|) = \beta \frac{\delta^2 \mathcal{F}^{ex}}{\delta\rho(\mathbf{r})\delta\rho(\mathbf{r}')}. \quad (2.64)$$

In combination with Eq.(2.62), the first derivative of $\mathcal{F}^{ex}[\rho]$ with respect to $\rho(\mathbf{r})$ is

$$\beta \frac{\delta \mathcal{F}^{ex}[\rho]}{\delta\rho(\mathbf{r})} = \sum_\alpha \int d\mathbf{r}'' \frac{\partial\Phi}{\partial n_\alpha}(\mathbf{r}'') \frac{\delta n_\alpha(\mathbf{r}'')}{\delta\rho(\mathbf{r})}. \quad (2.65)$$

With

$$n_\alpha(\mathbf{r}'') = \int d\mathbf{r}''' \rho(\mathbf{r}''-\mathbf{r}''') w_\alpha(\mathbf{r}''') = \int d\mathbf{r}''' \rho(\mathbf{r}''') w_\alpha(\mathbf{r}''-\mathbf{r}''') \quad (2.66)$$

$$\frac{\delta n_\alpha(\mathbf{r}'')}{\delta\rho(\mathbf{r})} = \int d\mathbf{r}''' \frac{\delta\rho(\mathbf{r}''')}{\delta\rho(\mathbf{r})} w_\alpha(\mathbf{r}''-\mathbf{r}''') = w_\alpha(\mathbf{r}''-\mathbf{r}), \quad (2.67)$$

the first derivative reads as

$$\beta \frac{\delta \mathcal{F}^{ex}[\rho]}{\delta\rho(\mathbf{r})} = \sum_\alpha \int d\mathbf{r}'' \frac{\partial\Phi}{\partial n_\alpha}(\mathbf{r}'') w_\alpha(\mathbf{r}''-\mathbf{r}), \quad (2.68)$$

and the second derivative becomes

$$\begin{aligned} \beta \frac{\delta^2 \mathcal{F}^{ex}[\rho]}{\delta \rho(\mathbf{r}) \delta \rho(\mathbf{r}')} &= \sum_{\alpha, \beta} \int d\mathbf{r}'' \frac{\partial^2 \Phi}{\partial n_\alpha \partial n_\beta}(\mathbf{r}'') w_\alpha(\mathbf{r}'' - \mathbf{r}) \frac{\delta n_\beta(\mathbf{r}'')}{\delta \rho(\mathbf{r}')} \\ &= \sum_{\alpha, \beta} \int d\mathbf{r}'' \frac{\partial^2 \Phi}{\partial n_\alpha \partial n_\beta}(\mathbf{r}'') w_\alpha(\mathbf{r}'' - \mathbf{r}) w_\beta(\mathbf{r}'' - \mathbf{r}'). \end{aligned} \quad (2.69)$$

In a homogeneous fluid, $\frac{\partial^2 \Phi}{\partial n_\alpha \partial n_\beta}(\mathbf{r}'')$ is independent of the spatial position \mathbf{r}'' and the above equation in combination with Eq.(2.64) yields

$$\begin{aligned} -c(|\mathbf{r} - \mathbf{r}'|) &= \beta \frac{\delta^2 \mathcal{F}^{ex}[\rho]}{\delta \rho(\mathbf{r}) \delta \rho(\mathbf{r}')} = \sum_{\alpha, \beta} \frac{\partial^2 \Phi}{\partial n_\alpha \partial n_\beta} \int d\mathbf{r}'' w_\alpha(\mathbf{r}'' - \mathbf{r}) w_\beta(\mathbf{r}'' - \mathbf{r}') \\ &= \sum_{\alpha, \beta} \frac{\partial^2 \Phi}{\partial n_\alpha \partial n_\beta} \int w_\alpha(-\mathbf{r}''') w_\beta(\mathbf{r} - \mathbf{r}' - \mathbf{r}''') d\mathbf{r}''' \quad (2.70) \\ &= \sum_{\alpha, \beta} \pm \frac{\partial^2 \Phi}{\partial n_\alpha \partial n_\beta} w_\alpha \otimes w_\beta(\mathbf{r} - \mathbf{r}'). \end{aligned}$$

The last term of Eq.(2.70) is the convolution of the weight functions $w_\alpha(-\mathbf{r})$ and $w_\beta(\mathbf{r})$ of two particles α and β located at \mathbf{r} and \mathbf{r}' , respectively. If the functions w_α are even (scalar functions) the sign is "+", if the functions are odd (vector functions) the sign is "-". Therefore, the products of scalar functions are standard convolutions, the vector convolutions must be preceded by a sign "-" and products of scalar and vector functions cancel out by the permutation of the indices α and β . The similarity of the expressions Eq.(2.60) and Eq.(2.70) justifies the choice to use the characteristic functions ω_α and $\boldsymbol{\omega}_\alpha$ as weight functions w_α . Therefore

$$n_\alpha(\mathbf{r}) = \int \omega_\alpha(\mathbf{r} - \mathbf{r}') \rho(\mathbf{r}') d\mathbf{r}', \quad \alpha = 0 \text{ to } 3 \quad (2.71)$$

$$\mathbf{n}_\alpha(\mathbf{r}) = \int \boldsymbol{\omega}_\alpha(\mathbf{r} - \mathbf{r}') \rho(\mathbf{r}') d\mathbf{r}', \quad \alpha = 1, 2 \quad (2.72)$$

where the functions ω_α and $\boldsymbol{\omega}_\alpha$ are given by the relations Eq.(2.54-2.59). The scalar densities n_α and vector densities \mathbf{n}_α have the dimensions of the weight function ω_α and $\boldsymbol{\omega}_\alpha$ ($\text{length}^{\alpha-3}$).

The reduced excess free energy density Φ is now determined by expressing it as a linear combination of the lowest powers of the weighted densities and their products in the spirit of a virial expansion. Since Φ is a scalar with the dimension of a number density, the only possible terms are: n_0 , $n_1 n_2$, n_2^3 , $\mathbf{n}_1 \cdot \mathbf{n}_2$ and $n_2 \mathbf{n}_2 \cdot \mathbf{n}_2$. Thus

$$\Phi(\{n_\alpha\}) = \phi_0 n_0 + \phi_1 n_1 n_2 + \phi_2 n_2^3 + \phi_3 \mathbf{n}_1 \cdot \mathbf{n}_2 + \phi_4 n_2 \mathbf{n}_2 \cdot \mathbf{n}_2, \quad (2.73)$$

where the coefficients ϕ_0 , ϕ_1 , ϕ_2 , ϕ_3 and ϕ_4 are functions without dimension of the quantity without dimension n_3 . If the fluid is homogeneous, the scalar weighted densities reduce to the SPT variables Eq.(2.52) and the vector densities vanish. Therefore,

$$\Phi(\{n_\alpha\}) = \phi_0 \xi_0 + \phi_1 \xi_1 \xi_2 + \phi_2 \xi_2^3. \quad (2.74)$$

In order to establish a relation between the excess pressure P^{ex} and Φ , one can write

$$\begin{aligned} \Omega^{ex}[\rho] &= - \int P^{ex}[\rho] d\mathbf{r} \\ &= \mathcal{F}^{ex} - \int \rho(\mathbf{r}) \frac{\delta \mathcal{F}^{ex}}{\delta \rho(\mathbf{r})} d\mathbf{r}. \end{aligned} \quad (2.75)$$

Using the definition of the weighted densities Eq.(2.71) and Eq.2.72) and the relation of the derivative of the free energy Eq.(2.68), the second term of the above relation becomes

$$\int \rho(\mathbf{r}) \beta \frac{\delta \mathcal{F}^{ex}}{\delta \rho(\mathbf{r})} d\mathbf{r} = \sum_{\alpha} \int d\mathbf{r} \int d\mathbf{r}' \rho(\mathbf{r}) \frac{\partial \Phi}{\partial n_{\alpha}}(\mathbf{r}') \omega_{\alpha}(\mathbf{r}' - \mathbf{r}) = \sum_{\alpha} \int d\mathbf{r}' \frac{\partial \Phi}{\partial n_{\alpha}}(\mathbf{r}') n_{\alpha}(\mathbf{r}'). \quad (2.76)$$

The excess pressure P^{ex} is then given by

$$\beta P^{ex}[\rho] = -\Phi + \sum_{\alpha} \frac{\partial \Phi}{\partial n_{\alpha}} n_{\alpha}, \quad (2.77)$$

where the sum covers all scalar densities.

The scaled particle theory ([44], page 233 and Appendix E, page 599) shows the intuitive result that the excess chemical potential of a hard sphere of radius R is nearly equal to the reversible work required for the creation in the fluid of a cavity of volume $4/3\pi R^3$ that can hold this particle. In the limit $R \rightarrow \infty$, this term dominates and $\mu^{ex} \rightarrow (4/3\pi R^3)P$. In the bulk, we have the classical relation

$$\beta \mu^{ex} = \beta \left. \frac{\partial (\mathcal{F}^{ex}/V)}{\partial \rho} \right|_T = \left. \frac{\partial \Phi}{\rho} \right|_T = \sum_{\alpha} \frac{\partial \Phi}{\partial \xi_{\alpha}} \frac{\partial \xi_{\alpha}}{\partial \rho} = \frac{\partial \Phi}{\partial \xi_3} V + \mathcal{O}(R^2). \quad (2.78)$$

For large particles ($R \rightarrow \infty$), the preceding evaluation of μ^{ex} in powers of R indicates that the derivative $\partial \Phi / \partial \xi_3$ has to be identified with βP . This relation is assumed to be valid also in the inhomogeneous case allowing to substitute ξ_3 by n_3 :

$$\frac{\partial \Phi}{\partial n_3} = \beta P = \beta P^{id} + \beta P^{ex} = n_0 + \beta P^{ex}. \quad (2.79)$$

Using Eq.(2.77) to express P^{ex} in Eq.(2.79) gives the fundamental relation for the excess free energy density in the FMT

$$\frac{\partial \Phi}{\partial n_3} = -\Phi + \sum_{\alpha} \frac{\partial \Phi}{\partial n_{\alpha}} n_{\alpha} + n_0. \quad (2.80)$$

By use of Eq.(2.73) to replace Φ in Eq.(2.80) (note that ϕ_i depends only on n_3), the different terms can be identified successively

- Term in n_0

$$-\phi_0 n_0 + \phi_0 n_0 + n_3 \frac{d\phi_0}{dn_3} n_0 + n_0 = \frac{d\phi_0}{dn_3} n_0. \quad (2.81)$$

Hence

$$\frac{d\phi_0}{dn_3} = \frac{1}{1-n_3} \quad \longrightarrow \quad \phi_0 = -\ln(1-n_3) + c_0. \quad (2.82)$$

- Term in $n_1 n_2$

$$-\phi_1 n_1 n_2 + 2\phi_1 n_1 n_2 + \frac{d\phi_1}{dn_3} n_3 n_1 n_2 = n_1 n_2 \frac{d\phi_1}{dn_3}. \quad (2.83)$$

Hence

$$\frac{d\phi_1}{dn_3} = \frac{\phi_1}{1-n_3} \quad \longrightarrow \quad \phi_1 = \frac{c_1}{1-n_3}. \quad (2.84)$$

- Term in n_2^3

$$-\phi_2 n_2^3 + 3\phi_2 n_2^3 + \frac{d\phi_2}{dn_3} n_2^3 n_3 = n_2^3 \frac{d\phi_2}{dn_3}. \quad (2.85)$$

Hence

$$\frac{d\phi_2}{dn_3} = \frac{2\phi_2}{1-n_3} \quad \longrightarrow \quad \phi_2 = \frac{c_2}{(1-n_3)^2}. \quad (2.86)$$

- Term in $\mathbf{n}_1 \cdot \mathbf{n}_2$

$$\frac{d\phi_3}{dn_3} = \frac{\phi_3}{1-n_3} \quad \longrightarrow \quad \phi_3 = \frac{c_3}{1-n_3}. \quad (2.87)$$

- Term in $n_2 \mathbf{n}_2 \cdot \mathbf{n}_2$

$$-\phi_4 + 3\phi_4 + \frac{d\phi_4}{dn_3} n_3 = \frac{d\phi_4}{dn_3}. \quad (2.88)$$

Hence

$$\frac{d\phi_4}{dn_3} = \frac{2\phi_4}{1-n_3} \quad \longrightarrow \quad \phi_4 = \frac{c_4}{(1-n_3)^2}, \quad (2.89)$$

where c_0 – c_4 are integration constants. With the above relations Eq.(2.73) becomes then

$$\begin{aligned} \Phi(\{n_\alpha\}) &= [c_0 - \ln(1-n_3)] n_0 + \frac{c_1}{1-n_3} n_1 n_2 + \frac{c_2}{(1-n_3)^2} n_2^3 \\ &+ \frac{c_3}{1-n_3} \mathbf{n}_1 \cdot \mathbf{n}_2 + \frac{c_4}{(1-n_3)^2} n_2 \mathbf{n}_2 \cdot \mathbf{n}_2. \end{aligned} \quad (2.90)$$

It remains to determine the constants $c_0 - c_4$. The key idea is to identify these constants in order to satisfy the classical relation ([44], page 72)

$$c(\mathbf{r}, \mathbf{r}') = -\beta \frac{\delta^2 \mathcal{F}^{ex}}{\delta \rho(\mathbf{r}) \delta \rho(\mathbf{r}')} \quad (2.91)$$

where $c(\mathbf{r}, \mathbf{r}')$ is given by the Percus-Yevick relation Eq.(2.60). This is a rather technical task which is developed in Appendix A.2.1. The final result for the expression of the excess free energy Φ is the original FMT version of Rosenfeld

$$\begin{cases} \Phi^{RF} &= \Phi_1^{RF} + \Phi_2^{RF} + \Phi_3^{RF} \\ \Phi_1^{RF} &= -n_0 \ln(1-n_3) \\ \Phi_2^{RF} &= \frac{n_1 n_2 - \mathbf{n}_1 \cdot \mathbf{n}_2}{1-n_3} \\ \Phi_3^{RF} &= \frac{n_2^3 - 3n_2 \mathbf{n}_2 \cdot \mathbf{n}_2}{24\pi(1-n_3)^2}. \end{cases} \quad (2.92)$$

Rosenfeld's approximation of the excess free energy is in good agreement with MC results when applying it to one component inhomogeneous hard sphere fluids [61, 66] as well as for HS fluid mixtures [67]. However, the Rosenfeld functional based on the Percus-Yevick closure leads to the Percus-Yevick compressibility equation of state [68]

$$\beta P_{PY} = \frac{\partial \Phi}{\partial n_3} = \frac{n_0}{1-n_3} + \frac{n_1 n_2}{(1-n_3)^2} + \frac{n_2^3}{12\pi(1-n_3)^3}, \quad (2.93)$$

In a homogeneous HS fluid, where the scalar weighted densities reduce to the SPT variables $n_\alpha \rightarrow \xi_\alpha$ given by Eq.(2.52) ($\xi_0 = \rho$, $\xi_1 = \rho R$, $\xi_2 = \rho 4\pi R^2$, $\xi_3 = \rho(4/3\pi R^3) = \eta$), P_{PY} can be expressed in terms of the particle packing fraction η as follows

$$\beta P_{PY} = \rho_b \frac{1 + \eta + \eta^2}{(1-\eta)^3}, \quad (2.94)$$

If the Rosenfeld functional turns out to satisfy simulation data for the one-component hard sphere fluid at low densities, the Percus-Yevick Eq.(2.94) overestimates the pressure of about 7% when approaching the liquid-solid phase transition [63]. The semi-empirical Carnahan-Starling-Boublik (CS) equation of state (EOS) [69] (extended by Mansoori-Carnahan-Starling-Leland (MCSL) to mixtures) is a simple and very accurate EOS of one-component HS fluids:

$$\beta P_{\text{MCSL}} = \frac{1 + \eta + \eta^2 - \eta^3}{(1 - \eta)^3} = \frac{n_0}{1 - n_3} + \frac{n_1 n_2}{(1 - n_3)^2} + \frac{n_2^3}{12\pi(1 - n_3)^3} - \frac{n_3 n_2^3}{36\pi(1 - n_3)^3}. \quad (2.95)$$

An improved version of FMT called the ‘‘White-Bear’’ version of FMT has therefore been developed, which is given in the appendix §A.2.2 [64]:

$$\begin{cases} \Phi^{WB} &= \Phi_1^{WB} + \Phi_2^{WB} + \Phi_3^{WB} \\ \Phi_1^{WB} &= -n_0 \ln(1 - n_3) \\ \Phi_2^{WB} &= \frac{n_1 n_2 - \mathbf{n}_1 \cdot \mathbf{n}_2}{1 - n_3} \\ \Phi_3^{WB} &= \frac{n_3 + (1 - n_3)^2 \ln(1 - n_3)}{36\pi n_3^2 (1 - n_3)^2} [n_2^3 - 3n_2 \mathbf{n}_2 \cdot \mathbf{n}_2]. \end{cases} \quad (2.96)$$

2.5 Application of the hard sphere fluid in EDL model approaches

The hard sphere fluid is the simplest model approach of discontinuous fluids. Most descriptions consider the hard sphere fluid as a fundamental reference system to which particle interactions (of dipolar and/or electrical nature) are added.

As a starting point of the present work, the water solvent in the interplatelet pores is modeled by an inhomogeneous hard sphere fluid confined between two planar hard walls and in equilibrium with an external homogeneous bulk fluid as represented schematically in Fig.2.3.

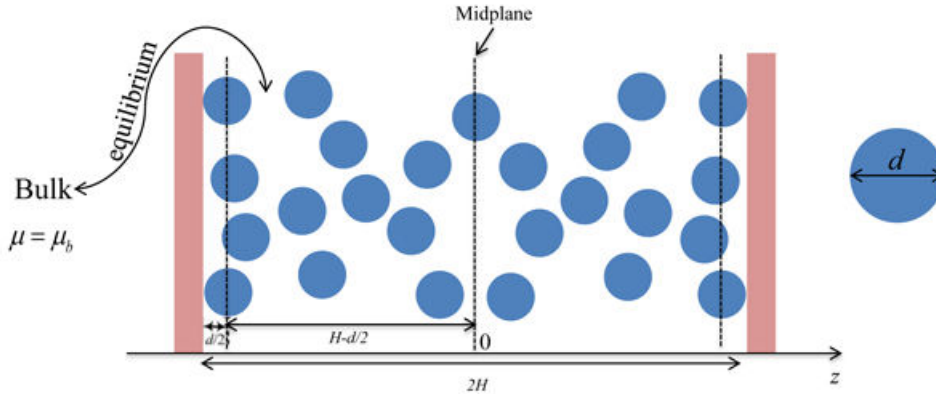


Figure 2.3: HS model for the water solvent in an Electrical Double Layer.

Roth calculates the density profile of HS fluids in various geometries by using the different versions of FMT. By comparing the numerical results with MC data, he shows that the White Bear and the White Bear Mark II give almost the same results which are more accurate than those obtained with the Rosenfeld version [64]. For the sake of simplicity, the White Bear version of FMT Eq.(2.96) is therefore used to study such a hard sphere system in which the intermolecular and external potentials incorporated solely finite particle size effects. In the planar geometry of Fig.2.3, these potentials read as

$$u_{\text{HS}}(r) = \begin{cases} 0, & r \geq d \\ \infty, & r < d \end{cases} \quad (2.97)$$

and

$$V_{\text{ext}}(z) = \begin{cases} 0, & z \geq R = d/2 \\ \infty, & z < R = d/2 \end{cases} \quad (2.98)$$

with r the interparticle distance and z the distance perpendicular to the walls

2.5.1 FMT applied to planar geometry cases

For a planar geometry as in Fig.2.3 the fundamental equations of FMT presented in the previous sections depend only on the distance from the wall z . Consequently it follows

$$n_\alpha(\mathbf{r}) \equiv n_\alpha(z) = \int \rho(z') \omega_\alpha(z - z') dz', \quad (2.99)$$

$$\beta \frac{\delta \mathcal{F}_{HS}^{\text{ex}}[\rho]}{\delta \rho(z)} = \sum_\alpha \int \frac{\partial \Phi}{\partial n_\alpha} \frac{\delta n_\alpha(z')}{\delta \rho(z)} dz', \quad (2.100)$$

$$\frac{\delta n_\alpha(z')}{\delta \rho(z)} = \frac{\delta}{\delta \rho(z)} \int \rho(z'') \omega_\alpha(z' - z'') dz'' = \omega_\alpha(z' - z). \quad (2.101)$$

From these above definitions, it comes

$$\beta \frac{\delta \mathcal{F}_{HS}^{\text{ex}}[\rho]}{\delta \rho(z)} = \sum_\alpha \int \frac{\partial \Phi}{\partial n_\alpha} \omega_\alpha(z' - z) dz', \quad (2.102)$$

which can be expressed in the form of convolutions recalling that the scalar weight functions are even and the vectorial ones are odd

$$\beta \frac{\delta \mathcal{F}_{HS}^{\text{ex}}[\rho]}{\delta \rho(z)} = \sum_{\alpha=0}^3 \frac{\partial \Phi}{\partial n_\alpha} \otimes \omega_\alpha - \sum_{\alpha=1}^2 \frac{\partial \Phi}{\partial \mathbf{n}_\alpha} \otimes \omega_\alpha. \quad (2.103)$$

In the present case of a HS fluid confined between two planar hard walls, the density distribution defined in Eq.(2.9) can thus be rewritten as

$$\rho(z) = \rho_b \exp \left[\beta \mu_b^{\text{ex}} - \sum_{\alpha=0}^3 \frac{\partial \Phi}{\partial n_\alpha} \otimes \omega_\alpha + \sum_{\alpha=1}^2 \frac{\partial \Phi}{\partial \mathbf{n}_\alpha} \otimes \omega_\alpha - \beta V_{\text{ext}}(z) \right], \quad (2.104)$$

where the one-dimensional weight functions $\omega_\alpha(z)$ and $\omega_\alpha(z)$ are presented in the Appendix A.3.

2.5.2 Bulk hard sphere fluid equations

The first step in modeling inhomogeneous HS fluids is to determine the thermodynamic properties of the corresponding homogeneous bulk reference HS fluid. The bulk pressure is determined using the accurate semi-empirical Carnahan-Starling-Boublik EOS

$$P_{\text{CS}} = k_B T \rho_b \frac{1 + \eta + \eta^2 - \eta^3}{(1 - \eta)^3}, \quad (2.105)$$

The excess free energy and the excess chemical potential are calculated analytically from the Carnahan-Starling equation of state Eq.(2.105).

Starting from the definition of the intrinsic free energy \mathcal{F}

$$\mathcal{F} = N\mu - PV, \quad (2.106)$$

$$d\mathcal{F} = -SdT - PdV + \mu dN, \quad (2.107)$$

the relation between the pressure P and the intrinsic free energy \mathcal{F} is given by

$$P = - \left(\frac{\partial \mathcal{F}}{\partial V} \right)_{T,N}. \quad (2.108)$$

For the HS homogeneous fluid

$$\mathcal{F}_{HS}^{ex} = \mathcal{F}_{HS} - \mathcal{F}^{id} = \int_V^\infty (P^{HS} - P^{id}) dV = Nk_B T \int_V^\infty \left(\frac{\beta P^{HS}}{\rho_b} - 1 \right) \frac{dV}{V}, \quad (2.109)$$

with $dV/V = -d\eta/\eta$ and Eq.(2.105) it comes,

$$\beta f_{HS}^{ex} = \frac{\beta \mathcal{F}_{HS}^{ex}}{N} = \int_0^\eta \left(\frac{\beta P^{HS}}{\rho_b} - 1 \right) \frac{d\eta}{\eta} = \int_0^\eta \frac{4\eta - 2\eta^2}{(1-\eta)^3} \frac{d\eta}{\eta} = \frac{4\eta - 3\eta^2}{(1-\eta)^2}. \quad (2.110)$$

The excess chemical potential is then given by

$$\mu_{HS}^{ex} = \frac{\mathcal{F}_{HS}^{ex}}{N} + \frac{P_{HS}^{ex}}{\rho_b} = k_B T \left[\frac{4\eta - 3\eta^2}{(1-\eta)^2} + \frac{1 + \eta + \eta^2 - \eta^3}{(1-\eta)^3} - 1 \right] = k_B T \frac{8\eta - 9\eta^2 + 3\eta^3}{(1-\eta)^3}. \quad (2.111)$$

2.5.3 Results and discussion

The density profile is determined numerically by the solution of Eq.(2.104) with MATLAB[®] using an iterative Picard method [64]. In the numerical calculations, all integral convolutions are evaluated by using the “conv” function of the MATLAB[®] toolbox. Before performing the calculations, an appropriate step size Δz should be chosen in order that the results are insensitive to the step size. As shown in Fig.2.4, this can be done with a step size Δz which allows to recover the Carnahan-Starling bulk pressure by the value of density of the hard sphere fluid at contact $\rho_{\text{contact}} = \rho(z = d/2)$ in the case of a unique hard wall with the help of the contact theorem [63]

$$\rho_{\text{contact}} \Big|_{\Delta z \rightarrow 0} = \rho_b \frac{1 + \eta + \eta^2 - \eta^3}{(1-\eta)^3} = \rho_{CS}. \quad (2.112)$$

As a compromise between numerical calculation costs and the numerical accuracy, $\Delta z = 0.001d$ is selected in the present case leading to a relative error of 0.15% for $\rho_b d^3 = 0.7$.

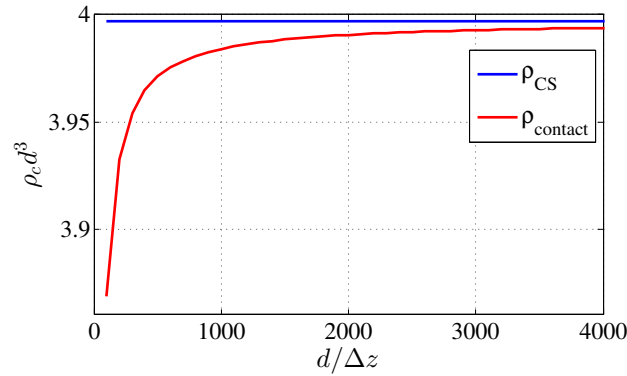


Figure 2.4: Contact value of the hard-sphere fluid near a hard wall versus the grid point number $d/\Delta z$ for a reduced bulk density $\rho_b d^3 = 0.7$.

To solve Eq.(2.104) by iteration with the Picard method, a suitable initial guess for $\rho(z)$ is the bulk density ρ_b . The new estimate of $\rho(z)$ is obtained by the right hand side of Eq.(2.104).

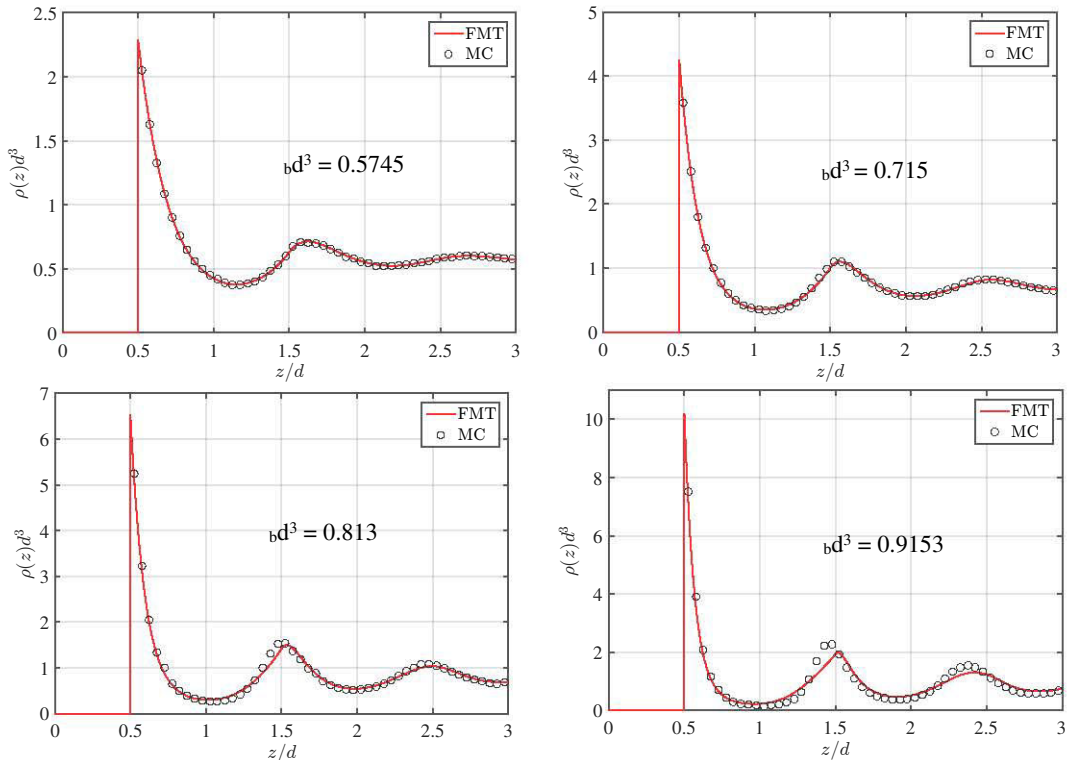


Figure 2.5: Density profiles of inhomogeneous hard sphere fluids at different reduced bulk densities near a hard wall in comparison with Monte Carlo simulation taken from [6].

The iteration is repeated until the change in the density profile $\rho(z)$ at each point is smaller than the convergence criterion.

Fig.(2.5) presents the density profiles of a HS fluid in contact with a unique planar hard wall placed at the origin ($z = 0$), obtained with the present FMT compared with the MC results taken from [6] for different normalized bulk densities.

Due to their finite size d , no particles can be found at a distance of half a diameter away from the wall. This zone is the so-called the “exclusion zone”. The density distributions have an oscillatory behavior. The density is maximum at the boundary of the exclusion zone at $z = d/2$. The following maxima are situated nearly at entire multiples of the particle diameter with an amplitude diminishing continuously until reaching the bulk density far away from the wall.

As expected, since the FMT formalism has been developed for low bulk densities [64], the agreement between FMT and MC results is very good at low bulk densities (e.g $\rho_b d^3 = 0.5745$), but is less accurate when increasing the bulk density.

The density profiles obtained by the FMT formalism for HS fluids confined between two planar hard walls at different separation distances are depicted in Fig.2.6. Similar to the former case of one planar hard wall, the density distribution is also oscillatory. However, the number of fluid layers is strongly dependent of the separation distance $2H$ between the two walls.

Another important mechanical property of confined fluids is the disjoining pressure Π_d which is defined as the force per unit area over the bulk pressure that has to be applied on the two walls to keep them at a fixed distance $2H$.

$$\Pi_d = P - P_b, \quad (2.113)$$

where the fluid pressure can be expressed as a function of the particle density at the wall by the so-called contact theorem

$$P = k_B T \rho(z = d/2). \quad (2.114)$$

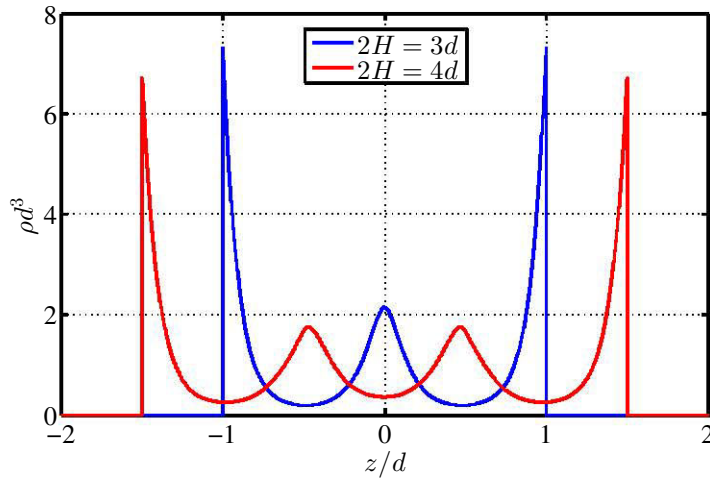


Figure 2.6: Density profiles of a hard sphere fluid confined between two hard walls for different separation distances between the walls for the reduced bulk density $\rho_b d^3 = 0.813$.

The disjoining pressure profile of the confined hard sphere fluid at the reduced bulk density $\rho_b d^3 = 0.73$ (corresponding to the water density with $d = 2.8 \times 10^{-10}$ m) as a function of the separation distance $2H$ is shown in Fig.2.7. Identically to the density profiles, Π_d exhibits an oscillatory shape alternating between repulsive and attractive parts. Note that only the parts of the curve represent equilibrium configurations, justifying the hypothesis of discrete numbers of water layers in the crystalline swelling regime at small interplatelet distances. This is clearly an important improvement compared to the classical Poisson-Boltzmann theory which results in a monotonously decreasing purely repulsive disjoining pressure (Fig.1.12).

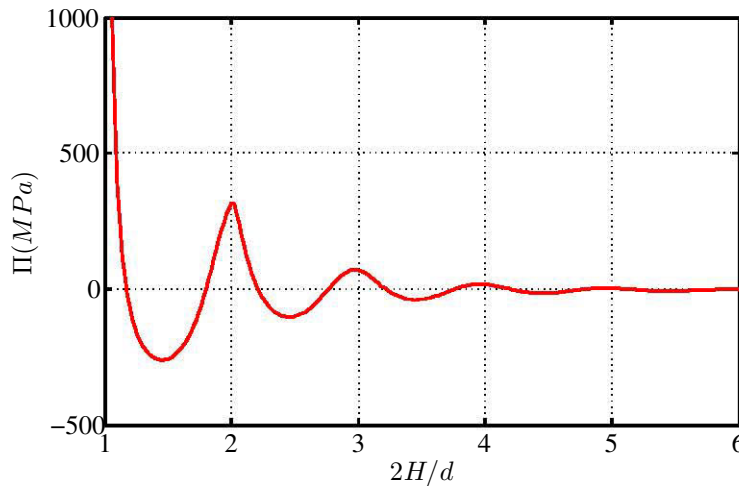


Figure 2.7: Disjoining pressure profile of a hard-sphere fluid confined between two planar hard walls as a function of the separation distance $2H$ at the reduced bulk density $\rho_b d^3 = 0.73$.

It has to be noted however that the disjoining pressure obtained for the simple HS fluid is highly repulsive, especially at small separation distances, overestimating the values expected for the water solvent in the nano-scale pores of clayey soils. In addition, the bulk pressure calculated by Eq.(2.105) is of about 10^8 Pa which is significantly higher than the expected value of about 10^5 Pa. In order to overcome this shortcoming, an attractive force should be added to the particle interaction potential which can counterbalance the excessive hard core repulsive force.

2.6 Conclusion

In this chapter, we have presented the derivation of classical Density Functional Theory which is probably the most effective theory to study molecular fluids. Density-Functional Perturbation Theory is a DFT approach, which allows to calculate exactly the particle density profiles of inhomogeneous fluids by determining their total correlation function. DFPT is the common theoretical foundation to study different fluid models presented in the following.

The simplest way to consider the molecular nature of the water solvent in clayey soils is to account for the finite size of the molecules. This can be done by modeling water solvent as a simple HS fluid with a purely repulsive interparticular potential accounting only for particle size exclusion. The Fundamental Measure Theory and especially the so-called “White Bear” version is an efficient tool to solve accurately HS fluids in any geometry.

According to our expectations, the resulting density distribution profiles for an inhomogeneous HS fluid in contact with a planar hard wall exhibit an oscillating behavior and are in good agreement with MC data.

As a first model of interplatelet pores as in clay minerals, this chapter depicts the results obtained with the “White-Bear” version of FMT for a HS fluid confined between two planar hard walls. The fluid molecules are organized in layers whose number is strongly dependent of the interplatelet distance which is similar to hydration behavior in the interplatelet pores observed during the crystalline swelling regime of hydrated expansive clays. The disjoining pressure obtained in this case has also an oscillatory behavior in function of the interplatelet distance allowing to account for repulsion and attraction. Such a profile allows to explain the formation of discrete water layers during the hydration process in the crystalline swelling regime at small interplatelet distances.

However, such a HS fluid model yields high repulsive values of the fluid pressure at small interplatelet distances and in the bulk fluid. To overcome this shortcoming, an attractive interparticle potential should be added to counterbalance the purely repulsive HS fluid interaction potential. The effect of different attractive particle interactions will therefore be treated in the two following chapters of this work.

Appendix A

A.1 Fourier transform of $\Theta(d - |\mathbf{r}|)$

The three-dimensional Fourier transform $\widehat{V}(\mathbf{k})$ of the function $V(\mathbf{r})$ and its inverse transform are defined by:

$$\widehat{V}(\mathbf{k}) = \int \int \int_{-\infty}^{\infty} V(\mathbf{r}) \exp(-i \mathbf{k} \cdot \mathbf{r}) \, d\mathbf{r}, \quad (\text{A.1})$$

$$V(\mathbf{r}) = \frac{1}{(2\pi)^3} \int \int \int_{-\infty}^{\infty} \widehat{V}(\mathbf{k}) \exp(i \mathbf{k} \cdot \mathbf{r}) \, d\mathbf{k}. \quad (\text{A.2})$$

If the function $V(r)$ is only dependent on $r = |\mathbf{r}|$, its Fourier transform depends only on k :

$$\widehat{V}(k) = 4\pi \int_0^{\infty} V(r) \frac{r \sin(kr)}{k} \, dr. \quad (\text{A.3})$$

For the Heaviside function $H(d - r)$, it comes hence

$$\widehat{H}(d - r) = 4\pi \int_0^d \frac{r \sin(kr)}{k} \, dr = 4\pi \frac{\sin(kd) - kd \cos(kd)}{k^3}. \quad (\text{A.4})$$

For the sphere characteristic functions

$$\omega_3(r) = \Theta(R - r), \quad (\text{A.5})$$

$$\omega_2(r) = \delta(R - |\mathbf{r}|), \quad (\text{A.6})$$

$$\omega_1(r) = \frac{\omega_2(r)}{4\pi R}, \quad (\text{A.7})$$

$$\omega_0(r) = \frac{\omega_2(r)}{4\pi R^2}, \quad (\text{A.8})$$

$$\omega_2(\mathbf{r}) = \nabla \omega_3 = \delta(r - R) \frac{\mathbf{r}}{r}, \quad (\text{A.9})$$

$$\omega_1(\mathbf{r}) = \frac{\omega_2}{4\pi R}, \quad (\text{A.10})$$

and their Fourier transforms are given by

$$\widehat{\omega}_3(k) = 4\pi \frac{\sin(kR) - kR \cos(kR)}{k^3}, \quad (\text{A.11})$$

$$\widehat{\omega}_2(k) = 4\pi R \frac{\sin(kR)}{k}, \quad (\text{A.12})$$

$$\widehat{\omega}_1(k) = \frac{\sin(kR)}{k}, \quad (\text{A.13})$$

$$\widehat{\omega}_0(k) = \frac{\sin(kR)}{kR}, \quad (\text{A.14})$$

$$\widehat{\omega}_2(\mathbf{k}) = i\mathbf{k}\widehat{\omega}_3 = i4\pi \frac{\sin(kR) - kR \cos(kR)}{k^3} \mathbf{k}, \quad (\text{A.15})$$

$$\widehat{\omega}_1(\mathbf{k}) = \frac{\widehat{\omega}_2}{4\pi R} = i\mathbf{k}\widehat{\omega}_3 = i \frac{\sin(kR) - kR \cos(kR)}{k^3 R} \mathbf{k}, \quad (\text{A.16})$$

We calculate now

$$\begin{aligned} & 2(\widehat{\omega}_3 \otimes \widehat{\omega}_0 + \widehat{\omega}_1 \otimes \widehat{\omega}_2 + \widehat{\omega}_1 \otimes \widehat{\omega}_2) = \\ & 2 \left\{ 4\pi \frac{\sin(kR) - kR \cos(kR)}{k^3} \frac{\sin(kR)}{kR} + 4\pi \frac{R \sin^2(kR)}{k^2} - \frac{4\pi}{k^4 R} [\sin(kR) - kR \cos(kR)]^2 \right\} = \\ & \frac{8\pi}{k^4 R} \left\{ [\sin(kR) - kR \cos(kR)] \sin(kR) + (kR)^2 \sin^2(kR) - [\sin(kR) - kR \cos(kR)]^2 \right\} = \\ & \frac{8\pi}{k^3} \left\{ \cos(kR) \sin(kR) - kR [\cos^2(kR) - \sin^2(kR)] \right\} = \\ & \frac{4\pi}{k^3} [\sin(kd) - kd \cos(kd)]. \end{aligned} \quad (\text{A.17})$$

Finally, we have

$$\widehat{H} = 2(\widehat{\omega}_3 \otimes \widehat{\omega}_0 + \widehat{\omega}_1 \otimes \widehat{\omega}_2 + \widehat{\omega}_1 \otimes \widehat{\omega}_2) \quad (\text{A.18})$$

A.2 Development of the Fundamental Measure Theory

A.2.1 Determination of the constants c_1 - c_4

To determine the constants c_1 - c_4 of Eq.(2.90), let us start considering the case of low densities ($n_3 \rightarrow 0$). In this case, the radial distribution function g is equal to $\exp(-\beta u(r))$ [41] (page 263). This is a rather intuitive result for the case of hard spheres with $g = 0$ inside the sphere and $g = 1$ outside. Therefore using Eq.(A.18), the Ornstein-Zernike Eq.(2.22) leads to

$$\begin{aligned} c(|\mathbf{r} - \mathbf{r}'|) &= -\beta \frac{\delta^2 \mathcal{F}^{ex}}{\delta \rho(\mathbf{r}) \delta \rho(\mathbf{r}')} = -\Theta(2R - |\mathbf{r} - \mathbf{r}'|) \\ &= -2(\omega_0 \otimes \omega_3 + \omega_1 \otimes \omega_2 + \omega_1 \otimes \omega_2)(|\mathbf{r} - \mathbf{r}'|) \end{aligned} \quad (\text{A.19})$$

where Θ is the Heaviside function.

The functional integration of the previous relation leads to

$$\beta \mathcal{F}^{ex} = \frac{1}{2} \int \int d\mathbf{r} d\mathbf{r}' \rho(\mathbf{r}) \rho(\mathbf{r}') \Theta(2R - |\mathbf{r} - \mathbf{r}'|). \quad (\text{A.20})$$

Note that

$$\int d\mathbf{r}''' \omega_\alpha(\mathbf{r} - \mathbf{r}' - \mathbf{r}''') \omega_\beta(\mathbf{r}''') = \int d\mathbf{r}'' \omega_\alpha(\mathbf{r} - \mathbf{r}'') \omega_\beta(\mathbf{r}'' - \mathbf{r}'), \quad (\text{A.21})$$

where $\mathbf{r}'' = \mathbf{r}' + \mathbf{r}'''$ and note also that the scalar weight functions are even and the vector weight functions odd

$$\begin{aligned} \omega_\beta(\mathbf{r} - \mathbf{r}') &= \omega_\beta(\mathbf{r}' - \mathbf{r}) \\ \boldsymbol{\omega}_\beta(\mathbf{r} - \mathbf{r}') &= -\boldsymbol{\omega}_\beta(\mathbf{r}' - \mathbf{r}). \end{aligned} \quad (\text{A.22})$$

It comes then finally

$$\begin{aligned} \beta \mathcal{F}^{ex} &= \int d\mathbf{r} \int d\mathbf{r}' \rho(\mathbf{r}) \rho(\mathbf{r}') \int d\mathbf{r}'' [\omega_0(\mathbf{r}'' - \mathbf{r}) \omega_3(\mathbf{r}'' - \mathbf{r}') + \omega_1(\mathbf{r}'' - \mathbf{r}) \omega_2(\mathbf{r}'' - \mathbf{r}') \\ &\quad - \boldsymbol{\omega}_1(\mathbf{r}'' - \mathbf{r}) \cdot \boldsymbol{\omega}_2(\mathbf{r}'' - \mathbf{r}')] = \int d\mathbf{r}'' (n_0 n_3 + n_1 n_2 - \mathbf{n}_1 \cdot \mathbf{n}_2). \end{aligned} \quad (\text{A.23})$$

The comparison with Eq.(2.90) for $n_3 \rightarrow 0$ yields

$$c_0 = 0 \quad c_1 = 1 \quad c_3 = -1 \quad , \quad (\text{A.24})$$

which allows to rewrite the expression of Φ in Eq.(2.90) as

$$\begin{aligned} \Phi(\{n_\alpha\}) &= -\ln(1-n_3)n_0 + \frac{1}{1-n_3}n_1n_2 + \frac{c_2}{(1-n_3)^2}n_2^3 \\ &\quad - \frac{1}{1-n_3}\mathbf{n}_1 \cdot \mathbf{n}_2 + \frac{c_4}{(1-n_3)^2}n_2\mathbf{n}_2 \cdot \mathbf{n}_2. \end{aligned} \quad (\text{A.25})$$

The remaining terms (in c_2, c_4) are obtained with the higher order terms of the virial development of \mathcal{F}^{ex} . With the above relation, the direct correlation function $c(r)$ becomes

$$\begin{aligned} c(|\mathbf{r} - \mathbf{r}'|) &= -\beta \frac{\delta^2 \mathcal{F}^{ex}}{\delta \rho(\mathbf{r}) \delta \rho(\mathbf{r}')} \\ c(r) &= -\sum_{\alpha, \beta} \frac{\partial^2 \Phi}{\partial n_\alpha \partial n_\beta} \omega_\alpha \otimes \omega_\beta + \sum_{\alpha, \beta} \frac{\partial^2 \Phi}{\partial \mathbf{n}_\alpha \partial \mathbf{n}_\beta} \omega_\alpha \otimes \omega_\beta, \end{aligned} \quad (\text{A.26})$$

where the first derivative terms are given by

$$\begin{aligned} \frac{\partial \Phi}{\partial n_0} &= -\ln(1-n_3) \\ \frac{\partial \Phi}{\partial n_1} &= \frac{n_2}{1-n_3} \\ \frac{\partial \Phi}{\partial n_2} &= \frac{n_1}{1-n_3} + 3c_2 \frac{n_2^2}{(1-n_3)^2} + c_4 \frac{\mathbf{n}_2 \cdot \mathbf{n}_2}{(1-n_3)^2} \\ \frac{\partial \Phi}{\partial n_3} &= \frac{n_0}{1-n_3} + 2c_2 \frac{n_2^3}{(1-n_3)^2} + \frac{n_1n_2}{(1-n_3)^2} - \frac{\mathbf{n}_1 \cdot \mathbf{n}_2}{(1-n_3)^2} + 2c_4 \frac{n_2(\mathbf{n}_2 \cdot \mathbf{n}_2)}{(1-n_3)^3} \\ \frac{\partial \Phi}{\partial \mathbf{n}_1} &= -\frac{\mathbf{n}_2}{1-n_3} \\ \frac{\partial \Phi}{\partial \mathbf{n}_2} &= -\frac{\mathbf{n}_1}{1-n_3} + 2c_4 \frac{n_2\mathbf{n}_2}{(1-n_3)^2}, \end{aligned} \quad (\text{A.27})$$

and the second derivatives read as

$$\begin{aligned} \frac{\partial^2 \Phi}{\partial n_0 \partial n_3} &= \frac{1}{1-n_3} \\ \frac{\partial^2 \Phi}{\partial n_1 \partial n_2} &= \frac{1}{1-n_3} \\ \frac{\partial^2 \Phi}{\partial n_1 \partial n_3} &= \frac{n_2}{(1-n_3)^2} \\ \frac{\partial^2 \Phi}{\partial n_2^2} &= 6c_2 \frac{n_2}{(1-n_3)^2} \\ \frac{\partial^2 \Phi}{\partial n_2 \partial n_3} &= \frac{n_1}{(1-n_3)^2} + 6c_2 \frac{n_2^2}{(1-n_3)^3} + 2c_4 \frac{\mathbf{n}_2 \cdot \mathbf{n}_2}{(1-n_3)^3} \\ \frac{\partial^2 \Phi}{\partial n_3^2} &= \frac{n_0}{(1-n_3)^2} + 4c_2 \frac{n_2^3}{(1-n_3)^3} + 2 \frac{n_1n_2}{(1-n_3)^3} - 2 \frac{\mathbf{n}_1 \cdot \mathbf{n}_2}{(1-n_3)^3} + 6c_4 \frac{n_2(\mathbf{n}_2 \cdot \mathbf{n}_2)}{(1-n_3)^4} \\ \frac{\partial^2 \Phi}{\partial \mathbf{n}_1 \partial n_3} &= -\frac{\mathbf{n}_2}{(1-n_3)^2} \\ \frac{\partial^2 \Phi}{\partial \mathbf{n}_1 \partial \mathbf{n}_2} &= -\frac{1}{1-n_3} \end{aligned} \quad (\text{A.28})$$

$$\begin{aligned}\frac{\partial^2 \Phi}{\partial \mathbf{n}_2 \partial n_2} &= 2c_4 \frac{\mathbf{n}_2}{(1-n_3)^2} \\ \frac{\partial^2 \Phi}{\partial \mathbf{n}_2 \partial n_3} &= -\frac{\mathbf{n}_1}{(1-n_3)^2} + 4c_4 \frac{n_2 \mathbf{n}_2}{(1-n_3)^3} \\ \frac{\partial^2 \Phi}{\partial \mathbf{n}_2 \partial \mathbf{n}_2} &= 2c_4 \frac{n_2}{(1-n_3)^2}.\end{aligned}$$

The direct correlation function is hence written as

$$\begin{aligned}-c(r) &= \frac{2}{1-n_3} \omega_0 \otimes \omega_3 + \frac{2}{1-n_3} \omega_1 \otimes \omega_2 + \frac{2n_2}{(1-n_3)^2} \omega_1 \otimes \omega_3 + 6c_2 \frac{n_2}{(1-n_3)^2} \omega_2 \otimes \omega_2 \\ &+ 2 \left[\frac{n_1}{(1-n_3)^2} + 6c_2 \frac{n_2^2}{(1-n_3)^3} + 2c_4 \frac{\mathbf{n}_2 \cdot \mathbf{n}_2}{(1-n_3)^3} \right] \omega_2 \otimes \omega_3 \\ &+ \left[\frac{n_0}{(1-n_3)^2} + 6c_2 \frac{n_2^3}{(1-n_3)^4} + 2 \frac{n_1 n_2}{(1-n_3)^3} - 2 \frac{\mathbf{n}_1 \cdot \mathbf{n}_2}{(1-n_3)^2} + 6c_4 \frac{n_2 (\mathbf{n}_2 \cdot \mathbf{n}_2)}{(1-n_3)^4} \right] \omega_3 \otimes \omega_3 \\ &+ \frac{2}{1-n_3} \omega_1 \otimes \omega_2 - 2c_4 \frac{n_2}{(1-n_3)^2} \omega_2 \otimes \omega_2.\end{aligned}\tag{A.29}$$

In a homogeneous fluid, $n_\alpha \rightarrow \xi_\alpha$ and the vector quantities \mathbf{n}_α vanish, the direct correlation function $c(r)$ reduces then to

$$\begin{aligned}-c(r) &= \frac{2}{1-\xi_3} \omega_0 \otimes \omega_3 + \frac{2}{1-\xi_3} \omega_1 \otimes \omega_2 + \frac{2\xi_2}{(1-\xi_3)^2} \omega_1 \otimes \omega_3 + 6c_2 \frac{\xi_2}{(1-\xi_3)^2} \omega_2 \otimes \omega_2 \\ &+ 2 \left[\frac{\xi_1}{(1-\xi_3)^2} + 6c_2 \frac{\xi_2^2}{(1-\xi_3)^3} \right] \omega_2 \otimes \omega_3 \\ &+ \left[\frac{\xi_0}{(1-\xi_3)^2} + 6c_2 \frac{\xi_2^3}{(1-\xi_3)^4} + 2 \frac{\xi_1 \xi_2}{(1-\xi_3)^3} \right] \omega_3 \otimes \omega_3 \\ &+ \frac{2}{1-\xi_3} \omega_1 \otimes \omega_2 - 2c_4 \frac{\xi_2}{(1-\xi_3)^2} \omega_2 \otimes \omega_2.\end{aligned}\tag{A.30}$$

Rearranging the terms according to

$$\begin{aligned}-c(r) &= \frac{2}{1-\xi_3} [\omega_0 \otimes \omega_3 + \omega_1 \otimes \omega_2 + \omega_1 \otimes \omega_2] \\ &+ \left[\frac{\xi_0}{(1-\xi_3)^2} + 6c_2 \frac{\xi_2^3}{(1-\xi_3)^4} + 2 \frac{\xi_1 \xi_2}{(1-\xi_3)^3} \right] \omega_3 \otimes \omega_3 \\ &- 8\pi R c_4 \frac{\xi_2}{(1-\xi_3)^2} \omega_1 \otimes \omega_2 \\ &+ 24\pi c_2 \frac{\xi_2}{(1-\xi_3)^2} \omega_1 \otimes \omega_2 \\ &+ 2 \left[\frac{\xi_1}{(1-\xi_3)^2} + 6c_2 \frac{\xi_2^2}{(1-\xi_3)^3} + \frac{\xi_2}{4\pi R (1-\xi_3)^2} \right] \omega_2 \otimes \omega_3,\end{aligned}\tag{A.31}$$

and identifying Eq.(A.31) with the expression of the direct correlation function in Eq.(2.60), one obtains

$$c_2 = \frac{1}{24\pi} \quad c_4 = -\frac{1}{8\pi}.\tag{A.32}$$

Introducing these results in Eq.(A.25) yields finally in the expression of the excess free energy

in the original FMT version of Rosenfeld

$$\begin{cases} \Phi^{RF} &= \Phi_1^{RF} + \Phi_2^{RF} + \Phi_3^{RF} \\ \Phi_1^{RF} &= -n_0 \ln(1 - n_3) \\ \Phi_2^{RF} &= \frac{n_1 n_2 - \mathbf{n}_1 \cdot \mathbf{n}_2}{1 - n_3} \\ \Phi_3^{RF} &= \frac{n_2^3 - 3n_2 \mathbf{n}_2 \cdot \mathbf{n}_2}{24\pi(1 - n_3)^2}. \end{cases} \quad (\text{A.33})$$

A.2.2 “White Bear” version

As mentioned in earlier, the Rosenfeld functional turns out to satisfy simulation data for the one-component hard sphere fluid but overestimates the pressure of about 7% when approaching the liquid-solid phase transition [63]. The semi-empirical Carnahan-Starling-Boublik (CS) equation of state (EOS) [69] (extended by Mansoori-Carnahan-Starling-Leland (MCSL) to mixtures) is known to be a simple and very accurate EOS of one-component HS fluids:

$$\beta P_{\text{MCSL}} = \frac{1 + \eta + \eta^2 - \eta^3}{(1 - \eta)^3} = \frac{n_0}{1 - n_3} + \frac{n_1 n_2}{(1 - n_3)^2} + \frac{n_2^3}{12\pi(1 - n_3)^3} - \frac{n_3 n_2^3}{36\pi(1 - n_3)^3}. \quad (\text{A.34})$$

In an improved version of FMT, called the “White-Bear” version of FMT, the reduced excess free energy density Φ is thus determined by imposing the MCSL equation of state Eq.(A.34) as an input [64]. In the homogeneous fluid, Φ is now postulated on the form

$$\Phi = f_1(n_3)n_0 + f_2(n_3)n_1 n_2 + f_3(n_3)n_2^3. \quad (\text{A.35})$$

Since the MCSL equation of state Eq.(A.34) is now imposed as an input, the relation Eq.(2.79) can no longer be verified. A thermodynamic relation between P_{MCSL} and the new functional expression of Φ can be established by starting from the expression of Ω in the homogeneous fluid

$$\frac{\Omega}{V} = -P = \left(k_B T \Phi + \tilde{f}_b^{id} - \rho_b \mu_b \right), \quad (\text{A.36})$$

where \tilde{f}_b^{id} is the ideal free energy per volume unit, which is given by

$$\tilde{f}_b^{id} = \rho_b k_B T \left[\ln(\Lambda^3 \rho_b) - 1 \right]. \quad (\text{A.37})$$

Starting from the definition of the chemical potential

$$\mu = \left. \frac{\partial(F/V)}{\partial \rho} \right|_T, \quad (\text{A.38})$$

the bulk chemical potential takes the form

$$\begin{aligned} \mu_b &= \left. \frac{\partial}{\partial \rho_b} \left(k_B T \Phi + \tilde{f}_b^{id} \right) \right|_T \\ &= k_B T \left. \frac{\partial \Phi}{\partial \rho_b} \right|_T + k_B T \left[\ln(\Lambda^3 \rho_b) - 1 \right] + k_B T. \end{aligned} \quad (\text{A.39})$$

Since

$$\frac{\partial \Phi}{\partial \rho_b} = \sum_{\alpha} \frac{\partial \Phi}{\partial n_{\alpha}} \frac{\partial n_{\alpha}}{\partial \rho_b}, \quad (\text{A.40})$$

where n_{α} are only scalar weighted densities and remarking that $\rho_b \frac{\partial n_{\alpha}}{\partial \rho_b} = n_{\alpha}$, it comes

$$- \beta P = \Phi - \sum_{\alpha} \frac{\partial \Phi}{\partial n_{\alpha}} n_{\alpha} - n_0. \quad (\text{A.41})$$

Using the expression of Φ given by Eq.(A.34) and Φ to the expression of Eq.(A.35) the above relation becomes

$$\beta P = n_0(1 + n_3 f'_1) + n_1 n_2 (f_2 + n_3 f'_2) + n_2^3 (2f_3 + n_3 f'_3). \quad (\text{A.42})$$

and identifying P to P_{MCSL} given by Eq.(A.34), the identification of the different terms in n_0 , $n_1 n_2$ and n_2^3 gives

$$\begin{aligned} 1 + n_3 f'_1 &= \frac{1}{1 - n_3} \\ f'_1 &= \frac{1}{1 - n_3} \\ f_1 &= -\ln(1 - n_3) + d_1 = -\ln(1 - n_3), \end{aligned} \quad (\text{A.43})$$

where the constant d_1 has been chosen so that the function $\Phi_1 = f_1(n_3)n_0$ coincides with the expression of Rosenfeld Eq.(2.92) for $n_3 \rightarrow 0$.

In the same manner, the function f_2 is solution of

$$f_2 + n_3 f'_2 = \frac{1}{(1 - n_3)^2}, \quad (\text{A.44})$$

Setting $f_2 = \frac{A}{n_3}$, where A is an arbitrary function of n_3 , yields

$$\begin{aligned} A' &= \frac{1}{(1 - n_3)^2}, \\ A &= \frac{1}{1 - n_3} + d_2. \end{aligned} \quad (\text{A.45})$$

Hence

$$f_2 = \frac{1}{n_3(1 - n_3)} + \frac{d_2}{n_3} = \frac{(1 + d_2) - d_2 n_3}{n_3(1 - n_3)} = \frac{1}{1 - n_3}, \quad (\text{A.46})$$

which gives $d_2 = -1$ in order to find the original Rosenfeld functional Eq.(2.92) when $n_3 \rightarrow 0$. Finally, the problem for f_3 is written as

$$2f_3 + n_3 f'_3 = \frac{1 - n_3/3}{12\pi(1 - n_3)^3}, \quad (\text{A.47})$$

whose general solution is given by $f_3 = \frac{A}{n_3^2}$, so that the above equation can be rewritten as the derivative of function A

$$A' = \frac{3n_3 - n_3^2}{36\pi(1 - n_3)^3} = \frac{1}{36\pi} \left[\frac{2}{(1 - n_3)^3} - \frac{1}{(1 - n_3)^2} - \frac{1}{1 - n_3} \right], \quad (\text{A.48})$$

and thus

$$\begin{aligned} A &= \frac{1}{36\pi} \left[\frac{1}{(1 - n_3)^2} - \frac{1}{1 - n_3} + \ln(1 - n_3) + d_4 \right] \\ &= \frac{1}{36\pi(1 - n_3)^2} \left[n_3 + (1 - n_3)^2 \ln(1 - n_3) + d_4(1 - n_3)^2 \right]. \end{aligned} \quad (\text{A.49})$$

In order to find the original Rosenfeld form when $n_3 \rightarrow 0$, d_4 must be zero, verifying that $\lim_{n_3 \rightarrow 0} f_3 = 1/(24\pi)$ and finally

$$f_3 = \frac{1}{36\pi n_3^2 (1 - n_3)^2} [n_3 + (1 - n_3)^2 \ln(1 - n_3)]. \quad (\text{A.50})$$

Keeping the structure of Eq.(2.92) for the vector-like weighted densities, the reduced excess free energy density in the ‘‘White Bear’’ version of FMT is then given by

$$\begin{cases} \Phi^{WB} &= \Phi_1^{WB} + \Phi_2^{WB} + \Phi_3^{WB} \\ \Phi_1^{WB} &= -n_0 \ln(1 - n_3) \\ \Phi_2^{WB} &= \frac{n_1 n_2 - \mathbf{n}_1 \cdot \mathbf{n}_2}{1 - n_3} \\ \Phi_3^{WB} &= \frac{n_3 + (1 - n_3)^2 \ln(1 - n_3)}{36\pi n_3^2 (1 - n_3)^2} [n_2^3 - 3n_2 \mathbf{n}_2 \cdot \mathbf{n}_2]. \end{cases} \quad (\text{A.51})$$

This approach obviously results in a different expression of the direct correlation function than the one originally proposed by Rosenfeld and which is also accurate in comparison with MC simulation data [63]. As a test for self-consistency, the bulk pressure is recalculated from Eq.(A.51)

$$\frac{\partial \Phi}{\partial n_3} = \frac{n_0}{1 - n_3} + \frac{n_1 n_2}{(1 - n_3)^2} - \frac{n_2^3 (2 + n_3 (n_3 - 5))}{36\pi n_3^2 (1 - n_3)^3} - \frac{n_2^3 \ln(1 - n_3)}{18\pi n_3^3}, \quad (\text{A.52})$$

which differs slightly from the MCSL expression Eq.(A.34). For the seek of minimizing this inconsistency, another equation of state was proposed [70]

$$\beta P_{CSIII} = \frac{n_0}{1 - n_3} + \frac{n_1 n_2 \left(1 + \frac{1}{3} n_3^2\right)}{(1 - n_3)^2} + \frac{n_2^3 \left(1 - \frac{2}{3} n_3 + \frac{1}{3} n_3^2\right)}{12\pi (1 - n_3)^3} - \frac{n_3 n_2^3}{36\pi (1 - n_3)^3}. \quad (\text{A.53})$$

When setting $P = P_{CSIII}$ in Eq.(A.41) and applying the same procedure as before, the reduced excess free energy Φ takes the form

$$\begin{cases} \Phi^{WBII} &= \Phi_1^{WBII} + \Phi_2^{WBII} + \Phi_3^{WBII}, \\ \Phi_1^{WBII} &= -n_0 \ln(1 - n_3), \\ \Phi_2^{WBII} &= \frac{n_1 n_2 - \mathbf{n}_1 \cdot \mathbf{n}_2}{1 - n_3} \left[1 + \frac{1}{3} \phi_2(n_3)\right], \\ \Phi_3^{WBII} &= \frac{n_2^3 - 3n_2 \mathbf{n}_2 \cdot \mathbf{n}_2}{24\pi (1 - n_3)^2} \left[1 - \frac{1}{3} \phi_3(n_3)\right], \\ \phi_2(n_3) &= \frac{1}{n_3} [2n_3 - n_3^2 + 2(1 - n_3) \ln(1 - n_3)] \\ \phi_3(n_3) &= \frac{1}{n_3^2} [2n_3 - 3n_3^2 + 2n_3^3 + 2(1 - n_3)^2 \ln(1 - n_3)] \end{cases} \quad (\text{A.54})$$

which is called ‘‘White Bear Mark II’’ version of FMT and which has the advantage of recovering the Carnahan-Starling-Boublik EOS in the limit of a uniform bulk fluid [71]

$$\frac{\partial \Phi}{\partial n_3} = \beta P_{CS} = \rho_b \frac{1 + \eta + \eta^2 - \eta^3}{(1 - \eta)^3}. \quad (\text{A.55})$$

A.3 One-dimensional weight functions $\omega_\alpha(z)$

To calculate the convolutions $f \otimes \omega_\alpha$, where the function f depends only on the spatial coordinate z perpendicular to the walls. The coordinate z being at the origin of the sphere, it comes:

$$\begin{aligned} F_3(z) &= f \otimes \omega_3 = \int r^2 dr \int_0^\pi d\theta \sin \theta \int_0^{2\pi} d\varphi \Theta_H(R - r) f(z - r \cos \theta) \\ &= 2\pi \int_0^R r^2 dr \int_0^\pi d\theta \sin \theta f(z - r \cos \theta). \end{aligned} \quad (\text{A.56})$$

Performing the change of variables $(r, -\cos \theta) \longrightarrow (r, z')$ with $z - z' = r \cos \theta$, we have

$$-dr d\cos \theta = |J| dr dz', \quad (\text{A.57})$$

with

$$J = \begin{vmatrix} \frac{\partial r}{\partial r} \Big|_{z'} & \frac{\partial r}{\partial z'} \Big|_r \\ -\frac{\partial \cos \theta}{\partial z} \Big|_{z'} & -\frac{\partial \cos \theta}{\partial z'} \Big|_r \end{vmatrix} = \begin{vmatrix} 1 & 0 \\ \frac{z-z'}{r^2} & \frac{1}{r} \end{vmatrix} = \frac{1}{r}. \quad (\text{A.58})$$

Hence,

$$\begin{aligned} F_3(z) &= 2\pi \int_{z'=-R}^{z'=R} \int_{r=|z'|}^{r=R} f(z-z') r dr dz' = \int_{z'=-R}^{z'=R} f(z-z') \omega^{(3)}(z') dz' \\ &= \int_{z'=z-R}^{z'=z+R} f(z') \omega^{(3)}(z-z') dz', \end{aligned} \quad (\text{A.59})$$

with $\omega^{(3)}(z) = 2\pi \int_{r=|z'|}^{r=R} r dr \Theta_H(R-|z'|) = \pi(R^2 - z'^2) \Theta_H(R-|z'|)$. If we suppose $f(z) = f_j$ for $z_j - \Delta z/2 < z < z_j + \Delta z/2$ on $2N$ intervals regularly separated by Δz , it comes

$$F_3(z) = \int_{z'=z-R}^{z'+R} f(z') \pi [R^2 - (z-z')^2] \quad (\text{A.60})$$

$$\begin{aligned} F_3(z_k) &= f_{k-N} \int_R^{R+\Delta z/2} \pi [R^2 - (z_k - z')^2] dz' + \sum_{j=k-N+1}^{k+N-1} f_j \int_{z_j-\Delta z/2}^{z_j+\Delta z/2} \pi [R^2 - (z_k - z')^2] dz' \\ &+ f_{k+N} \int_{R-\Delta z/2}^R \pi [R^2 - (z_k - z')^2] dz' = \sum_{j=1}^{2N+1} \Omega_j^{(3)} f_{k+N+1-j} = \sum_{j=-N}^N \Omega_{j+N+1}^{(3)} f_{k-j}. \end{aligned} \quad (\text{A.61})$$

The previous expressions coincide with the definition of the function *conv* of Matlab with the option (“*same*”), where the values of $\Omega_j^{(3)}$ are given by

$$\begin{aligned} j=1 \quad \Omega_1^{(3)} &= \pi \int_{R-\Delta z/2}^R [R^2 - (z_k - z')^2] dz' = \frac{\pi R^3 (\Delta z)^2}{4 R^2} \left[1 - \frac{\Delta z}{6R} \right] \\ 2 \leq j \leq 2N \quad \Omega_j^{(3)} &= \pi \int_{z_k+N+1-j-\Delta z/2}^{z_k+N+1-j+\Delta z/2} [R^2 - (z_k - z')^2] dz' \\ &= \pi R^2 \Delta z \left[1 - (N+1-j)^2 \left(\frac{\Delta z}{R} \right)^2 - \frac{1}{12} \left(\frac{\Delta z}{R} \right)^2 \right] \\ j=2N+1 \quad \Omega_{2N+1}^{(3)} &= \pi \int_{-R}^{-R+\Delta z/2} (R^2 - z'^2) dz' = \frac{\pi R^3 (\Delta z)^2}{4 R^2} \left[1 - \frac{\Delta z}{6R} \right] \end{aligned} \quad (\text{A.62})$$

For the kind of convolutions $f \otimes \omega_2$, where the function f depends only on the coordinate z , it comes

$$\begin{aligned} F_2(z) &= f \otimes \omega_2 = \int r^2 dr \int_0^\pi \sin \theta d\theta \int_0^{2\pi} d\varphi \delta(R-r) f(z - r \cos \theta) \\ &= 2\pi R^2 \int_0^\pi f(z - R \cos \theta) \sin \theta d\theta. \end{aligned} \quad (\text{A.63})$$

Imposing $z' = z - R \cos \theta$:

$$F_2(z) = f \otimes \omega_2 = 2\pi R \int_{z-R}^{z+R} f(z') dz' = 2\pi R \int f(z') \Theta_H(R - |z - z'|) dz'. \quad (\text{A.64})$$

Finally, with the kind of convolutions $f \otimes \omega_2$, where the function f depends only on the coordinate z , it comes

$$\begin{aligned} \mathbf{F}_2(z) &= f \otimes \omega_2 = \int r^2 dr \int_0^\pi \sin \theta d\theta \int_0^{2\pi} d\varphi \delta(R-r) \frac{\mathbf{r}}{r} f(z-r \cos \theta) \\ &= R^2 \int_0^{2\pi} \begin{pmatrix} \sin \theta \cos \varphi \\ \sin \theta \sin \varphi \\ \cos \theta \end{pmatrix} d\varphi \sin \theta f(z-R \cos \theta) d\theta. \end{aligned} \quad (\text{A.65})$$

The only non-zero component is the component along with Oz

$$(\mathbf{F}_2)_z(z) = 2\pi R^2 \int_0^\pi \cos \theta \sin \theta f(z-R \cos \theta) d\theta. \quad (\text{A.66})$$

Imposing $z' = z - R \cos \theta$:

$$\begin{aligned} (\mathbf{F}_2)_z(z) &= 2\pi \int_{z-R}^{z+R} (z-z') f(z') dz' = 2\pi \int (z-z') \Theta_H(R-|z-z'|) f(z') dz' \\ &= \omega^{(v2)}(z-z') dz', \end{aligned} \quad (\text{A.67})$$

with

$$\omega^{(v2)}(z-z') = 2\pi(z-z') \Theta_H(R-|z-z'|). \quad (\text{A.68})$$

If we suppose $f(z) = f_j$ on intervals which are regularly separated by Δz , it comes

$$\begin{aligned} (\mathbf{F}_2)_z(z) &= 2\pi \int (z-z') \Theta_H(R-|z-z'|) f(z') dz' \\ &= 2\pi \int_{z'-z-R}^{z'+R} (z-z') f(z') dz' = 2\pi \int_{z'=-R}^R z' f(z-z') dz' \\ (\mathbf{F}_2)_z(z_k) &\simeq \sum_j \Omega_{k-j+1}^{(2v)} f_j = \sum_j \Omega_j^{(2v)} f_{k-j+1} \end{aligned} \quad (\text{A.69})$$

$$\begin{aligned} (\mathbf{F}_2)_z(z_k) &\simeq 2\pi \int_{z_k-R}^{z_k+R} (z_k-z') dz' \\ &= 2\pi f_{k+N} \int_{z_{k+N}-\Delta z/2}^{z_{k+N}} (z_k-z') dz' \\ &\quad + 2\pi \sum_{j=2}^{2N} f_{k+N+1-j} \int_{z_{k+N+1-j}-\Delta z/2}^{z_{k+N+1-j}+\Delta z/2} (z_k-z') dz' \\ &\quad + 2\pi f_{k-N} \int_{z_{k-N}}^{z_{k-N}+\Delta z/2} (z_k-z') dz' \\ &= \sum_{j=1}^{2N+1} \Omega_j^{(2v)} f_{k+N+1-j} = \sum_{j=-N}^N \Omega_{j+N+1}^{(2v)} f_{k-j}, \end{aligned} \quad (\text{A.70})$$

with

$$\begin{aligned} \Omega_1^{(2v)} &= 2\pi \int_{z_{k+N}-\Delta z/2}^{z_{k+N}} (z_k-z') dz' = \pi \Delta z (z_k - z_{k+N} + \Delta z/4) = -\pi \Delta z^2 (N-1/4) \\ \Omega_j^{(2v)} &= 2\pi \int_{z_{k+N+1-j}-\Delta z/2}^{z_{k+N+1-j}+\Delta z/2} (z_k-z') dz' \\ &= 2\pi (z_k - z_{k+N+1-j}) \Delta z = -2\pi (N+1-j) \Delta z^2 \\ \Omega_{2N+1}^{(2v)} &= 2\pi \int_{z_{k-N}}^{z_{k-N}+\Delta z/2} (z_k-z') dz' = \pi \Delta z (z_k - z_{k-N} - \Delta z/4) = \pi \Delta z^2 (N-1/4) \end{aligned} \quad (\text{A.71})$$

Chapter 3

Lennard-Jones fluid

3.1 Introduction

The Lennard-Jones fluid is a classical model for simple fluids containing both a short-range repulsive and a long-range attractive part in the interparticle potential which is given by

$$u_{LJ}(r) = 4\epsilon \left[\left(\frac{\sigma}{r} \right)^{12} - \left(\frac{\sigma}{r} \right)^6 \right], \quad (3.1)$$

where ϵ is the depth of the potential well and σ the finite distance at which the interparticle potential is zero (see Fig.3.1). This fluid model is selected to account for the molecular nature of the water solvent expecting to lower the pressure due to the attractive term in r^{-6} . This term expresses the polar nature of the water solvent averaging all the different Van der Waals contributions, namely Keesom, Debye and London forces, which are all attractive in r^6 . The first term in r^{-12} expresses the Pauli repulsion at short distance.

The most powerful tool for theoretical analyses of inhomogeneous LJ fluids is probably the classical Density-Functional Theory (DFT), which treats the Helmholtz free energy as a functional of density distribution. In the framework of DFT, the behavior of LJ fluids can be effectively studied by splitting the intermolecular potential into a short-range repulsive and a long-range attractive part. The repulsive part is considered as an effective hard sphere reference system which is successfully treated by FMT, and the Mean-Field Approximation (MFA) is generally used for the attractive part [44]. MFA is computationally efficient due to its simplicity by entirely neglecting interparticle correlations while being able to describe qualitatively some inhomogeneous phenomena [60]. However, the limitations of the MFA are outstanding: it completely disregards the fluid structure and its performance is strongly system-dependent.

Various attempts have been made to remedy the MFA, such as done by Tang et al.[72] who extended the Barker-Henderson (BH) theory of uniform LJ fluids [73] to inhomogeneous LJ fluids. Their approach improves qualitatively the density profiles near a hard wall for low bulk densities but yields significant errors at high densities. Therefore, more sophisticated DFT models have been proposed to take into account correlations in inhomogeneous LJ fluids [58]. In the framework of these theories, the correlation effects are evaluated by computing the Radial Distribution Function (RDF) for the corresponding bulk fluid at a suitable averaged "coarse-grained" density. Such approaches are quite successful in predicting the structure of inhomogeneous fluids. Nevertheless, the use of homogeneous RDF to represent inhomogeneous fluids is highly questionable and very often the numerical computation is not stable in case of computationally demanding conditions (e.g. high densities and strongly correlated systems).

This chapter uses an exact Density-Functional Perturbation Theory (DFPT) presented in chapter 2, which can give a complete description of inhomogeneous LJ fluids in terms of their density profile and their RDF. Although this approach is computationally more demanding, it is stable and uses exact formula for predicting density profiles.

3.2 DFPT applied to Lennard-Jones fluids

According to Eq.(2.38), the interparticle LJ potential, $u_{LJ}(r)$ given by Eq.(3.1) needs to be split into a repulsive term $u_0(r)$ considered as the interparticle potential of the reference system and a weak attractive term $u_a(r)$, being the perturbation potential in the present DFPT approach. We use in this work a common separation which has been suggested by Weeks-Chandler-Andersen (WCA) [74] (Fig.3.1)

$$u_0(r) = \begin{cases} u_{LJ}(r) + \epsilon, & r < 2^{1/6}\sigma \\ 0, & r \geq 2^{1/6}\sigma \end{cases} \quad (3.2)$$

and

$$u_a(r) = \begin{cases} -\epsilon, & r < 2^{1/6}\sigma \\ u_{LJ}(r), & r \geq 2^{1/6}\sigma. \end{cases} \quad (3.3)$$

In the WCA theory, the thermodynamic properties of the reference system such as the pair

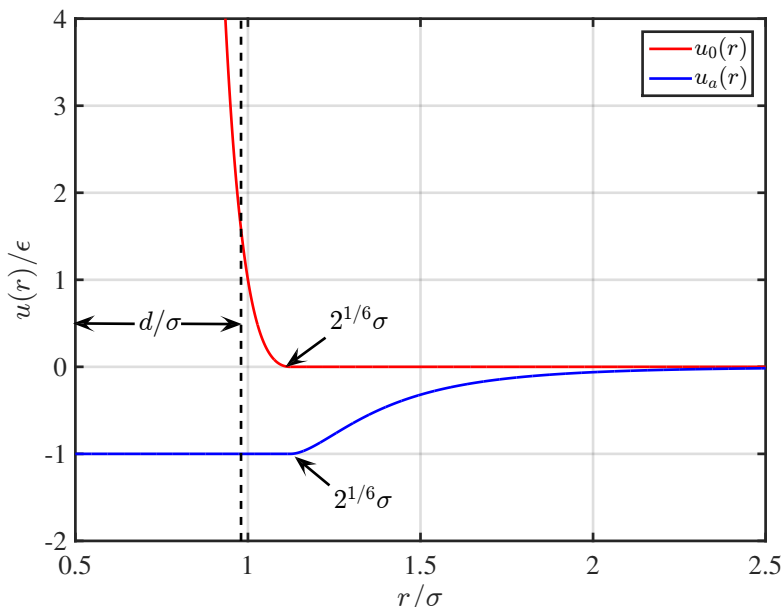


Figure 3.1: WCA separation of the intermolecular LJ potential.

correlation function and the excess free energy need to be determined, which represents a numerically quite expensive task. The authors have therefore proposed to approximate the reference system by an equivalent hard sphere system. The main task of this approximation is thus to determine an appropriate hard sphere diameter d . To do this, the cavity distribution function $y_0(r)$ of the reference system is introduced

$$y_0(r) = g_0(r) \exp[\beta u_0(r)], \quad (3.4)$$

where $g_0(r)$ is the corresponding RDF. Since the reference interaction is harshly repulsive, it is reasonable to approximate $y_0(r)$ by that of a hard sphere system of diameter d , $y_{HS}(r)$ so that the above equation reads as

$$g_0(r) \simeq y_{HS}(r) \exp[-\beta u_0(r)]. \quad (3.5)$$

The particle diameter d can be determined by approximating the thermodynamics of the reference system with those of the hard sphere system within the framework of the compressibility theorem [74]

$$\int d\mathbf{r} \{y_{HS}(\mathbf{r}) \exp[-\beta u_0(\mathbf{r})] - 1\} = \int d\mathbf{r} \{y_{HS}(\mathbf{r}) \exp[-\beta u_{HS}(\mathbf{r})] - 1\}. \quad (3.6)$$

This criterion yields an effective hard sphere diameter dependent on both temperature and density. However, this approximation is no longer valid when dealing with an arbitrary inhomogeneous fluid. For this physical reason, the analytical expression suggested by Lu, Evans and Telo da Gama [75] is used in this study, which is only temperature dependent

$$\frac{d(T^*)}{\sigma} = \frac{\alpha_1 T^* + \alpha_3}{\alpha_2 T^* + 1}, \quad (3.7)$$

where $\alpha_1 = 0.3837$ and $\alpha_2 = 0.4293$ according to the work of Verlet and Weis [76] and α_3 is an adjustable parameter chosen such that the approximation yields a good fit of the homogeneous fluid properties with simulation data. For instance, Kierlik and Rosinberg [60] have selected $\alpha_3 = 1.032$ for the WCA separation of the Lennard-Jones potential with a cutoff radius $r_c = 2.5\sigma$ (the cutoff radius r_c is the distance from which the interparticle potential is set to zero) in the MFA such that the liquid-vapor coexistence curve is in good agreement with simulation results. In the present study, an effective way for the determination of α_3 is used, which is based on the contact theorem. The value of α_3 is adjusted in the way that the predicted contact density coincides with its value from simulation data [77]. Finally, in the context of the WCA perturbation theory (combination between the WCA theory and DFPT), the density distribution of an inhomogeneous LJ fluid is obtained by using the following expression

$$\rho(\mathbf{r}_1) = \rho_b \exp \left[\beta \left(\mu_b^{ex} - \frac{\delta \mathcal{F}^{HS}[\rho]}{\delta \rho(\mathbf{r}_1)} - \int_0^1 d\lambda \int \rho(\mathbf{r}_2) [1 + h(\mathbf{r}_1, \mathbf{r}_2; [\rho]; \lambda)] u_a(\mathbf{r}_1, \mathbf{r}_2) d\mathbf{r}_2 - V_{\text{ext}}(\mathbf{r}_1) \right) \right], \quad (3.8)$$

where $\mathcal{F}^{HS}[\rho]$ is the excess free energy of the equivalent hard sphere reference system (of diameter d), which can be very accurately estimated by the use of FMT (chapter 2).

In the bulk limit, the density is independent of spatial position. The excess free energy, excess chemical potential and bulk pressure are given by

$$\mathcal{F}_b^{ex} = \mathcal{F}_b^{HS} + \frac{\rho_b^2}{2} V \int_0^1 d\lambda \int g(r; \lambda) u_a(r) 4\pi r^2 dr, \quad (3.9)$$

$$\mu_b^{ex} = \left(\frac{\partial \mathcal{F}_b^{ex}}{\partial N} \right)_{T,V} = \mu_b^{HS} + \rho_b \int_0^1 d\lambda \int g(r; \lambda) u_a(r) 4\pi r^2 dr, \quad (3.10)$$

$$p_b = - \left(\frac{\partial \mathcal{F}}{\partial V} \right)_{T,N} = p_b^{HS} + \frac{\rho_b^2}{2} \int_0^1 d\lambda \int g(r; \lambda) u_a(r) 4\pi r^2 dr, \quad (3.11)$$

where V is the volume of the system, N the particle number. \mathcal{F}_b^{HS} , μ_b^{HS} and p_b^{HS} are respectively the corresponding values of the equivalent HS reference system which are formulated in subsection 2.5.2.

3.3 Determination of the RDF using integral equation theory

The RDF plays a crucial role in determining thermodynamic properties of simple fluids. In this subsection, integral equation theories are used to determine the RDFs of homogeneous and inhomogeneous Lennard-Jones fluids.

3.3.1 Homogeneous Lennard-Jones fluids

As mentioned in chapter 2, the Ornstein-Zernike relation Eq.(2.22) and an appropriate closure Eq.(2.24) are the main ingredients of an integral equation theory. Some simple closures such as the HNC and PY can be obtained by setting the bridge function $B(r) = 0$, which have

been used to study Lennard-Jones fluids, and their failure is reported in the literature [78]. Therefore, several other closures have been developed recently to overcome this shortcoming. From the simulation data of correlation functions, Duh, Haymet and Handerson propose a new approximation for the bridge function of a homogeneous Lennard-Jones fluid (DHH closure) [78, 79], namely the functional form

$$B(s) = \frac{-s^2}{2 \left[1 + \left(\frac{5s + 11}{7s + 9} \right) s \right]}, \quad (3.12)$$

where $s(r) = \gamma(r) - \beta u_a(r)$ is the so-called “normalization” of the indirect correlation function $\gamma(r)$. From Fig.3.2, it is obvious that the role of $B(r)$ in predicting the RDF $g(r)$ of homoge-

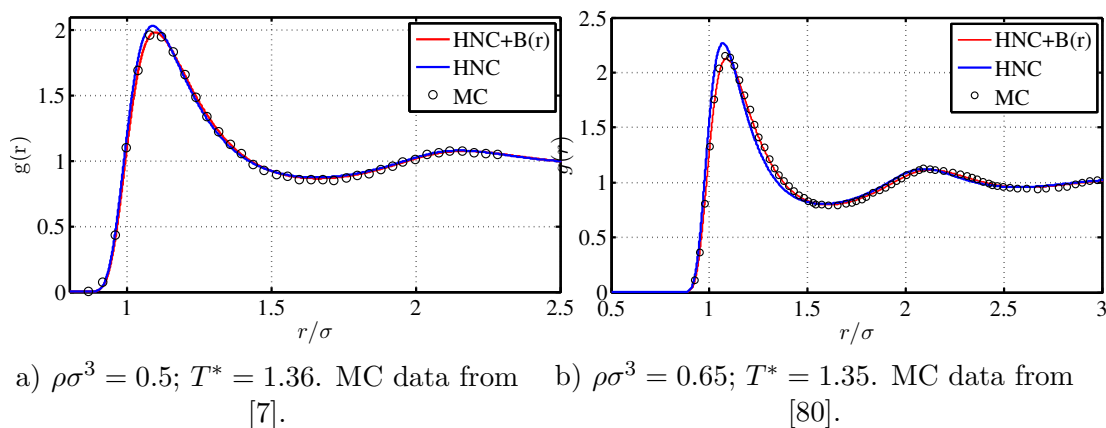


Figure 3.2: Radial Distribution Function $g(r)$ of bulk Lennard-Jones fluids obtained with two closures: HNC + $B(r)$ and HNC and comparison with simulation results.

neous fluids is negligible at low densities ($\rho\sigma^3 = 0.5$, Fig.3.2a), but it becomes significant at higher densities ($\rho\sigma^3 = 0.65$, Fig.3.2b). Especially, at very high densities and low temperature ($\rho\sigma^3 = 0.85$ and $\frac{k_B T}{\epsilon} = 0.88$), HNC without $B(r)$ fails in computing RDF, while HNC combined with a convenient $B(r)$ gives a very good agreement with Monte-Carlo data (Fig.3.3).

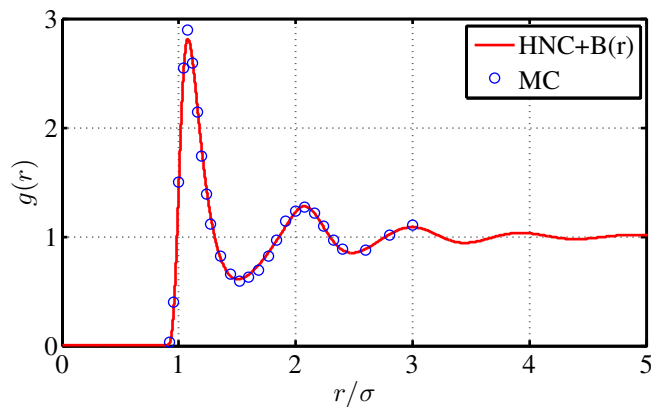


Figure 3.3: Radial distribution function of a homogeneous LJ fluid at high density and low temperature: $\rho\sigma^3 = 0.85$, $\frac{k_B T}{\epsilon} = 0.88$. The circles are MC results taken from [7].

3.3.2 Inhomogeneous LJ fluids

In the presence of an external potential $V_{\text{ext}}(r)$, LJ fluids become inhomogeneous systems in which the density distribution is position-dependent. Integral equation theories for inhomogeneous fluids are rigorously studied in the literature for example by Plischke and Henderson [81], and Kjellander and Sarman [82, 83]. The theories are developed in the same way as for the homogeneous case by solving the O-Z equation coupled with an appropriate closure.

Now, the inhomogeneous situation is considered where the fluid is confined between two infinite plates located at $z = \pm H$ with the particle density function $\rho(z)$. For our computations, a cylindrical coordinate system is adopted, which is depicted in Fig.3.4, with the radial direction r lying in the Oxy plane parallel to the plates and the axial coordinate z being orthogonal to the solid surfaces ($-H < z < H$). The first particle is placed on the Oz axis at the position z_1 . The second particle is at the position z_2 and χ_{12} is the projection of the distance between the two particles $r_{12} = \sqrt{(z_1 - z_2)^2 + \chi_{12}^2}$ on the plane Oxy . Note that the two particles interact with each other by the pair potential $u(z_1, z_2, \chi_{12})$. In what follows the correlation

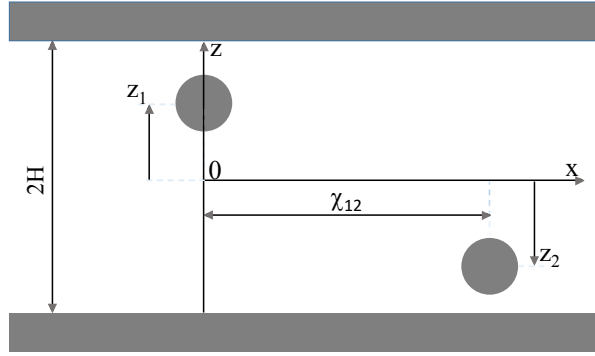


Figure 3.4: Two-dimensional geometry of Lennard-Jones fluids confined between two walls.

functions of inhomogeneous Lennard-Jones fluids are computed by solving the O-Z Eq.(2.22) in this cylindrical coordinate system. To start, the three-dimensional inhomogeneous problem is written as a two-dimensional one in the Oxy plane. The two-dimensional Ornstein-Zernike equation reads as

$$h(z_1, z_2, \chi_{12}) = c(z_1, z_2, \chi_{12}) + \int \rho(z_3) dz_3 \int c(z_1, z_3, \chi_{13}) h(z_2, z_3, \chi_{23}) 2\pi \chi_3 d\chi_3 \quad (3.13)$$

To simplify the notation, χ is used instead of χ_{12} . The above equation can be solved in combination with the extension of the DHH closure Eq.(3.12) for inhomogeneous Lennard-Jones fluids given by

$$h(z_1, z_2, \chi) = \exp[-\beta u(z_1, z_2, \chi) + \gamma(z_1, z_2, \chi) + B(z_1, z_2, \chi)] - 1, \quad (3.14)$$

$$B(s) = \frac{-s^2}{2 \left[1 + \left(\frac{5s + 11}{7s + 9} \right) s \right]}, \quad (3.15)$$

where $\gamma(z_1, z_2, \chi) = h(z_1, z_2, \chi) - c(z_1, z_2, \chi)$ designates the indirect correlation function and $s(z_1, z_2, \chi) = \gamma(z_1, z_2, \chi) - \beta u_a(z_1, z_2, \chi)$. In order to solve the anisotropic Ornstein-Zernike equation (3.13) with the DHH closure, the Hankel transform in χ is used

$$\tilde{f}(k) = \int f(\chi) J_0(k\chi) d\chi, \quad (3.16)$$

$$f(\chi) = \frac{1}{2\pi} \int \tilde{f}(k) J_0(k\chi) dk, \quad (3.17)$$

with k denoting the variable in the Hankel space, J_0 the Bessel function of order 0, $d\chi = 2\pi\chi d\chi$ and $d\mathbf{k} = 2\pi k dk$. Note that by treating z_1 and z_2 as parameters, the Hankel transform of the Ornstein-Zernike relation Eq.(3.13) is written as

$$\tilde{h}(k, z_1, z_2) = \tilde{c}(k, z_1, z_2) + \int dz_3 \rho(z_3) \tilde{c}(k, z_1, z_3) \tilde{h}(k, z_3, z_2). \quad (3.18)$$

The space between the two plates ($-H < z < H$) is divided in M equally spaced layers parallel to the Oxy plane of center z_m ($1 \leq m \leq M$) and of thickness Δz . Assuming that the density ρ_m in a layer m is uniform and denoting $\tilde{c}_{ij}(k) = \tilde{c}(z_i, z_j, k)$, $\tilde{\gamma}_{ij}(k) = \gamma(z_i, z_j, k)$, $\rho_m = \rho(z_m)$, Eq.(3.18) reads as

$$\tilde{\gamma}_{ij}(k) = \sum_m \rho_m \Delta z \tilde{c}_{im}(k) [\tilde{\gamma}_{mj}(k) + \tilde{c}_{mj}(k)], \quad (3.19)$$

or

$$\sum_m [\delta_{mi} - \rho_m \Delta z \tilde{c}_{im}(k)] \tilde{\gamma}_{mj}(k) = \sum_m \rho_m \Delta z \tilde{c}_{im}(k) \tilde{c}_{mj}(k), \quad (3.20)$$

where δ_{mi} is the Kronecker delta functions. Knowing $\tilde{c}_{ij}(k)$, for each value of k , the system Eq.(3.20) is a linear system which is easy to solve in $\tilde{\gamma}_{ij}(k)$ ($1 \leq i \leq M$ and $1 \leq j \leq M$).

For a given density distribution $\rho(r)$, the algorithm for the computation of the RDF is then

1. Chose an initial guess for $\gamma(z_1, z_2, \chi)$;
2. Calculate the total correlation function $h(z_1, z_2, \chi)$ from Eq.(3.14);
3. Calculate the direct correlation function $c(z_1, z_2, \chi) = h(z_1, z_2, \chi) - \gamma(z_1, z_2, \chi)$;
4. Perform the Hankel transform of $c(z_1, z_2, \chi) \rightarrow \tilde{c}(z_1, z_2, k)$ by use of Eq.(3.16);
5. Calculate $\tilde{\gamma}(z_1, z_2, k)$ from Eq.(3.18) for each value of k ;
6. Recalculate the indirect correlation function $\gamma(z_1, z_2, \chi)$ by the inverse Hankel transform with Eq.(3.17);
7. Iterate until convergence.

3.4 Results and discussions

3.4.1 Effective intermolecular potential

In the present approach, the calculation of the mean radial distribution function $g(r) = \int_0^1 d\lambda g(r; \lambda)$ is necessary for the determination of the thermodynamic properties of LJ fluids (both homogeneous and inhomogenous case). As this procedure is time consuming, an effective pair potential which accounts for the effects of λ while eliminating the explicit λ -dependence of the model formula would be useful. To this end, the RDF for different values of the λ parameter are illustrated in Fig.3.5. It is obvious that the averaged pair distribution function $\int_0^1 d\lambda g(r; \lambda)$ is very close to the curve corresponding to $\lambda = 0.5$. This remains valid for any Lennard-Jones fluid at low densities and temperatures as shown in Fig.3.6. According to this analysis, an effective pair potential will be used, instead of the λ -dependent Lennard-Jones potential to calculate the mean RDF. From now, the calculations of the λ -averaged RDFs are replaced by those of a fluid with an effective pair potential at $\lambda = 0.5$ according to

$$u_{eff} = u_0 + \frac{1}{2}u_a. \quad (3.21)$$

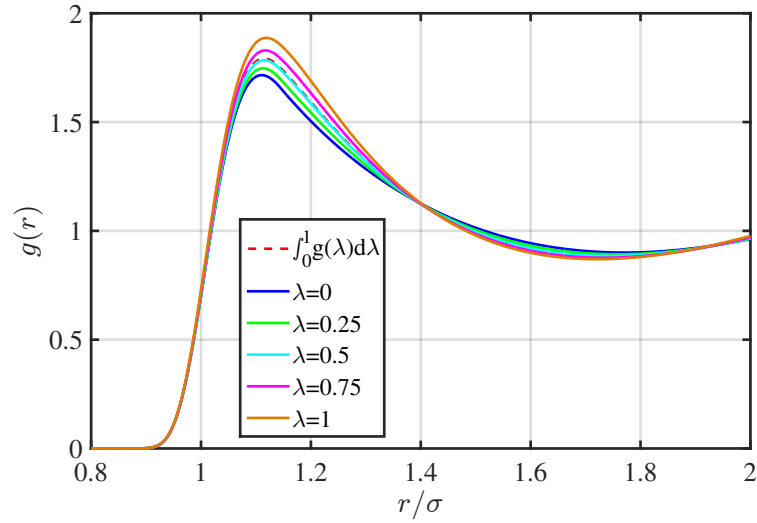


Figure 3.5: Influence of λ on the radial distribution function of a bulk Lennard-Jones fluid at $\rho\sigma^3 = 0.5$ and $T^* = 1.35$.

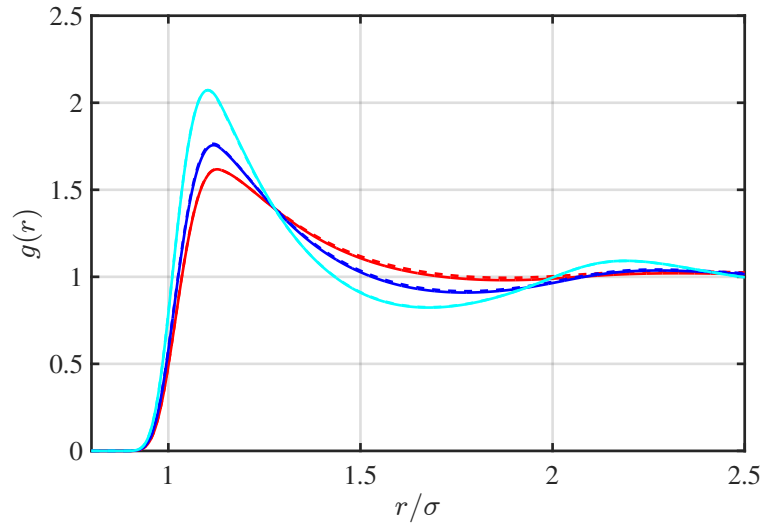


Figure 3.6: λ -dependency of the radial distribution function for various densities at $T^* = 1$. The red, blue and sky blue curves correspond to $\rho\sigma^3 = 0.2$, $\rho\sigma^3 = 0.4$ and $\rho\sigma^3 = 0.6$, respectively. The solid curves are calculated with $\lambda = 0.5$ and the dashed curves are the averaged curves in terms of λ .

3.4.2 Density profiles of inhomogeneous Lennard-Jones fluids

This section presents the density profiles of inhomogeneous LJ fluids near a planar hard wall and confined between two hard walls or in a slit pore obtained by the present perturbation theory. In order to verify the accuracy of the present approach, the results are compared with MC simulation data. The MC simulations use an exact LJ potential Eq.(3.1) with a possible cutoff whereas this study uses the WCA interparticle potential where u_0 given by Eq.(3.2) is approximated by an HS potential and u_a is given by Eq.(3.3) with the same parameters as the exact LJ model with a possible identical cutoff.

3.4.2.1 Lennard-Jones fluids near a hard wall

Consider a LJ fluid near a planar hard wall located at $z = 0$ whose external potential is given by

$$V_{\text{ext}}(z) = \begin{cases} \infty, & z < \sigma/2 \\ 0, & z \geq \sigma/2 \end{cases} \quad (3.22)$$

where z is the coordinate in the direction perpendicular to the solid surface. The computations are performed at fixed temperature $T^* = 1.35$ for various bulk densities in order to compare with the available MC data of Lutsko [8]. This is a typical test case for various density perturbation theories applied to LJ fluids [72, 84, 8, 85]. In the present study, the intermolecular pair potential is decomposed as in Eqs.(3.2) and (3.3), and the long-range attractive part is truncated at the cut-off radius $r_c = 4\sigma$, according to the MC simulation work of Lutsko [8]

$$u_{LJ}(r, r_c) = \begin{cases} u_{LJ}(r) - u_{LJ}(r_c), & r < r_c, \\ 0, & r > r_c. \end{cases} \quad (3.23)$$

The results of both the MFA and the present perturbation theory are depicted in Figs.(3.7-3.9). At relatively low bulk density ($\rho_b \sigma^3 = 0.5$), the mean distance between the fluid particles is relatively large and the attractive interparticle forces are consequently dominant. This leads to a depletion of fluid particles in the vicinity of the wall and the disappearance of oscillations in the density profile as shown in Fig.3.7. In contrast to the present theory which predicts correctly the monotonic increase of the density profile, the MFA is obviously unable to capture these two phenomena and fails in this case. When increasing the bulk density (Fig.3.8 and 3.9),

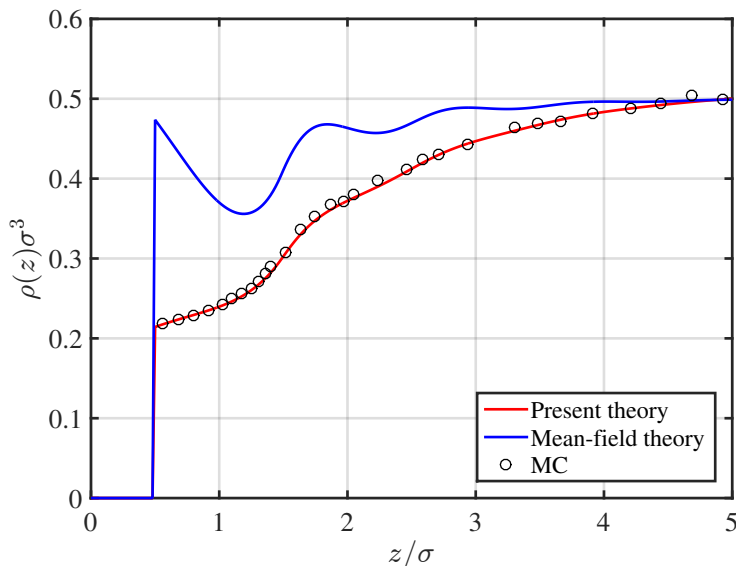
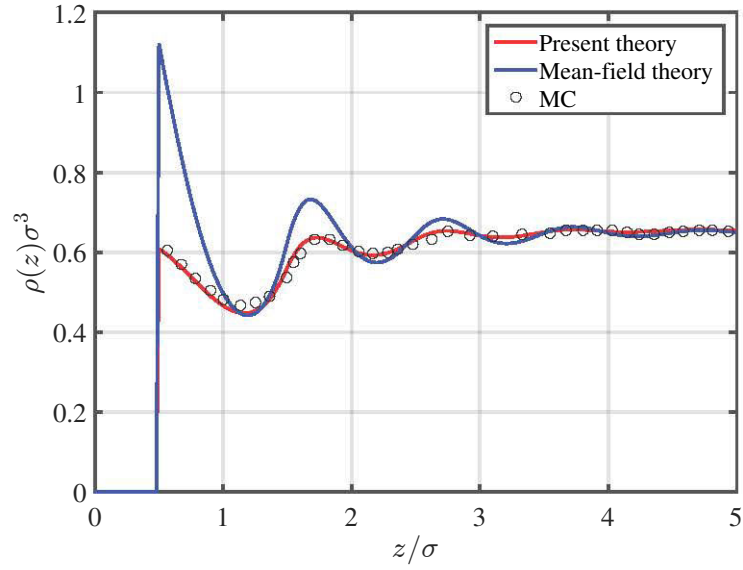
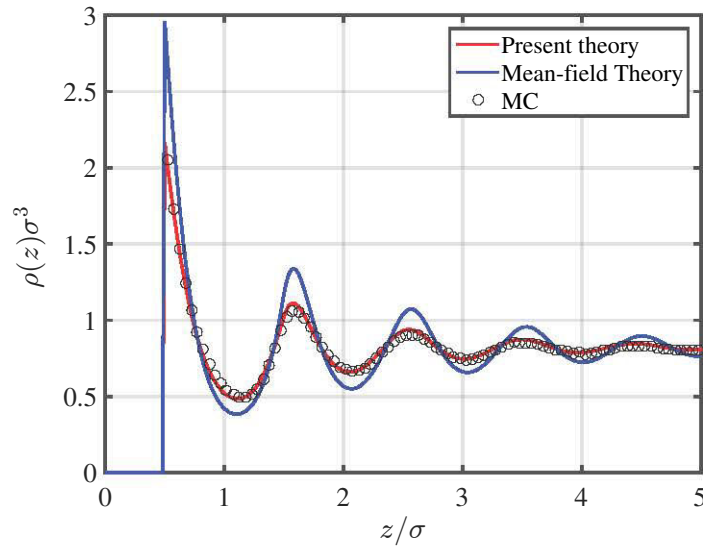


Figure 3.7: Density distribution profile of an inhomogeneous LJ fluid near a hard wall: $\rho_b \sigma^3 = 0.5$, $T^* = 1.2$. The MC simulation results are reported in the work of Lutsko [8].

the mean distance between the fluid particles is smaller, which enhances the contribution of the short-range repulsive interactions. Therefore, the density profiles oscillate around the bulk density value. In these intermediate and high density cases, MFA considerably overestimates the oscillation strength, especially in the vicinity of the wall while the present theory is still in excellent agreement with the MC data. To conclude, the present perturbation theory clearly captures the different physical phenomena occurring at the interface between inhomogeneous LJ fluids and a hard wall across the range of studied densities, and is in excellent agreement with MC results.


 Figure 3.8: As Fig.3.7 for $\rho_b\sigma^3 = 0.65$.

 Figure 3.9: As Fig.3.7 for $\rho_b\sigma^3 = 0.82$.

3.4.2.2 Confined Lennard-Jones fluids

This section presents the density profiles of inhomogeneous LJ fluids confined between two hard walls and in slit pores obtained with the present perturbation theory. According to the conditions used in the computer simulations [9, 10], the interparticle LJ potential given by Eq.(3.23) is used with a cut-off radius $r_c = 2.5\sigma$. The two walls are placed at $-H$ and H , respectively and generate an external potential given by

$$V_{\text{ext}}(z) = \begin{cases} \infty, & |z| > H - \sigma/2, \\ 0, & |z| \leq H - \sigma/2, \end{cases} \quad (3.24)$$

where z is the coordinate in the direction perpendicular to the walls. The density profiles predicted by the present theory, MFA and MC simulation data are shown in Fig.3.10. In comparison with the MC simulation results, the MFA exaggerates the oscillations of the density profile while the profile obtained from the present theory is quite accurate. In a next step the validity of the present theory is tested for the case of gas adsorption in slit-like pores. The

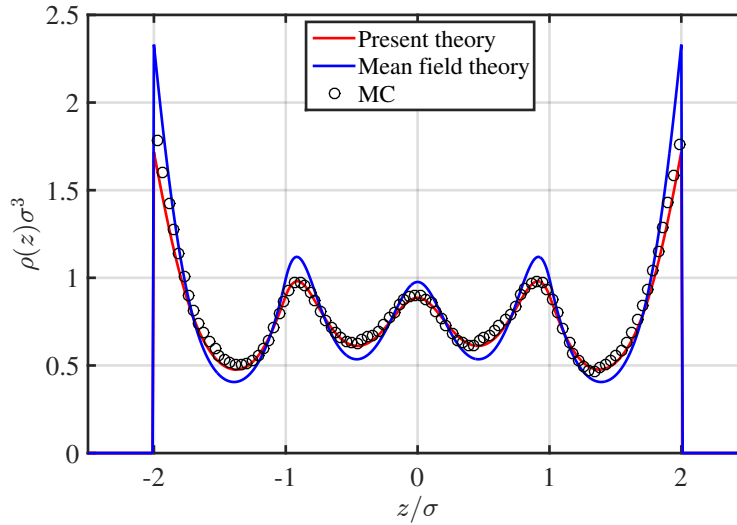


Figure 3.10: Density profiles of an inhomogeneous Lennard-Jones fluid confined between two hard walls: $\rho_b \sigma^3 = 0.75$; $T^* = 1.304$, and $2H = 5\sigma$. The open circles represent the MC simulation results [9].

fluid-solid interaction potential is modeled by the LJ 10-4-3 potential [86] written as

$$V_w(z) = 2\pi\epsilon \left[\frac{2}{5} \left(\frac{\sigma}{z} \right)^{10} - \left(\frac{\sigma}{z} \right)^4 - \frac{\sigma^4}{3\Delta(z + 0.61\Delta)^3} \right], \quad (3.25)$$

with $\Delta = 1/\sqrt{2}\sigma$. This type of fluid-solid potential contains a short-range repulsive and a long-range attractive part similar to the classical LJ potential as shown in Fig.3.11. The reduced

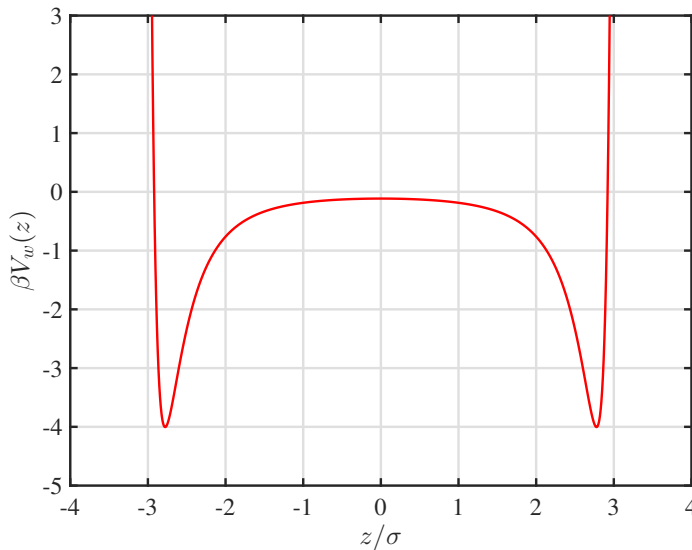


Figure 3.11: Solid-fluid LJ 10-4-3 potential at $2H = 7.5\sigma$.

bulk density $\rho_b \sigma^3$ is set to 0.5925 and the reduced temperature T^* to 1.2 identically to the MC simulation [10]. The density distribution profiles obtained with the MFA and the present theory along with the MC results are illustrated in Fig.3.12. It can be seen that both theories yield a satisfactory agreement with the MC data. The improvement of the present theory compared to the MFA is not significant. A possible explanation could be that correlations

between fluid constituents may be canceled out by the attractive forces coming from the walls.

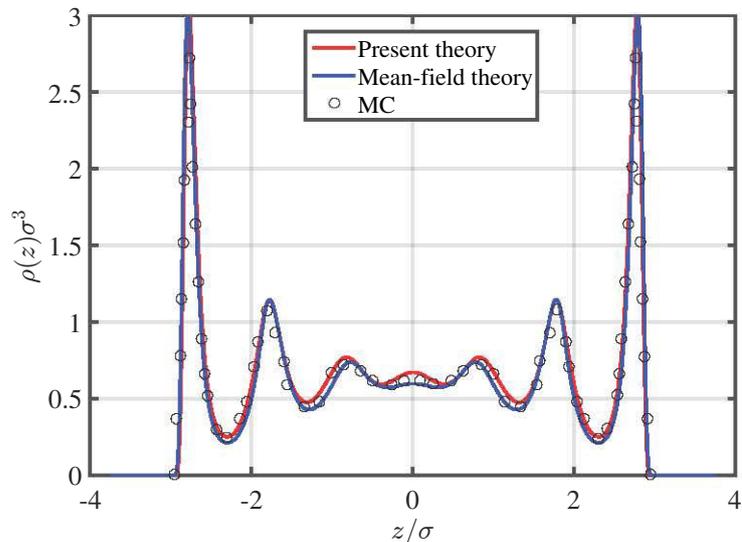


Figure 3.12: Density profiles of a Lennard-Jones fluid confined between two LJ walls: $\rho_b\sigma^3 = 0.5925$; $T^* = 1.2$, and $2H = 7.5\sigma$. The open circles represent the MC simulation results of [10].

3.4.3 Radial distribution function of inhomogeneous LJ fluids

Accounting for the spatial dependence in interparticle correlations of inhomogeneous fluids through their RDF $g(z_1, z_2, \chi)$ plays the key role in the present perturbation theory. Consequently, the RDFs of a LJ fluid near a hard wall for the density profiles of Fig.3.7-3.9 (for different spatial positions z) are presented in this section. For a relatively low bulk density $\rho_b\sigma^3 = 0.5$, no oscillation is observed in the density profile (Fig.3.7) and the RDF is isotropic at almost any position z (Fig.3.13). At the intermediate bulk density $\rho_b\sigma^3 = 0.65$, slight oscillations appear in the density profile close to the wall (Fig.3.8). At the same time, the profiles of the corresponding RDF exhibit an anisotropic behavior near the wall (Fig.3.14). The correlation between the anisotropy of the RDF $g(z_1, z_2, \chi)$ and the oscillations in the density profile is still more pronounced at high bulk density ($\rho_b\sigma^3 = 0.82$) (Fig.3.15). It is obvious that $g(z_1, z_2, \chi)$ is generally highly anisotropic in the vicinity of interfaces. Similarly to the oscillations observed in the density profiles, this anisotropic behavior is gradually reduced when moving away from the walls until the isotropic RDF of the corresponding bulk fluid is recovered. From these observations it can be deduced that replacing the anisotropic RDF $g(z_1, z_2, \chi)$ by its isotropic counterpart $g(r)$ of the corresponding bulk fluid yields satisfying density distribution profiles (in comparison with MC data) only at relatively low or intermediate bulk densities and fails at high bulk densities [72, 87, 84].

3.5 Application to Electrical Double Layer

The aim of this section is to derive an appropriate model for Electrical Double Layer (EDL) as they can be found in clayey soils. As shown above, the water solvent can be appropriately modeled by a LJ fluid. The electrolyte solution is represented by a mixture of three species of charged spheres with the respective point charges q_α ($\alpha = 0, 1, 2$) embedded at their center. The first species is the water solvent molecule whose charge is $q_0 = 0$, while the two other species are the solute ions (cation and anion) with their respective charges $\pm q$. The pair potential

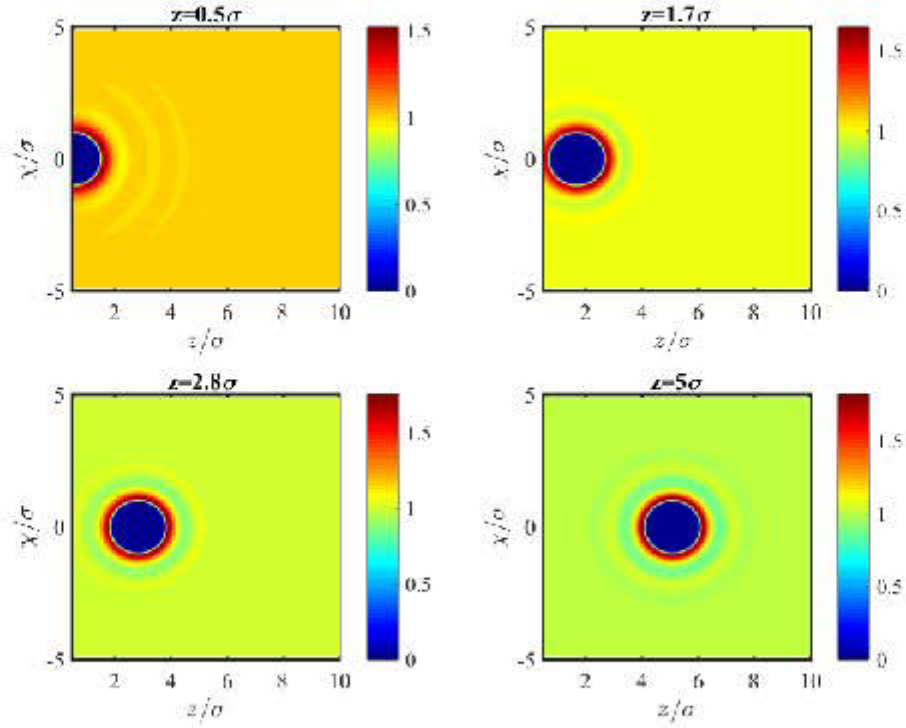


Figure 3.13: Radial distribution functions of an inhomogeneous LJ fluid near a hard wall at $\rho_b \sigma^3 = 0.5$ and $T^* = 1.35$. The corresponding density profile is presented in Fig.3.7.

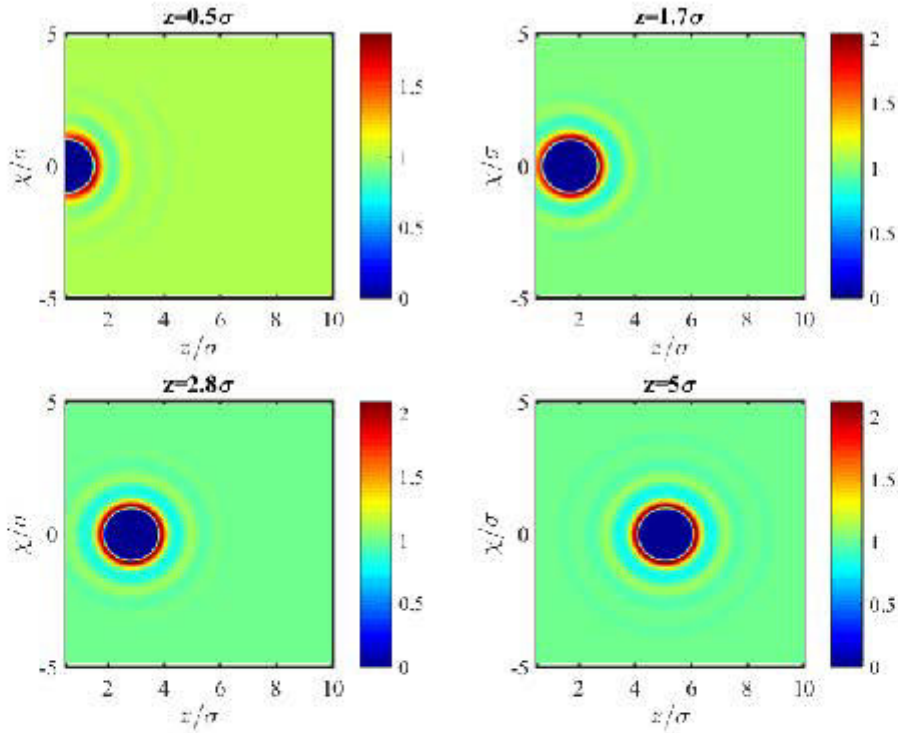


Figure 3.14: As Fig.3.13 for $\rho_b \sigma^3 = 0.65$. The corresponding density profile is presented in Fig.3.8.

between particle α at \mathbf{r}_1 and particle β at \mathbf{r}_2 is then given by

$$u_{\alpha,\beta}(r_{12}) = u_{\alpha,\beta}^{LJ}(r_{12}) + \frac{q_\alpha q_\beta}{\epsilon_0 \epsilon_r r_{12}}, \quad (3.26)$$

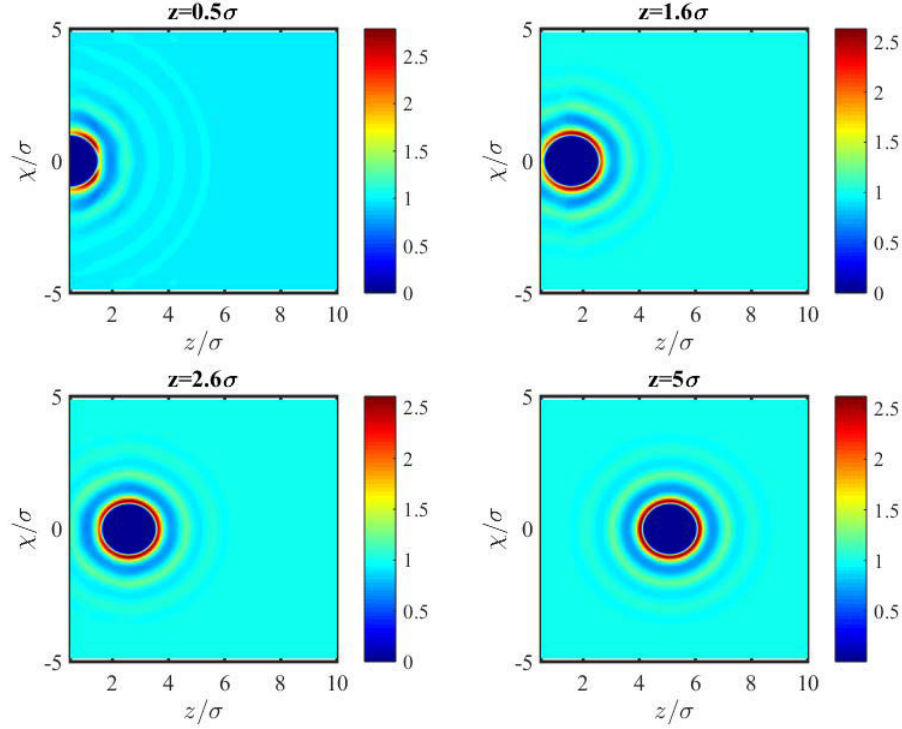


Figure 3.15: As Fig.3.13 for $\rho_b\sigma^3 = 0.82$. The corresponding density profile is presented in Fig.3.9.

where $r_{12} = |\mathbf{r}_1 - \mathbf{r}_2|$. The LJ potential $u_{\alpha,\beta}^{LJ}(r_{12})$ given by Eq.(3.1) is split into a short-range repulsive part $u_{\alpha,\beta}^0(r_{12})$ and a long-range attractive part $u_{\alpha,\beta}^a(r_{12})$, according to the WCA approximation [74]

$$u_{\alpha,\beta}^0(r_{12}) = \begin{cases} u_{\alpha,\beta}^{LJ}(r_{12}) + \epsilon_{\alpha,\beta}, & r_{12} < 2^{1/6}\sigma_{\alpha,\beta} \\ 0, & r_{12} \geq 2^{1/6}\sigma_{\alpha,\beta} \end{cases} \quad (3.27)$$

and

$$u_{\alpha,\beta}^a(r_{12}) = \begin{cases} -\epsilon_{\alpha,\beta}, & r_{12} < 2^{1/6}\sigma_{\alpha,\beta} \\ u_{\alpha,\beta}^{LJ}(r_{12}), & r_{12} \geq 2^{1/6}\sigma_{\alpha,\beta}. \end{cases} \quad (3.28)$$

For the sake of simplicity, the diameters of the species are identical and chosen equal to the equivalent hard sphere diameter d of the soft repulsive part $u_{\alpha,\beta}^0(r)$, calculated by Eq.(3.7), with $\alpha_3 = 1.032$ [60].

The equilibrium density distribution ρ_α of each molecular species is determined by minimizing the grand potential $\Omega[\rho_\alpha]$ of the system with respect to the corresponding density

$$\frac{\delta\Omega[\rho_\alpha]}{\delta\rho_\beta} = 0, \quad \beta \in \{0, +, -\}, \quad (3.29)$$

with

$$\Omega[\rho_\alpha] = \mathcal{F}[\rho_\alpha] + \sum_\alpha \int d\mathbf{r} \rho_\alpha(\mathbf{r}) [V_\alpha(\mathbf{r}) - \mu_\alpha]. \quad (3.30)$$

The intrinsic free energy $\mathcal{F}[\rho_\alpha]$ is composed of contributions from ideal gas behavior, Lennard-Jones and electric interactions

$$\mathcal{F}[\rho_\alpha] = \mathcal{F}^{id}[\rho_\alpha] + \mathcal{F}^{LJ}[\rho_\alpha] + \mathcal{F}^{el}[\rho_\alpha], \quad (3.31)$$

where the ideal gas contribution is written as

$$\mathcal{F}^{id}[\rho_\alpha] = k_B T \sum_\alpha \int \rho_\alpha(\mathbf{r}) \left\{ \ln \left[\Lambda_\alpha^3 \rho_\alpha(\mathbf{r}) - 1 \right] \right\} d\mathbf{r}. \quad (3.32)$$

Similarly to the WCA separation of the interparticle LJ potential (Eqs.(3.27) and (3.28)), the LJ term $\mathcal{F}^{LJ}[\rho_\alpha]$ can be split into a repulsive $\mathcal{F}_0^{LJ}[\rho_\alpha]$ and an attractive contribution $\mathcal{F}_a^{LJ}[\rho_\alpha]$. The repulsive term is approximated by that of a hard sphere fluid of equivalent diameter d which is successfully treated by the FMT, while the remaining term can be exactly computed as

$$\mathcal{F}_a^{LJ}[\rho_\alpha] = \frac{1}{2} \sum_\alpha \sum_\beta \int \int \rho_\alpha(\mathbf{r}_1) \rho_\beta(\mathbf{r}_2) g_{\alpha,\beta}^{LJ}(\mathbf{r}_1, \mathbf{r}_2; \lambda = 0.5) u_{\alpha,\beta}^a(\mathbf{r}_1, \mathbf{r}_2) d\mathbf{r}_1 d\mathbf{r}_2. \quad (3.33)$$

Since the ionic densities are evidently negligible in comparison with the water solvent density, the term accounting for electric interactions $\mathcal{F}_{el}[\{\rho_\alpha\}]$ can be considered in the MFA, in which correlations between ion components are completely neglected

$$\mathcal{F}_{el}[\{\rho_\alpha\}] = \frac{1}{2} \sum_\alpha \sum_\beta \int \int \rho_\alpha(\mathbf{r}_1) \rho_\beta(\mathbf{r}_2) \frac{q_\alpha q_\beta}{4\pi\epsilon\epsilon_0 r_{12}} d\mathbf{r}_1 d\mathbf{r}_2. \quad (3.34)$$

The equation to solve for obtaining the density distribution of species α Eq.(3.8) is hence rewritten as

$$\begin{aligned} \rho_\alpha(\mathbf{r}_1) = & \rho_\alpha^b \exp \left\{ \beta \left[\mu_b^{ex}[\{\rho_\alpha\}] - \frac{\delta \mathcal{F}^{HS}[\{\rho_\alpha\}]}{\delta \rho_\alpha(\mathbf{r}_1)} \right. \right. \\ & \left. \left. - \sum_\beta \left(\int \rho_\beta(\mathbf{r}_2) g_{\alpha,\beta}^{LJ}(\mathbf{r}_1, \mathbf{r}_2; \lambda = 0.5) u_{\alpha,\beta}^a(\mathbf{r}_1, \mathbf{r}_2) d\mathbf{r}_2 - \int \rho_\beta(\mathbf{r}_2) \frac{q_\alpha q_\beta}{4\pi\epsilon\epsilon_0 r_{12}} d\mathbf{r}_2 \right) - V_\alpha(\mathbf{r}_1) \right] \right\}. \end{aligned} \quad (3.35)$$

Applying the above relation to an EDL geometry (Fig.3.4) with $-H < z < H$, the densities ρ_α depend only on the spatial coordinate z perpendicular to the layer surfaces placed at $z = \pm H$, respectively. It follows

$$\begin{aligned} \rho_\alpha(z_1) = & \rho_\alpha^b \exp \left[\beta \left(\mu_b^{ex}[\{\rho_\alpha\}] - \mu_{HS}^{ex}[\{\rho_\alpha\}] - \mu_{LJ}^{ex}[\{\rho_\alpha\}] \right. \right. \\ & \left. \left. - \sum_\beta \int_{-H}^H \rho_\beta(z_2) dz_2 \int_0^\infty 2\pi\chi d\chi \frac{q_\alpha q_\beta}{4\pi\epsilon\epsilon_0 r_{12}} - V_\alpha(z_1) \right) \right], \end{aligned} \quad (3.36)$$

where

$$\begin{aligned} \mu_b^{ex}[\{\rho_\alpha\}] &= \mu_b^{HS}[\{\rho_\alpha\}] + \sum_\beta \rho_\beta^b \int g_{\alpha,\beta}^{LJ}(\mathbf{r}; \lambda = 0.5) u_{\alpha,\beta}^a(\mathbf{r}) d\mathbf{r}, \\ \mu_{LJ}^{ex}[\{\rho_\alpha\}] &= \sum_\beta \int \rho_\beta(\mathbf{r}_2) g_{\alpha,\beta}^{LJ}(\mathbf{r}_1, \mathbf{r}_2; \lambda = 0.5) u_{\alpha,\beta}^a(\mathbf{r}_1, \mathbf{r}_2) d\mathbf{r}_2, \\ r_{12} &= \sqrt{\chi^2 + (z_1 - z_2)^2}. \end{aligned}$$

The external potential $V_\alpha(z_1)$ is imposed by the two charged LJ walls:

$$V_\alpha(z_1) = V_\alpha^{LJ}(z_1) + V_\alpha^{el}(z_1), \quad (3.37)$$

where $V_\alpha^{LJ}(z_1)$ accounts for the LJ interactions between oxygen atoms of the rigid clay particles and the species α of the electrolyte solution as reported by the SPCE (Extended Single Point Charge) model of the bulk water [40]. According to Delville [38, 39], $V_\alpha^{LJ}(z_1)$ is expressed as

$$V_\alpha^{LJ}(z_1) = \pi \rho_O^s \epsilon_{O-\alpha} \left\{ \frac{\sigma_{O-\alpha}^{12}}{45} \left[\frac{1}{\left(z_1 - \frac{L}{2}\right)^9} - \frac{1}{\left(z_1 + \frac{L}{2}\right)^9} \right] - \frac{\sigma_{O-\alpha}^6}{3} \left[\frac{1}{\left(z_1 - \frac{L}{2}\right)^3} - \frac{1}{\left(z_1 + \frac{L}{2}\right)^3} \right] \right\} \quad (3.38)$$

where $\sigma_{O-\alpha}$, $\epsilon_{O-\alpha}$ represent interaction length and strength, ρ_O^s the oxygen density within the walls and L the wall thickness. Similarly to the form of the interparticle LJ potential, such fluid-solid potential comprises a short-range repulsive and a long-range attractive parts as shown in Fig.3.16. Since the two walls are identically charged, the electric fields introduced

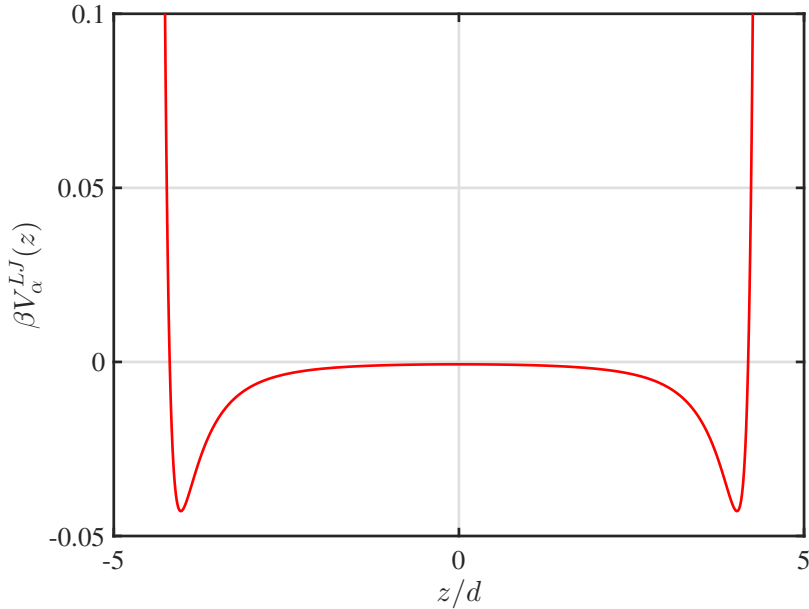


Figure 3.16: Fluid-solid LJ potential $V_\alpha^{LJ}(z) + V_\alpha^{LJ}(2H - z)$ between two clay surfaces placed at $\pm H$ and species α of an electrolyte solution for $L = 7 \times 10^{-10}$ m, $\rho_O^s d^3 = 0.052$, $\beta \epsilon_{O-\alpha} = 0.2669$ and $2H = 10d$.

by the charged surfaces have the same strength, but opposite directions. As a result, the total external electric field between the two walls is zero and the electrical potential is given by

$$V_\alpha^{el}(z_1) = q_\alpha \Upsilon, \quad (3.39)$$

where Υ is a constant. Another quantity is of more interest, namely the mean electrostatic potential $\psi(z_1)$ accounting for both, the charged walls and the ionic charges in the electrolyte solution which is defined by

$$\psi(z_1) = \sum_\beta \int_{-H}^H \rho_\beta(z_2) dz_2 \int_0^\infty 2\pi \chi dx \frac{q_\beta}{4\pi \epsilon \epsilon_0 r_{12}} + \Upsilon. \quad (3.40)$$

The one-dimensional Poisson equation reads as

$$\epsilon \epsilon_0 \frac{d^2 \psi}{dz^2} = - \sum_\alpha \rho_\alpha q_\alpha \equiv Q(z). \quad (3.41)$$

The solution of this problem is easily obtained by the superposition of the charge profiles at different inter-platelet distances. The electrostatic potential due to a surface charge density $Q(z_2)dz_2$ is given by

$$d\psi(z_1) = -\frac{Q(z_2)dz_2}{2\epsilon\epsilon_0}|z_1 - z_2| + \text{const}, \quad (3.42)$$

which results after integration in

$$\psi(z_1) = -\int_{-H}^H \frac{Q(z_2)}{2\epsilon\epsilon_0}|z_1 - z_2| dz_2 + C. \quad (3.43)$$

Note that the identical surface charge of the two walls has only an impact on the constant C . Because of the planar symmetry of the system ($z'_2 = -z_2$), it follows

$$\begin{aligned} \psi(z_1) &= -\int_{-H}^0 \frac{Q(z_2)}{2\epsilon\epsilon_0}|z_1 - z_2| dz_2 - \int_0^H \frac{Q(z_2)}{2\epsilon\epsilon_0}|z_1 - z_2| dz_2 + C \\ &= -\int_0^H \frac{Q(-z'_2)}{2\epsilon\epsilon_0}|z_1 + z'_2| dz'_2 - \int_0^H \frac{Q(z_2)}{2\epsilon\epsilon_0}|z_1 - z_2| dz_2 + C \\ &= -\int_0^H \frac{Q(z_2)}{2\epsilon\epsilon_0} (|z_1 - z_2| + |z_1 + z_2|) dz_2 + C. \end{aligned} \quad (3.44)$$

To eliminate the unknown constant C , the potential ζ is imposed on the two solid interfaces such that

$$\begin{aligned} \psi(z_1) - \zeta &= -\int_0^H \frac{Q(z_2)}{2\epsilon\epsilon_0} (|z_1 - z_2| - |H - z_2| + |z_1 + z_2| - |H + z_2|) dz_2 \\ &= -\int_0^H \frac{Q(z_2)}{2\epsilon\epsilon_0} (|z_1 - z_2| + |z_1 + z_2| - 2H) dz_2. \end{aligned} \quad (3.45)$$

The density profiles of solvent, anions and cations are then calculated with

$$\rho_0(z_1) = \rho_0^b \exp \left\{ \beta \left[\mu_b^{ex}[\{\rho_0^b\}] - \mu_{HS}^{ex}[\rho] - \mu_{LJ}^{ex}[\{\rho_0\}] - V_0^{LJ}(z_1) \right] \right\}, \quad (3.46)$$

$$\rho_+(z_1) = \rho_+^b \exp \left\{ \beta \left[\mu_b^{ex}[\{\rho_+^b\}] - \mu_{HS}^{ex}[\rho] - \mu_{LJ}^{ex}[\{\rho_+\}] - V_+^{LJ}(z_1) \right] - \beta e\psi(z_1) \right\}, \quad (3.47)$$

$$\rho_-(z_1) = \rho_-^b \exp \left\{ \beta \left[\mu_b^{ex}[\{\rho_-^b\}] - \mu_{HS}^{ex}[\rho] - \mu_{LJ}^{ex}[\{\rho_-\}] - V_-^{LJ}(z_1) \right] + \beta e\psi(z_1) \right\}, \quad (3.48)$$

where $\rho = \sum_{\beta} \rho_{\beta}$. Taking advantage of the symmetry of the Q profile and the condition of overall electroneutrality written as

$$2\Sigma + \int_{-H}^H Q(z_2)dz_2 = 0, \quad (3.49)$$

where Σ is the electric surface charge density of each of the two plates, this results in

$$\begin{aligned} \psi(z_1) &= \zeta - \int_{-H}^H \frac{Q(z_2)}{2\epsilon\epsilon_0} [|z_1 - z_2| - (H - z_2)] dz_2 \\ &= -\int_{-H}^H \frac{Q(z_2)}{2\epsilon\epsilon_0}|z_1 - z_2| dz_2 + \zeta - \frac{\Sigma H}{\epsilon\epsilon_0}. \end{aligned} \quad (3.50)$$

The density profiles can hence be rewritten as

$$\begin{aligned} \rho_0(z_1) &= \rho_0^b \exp \left\{ \beta \left[\mu_b^{ex}[\{\rho_0^b\}] - \mu_{HS}^{ex}[\rho] - \mu_{LJ}^{ex}[\{\rho_0\}] - V_0^{LJ}(z_1) \right] \right\}, \quad (3.51) \\ \rho_+(z_1) &= \rho_+^b K \exp \left\{ \beta \left[\mu_b^{ex}[\{\rho_+^b\}] - \mu_{HS}^{ex}[\rho] - \mu_{LJ}^{ex}[\{\rho_+\}] - V_+^{LJ}(z_1) \right] + \frac{\beta e}{2\epsilon\epsilon_0} \int_{-H}^H Q(z_2)|z_1 - z_2| dz_2 \right\} \end{aligned}$$

$$\equiv \rho_+^b K \exp\{+\}, \quad (3.52)$$

$$\rho_-(z_1) = \rho_-^b \exp \left\{ \beta \left[\mu_b^{ex}[\{\rho_-^b\}] - \mu_{HS}^{ex}[\rho] - \mu_{LJ}^{ex}[\{\rho_-\}] - V_{-}^{LJ}(z_1) \right] - \frac{\beta e}{2\epsilon\epsilon_0} \int_{-H}^H Q(z_2) |z_1 - z_2| dz_2 \right\}$$

$$\equiv \rho_-^b \frac{1}{K} \exp\{-\}, \quad (3.53)$$

where $K = \exp \left[-\beta e \left(\zeta - \frac{\Sigma H}{\epsilon\epsilon_0} \right) \right]$ is a positive constant which is obtained by solving the following second degree equation

$$2\Sigma + e \int_{-H}^H [\rho_+(z_1) - \rho_-(z_1)] dz_1 = 0, \quad (3.54)$$

and more explicitly

$$K^2 + \frac{2\Sigma}{e\rho^b} \frac{K}{\int_{-H}^H \exp\{+\} dz_1} - \frac{\int_{-H}^H \exp\{-\} dz_1}{\int_{-H}^H \exp\{+\} dz_1} = 0, \quad (3.55)$$

where $\rho_+^b = \rho_-^b \equiv \rho^b$.

3.5.1 Density profile of the pure solvent

In what follows, the water solvent is considered in the absence of ions, confined between two parallel clay lamellae. The water solvent is modeled by a LJ fluid with: $d = 2.8 \times 10^{-10}$ m the water molecule diameter, $\rho_b d^3 = 0.7344$ the bulk water density, $T = 300$ K the temperature and σ is calculated with Eq.(3.7). The parameter ϵ plays the most important role in modeling water as a LJ fluid. It should be high enough to result in a reasonable bulk pressure p_b of about 10^5 Pa calculated with Eq.(3.11). With the bulk density $\rho_b d^3 = 0.7344$, $\epsilon/k_B T$ is found equal to 1.077 which satisfies the bulk pressure criterion. In addition, from the phase diagram of LJ fluids [88], it can be seen that these values correspond to the liquid phase.

The external LJ potential stems from the interactions between oxygen atoms of the clay particles and those of the water solvent so that the water-wall interaction parameters are selected conforming to the SPCE model [40, 36], namely $\sigma_{O-O} = 3.5532 \times 10^{-10}$ m, $\epsilon_{O-O}/k_B T = 0.2669$, $L = 7 \times 10^{-10}$ m. The resulting density distribution is presented in Fig.3.17. In

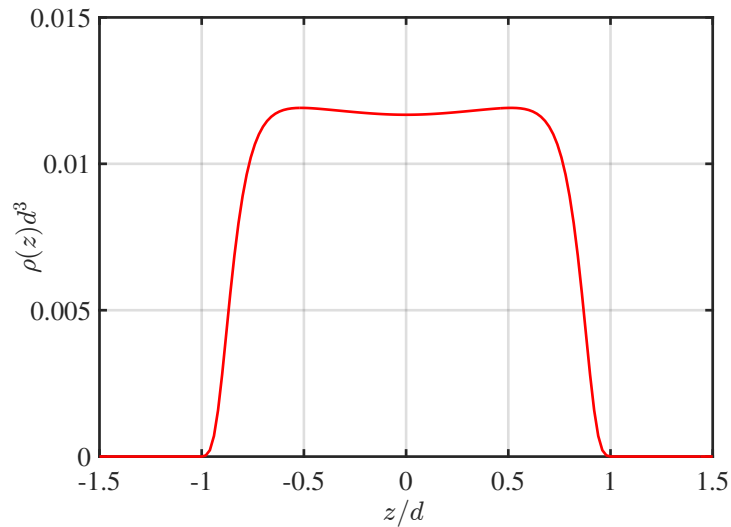


Figure 3.17: Density profile of water considered as a LJ fluid confined between two clay lamellae represented by rigid LJ walls separated by a distance of $2H = 3d$ at: $\rho_b d^3 = 0.7344$, $\beta\epsilon = 1.077$.

comparison with the bulk value $\rho_b d^3 = 0.7344$, the water density between the two clay surfaces are negligible. In other words, no liquid is present between the two solid particles. This can be explained by the strong attraction between fluid particles compared to the wall-fluid attractive interactions ($\epsilon_{O-O}/k_B T = 0.2669$), which are not strong enough to retain the water molecules between the two walls. Increasing the wall-fluid interaction strength is therefore the unique solution to attract water. Fig.3.18 shows the expected profile of the confined water solvent after multiplying ϵ_{O-O} by a factor 50 and increasing the distance between the two clay lamellae to $2H = 15d$. However, this violent increase of the water-wall interaction strength has no physical meaning. Hence, the present LJ model fails in modeling the water solvent confined in an EDL.

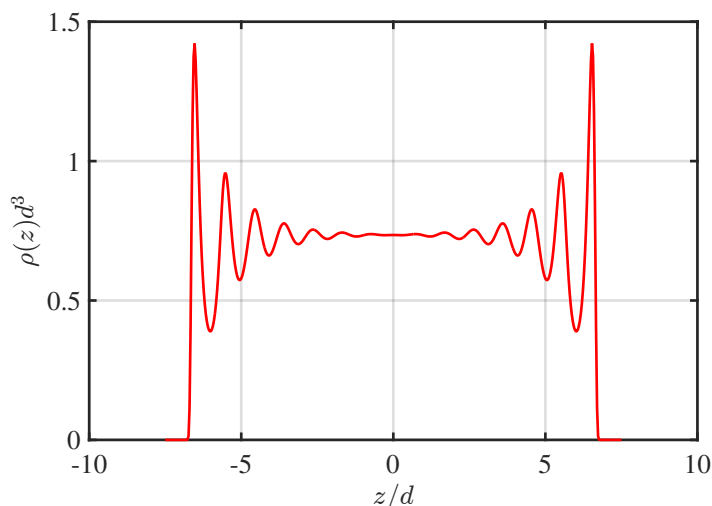


Figure 3.18: Density profile of water LJ fluid confined between two extremely attractive clay lamellae at: $\rho_b d^3 = 0.7344$, $\beta\epsilon = 1.077$, $2H = 15d$.

3.5.2 Density profiles of the constituents of the electrolyte solution

This section depicts the results of the density profiles when adding ions to the pure water solvent to complete the EDL description. In the case of a pure water solvent, no liquid was observed between the two clay lamellae, which probably stems from the extremely attractive forces between the water molecules. Consequently, two cases are considered in modeling the solvent:

1. the solvent is a LJ fluid with low LJ interaction strength $\beta\epsilon = 0.7407$ (or $T^* = 1.35$);
2. the water solvent is modeled by a LJ fluid with $\beta\epsilon = 1.077$.

These two cases allow to study the effects of the LJ interaction strength between the fluid particles on the ion density profiles.

3.5.2.1 Lennard-Jones fluid solvent with low interaction strength

To simplify the numerical calculations, the LJ interactions between the different constituents of the EDL (water-water, ion-water, ion-ion) are identical and characterized by the interaction strength $\beta\epsilon = 0.7407$ ($T^* = 1.35$). The density profiles of the different EDL components are obtained by solving the three density equations Eq.(3.51)-(3.53) and the second order equation Eq.(3.55) iteratively. In this study, a 1:1 electrolyte at the bulk ion concentration $c_b = 0.1M$ is studied. The two clay surfaces separated by a distance of $2H = 4d$ generate the external LJ potential given in Eq.(3.38) as well as an electrostatic potential due to their surface charge

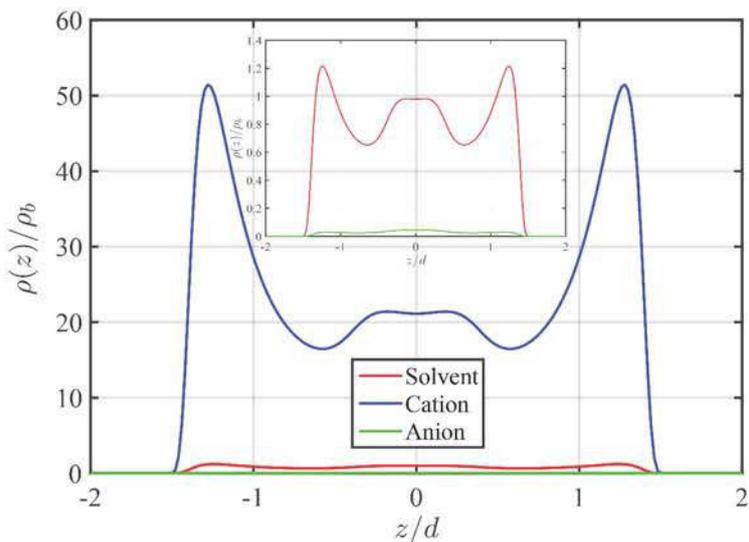


Figure 3.19: Density profiles of the different components for an electrolyte solution 1:1; $c_b = 0.1M$, $\rho_0 d^3 = 0.7344$, $\beta\epsilon = 0.7407$ confined between two clay lamellae separated by a distance $2H = 4d$.

density $\Sigma = -0.1 \text{ C/m}^2$. The numerical results are presented in Fig.3.19. The LJ interaction effects are characterized by the layered density distribution of the ionic components, especially for the cations. Such effects are similar to those of hard sphere solvent EDL models as they can be found in literature [89, 90].

3.5.2.2 Realistic water solvent

The LJ parameters for ion-water and ion-ion interactions are now set to $\beta\epsilon = 0.6667$ (or $T^* = 1.5$), $\sigma/d = 1.0152$ respectively, while those of water-water interactions are identical to the case of the pure water solvent (i.e. $\beta\epsilon = 1.077$). As shown in Fig.3.20, similarly to the case of the pure water solvent (Fig.3.17), the water density is negligible in the EDL space while the ion concentration profiles are monotonous, which is similar to the behavior obtained with classical EDL models considering a continuous solvent [20]. This means that the water density $\rho_0(z)$ has no impact in predicting the ion density profiles $\rho_{\pm}(z)$ in an EDL. The present EDL model hence confirms the accuracy of the continuous solvent approach within EDL models commonly considered in literature due to their simplicity.

3.6 Conclusion

This chapter considers the molecular and polar nature of the water solvent by studying an inhomogeneous Lennard-Jones fluid. To do this, an exact Density-Functional Perturbation Theory is used to predict the density profiles as well as the RDF of inhomogeneous LJ fluids. The LJ potential is separated into repulsive and attractive parts according to the WCA approximation [74], which results in the decomposition of the excess free energy in a short-range repulsive and a long-range attractive part. The first one is commonly considered as that of a temperature-dependent effective hard sphere fluid, while the last one is computed by the exact relation accounting for interparticle correlations of the inhomogeneous LJ fluid. The results obtained with the present perturbation theory are in excellent agreement with those from MC simulations for various densities and configurations (e.g. inhomogeneous LJ fluids near a hard wall, confined between two hard walls and in slit-like pores). The key issue of the present the-

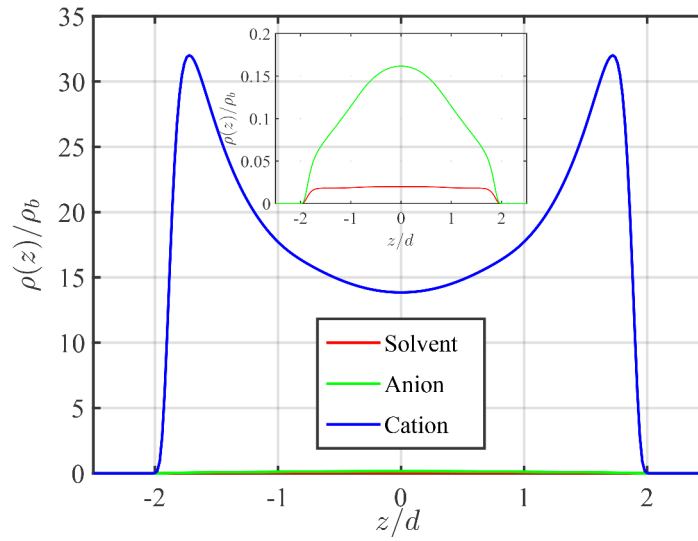


Figure 3.20: Density profiles of different components for a 1:1 electrolyte solution: $\rho_0 d^3 = 0.7344$, $\beta\epsilon_{\text{water-water}} = 1.077$, $2H = 5d$, $\beta\epsilon_{\text{water-ion};\text{ion-ion}} = 0.6667$.

ory is to exactly compute the anisotropic RDFs of the inhomogeneous LJ fluids. This makes our approach more stable and more accurate than other DFT models proposed in literature [72, 87, 84, 85], in which the RDF is approximated by that of the corresponding bulk LJ fluids. An application of the present approach of inhomogeneous LJ fluids to compute the density profiles inside EDL as they can be found in clayey soils confirms the layered ion concentration profiles in the case of a LJ fluid solvent characterized by a low LJ interaction strength $\beta\epsilon = 0.7407$, which is similar to those obtained for hard sphere solvent EDL models. A more realistic approach for the water solvent consists in imposing a high attractive strength $\beta\epsilon = 1.077$ of the interparticle LJ potential to obtain a reasonable bulk pressure (10^5 Pa). However, in this case there are almost no water molecules in the EDL because they are not strongly enough retained by the platelet walls. This results in monotonous ion density profiles similar to the continuous solvent approach commonly considered in classical EDL models.

Appendix B

B.1 Fourier 1D transform

The 1D Fourier transform, $F(k)$, of a function $f(x)$ ($f(x < 0) = 0$) is given by

$$F(k) = \int_0^{+\infty} f(x) \exp(-i k x) dx. \quad (\text{B.1})$$

If performing this transform (and its inverse) by *Matlab* tool, the functions `fft` that associates $X(m)$ to $x(n)$ and `ifft` that associates $x(n)$ to $X(m)$ are defined as

$$X(m) = \sum_{n=1}^N x(n) \exp \left[-2 \pi i (m-1) \frac{(n-1)}{N} \right] \quad \text{if } 1 \leq m \leq N, \quad (\text{B.2})$$

$$x(n) = \frac{1}{N} \sum_{m=1}^N X(m) \exp \left[2 \pi i (m-1) \frac{(n-1)}{N} \right] \quad \text{if } 1 \leq n \leq N. \quad (\text{B.3})$$

We have

$$\begin{aligned} x_n &= (n-1)\Delta x = \frac{n-1}{N} x_{max}, \\ k_m &= (m-1)\Delta k = \frac{m-1}{N} k_{max}, \end{aligned} \quad (\text{B.4})$$

$$\text{with} \quad \begin{cases} \Delta x = \frac{x_{max}}{N} \\ \Delta k = \frac{k_{max}}{N} \\ k_{max} = \frac{2 \pi N}{r_{max}} \end{cases}. \quad (\text{B.5})$$

Imposing $m' = m - 1 - N/2$ ($-N/2 \leq m' \leq N/2 - 1$), it follows

$$\begin{aligned} X'(m') &= X(1 + m' + \frac{N}{2}) = \sum_{n=1}^N x(n) \exp \left[-2 i \pi (m' + \frac{N}{2}) \frac{(n-1)}{N} \right] \\ &= \sum_{n=1}^N x(n) \exp \left[-2 i \pi \frac{m'(n-1)}{N} \right] \exp[-i \pi (n-1)] \\ &= \sum_{n=1}^N (-1)^{n-1} x(n) \left\{ \cos \left[2 \pi \frac{m'(n-1)}{N} \right] - i \sin \left[2 \pi \frac{m'(n-1)}{N} \right] \right\}. \end{aligned} \quad (\text{B.6})$$

Obviously, we find that

$$\begin{aligned} \mathcal{R}e[X'(-m')] &= +\mathcal{R}e[X'(m')] \\ \mathcal{I}m[X'(-m')] &= -\mathcal{I}m[X'(m')] \end{aligned} \quad (\text{B.7})$$

The 1D Fourier transformation is therefore symmetrical with respect to midpoint. When the frequency (k) increases, the calculation of the integral (B.1) becomes increasingly difficult, the

number of values of f used by period which will decrease.

If one wants to obtain the Fourier transform of the function $f(x)$, it is necessary that for $m = N/2$ the Fourier transform $F(k)$ tends to 0 and extends the transform beyond $m = N/2$ by 0. The same comment applies to the inverse transform. In 3D case of the following section, the symmetry no longer exists because of the factor $1/k$ in the denominator but the previous comment also remains valid.

B.2 3D transform

If $V(\mathbf{r})$ is a function of the vector $\mathbf{r} = (x, y, z)$ and $\widehat{V}(\mathbf{k})$ its Fourier transform, we have hence

$$\widehat{V}(\mathbf{k}) = \frac{1}{(2\pi)^{3/2}} \iiint_{-\infty}^{\infty} V(\mathbf{r}) \exp(-i \mathbf{k} \cdot \mathbf{r}) d\mathbf{r}, \quad (\text{B.8})$$

$$V(\mathbf{r}) = \frac{1}{(2\pi)^{3/2}} \iiint_{-\infty}^{\infty} \widehat{V}(\mathbf{k}) \exp(i \mathbf{k} \cdot \mathbf{r}) d\mathbf{k}. \quad (\text{B.9})$$

$$(\text{B.10})$$

A triple integral of the following form

$$\widehat{V}(|\mathbf{k}|) = \frac{1}{(2\pi)^{3/2}} \iiint_{-\infty}^{\infty} V(|\mathbf{r}|) \exp(-i \mathbf{k} \cdot \mathbf{r}) d\mathbf{r}, \quad (\text{B.11})$$

can be converted to a simple integral by using spherical coordinates

$$\begin{cases} x = r \sin \theta \cos \phi & 0 \leq r < \infty \\ y = r \sin \theta \sin \phi & 0 \leq \theta < \pi \\ z = r \cos \theta & 0 \leq \phi < 2\pi \end{cases} \quad (\text{B.12})$$

$$d\mathbf{r} = dx dy dz \rightarrow r^2 \sin \theta dr d\theta d\phi$$

$$\mathbf{k} \cdot \mathbf{r} \rightarrow k r \cos \theta \quad \text{with} \quad \mathbf{k} = (0 \ 0 \ k)^T$$

and then

$$\begin{aligned} \widehat{V}(|\mathbf{k}|) &= \frac{1}{(2\pi)^{3/2}} \int_0^{\infty} \int_0^{\pi} \int_0^{2\pi} V(r) \exp(-i k r \cos \theta) r^2 \sin \theta dr d\theta d\phi \\ &= \left(\frac{2}{\pi}\right)^{1/2} \int_0^{\infty} V(r) \frac{r \sin(k r)}{k} dr \end{aligned} \quad (\text{B.13})$$

By the similar way

$$\begin{aligned} V(\mathbf{r}) &= \frac{1}{(2\pi)^{3/2}} \int \int \int \widehat{V}(\mathbf{k}) \exp(i \mathbf{k} \cdot \mathbf{r}) d\mathbf{k} \\ &= \frac{1}{(2\pi)^{3/2}} \int_0^{\infty} \int_0^{\pi} \int_0^{2\pi} \widehat{V}(k) \exp(i k r \cos \theta) k^2 \sin \theta dk d\theta d\phi \\ &= \frac{1}{(2\pi)^{1/2}} \int_0^{\infty} \int_0^{\pi} \widehat{V}(k) \exp(i k r \cos \theta) k^2 \sin \theta dk d\theta \\ &= \frac{1}{(2\pi)^{1/2}} \int_0^{\infty} \widehat{V}(k) \left[-\frac{\exp(i k r \cos \theta)}{i k r} \right]_{\theta=0}^{\theta=\pi} k^2 dk \\ &= \left(\frac{2}{\pi}\right)^{1/2} \int_0^{\infty} \widehat{V}(k) \frac{k \sin(k r)}{r} dk \end{aligned} \quad (\text{B.14})$$

If we perform this transform by using Matlab, knowing that

$$\begin{aligned} r_n &= (n-1)\Delta r = \frac{n-1}{N} r_{max} \\ k_m &= (m-1)\Delta k = \frac{m-1}{N} k_{max} \end{aligned} \quad (\text{B.15})$$

$$\text{with} \quad \begin{cases} \Delta r = \frac{r_{max}}{N} \\ \Delta k = \frac{k_{max}}{2\pi N} \\ k_{max} = \frac{2\pi N}{r_{max}} \end{cases} \quad (\text{B.16})$$

It follows

$$\widehat{V}(k_m) = \sqrt{\frac{2}{\pi}} \frac{\Delta r}{k_m} \text{imag}[-\text{fft}(\mathbf{V}.*\mathbf{r})], \quad (\text{B.17})$$

$$V(r_n) = \sqrt{\frac{2}{\pi}} \frac{k_{max}}{r_n} \text{imag}[\text{ifft}(\widehat{\mathbf{V}}.*\mathbf{k})]. \quad (\text{B.18})$$

Difficulty is the Fourier transform of a convolution

$$\widehat{\mathbf{U}*\mathbf{V}} = (2\pi)^{3/2} \widehat{\mathbf{U}} \widehat{\mathbf{V}} \quad (\text{B.19})$$

$$= 4\pi \frac{\Delta r^2}{k_m^2} \text{imag}[-\text{fft}(\mathbf{U}.*\mathbf{r})] \cdot \text{imag}[-\text{fft}(\mathbf{V}.*\mathbf{r})]. \quad (\text{B.20})$$

To overcome this difficulty, it may be efficient to redefine the Fourier transform. It is therefore possible to choose use one of the two columns of the below table

$\widehat{V}(\mathbf{k}) = \frac{1}{(2\pi)^{3/2}} \iiint_{-\infty}^{\infty} V(\mathbf{r}) \exp(-i\mathbf{k}\cdot\mathbf{r}) d\mathbf{r}$	$\widehat{V}(\mathbf{k}) = \iiint_{-\infty}^{\infty} V(\mathbf{r}) \exp(-i\mathbf{k}\cdot\mathbf{r}) d\mathbf{r}$
$V(\mathbf{r}) = \frac{1}{(2\pi)^{3/2}} \iiint_{-\infty}^{\infty} \widehat{V}(\mathbf{k}) \exp(i\mathbf{k}\cdot\mathbf{r}) d\mathbf{k}$	$V(\mathbf{r}) = \frac{1}{(2\pi)^3} \iiint_{-\infty}^{\infty} \widehat{V}(\mathbf{k}) \exp(i\mathbf{k}\cdot\mathbf{r}) d\mathbf{k}$
$\widehat{V}(k) = \sqrt{\frac{2}{\pi}} \int_0^{\infty} V(r) \frac{r \sin(kr)}{k} dr$	$\widehat{V}(k) = 4\pi \int_0^{\infty} V(r) \frac{r \sin(kr)}{k} dr$
$V(r) = \sqrt{\frac{2}{\pi}} \int_0^{\infty} \widehat{V}(k) \frac{k \sin(kr)}{r} dk$	$V(r) = \frac{1}{2\pi^2} \int_0^{\infty} \widehat{V}(k) \frac{k \sin(kr)}{r} dk$
$\widehat{V}(k_m) = \sqrt{\frac{2}{\pi}} \frac{\Delta r}{k_m} \text{imag}[-\text{fft}(\mathbf{V}.*\mathbf{r})]$	$\widehat{V}(k_m) = 4\pi \frac{\Delta r}{k_m} \text{imag}[-\text{fft}(\mathbf{V}.*\mathbf{r})]$
$V(r_n) = \sqrt{\frac{2}{\pi}} \frac{k_{max}}{r_n} \text{imag}[\text{ifft}(\widehat{\mathbf{V}}.*\mathbf{k})]$	$V(r_n) = \frac{1}{2\pi^2} \frac{k_{max}}{r_n} \text{imag}[\text{ifft}(\widehat{\mathbf{V}}.*\mathbf{k})]$
$\widehat{\mathbf{U}*\mathbf{V}} = (2\pi)^{3/2} \widehat{\mathbf{U}} \widehat{\mathbf{V}}$	$\widehat{\mathbf{U}*\mathbf{V}} = \widehat{\mathbf{U}} \widehat{\mathbf{V}}$
$\mathcal{F} \left[\frac{\exp(-\kappa r)}{r} \right] = \sqrt{\frac{2}{\pi}} \frac{1}{\kappa^2 + k^2}$	$\mathcal{F} \left[\frac{\exp(-\kappa r)}{r} \right] = \frac{4\pi}{\kappa^2 + k^2}$

B.3 Hankel transform

The Hankel transform $\tilde{f}(k)$ of a function $f(r)$ is defined by

$$\tilde{f}(k) = 2\pi \int_0^{\infty} f(r) J_0(kr) r dr, \quad (\text{B.21})$$

and its inverse Hankel transform of $\tilde{f}(k)$ is defined as

$$f(r) = \frac{1}{2\pi} \int_0^{\infty} \tilde{f}(k) J_0(kr) k dk, \quad (\text{B.22})$$

where $J_0(kr)$ is the zero-order Bessel function of the first kind and k the spatial coordinate in the Hankel space. First of all, the Hankel transform is proven to be the 2-dimensional Fourier transform of a spherically symmetric function.

The 2-dimensional Fourier transform $F(\mathbf{k})$ of a function $f(\mathbf{r})$ is given by

$$F(\mathbf{k}) = \int \int f(\mathbf{r}) \exp(-i\mathbf{k} \cdot \mathbf{r}) d\mathbf{r}. \quad (\text{B.23})$$

Without any loss of generality, consider a polar coordinate system (z, θ) such that the \mathbf{k} vector lies on the $\theta = 0$ axis (in K-space). In these polar coordinates the Fourier transform is written as follows

$$F(\mathbf{k}) = \int_{r=0}^{r=\infty} \int_{\theta=0}^{\theta=2\pi} f(r, \theta) \exp(-i k r \cos \theta) r dr d\theta. \quad (\text{B.24})$$

If the function f depends only on r , and is independent of the angular variable θ . The Fourier transform becomes

$$F(k) = \tilde{f}(k) = 2\pi \int_0^{\infty} f(r) J_0(kr) r dr, \quad (\text{B.25})$$

where $J_0(z)$ is given by

$$J_0(z) = \frac{1}{2\pi} \int_0^{2\pi} \exp(-i z \cos \theta) d\theta. \quad (\text{B.26})$$

Based on the properties of the Fourier transform, the Hankel transform of a convolution integral can be written as

$$\mathcal{H} \left[\int f(\mathbf{r} - \mathbf{r}') g(\mathbf{r}') d\mathbf{r}' \right] = \tilde{f}(k) \tilde{g}(k). \quad (\text{B.27})$$

Finally, from the Parseval's theorem which states

$$\int_0^{\infty} |f(r)|^2 r dr = \int_0^{\infty} |\tilde{f}(k)|^2 k dk, \quad (\text{B.28})$$

and by using the orthogonality relation of Bessel functions

$$\int_0^{\infty} r J_{\alpha}(ur) J_{\alpha}(vr) dr = \frac{1}{u} \delta(u - v), \quad (\text{B.29})$$

the following expression is obtained

$$\int_0^{\infty} f(r) g(r) r dr = \frac{1}{4\pi^2} \int_0^{\infty} \tilde{f}(k) \tilde{g}(k) k dk. \quad (\text{B.30})$$

The table B.1 gives some examples of Hankel transform.

B.4 Numerical Hankel transform

The numerical Hankel transform and its inverse can be performed by using the method proposed by Lado [91]. The function $f(r)$ is assumed zero for $r \geq R$ and can be written in a series of $J_0(\frac{\mu_j r}{R})$ where μ_j is the j -th positive root of J_0

$$f(r) = \sum_{j=1}^{\infty} A_j J_0\left(\frac{\mu_j r}{R}\right). \quad (\text{B.31})$$

$f(r)$	$\tilde{f}(k)$
1	$\frac{2\pi\delta(k)}{k}$
$\frac{1}{r}$	$\frac{2\pi}{k}$
$\frac{r}{\sqrt{r^2+z^2}}$	$2\pi\frac{\exp(-k z)}{k}$
$\exp(-\alpha r)$	$\frac{2\pi\alpha}{(\alpha^2+k^2)^{3/2}}$
$\frac{\exp(-\alpha r)}{r}$	$\frac{2\pi}{\sqrt{\alpha^2+k^2}}$
$\exp(-\pi r^2)$	$\exp\left(-\frac{k^2}{4\pi}\right)$
$\frac{1}{(r^2+z^2)^{3/2}}$	$2\pi\frac{\exp(- z k)}{ z }$
$\frac{1}{r^2+z^2}$	$2\pi K_0(z k)$
$\frac{2z^2}{(r^2+z^2)^2}$	$2\pi z k K_1(z k)$
$\frac{d^2f}{dr^2} + \frac{1}{r}\frac{df}{dr}$	$-k^2\tilde{f}(k)$

Table B.1: Hankel transform.

To determine A_j , one uses the orthogonality nature of the Bessel functions [92]

$$\int_0^R J_0\left(\frac{\mu_j r}{R}\right) J_0\left(\frac{\mu_l r}{R}\right) r dr = \frac{R^2 J_1^2(\mu_j)}{2} \delta_{jl}. \quad (\text{B.32})$$

It follows

$$A_j = \frac{2}{R^2 J_1^2(\mu_j)} \int_0^R f(r) J_0\left(\frac{\mu_j r}{R}\right) r dr, \quad (\text{B.33})$$

and finally

$$\begin{aligned} f(r) &= \frac{2}{R^2} \sum_{j=1}^{\infty} \frac{1}{J_1^2(\mu_j)} \left(\int_0^R f(r') J_0\left(\frac{\mu_j r'}{R}\right) r' dr' \right) J_0\left(\frac{\mu_j r}{R}\right) \\ &= \frac{1}{\pi R^2} \sum_{j=1}^{\infty} \frac{1}{J_1^2(\mu_j)} \tilde{f}(k_j) J_0\left(\frac{\mu_j r}{R}\right) \end{aligned} \quad (\text{B.34})$$

wit $k_j = \mu_j/R$. If $r = r_i = \frac{\mu_i R}{\mu_N}$, it becomes

$$f(r_i) = f\left(\frac{\mu_i R}{\mu_N}\right) = \frac{2}{\mu_N} \sum_{j=1}^{\infty} \frac{J_0\left(\frac{\mu_i \mu_j}{\mu_N}\right)}{J_1^2(\mu_j)} \tilde{f}(k_j). \quad (\text{B.35})$$

By the similar way, we have

$$\tilde{f}(k) = \sum_{j=1}^{\infty} B_j J_0\left(\frac{\mu_j k R}{\mu_N}\right). \quad (\text{B.36})$$

As

$$\int_0^R J_0\left(\frac{\mu_j k R}{\mu_N}\right) J_0\left(\frac{\mu_l k R}{\mu_N}\right) k \, dk = \frac{\mu_N^2}{R^2} \frac{J_1^2(\mu_j)}{2} \delta_{jl}, \quad (\text{B.37})$$

the B_j coefficients are given by

$$B_j = \frac{2 R^2}{\mu_N^2 J_1^2(\mu_j)} \int_0^{\mu_N/R} \tilde{f}(k') J_0\left(\frac{\mu_j k' R}{\mu_N}\right) k' \, dk'. \quad (\text{B.38})$$

Consequently

$$\begin{aligned} \tilde{f}(k) &= \frac{2 R^2}{\mu_N^2} \sum_{j=1}^N \frac{J_0\left(\frac{\mu_j k R}{\mu_N}\right)}{J_1^2(\mu_j)} \left(\int_0^{\mu_N/R} \tilde{f}(k') J_0\left(\frac{\mu_j k' R}{\mu_N}\right) k' \, dk' \right) \\ &= \frac{4\pi R^2}{\mu_N^2} \sum_{j=1}^N \frac{J_0\left(\frac{\mu_j k R}{\mu_N}\right)}{J_1^2(\mu_j)} f\left(\frac{\mu_j R}{\mu_N}\right). \end{aligned} \quad (\text{B.39})$$

If $k = k_i = \frac{\mu_i}{R}$ and $r_j = \frac{\mu_j R}{\mu_N}$, one obtains

$$\tilde{f}(k_i) = \frac{4\pi R^2}{\mu_N^2} \sum_{j=1}^{N-1} \frac{J_0\left(\frac{\mu_j \mu_i}{\mu_N}\right)}{J_1^2(\mu_j)} f(r_j). \quad (\text{B.40})$$

Chapter 4

Dipolar Hard-Sphere fluid

4.1 Introduction

In Chapter 3, the molecular and polar nature of the water solvent is implicitly considered through the approach of a LJ fluid. Now the dipolar nature of water molecules will be explicitly considered by modeling a Dipolar Hard Sphere fluid (DHS). In order to study such a fluid

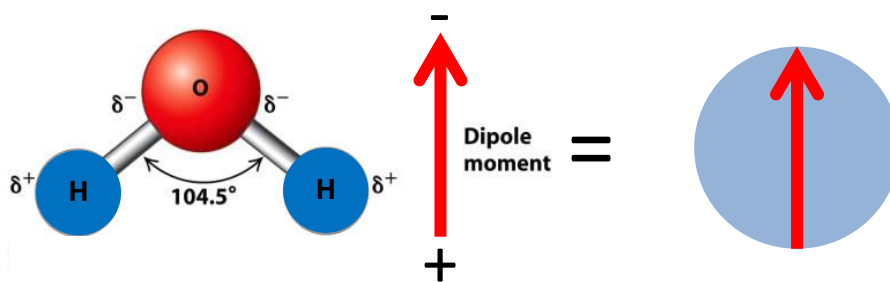


Figure 4.1: Modeling the water molecule as a dipolar hard sphere.

Chapter 3, the molecular nature of the water solvent is now explicitly taken into account by considering it as a Dipolar Hard Sphere (DHS) fluid. This allows to capture two important physical features of molecular interactions: short-range repulsions and long-range orientation-dependent electrostatic interactions [93] which are classified into three kinds of dipole-dipole interactions.

- **Keesom interaction (Fig 4.2):** The interaction between permanent dipoles is referred to as Keesom interaction. Because of their free rotating capacity, two dipoles may find favorable orientations to maximize the attraction between them. These interactions are partially responsible for the cohesion of liquids composed of polar molecules.

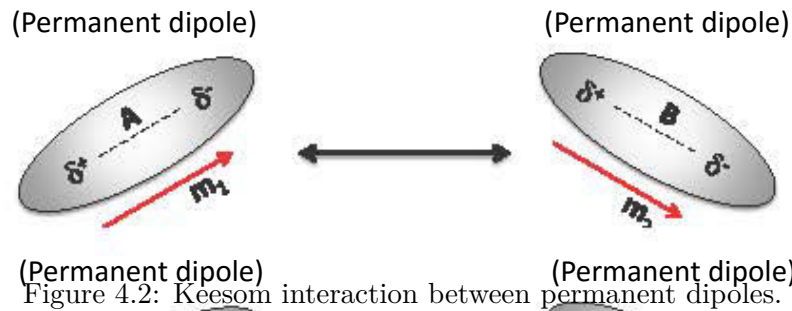


Figure 4.2: Keesom interaction between permanent dipoles.

- Debye interaction (Fig. 4.3):** These interactions are also known as polarization resulting from the interactions between permanent and induced dipoles. The latter appears when the electric field created by a polar molecule deforms the electron cloud of another adjacent (polar or nonpolar) molecule, inducing a dipole moment within the so-called polarized molecule.

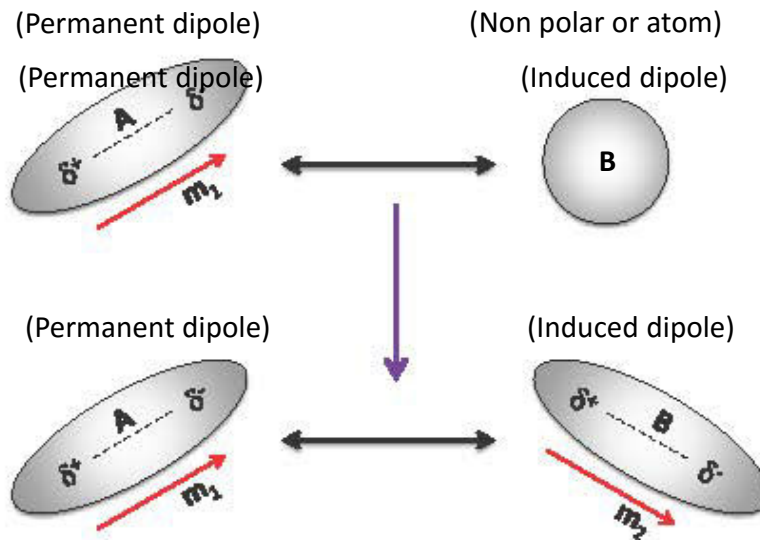


Figure 4.3: Debye interaction between permanent and induced dipoles.

- London dispersion force (Fig. 4.4):** This kind of attractive force occurs even between nonpolar molecules or atoms. As the electrons are in constant motion, their distribution at any given instant creates a short-lived instantaneous dipole moment (although, on average, the dipole moment is zero). This instantaneous dipole creates an electrical field which induces temporarily another dipole within an adjacent atom. Such instantaneous induced-dipole interactions between nonpolar molecules are the so-called London dispersion forces.

Among the three types of dipole interactions contributing to the Van-der-Waals forces between water molecules, only Keesom (permanent-permanent dipoles) interactions linked to the orientation of the water molecules will be considered in the following. Debye (permanent-induced dipoles) and London dispersion (instantaneous-induced dipoles) forces are either neglected in the present approach or added in an average Lennard-Jones term.

The complexity in comparison with simple (atomic) fluids is the anisotropy of the dipole-dipole interaction (Fig. 4.5): it depends not only on the spatial position \mathbf{r}_i of a fluid molecule i , but also on the dipole orientation ω_i which is specified by the dipole moment strength m_i and orientation angles located with respect to a fixed direction ($\omega_i = (\theta_i, \phi_i)$ where $0 \leq \theta_i \leq \pi$

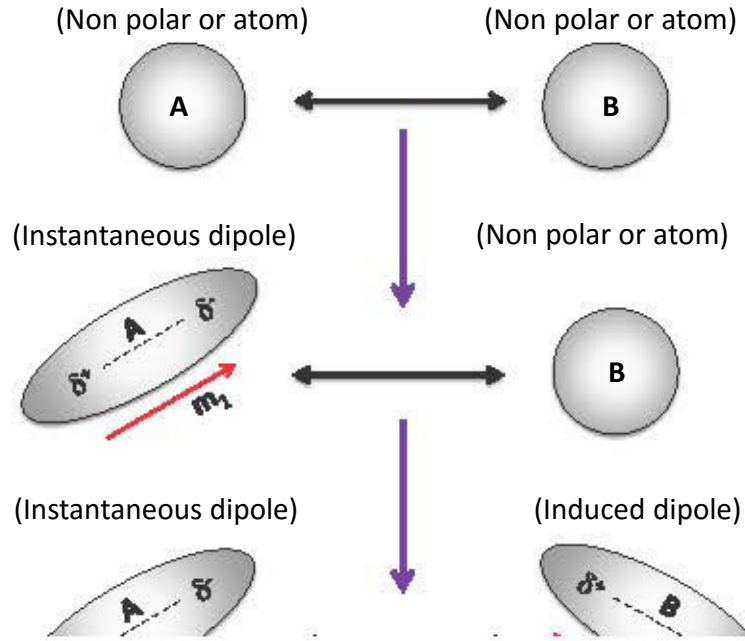


Figure 4.4: London dispersion force between fluctuating and induced dipoles.

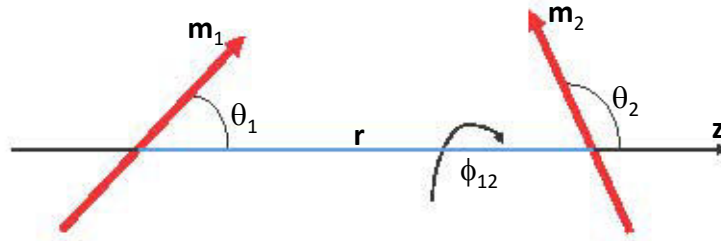


Figure 4.5: Geometrical configuration of dipole-dipole interactions.

is the angle with the fixed direction and $0 \leq \phi_i \leq 2\pi$ the angle in the plane perpendicular to the fixed direction). To simplify the notation, the symbol $i \equiv (\mathbf{r}_i, \boldsymbol{\omega}_i)$ is used to denote the coordinates of the fluid molecule i which occupies the position \mathbf{r}_i with a dipole oriented along the direction $\boldsymbol{\omega}_i$. The dipolar hard sphere fluid is characterized by the DHS interaction² potential between molecules 1 and 2

$$u(1,2) = \begin{cases} \infty, & r < d \\ -\frac{m^2}{4\pi\epsilon_0 r^3} D(1,2), & r > d. \end{cases} \quad (4.1)$$

If $\mathbf{r} = \mathbf{r}_1 - \mathbf{r}_2$ is the direction between the two sphere centers (chosen as the fixed direction), $r = |\mathbf{r}|$ the distance between the two sphere centers with $\hat{\mathbf{m}}_1$, $\hat{\mathbf{m}}_2$ and $\hat{\mathbf{r}}$ the unit vectors in the directions of \mathbf{m}_1 , \mathbf{m}_2 and \mathbf{r} , we define

$$\begin{cases} S(1,2) & = & 1 \\ \Delta(1,2) & = & \hat{\mathbf{m}}_1 \cdot \hat{\mathbf{m}}_2 = \cos \theta_1 \cos \theta_2 + \sin \theta_1 \sin \theta_2 \cos(\phi_1 - \phi_2) \\ D(1,2) & = & 3(\hat{\mathbf{m}}_1 \cdot \hat{\mathbf{r}})(\hat{\mathbf{m}}_2 \cdot \hat{\mathbf{r}}) - \hat{\mathbf{m}}_1 \cdot \hat{\mathbf{m}}_2 = 2 \cos \theta_1 \cos \theta_2 - \sin \theta_1 \sin \theta_2 \cos(\phi_1 - \phi_2). \end{cases} \quad (4.2)$$

In spherical coordinates (Fig. 4.6), the elementary solid angle is $d\boldsymbol{\omega} = \sin \theta d\theta d\phi$ and therefore

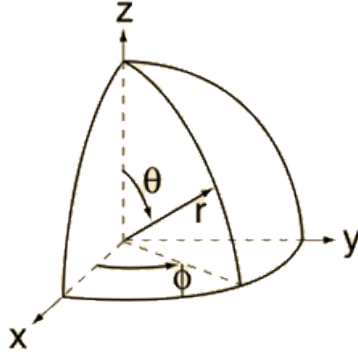


Figure 4.6: Representation of a vector in spherical coordinates: θ and ϕ are respectively the polar and the azimuth angles.

$\int d\omega = \int_0^\pi \sin\theta d\theta \int_0^{2\pi} d\phi = 4\pi$. Denoting by angular brackets with orientations ω_i as subscripts the average over the orientations of the involved molecules

$$\langle \dots \rangle_{\omega_1} \equiv \frac{1}{4\pi} \int \dots d\omega_1, \quad \langle \dots \rangle_{\omega_1, \omega_2} \equiv \frac{1}{(4\pi)^2} \iint \dots d\omega_1 d\omega_2, \quad (4.3)$$

and performing simple integrals (possibly with the help of the *Matlab Symbolic Toolbox*) gives

$$\begin{aligned} \langle S(1,2)\Delta(1,2) \rangle_{\omega_1, \omega_2} &= 0, & \langle S(1,2)D(1,2) \rangle_{\omega_1, \omega_2} &= 0, & \langle \Delta(1,2)D(1,2) \rangle_{\omega_1, \omega_2} &= 0, \\ \langle S^2(1,2) \rangle_{\omega_1, \omega_2} &= 1, & \langle \Delta^2(1,2) \rangle_{\omega_1, \omega_2} &= \frac{1}{3}, & \langle D^2(1,2) \rangle_{\omega_1, \omega_2} &= \frac{2}{3}. \end{aligned} \quad (4.4)$$

This means that $S(1,2)$, $D(1,2)$, and $\Delta(1,2)$ are the components of an orthogonal basis set. Therefore, the solution for the distribution function $h(1,2)$ is assumed to be of the form [21, 94]

$$h(1,2) = h_S(r) + h_\Delta(r)\Delta(1,2) + h_D(r)D(1,2), \quad (4.5)$$

where $h_S(r)$, $h_\Delta(r)$ and $h_D(r)$ are respectively the isotropic part of h , its projection on $\Delta(1,2)$ and on $D(1,2)$ calculated by multiplying Eq. (4.5) successively with S , Δ and D and integrating over all solid angles

$$h_S(r) = \langle h(1,2) \rangle_{\omega_1, \omega_2}, \quad (4.6)$$

$$h_\Delta(r) = 3 \langle h(1,2)\Delta(1,2) \rangle_{\omega_1, \omega_2}, \quad (4.7)$$

$$h_D(r) = \frac{3}{2} \langle h(1,2)D(1,2) \rangle_{\omega_1, \omega_2}. \quad (4.8)$$

The Direct Correlation Function (DCF) $c(1,2)$ can be treated in a similar way resulting in

$$c(1,2) = c_S(r) + c_\Delta(r)\Delta(1,2) + c_D(r)D(1,2). \quad (4.9)$$

It has to be noted that as the DHS fluid dipoles can turn around themselves, their orientation capacity is strongly influenced by their neighbors. Hence, the orientational correlations play a crucial role in the fluid behavior. Similarly to atomic fluids, there exist three common theoretical approaches for studying molecular fluids: integral equation theory, density functional theory and perturbation theory, in which the final expressions of the molecular distribution functions resemble closely those obtained for atomic fluids, except that all quantities are now functions of the dipole orientations. In what follows, this chapter presents a DFT approach for DHS fluids based on the nonlocal density functional theory developed by Tang et al [89] in which the orientational correlations between polar molecules are accounted for using the pair correlation functions of the corresponding homogeneous DHS fluid obtained with the Mean Spherical Approximation (MSA) approach proposed by Wertheim [21]. Finally, ions are added to complete the Electrical Double Layer (EDL) representation.

4.2 Mean spherical approximation for homogeneous DHS fluid

The first application of integral equation theory to dipolar hard sphere fluids is probably due to Wertheim [21] by using the MSA closure which is more specifically reported in the lecture note of Henderson [95].

Consider a DHS fluid characterized by the dipolar intermolecular potential of Eq. (4.1). The n -particle density $\rho^{(n)}(1, 2, \dots, n)$ is now the probability of finding n particles in the volume elements $(\mathbf{r}_1 + d\mathbf{r}_1, \mathbf{r}_2 + d\mathbf{r}_2, \dots, \mathbf{r}_n + d\mathbf{r}_n)$ with their dipole moments oriented along the solid angles $(\boldsymbol{\omega}_1 + d\boldsymbol{\omega}_1, \boldsymbol{\omega}_2 + d\boldsymbol{\omega}_2, \dots, \boldsymbol{\omega}_n + d\boldsymbol{\omega}_n)$. The Ornstein-Zernike (OZ) relation (2.22) has to be rewritten to take into account the distribution of the direction of the dipole moment as

$$h(1, 2) = c(1, 2) + \int \rho(3)h(1, 3)c(2, 3)d(3), \quad (4.10)$$

where $\rho(3)$ is the molecular density at position \mathbf{r}_3 with a dipole moment in the direction $\boldsymbol{\omega}_3$. Equation (4.10) is general. In a homogeneous situation (bulk fluid) $\rho(i) = \rho/4\pi$ is uniform where ρ is the molecule density irrespective of the direction of its dipole moment. The OZ equation becomes in this case

$$h(1, 2) = c(1, 2) + \frac{\rho}{4\pi} \int h(1, 3)c(2, 3)d(3) = c(1, 2) + \rho \int \langle h(1, 3)c(2, 3) \rangle_{\boldsymbol{\omega}_3} d\mathbf{r}_3. \quad (4.11)$$

To solve the above equation, it is convenient to use the Fourier transform. First, recall that a function $f(\mathbf{r})$ and its Fourier transform $\hat{f}(\mathbf{k})$ are linked by

$$\hat{f}(\mathbf{k}) = \int f(\mathbf{r}) \exp(-i\mathbf{k} \cdot \mathbf{r}) d\mathbf{r} \quad \text{and} \quad f(\mathbf{r}) = \frac{1}{(2\pi)^3} \int \hat{f}(\mathbf{k}) \exp(i\mathbf{k} \cdot \mathbf{r}) d\mathbf{k}. \quad (4.12)$$

The Fourier transform of a function $f(r)$ depending only on $r = |\mathbf{r}|$ (and not on \mathbf{r}) depends only on $k = |\mathbf{k}|$ (and not on \mathbf{k}). Assuming that \mathbf{k} coincides with the \mathbf{z} axis ($\mathbf{k} = (0 \ 0 \ k)$), $\hat{f}(k)$ reads then in spherical coordinates as

$$\begin{aligned} \hat{f}(k) &= \iiint f(r) \exp(-i\mathbf{k} \cdot \mathbf{r}) d\mathbf{r} = \int_0^\infty r^2 f(r) dr \int_0^{2\pi} d\phi \int_0^\pi \sin \theta d\theta \exp(ikr \cos \theta) \\ &= 2\pi \int_0^\infty r^2 f(r) dr \int_0^\pi \sin \theta d\theta \exp(ikr \cos \theta) = 4\pi \int_0^\infty r^2 f(r) j_0(kr) dr, \end{aligned} \quad (4.13)$$

where $j_0(z) = \frac{\sin z}{z}$ is the zero-order spherical Bessel function of the first kind. The Fourier transform of $h(1, 2)$ is then given by

$$\hat{h}(1, 2) = \hat{h}_S(k) + \hat{h}_\Delta(k)\Delta(1, 2) + \int h_D(r)D(1, 2) \exp(-i\mathbf{k} \cdot \mathbf{r}) d\mathbf{r}. \quad (4.14)$$

Obviously, the Fourier transforms of the terms with $S(1, 2)$ and $\Delta(1, 2)$ are straightforward, while those of $h_D(1, 2)$ and $c_D(1, 2)$ are more complicated because $D(1, 2)$ depends on $\hat{\mathbf{r}}$. Noting that $d\mathbf{r} = r^2 dr d\boldsymbol{\omega}_r$, first the integration is done over the dipole moment orientation, using the following property:

$$\int D(1, 2) \exp(-i\mathbf{k} \cdot \mathbf{r}) d\boldsymbol{\omega}_r = -4\pi j_2(kr) D_k(1, 2) \quad (4.15)$$

where (the proof which is rather technical and without difficulties has been omitted)

$$D_k(1, 2) = 3 \left(\hat{\mathbf{m}}_1 \cdot \hat{\mathbf{k}} \right) \left(\hat{\mathbf{m}}_2 \cdot \hat{\mathbf{k}} \right) - \hat{\mathbf{m}}_1 \cdot \hat{\mathbf{m}}_2, \quad (4.16)$$

and $j_2(z)$ is the second order spherical Bessel function of the first kind given by

$$j_2(z) = \left(\frac{3}{z^3} - \frac{1}{z} \right) \sin z - \frac{3}{z^2} \cos z . \quad (4.17)$$

Finally we obtain

$$\int h_D(r) D(1, 2) \exp(-i\mathbf{k} \cdot \mathbf{r}) d\mathbf{r} = -4\pi D_k(1, 2) \int_0^\infty j_2(kr) h_D(r) r^2 dr = D_k(1, 2) \bar{h}_D(k), \quad (4.18)$$

where $\bar{h}_D(k)$ is the Hankel transform in j_2

$$\bar{h}_D(k) = -4\pi \int_0^\infty j_2(kr) h_D(r) r^2 dr, \quad (4.19)$$

Eq. (4.14) can thus be rewritten in the form

$$\hat{h}(1, 2) = \hat{h}_S(k) + \hat{h}_\Delta(k) \Delta(1, 2) + \bar{h}_D(k) D_k(1, 2). \quad (4.20)$$

The same type of relation holds obviously for $(1, 2)$. Using the property that a convolution product (in \mathbf{r}_3) in the real space reduces to a simple product in the Fourier space, the Fourier transform of the OZ equation (4.11) is given by

$$\hat{h}(1, 2) = \hat{c}(1, 2) + \rho \left\langle \hat{c}(1, 3) \hat{h}(3, 2) \right\rangle_{\omega_3}. \quad (4.21)$$

The term $\left\langle \hat{c}(1, 3) \hat{h}(3, 2) \right\rangle_{\omega_3}$ in the preceding equation after substitution of \hat{h} and \hat{c} according to (4.20) contains convolution integrals over the direction ω_3 of the type

$$A * B = \frac{1}{4\pi} \int A(1, 3) B(3, 2) d\omega_3, \quad (4.22)$$

where the functions A and B are either S , Δ or D_k . The integral multiplication rules, which can easily be established, are shown in Table.4.1. It is obviously from Table.4.1 that the three

	S	Δ	D_k
S	S	0	0
Δ	0	$\Delta/3$	$D_k/3$
D_k	0	$D_k/3$	$(D_k + 2\Delta)/3$

Table 4.1: Evaluation of angular convolutions of the basic functions.

functions S , D and Δ form a closed set under the operation (4.22) so that the convolution of any two functions gives only a function in the same set (or zero).

We are now ready to solve the Ornstein-Zernike equation (4.20). As we have only one equation and two unknown functions h and c , another relation (closure) is required. In what follows, we will use the MSA closure in the case of a uniform DHS fluid. The MSA closure reads as

$$h(1, 2) = -1, \quad \text{for } r < d; \quad c(1, 2) = \frac{\beta m^2 D(1, 2)}{4\pi \epsilon_0 r^3}, \quad \text{for } r > d. \quad (4.23)$$

The first relation is exact. The second one $c(r) = -\beta w(r)$ where $w(r)$ is the intermolecular potential is only an approximation valid in the asymptotic case of large values of r . The MSA assumes that this asymptotic behavior for c is valid as soon as r is larger than the hard sphere diameter d .

From the MSA closure (4.23) and the developments (4.5–4.9) for h and c , it follows

$$\begin{cases} r < d : & h_S(r) = -1 & h_\Delta(r) = 0 & h_D(r) = 0 \\ r > d : & c_S(r) = 0 & c_\Delta(r) = 0 & c_D(r) = \frac{\beta m^2}{4\pi\epsilon_0 r^3}. \end{cases} \quad (4.24)$$

Note that $c_D(r)$ decays asymptotically as r^{-3} for $r > d$ and $h_D(r)$ also decays as r^{-3} for large values of r ($r \gg d$) (see section 11.5 in [44]). Hence, the projections $c_D(1,2)$ and $h_D(1,2)$ are long-range whereas the other projections are all short-ranged. To avoid numerical difficulties due to the slow decay of $c_D(1,2)$ and $h_D(1,2)$, it is convenient to introduce two short-range additional functions $h_D^0(r)$ and $c_D^0(r)$ to remove the asymptotic behavior in r^{-3} [44]

$$h_D^0(r) = h_D(r) - 3 \int_r^\infty \frac{h_D(r')}{r'} dr', \quad (4.25)$$

$$c_D^0(r) = c_D(r) - 3 \int_r^\infty \frac{c_D(r')}{r'} dr'. \quad (4.26)$$

Differentiating Eq. (4.25) leads to

$$\frac{dh_D^0}{dr} = \frac{dh_D}{dr} + \frac{3}{r} h_D = \frac{1}{r^3} \frac{d}{dr} (r^3 h_D). \quad (4.27)$$

Multiplying by r^3 and integrating from 0 to r yields

$$[r^3 h_D]_0^r = \int_0^r r'^3 \frac{dh_D^0}{dr'} dr' = [r'^3 h_D^0]_0^r - 3 \int_0^r r'^2 h_D^0 dr', \quad (4.28)$$

so that the inverse relations are easily obtained:

$$h_D(r) = h_D^0(r) - \frac{3}{r^3} \int_0^r h_D^0(r') r'^2 dr', \quad (4.29)$$

$$c_D(r) = c_D^0(r) - \frac{3}{r^3} \int_0^r c_D^0(r') r'^2 dr'. \quad (4.30)$$

Substituting $\hat{h}(1,2)$ and $\hat{c}(1,2)$ by their decompositions according to (4.20) in the Ornstein-Zernike relation (4.21) and making use of the table (4.1) for the integration over the dipole orientation, one obtains for the terms in S , Δ and D

$$\hat{h}_S(k) = \hat{c}_S(k) + \rho \hat{c}_S(k) \hat{h}_S(k), \quad (4.31)$$

$$\hat{h}_\Delta(k) = \hat{c}_\Delta(k) + \frac{\rho}{3} [\hat{c}_\Delta(k) \hat{h}_\Delta(k) + 2 \bar{c}_D(k) \bar{h}_D(k)], \quad (4.32)$$

$$\bar{h}_D(k) = \bar{c}_D(k) + \frac{\rho}{3} [\bar{c}_D(k) \bar{h}_D(k) + \bar{c}_D(k) \hat{h}_\Delta(k) + \hat{c}_\Delta(k) \bar{h}_D(k)]. \quad (4.33)$$

It can be shown that the Hankel transforms $\bar{h}_D(k)$ and $\bar{c}_D(k)$ of the functions $h_D(r)$ and $c_D(r)$ are respectively the Fourier transforms $\hat{c}_D^0(k)$ and $\hat{h}_D^0(k)$ of the functions $h_D^0(r)$ and $c_D^0(r)$ [96]. The inverse transforms can be consequently written in terms of spatial convolution integrals as follows

$$h_S(r) = c_S(r) + \rho c_S \otimes h_S, \quad (4.34)$$

$$h_\Delta(r) = c_\Delta(r) + \frac{\rho}{3} [c_\Delta \otimes h_\Delta + 2 c_D^0 \otimes h_D^0], \quad (4.35)$$

$$h_D^0(r) = c_D^0(r) + \frac{\rho}{3} [c_D^0 \otimes h_D^0 + c_D^0 \otimes h_\Delta + c_\Delta \otimes h_D^0]. \quad (4.36)$$

The closure relations for the projection functions $h_S(r)$, $h_\Delta(r)$ and $c_D(r)$, $c_\Delta(r)$ are already given by Eq. (4.24). For $h_D^0(r)$ and $c_D^0(r)$, the closure deduced from Eq. (4.24) using the relations (4.25) and (4.26) is given by

$$h_D^0(r) = -3K, \quad r < d; \quad c_D^0(r) = 0, \quad r > d, \quad (4.37)$$

where K is a constant defined as

$$K = \int_d^\infty \frac{h_D(r)}{r} dr. \quad (4.38)$$

It is obvious from Eq. (4.34) and the MSA closure for DHS fluids (4.24) that the functions $h_S(r)$ and $c_S(r)$ are the solution of the PY approximation for a hard sphere fluid of density ρ . This has an important consequence: the dipolar effects do not affect the distribution of the molecule centers in comparison with the hard sphere fluid.

To solve the problem for the Δ and D projections, the two equations (4.35) and (4.36) are linearly decorrelated introducing the auxiliary functions $c_+(r)$ and $c_-(r)$ defined by

$$c_+(r) = \frac{1}{3K} \left[c_D^0(r) + \frac{1}{2} c_\Delta(r) \right], \quad (4.39)$$

$$c_-(r) = \frac{1}{3K} \left[c_D^0(r) - c_\Delta(r) \right], \quad (4.40)$$

together with $h_+(r)$ and $h_-(r)$ defined in a similar way. The new functions satisfy

$$h_+(r) - c_+(r) = 2K\rho c_+ \otimes h_+, \quad (4.41)$$

$$h_-(r) - c_-(r) = -K\rho c_- \otimes h_-, \quad (4.42)$$

with the closure relations

$$\begin{cases} c_\pm(r) = 0, & r > d, \\ h_\pm(r) = -1, & r < d. \end{cases} \quad (4.43)$$

The couples (c_+, h_+) and (c_-, h_-) satisfy both an Ornstein-Zernike type equation complemented by the MSA closure i.e. the Percus-Yevick approximation for a hard sphere fluid. In the case (c_+, h_+) the fluid density is $2K\rho$ whereas in the case (c_-, h_-) , it is $-K\rho$. Solving the OZ equation with a negative density might appear surprising but will not cause any problem in practice. Denoting the Percus-Yevick solution for a hard sphere fluid of density ρ by $(c_{PY}(r; \rho), h_{PY}(r; \rho))$ (where $c_S(r; \rho)$ is analytic and given by Eq. (2.27)), we have

$$\begin{aligned} c_+(r) &= c_{PY}(r; 2K\rho), & h_+(r) &= h_{PY}(r; 2K\rho), \\ c_-(r) &= c_{PY}(r; -K\rho), & h_-(r) &= h_{PY}(r; -K\rho). \end{aligned} \quad (4.44)$$

The anisotropic parts $c_D^0(r)$ and c_Δ are given in terms of the PY-HS correlation function [93]

$$c_\Delta(r) = 2K [c_{PY}(r; 2K\rho) - c_{PY}(r; -K\rho)], \quad (4.45)$$

$$c_D^0(r) = K [2c_{PY}(r; 2K\rho) + c_{PY}(r; -K\rho)], \quad (4.46)$$

and

$$h_\Delta(r) = 2K [h_{PY}(r; 2K\rho) - h_{PY}(r; -K\rho)], \quad (4.47)$$

$$h_D^0(r) = K [2h_{PY}(r; 2K\rho) + h_{PY}(r; -K\rho)]. \quad (4.48)$$

The quantity K defined by Eq. (4.38) can be computed directly. As c_D^0 is null for $r > d$, Eq. (4.30) reduces to

$$\begin{aligned} r^3 c_D(r) &= \frac{\beta m^2}{4\pi\epsilon_0} = -3 \int_0^d c_D^0(r') r'^2 dr' \quad \text{for } r > d \\ &= -3K \int_0^d [2c_{PY}(r; 2K\rho) + c_{PY}(r; -K\rho)] r^2 dr, \end{aligned} \quad (4.49)$$

where Eq. (4.46) has been used. Denoting $Q(\eta)$ the quantity defined by

$$Q(\eta) = 1 - 4\pi\rho \int_0^d c_{PY}(r, \rho) r^2 dr = \frac{(1 + 2\eta)^2}{(1 - \eta)^4}, \quad (4.50)$$

where $\eta = \frac{1}{6}\pi\rho d^3$ is the solid volume fraction, K is solution of the following equation

$$3y \equiv \frac{\rho\beta m^2}{3\epsilon_0} = Q(2K\eta) - Q(-K\eta) . \quad (4.51)$$

The preceding equation allows to compute K for given y and η . The solution is unique for $K\eta$ comprised between 0 and $1/2$ when y increases monotonically from 0 to ∞ . For illustrative purposes, Figure 4.7 depicts the profiles of the projections $h_S(r)$, $h_\Delta(r)$ and $h_D(r)$ for $\rho d^3 = 0.7$ and $m^{*2} = \beta m^2 / (4\pi\epsilon_0 d^3) = 2$.

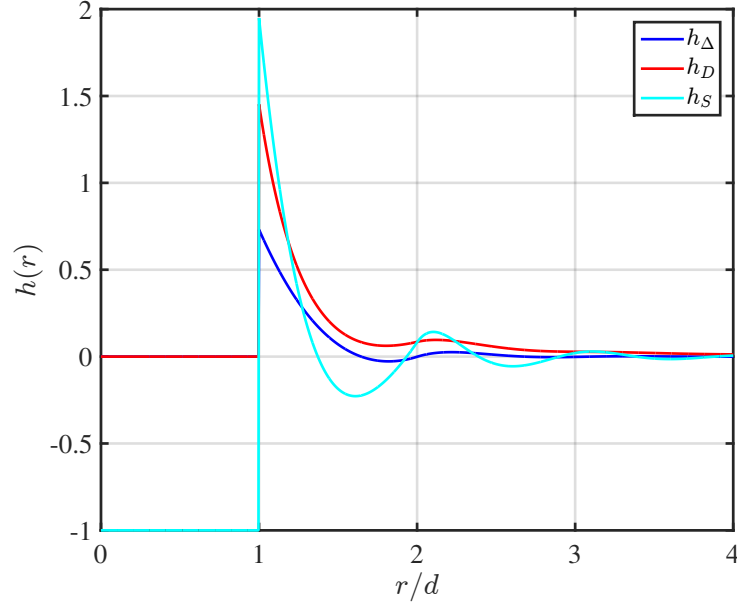


Figure 4.7: Projections of total correlation function $h(1, 2)$ for a dipolar hard spheres fluid with $\rho d^3 = 0.7$ and $m^{*2} = \frac{\beta}{4\pi\epsilon_0 d^3} m^2 = 2$.

4.3 Dielectric permittivity

The dielectric permittivity is a notion that is not trivial to introduce rigorously. Here we will follow the approach given by Fröhlich [97]. To start, we recall some classical notions of the macroscopic theory of dielectrics. The relative permittivity ϵ of a medium is defined by

$$\mathbf{D} = \epsilon\epsilon_0\mathbf{E} = \epsilon_0\mathbf{E} + \mathbf{P} , \quad (4.52)$$

where \mathbf{D} is the electric displacement field, ϵ_0 the vacuum permittivity and \mathbf{P} the medium polarisation (the mean polar moment per unit volume). In a dielectric material in the absence of charge, we have

$$\nabla \cdot \mathbf{D} = 0 \quad \text{or} \quad \nabla \cdot (\epsilon\epsilon_0\mathbf{E}) = 0 . \quad (4.53)$$

Consider an infinite dielectric medium of permittivity $\epsilon\epsilon_0$ submitted to an electric field E . In this medium consider a macroscopic free spherical void of volume V (prior to the introduction of N polar molecules) of permittivity ϵ_0 (Fig. 4.8).

In the spherical void cavity the electric field is given by the classical relation $\mathbf{E}' = 3\epsilon/(2\epsilon + 1)\mathbf{E}$. This field \mathbf{E}' will polarize the dipoles inside the cavity. The dipolar molecules with a total electric moment $\mathbf{M} = \sum_{i=1}^N \mathbf{m}_i$ submitted to the external potential \mathbf{E}' acquire a potential

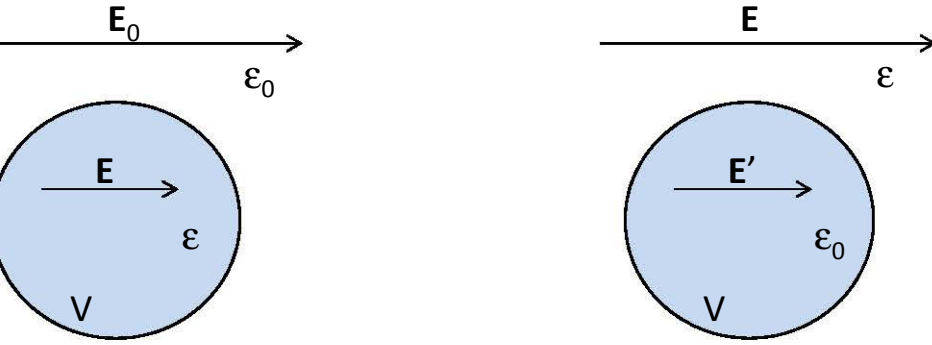


Figure 4.8: Fröhlich approach for the determination of the dielectric constant ϵ in an infinite dielectric medium of dielectric permittivity ϵ_0 is submitted to an electric field E ; inside this medium there is an empty spherical cavity of volume V (dielectric permittivity ϵ_0) occupied by N dipoles. Inside this medium there is a void spherical cavity of volume V (dielectric permittivity ϵ_0) occupied by N dipoles. E' is the electric field inside the cavity prior to the introduction of the N dipoles.

quantity $\exp(\beta \mathbf{M} \cdot \mathbf{E}')$ is now developed in power series of \mathbf{E} near $\mathbf{E} = 0$. Limiting the development to the linear term; energy $-\mathbf{M} \cdot \mathbf{E}'$. The canonical average $\langle \rangle^E$ is then introduced according to Kirkwood [98], where the superscript E indicates that the solicitation is due to the electric potential $\mathbf{E} \neq 0$. If the external electric field is oriented along Oz of unit vector \mathbf{k} , $\mathbf{E} = E\mathbf{k}$ it comes

where the mean value $\langle \rangle$ without superscript refers to the cavity in the absence of external field ($\mathbf{E} = \mathbf{E}' = 0$). Therefore $\langle \mathbf{m}_i \cdot \mathbf{k} \rangle = 0$ and the preceding relation leads to

$$\frac{\langle \mathbf{m}_i \cdot \mathbf{k} \rangle^E}{\langle \mathbf{m}_i \cdot \mathbf{k} \rangle} = \frac{\int \dots \int \mathbf{m}_i \cdot \mathbf{k} \exp[-\beta(U_N - \mathbf{M} \cdot \mathbf{E}')] d(1) \dots d(N)}{\int \dots \int \exp[-\beta(U_N - \mathbf{M} \cdot \mathbf{E}')] d(1) \dots d(N)}, \quad (4.54)$$

where U_N is the intermolecular potential. The quantity $\exp(\beta \mathbf{M} \cdot \mathbf{E}')$ is now developed in power series of \mathbf{E} near $\mathbf{E} = 0$. Limiting the development to the linear term, it comes

$$\langle \mathbf{M} \rangle^E = \sum_i \langle \mathbf{m}_i \cdot \mathbf{k} \rangle^E \mathbf{k} = \beta \frac{3\epsilon}{2\epsilon + 1} \left\langle \sum_i \mathbf{m}_i \cdot \mathbf{k} \right\rangle \mathbf{k} = \beta \frac{3\epsilon}{2\epsilon + 1} \langle M_z^2 \rangle \mathbf{E} \quad (4.55)$$

where the mean value $\langle \rangle$ without superscript refers to the cavity in the absence of any external field ($\mathbf{E} = \mathbf{E}' = 0$). Therefore $\langle \mathbf{m}_i \cdot \mathbf{k} \rangle = 0$ and the preceding relation reduces to

$$\frac{\mathbf{P}}{\epsilon_0} = \frac{\langle \mathbf{M} \rangle^E}{\epsilon_0 V} = \frac{\beta}{\epsilon_0 V} \frac{3\epsilon}{2\epsilon + 1} \langle M_z^2 \rangle \mathbf{E} \quad (4.56)$$

and thus

$$\langle \mathbf{M} \rangle^E = \sum_i \langle \mathbf{m}_i \cdot \mathbf{k} \rangle^E \mathbf{k} = \beta \frac{3\epsilon}{2\epsilon + 1} \frac{\beta}{9\epsilon_0 V} \langle M^2 \rangle \mathbf{E} = y g_K \frac{3\epsilon}{2\epsilon + 1} \langle M_z^2 \rangle \mathbf{E} \quad (4.57)$$

with $y = \beta \rho m^2 / (9\epsilon_0)$ and $g_K = \langle M^2 \rangle / (Nm^2)$ designates the Kirkwood factor. As $\mathbf{M} = \sum_i \mathbf{m}_i$, M^2 contains N terms of the type of $\langle \mathbf{m}_1 \cdot \mathbf{m}_1 \rangle$ and $N(N-1)$ terms of the type of $\langle \mathbf{m}_1 \cdot \mathbf{m}_2 \rangle$. In the absence of an electrical field, the electric moment is isotopic, $\langle M_z^2 \rangle = \langle M^2 \rangle / 3$. The medium polarization can thus be written as

$$g_K = \frac{\langle M^2 \rangle}{Nm^2} = 1 + \frac{(N-1) \langle \widehat{\mathbf{m}}_1 \cdot \widehat{\mathbf{m}}_2 \rangle}{Nm^2} \quad (4.58)$$

Hence:

$$\frac{\mathbf{P}}{\epsilon_0} = (\epsilon - 1) \mathbf{E} = \frac{\beta}{\epsilon_0 V} \frac{3\epsilon}{2\epsilon + 1} \langle M^2 \rangle \mathbf{E} \quad (4.58)$$

and thus

$$\frac{(\epsilon - 1)(2\epsilon + 1)}{9\epsilon} = y g_K = y [1 + (N-1) \langle \widehat{\mathbf{m}}_1 \cdot \widehat{\mathbf{m}}_2 \rangle] \quad (60)$$

This last result is now applied to the case of the MSA closure. Recalling the relation (7)

$$\frac{(\epsilon - 1)(2\epsilon + 1)}{9\epsilon} = \frac{\beta}{9\epsilon_0 V} \frac{\langle M^2 \rangle}{Nm^2} = \frac{\beta \rho m^2}{9\epsilon_0} \frac{\langle M^2 \rangle}{Nm^2} \quad (4.59)$$

with $y = \beta \rho m^2 / (9\epsilon_0)$ and $g_K = \langle M^2 \rangle / (Nm^2)$ (the latter designating the Kirkwood factor) As $\mathbf{M} = \sum_i \mathbf{m}_i$, M^2 contains N terms of the type of $\langle \mathbf{m}_1^2 \rangle$ and $N(N-1)$ terms of the type of $\langle \mathbf{m}_1 \cdot \mathbf{m}_2 \rangle$ so that the Kirkwood factor can be rewritten as

$$g_K = \frac{\langle M^2 \rangle}{Nm^2} = 1 + (N-1) \langle \widehat{\mathbf{m}}_1 \cdot \widehat{\mathbf{m}}_2 \rangle. \quad (4.60)$$

Introducing the above expression in (4.59) yields finally

$$\frac{(\epsilon - 1)(2\epsilon + 1)}{9\epsilon} = yg_K = y[1 + (N - 1)\langle \widehat{\mathbf{m}}_1 \cdot \widehat{\mathbf{m}}_2 \rangle]. \quad (4.61)$$

This last result is now applied to the case of the MSA closure. Recalling the relation (4.7)

$$\frac{1}{3}h_\Delta(r) = \frac{1}{(4\pi)^2} \int \Delta(1, 2)g(1, 2)d\omega_1 d\omega_2, \quad (4.62)$$

we have

$$\begin{aligned} (N - 1)\langle \widehat{\mathbf{m}}_1 \cdot \widehat{\mathbf{m}}_2 \rangle &= (N - 1) \frac{\left(\frac{\rho}{4\pi}\right)^2 \int \Delta(1, 2)g(1, 2)d\omega_1 d\omega_2 d\mathbf{r}_1 d\mathbf{r}_2}{\left(\frac{\rho}{4\pi}\right)^2 \int g(1, 2)d\omega_1 d\omega_2 d\mathbf{r}_1 d\mathbf{r}_2} \\ &= \frac{(N - 1)\rho^2 \int \frac{h_\Delta(r_{12})}{3} d\mathbf{r}_{12} d\mathbf{r}_1}{(N - 1)\frac{\rho}{4\pi} \int d\omega_1 d\mathbf{r}_1} = \frac{\rho}{3} \int h_\Delta(r) d\mathbf{r}, \end{aligned} \quad (4.63)$$

and thus

$$g_K = 1 + \frac{\rho}{3} \int h_\Delta(r) d\mathbf{r}. \quad (4.64)$$

Using relation (4.47) in the Fourier space for $k = 0$, we have

$$\tilde{h}_\Delta(0) = \int h_\Delta(r) d\mathbf{r} = 2K [\tilde{h}_{\text{PY}}(0; 2\rho K) - \tilde{h}_{\text{PY}}(0; -\rho K)]. \quad (4.65)$$

In combination with the Ornstein-Zernike relation in the Fourier space, Eq. (4.50) takes the form

$$\begin{aligned} Q(\eta) &= \frac{(1 + 2\eta)^2}{(1 - \eta)^4} = 1 - 4\pi\rho \int_0^d c_{\text{PY}}(r; \rho)r^2 dr \\ &= 1 - \rho \tilde{c}_{\text{PY}}(0; \rho) = \frac{1}{1 + \rho \tilde{h}_{\text{PY}}(0; \rho)}, \end{aligned} \quad (4.66)$$

so that $\tilde{h}_\Delta(0)$ can be expressed as

$$\rho \tilde{h}_\Delta(0) = \frac{1}{Q(2K\eta)} - 1 + 2 \left[\frac{1}{Q(-K\eta)} - 1 \right] = \frac{1}{Q(2K\eta)} + \frac{2}{Q(-K\eta)} - 3. \quad (4.67)$$

The relative permittivity ϵ is thus finally given by the equation

$$\frac{(\epsilon - 1)(2\epsilon + 1)}{9\epsilon} = y \left[1 + \frac{\rho}{3} \tilde{h}_\Delta(0) \right]. \quad (4.68)$$

Using Eq. (4.65) to express $\tilde{h}_\Delta(0)$ and writing y in terms of K according to Eq. (4.51), the following second order equation in ϵ is obtained

$$\begin{aligned} \frac{(\epsilon - 1)(2\epsilon + 1)}{9\epsilon} &= \frac{1}{9} [Q(2K\eta) - Q(-K\eta)] \left[\frac{1}{Q(2K\eta)} + \frac{2}{Q(-K\eta)} \right] \\ &= \frac{1}{9} \left[\frac{2Q(2K\eta)}{Q(-K\eta)} - \frac{Q(-K\eta)}{Q(2K\eta)} - 1 \right] \\ &= \frac{\left(\frac{Q(2K\eta)}{Q(-K\eta)} - 1 \right) \left(2\frac{Q(2K\eta)}{Q(-K\eta)} + 1 \right)}{9 \frac{Q(2K\eta)}{Q(-K\eta)}}, \end{aligned} \quad (4.69)$$

which has the unique positive solution

$$\epsilon = \frac{Q(2K\eta)}{Q(-K\eta)}. \quad (4.70)$$

This is Wertheim's result for the dielectric constant calculated with the MSA closure. Before this formula, there were two classical standard formula for its estimation:

$$\text{Clausius-Mossotti:} \quad \epsilon = \frac{1 + 2y}{1 - y}, \quad (4.71)$$

and

$$\text{Onsager:} \quad y = \frac{(\epsilon - 1)(2\epsilon + 1)}{9\epsilon}. \quad (4.72)$$

The Clausius-Mossotti is inaccurate and leads to the so-called polarization catastrophe because ϵ diverges when $y = 1$. The Clausius-Mossotti, Onsager and Wertheim-MSA results for the dielectric constant are plotted in Fig. 4.9 in comparison with Monte-Carlo data taken from the work of Valisko [99]. Obviously, the Onsager approach is much better than that of Clausius-Mossotti but less accurate than the MSA approach. However, the MSA is not able to capture ϵ at high values of y corresponding to the case of water ($\epsilon \approx 80$).

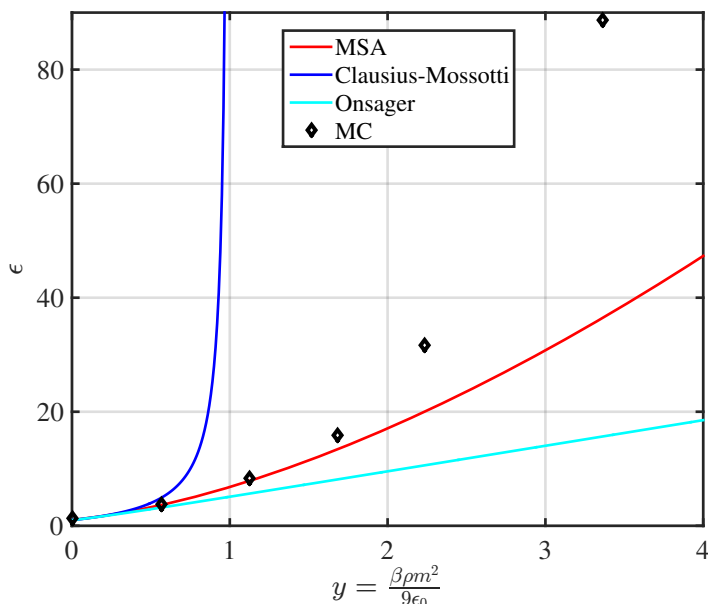


Figure 4.9: Relation between the relative permittivity of a homogeneous DHS fluid of a density $\rho d^3 = 0.7$ and the molecular parameter $y = \beta\rho m^2/(9\epsilon_0)$.

4.4 Density Functional Perturbation Theory (DFPT) approach for the DHS fluid

In a series of papers Oleksy and Hansen [100, 101, 102, 103] develop a theory for a polar fluid and ions using the DFT in the Mean Field Approximation (MFA). When the MFA is applied to a bulk subjected to a constant electric field, the electric permittivity is given by the Clausius-Mossotti formula leading inevitably to the polarization catastrophe [102]. The aim of this section is to include (in an approximate way) interparticle correlation effects in the DFT approach to see how the results are then modified. First, an introduction sets the basic framework for the modeling approach. The new theory is then applied to two cases: a bulk dipolar hard sphere fluid and the same fluid confined between two walls.

4.4.1 Introduction

The water solvent is explicitly considered as an inhomogeneous DHS fluid confined between two parallel charged plates located at $z = -H$ (charge density Σ) and at $z = H$ (charge density $-\Sigma$) to ensure overall charge neutrality of the system. The system is treated in cylindrical coordinates with the Oz axis parallel to the external electric field $E_{ext} = E_0 = \Sigma/\epsilon_0$ (E_0 is the electric field driven only by charges and not by dipoles). The molecule distribution profile depends both on the dipole orientation $\boldsymbol{\omega}$ and on the molecule center position \mathbf{r} as

$$\rho(\mathbf{r}, \boldsymbol{\omega}) = \rho(\mathbf{r})\alpha(\mathbf{r}, \boldsymbol{\omega}) \quad (4.73)$$

where the orientation-dependent function $\alpha(\mathbf{r}, \boldsymbol{\omega})$ is normalized by (see Fig. 4.6)

$$1 = \int \alpha(\mathbf{r}, \boldsymbol{\omega}) d\boldsymbol{\omega} = \int_0^{2\pi} d\phi \int_0^\pi \alpha(\mathbf{r}, \boldsymbol{\omega}) \sin\theta d\theta. \quad (4.74)$$

$\rho(\mathbf{r})$ is therefore the total density irrespective to the dipoles orientation. If α is independent of $\boldsymbol{\omega}$, $\alpha(\mathbf{r}) = 1/(4\pi)$.

According to the DFPT approach for LJ fluids presented in chapter 3, the complete intermolecular potential $u(1, 2, \lambda)$ can be written as

$$u(1, 2, \lambda) = u_{HS}(\mathbf{r}_1, \mathbf{r}_2) + \lambda u_{dd}(1, 2), \quad 0 \leq \lambda \leq 1 \quad (4.75)$$

where $u_{HS}(\mathbf{r}_1, \mathbf{r}_2)$ corresponds to the reference hard sphere system and $u_{dd}(1, 2)$ the dipole-dipole interaction potential given explicitly by

$$u_{dd}(1, 2) = -\frac{m^2}{4\pi\epsilon_0 r^3} D(1, 2), \quad (4.76)$$

where $D(1, 2)$ is given by Eq. (4.2c) which is the perturbation part. The intrinsic free energy of a DHS fluid is decomposed as

$$\mathcal{F} = \mathcal{F}^{id} + \mathcal{F}_{HS}^{ex} + \mathcal{F}_{dd}^{ex}. \quad (4.77)$$

The ideal gas contribution to the intrinsic free energy, \mathcal{F}^{id} , is

$$\mathcal{F}^{id} = k_B T \int d(1) \rho(1) \left\{ \ln \left[4\pi \Lambda^3 \rho(1) \right] - 1 \right\}, \quad (4.78)$$

with $d(1) = d\mathbf{r}_1 \sin\theta_1 d\theta_1 d\phi_1$. The introduction of the factor 4π in Eq. (4.78) can be justified considering the case of a bulk fluid where $\rho(1) \equiv \rho(\mathbf{r}_1, \boldsymbol{\omega}_1) = \rho_b/(4\pi)$, ρ_b being the total molecules density. The classic result $\mathcal{F}^{id} = k_B T \int \rho_b [\ln(\Lambda^3 \rho_b) - 1]$ is then recovered. The ideal chemical potential μ^{id} is then given by

$$\mu^{id} = \frac{\delta \mathcal{F}^{id}[\rho]}{\delta \rho(1)} = k_B T \ln[\Lambda^3 4\pi \rho(1)]. \quad (4.79)$$

The excess free energy part due to hard sphere exclusions, \mathcal{F}_{HS}^{ex} , is treated by the fundamental measure theory presented in chapter 2:

$$\beta \mathcal{F}_{HS}^{ex}[\rho] = \int \Phi[\{n_\alpha(\mathbf{r}')\}] d\mathbf{r}' = \frac{1}{4\pi} \iint \Phi[\{n_\alpha(\mathbf{r}')\}] d\mathbf{r}' d\boldsymbol{\omega}' \quad (4.80)$$

where

$$n_\alpha(\mathbf{r}) = \iint w_\alpha(\mathbf{r} - \mathbf{r}') \rho(\mathbf{r}', \boldsymbol{\omega}') d\mathbf{r}' d\boldsymbol{\omega}' \quad (4.81)$$

The functional derivative of $n_\alpha(\mathbf{r}')$ relative to $\rho(\mathbf{r}, \boldsymbol{\omega})$ is given by

$$\frac{\delta n_\alpha(\mathbf{r}')}{\delta \rho(\mathbf{r}, \boldsymbol{\omega})} = \iint d\mathbf{r}'' d\boldsymbol{\omega}'' \underbrace{\frac{\delta \rho(\mathbf{r}'', \boldsymbol{\omega}'')}{\delta \rho(\mathbf{r}, \boldsymbol{\omega})}}_{\delta(\mathbf{r} - \mathbf{r}'')\delta(\boldsymbol{\omega} - \boldsymbol{\omega}'')} w_\alpha(\mathbf{r}' - \mathbf{r}'') = w_\alpha(\mathbf{r}' - \mathbf{r}) \quad (4.82)$$

The functional derivative of $\mathcal{F}^{HS}[\rho]$ relative to $\rho(\mathbf{r}, \boldsymbol{\omega})$ reads then directly as

$$\begin{aligned} \beta \frac{\delta \mathcal{F}^{HS}[\rho]}{\delta \rho(\mathbf{r}, \boldsymbol{\omega})} &= \frac{1}{4\pi} \sum_\alpha \iint d\mathbf{r}' d\boldsymbol{\omega}' \frac{\partial \Phi}{\partial n_\alpha}(\mathbf{r}') \frac{\delta n_\alpha(\mathbf{r}')}{\delta \rho(\mathbf{r}, \boldsymbol{\omega})} = \frac{1}{4\pi} \sum_\alpha \iint d\mathbf{r}' d\boldsymbol{\omega}' \frac{\partial \Phi}{\partial n_\alpha} w_\alpha(\mathbf{r}' - \mathbf{r}) \\ &= \sum_\alpha \int d\mathbf{r}' \frac{\partial \Phi}{\partial n_\alpha}(\mathbf{r}') w_\alpha(\mathbf{r}' - \mathbf{r}) . \end{aligned} \quad (4.83)$$

The functional integration (see section 3.2 in chapter 3) allows to calculate the excess free energy part due to the dipole-dipole interactions as

$$\mathcal{F}_{dd}^{ex}[\rho] = \frac{1}{2} \iint d(1)d(2) \rho(1)\rho(2) u_{dd}(1, 2) \int_0^1 d\lambda g(1, 2; \lambda) , \quad (4.84)$$

where $g(1, 2; \lambda)$ is the radial distribution function of the inhomogeneous hard sphere fluid with an interaction potential $\lambda u_{dd}(1, 2)$ (see Eq. (4.75)). Finally, the density distribution given by Eq. (2.36) is rewritten for an inhomogeneous DHS fluid in the form

$$\rho(1) = \frac{\rho_b}{4\pi} \exp \left\{ \beta \left[\mu_b^{ex} - \frac{\delta \mathcal{F}_{HS}^{ex}[\rho]}{\delta \rho(\mathbf{r}_1)} - \mu_{dd}^{ex}(1) - V(1) \right] \right\} , \quad (4.85)$$

where μ_b^{ex} is the bulk excess chemical potential (hard sphere and dipole-dipole interactions), μ_{dd}^{ex} is the dipole-dipole interaction part of the excess chemical potential which follows directly from the corresponding contribution to the excess free energy (4.84) as

$$\mu_{dd}^{ex}(1) = \frac{\delta \mathcal{F}_{dd}^{ex}[\rho]}{\delta \rho(1)} = \int d(2) \rho(2) u_{dd}(1, 2) \int_0^1 d\lambda g(1, 2; \lambda) , \quad (4.86)$$

and $V_{ext}(1)$ is the external potential acting on dipole (1) which is given by

$$V_{ext}(1) = -\mathbf{m}_1 \cdot \mathbf{E}_0 = -mE_0 \cos \theta_1 , \quad (4.87)$$

where $E_0 = \Sigma/\epsilon_0$ is the external electric field only driven by the two charged planes at $z = \pm H$. As the bulk value and the hard sphere part of the chemical potential are not dependent of the dipole orientation, the density distribution can be rewritten as

$$\begin{aligned} \rho(1) &= \frac{\rho_b}{4\pi} \exp \left[\beta \mu_b^{ex} - \beta \frac{\delta \mathcal{F}_{HS}^{ex}(\rho_b)}{\delta \rho(\mathbf{r}_1)} \right] \times \exp [-\beta \mu_{dd}^{ex}(1) - \beta V_{ext}(1)] \\ &= C(\mathbf{r}) \times \exp [-\beta \mu_{dd}^{ex}(1) - \beta V_{ext}(1)] . \end{aligned} \quad (4.88)$$

The above equation together with Eq. (4.73) allows to write

$$\alpha(1) = \frac{\rho(1)}{\rho(\mathbf{r})} = \frac{\exp [-\beta \mu_{dd}^{ex}(1) - \beta V(1)]}{\int d\boldsymbol{\omega}_1 \exp [-\beta \mu_{dd}^{ex}(1) - \beta V(1)]} . \quad (4.89)$$

Because of the azimuthal symmetry and translational invariance in the Oxy plan, $\rho(\mathbf{r}, \boldsymbol{\omega}) = \rho(z, \theta) = \rho(z)\alpha(z, \theta)$. The orientation function $\alpha(1)$ can be calculated by using, for a given z , a development of the function $\alpha(z, \theta)$ in terms of Legendre polynomials (see Appendix §C.1) with respect to $\cos \theta$

$$\alpha(z, \theta) = \sum_{k=0}^{\infty} \alpha_k(z) P_k(\cos \theta) . \quad (4.90)$$

The orthogonality relation for the Legendre polynomials reads as

$$\int_{-1}^1 P_k(x)P_l(x)dx = \frac{2}{2k+1}\delta_{kl}, \quad (4.91)$$

where δ_{kl} is the Kronecker symbol. As $P_0 = 1$, it is immediate to verify that $\alpha_0 = 1/(4\pi)$, which is a direct consequence of the normalization condition (4.74).

The orthogonality of the Legendre polynomials allows to determine the α_k parameters in Eq. (4.90) by

$$\alpha_k(z_1) = \frac{2k+1}{4\pi} \frac{\int_{-1}^1 \exp[-\beta\mu_{dd}^{ex}(z_1, \theta_1) - \beta V(z_1, \theta_1)] P_k(\cos \theta_1) d(\cos \theta_1)}{\int_{-1}^1 \exp[-\beta\mu_{dd}^{ex}(z_1, \theta_1) - \beta V(z_1, \theta_1)] d(\cos \theta_1)}. \quad (4.92)$$

The central task of the present approach is to calculate the excess chemical potential $\mu_{dd}^{ex}(1)$ linked to dipole-dipole interactions starting from Eq. (4.86). The orientation density profile $\rho(1)$ can then be obtained with Eq. (4.85) and the dipole orientation distribution with Eq. (4.92). As the determination of the radial distribution function $g(1, 2; \lambda)$ is a tricky task, as suggested by Tang et al. [89], $g(1, 2; \lambda)$ is approximated by the radial distribution function of the corresponding homogeneous bulk DHS fluid $g_{MSA}(1, 2)$ which has been determined in §4.2 using the mean spherical approximation.

In what follows, the calculation is performed per unit area perpendicular to Oz by considering the first molecule (1) placed at $\mathbf{r}_1 = (0, 0, z_1)$ with $-H \leq z_1 \leq H$. The integration is carried out in cylindrical coordinates over a second molecule (2) placed at $\mathbf{r}_2 = (\chi \cos \phi, \chi \sin \phi, z_2)$ with $d\mathbf{r}_2 = \chi d\chi d\phi dz_2$ where $0 \leq \phi \leq 2\pi$, $0 \leq \chi < \infty$ and $-H \leq z_2 \leq H$. χ is the distance between the molecule (2) and the Oz axis as shown on Fig. (4.10). The integration must also be carried out over the dipole orientation of both molecules (1) ($d\omega_1 = \sin \theta_1 d\theta_1 d\phi_1$ with $0 \leq \theta_1 \leq \pi$ and $0 \leq \phi_1 \leq 2\pi$) and (2) ($d\omega_2$). Hence, the dipole-dipole excess free energy (per unit surface perpendicular to Oz), $\widehat{\mathcal{F}}_{dd}^{ex}$ is rewritten as

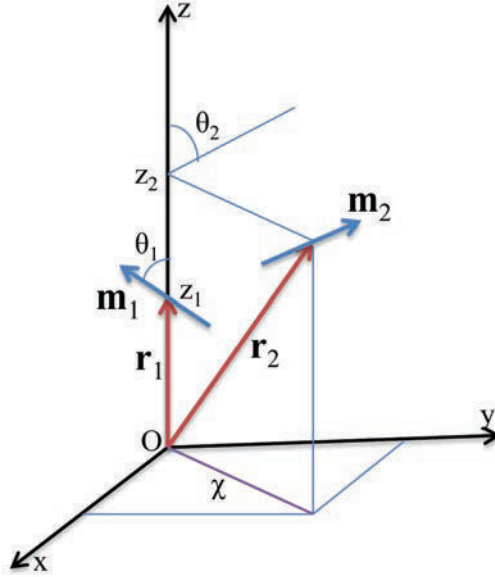


Figure 4.10: Dipole position and orientation.

$$\widehat{\mathcal{F}}_{dd}^{ex} = -\frac{m^2}{8\pi\epsilon_0} \iint \rho(1)\rho(2) g_{MSA}(1, 2) \frac{D(1, 2)}{r^3} d(1)d(2) \quad (4.93)$$

$$\begin{aligned}
&= -\frac{m^2}{8\pi\epsilon_0} \int_{-H}^H dz_1 \rho(z_1) \int_0^\pi \alpha(z_1, \theta_1) \sin \theta_1 d\theta_1 \int_0^{2\pi} d\phi_1 \int_{-H}^H dz_2 \rho(z_2) \int_0^{2\pi} d\phi \int_0^\infty \chi d\chi \\
&\times \int_0^\pi \sin \theta_2 d\theta_2 \int_0^{2\pi} d\phi_2 \alpha(z_2, \theta_2) [1 + h_S(r) + h_\Delta(r)\Delta(1, 2) + h_D(r)D(1, 2)] \frac{D(1, 2)}{r^3},
\end{aligned}$$

where $D(1, 2)$ is given by Eq. (4.2c)

$$\begin{aligned}
D(1, 2) &= 3(\widehat{\mathbf{m}}_1 \cdot \widehat{\mathbf{r}})(\widehat{\mathbf{m}}_2 \cdot \widehat{\mathbf{r}}) - \widehat{\mathbf{m}}_1 \cdot \widehat{\mathbf{m}}_2 \\
&= (3 \cos^2 \theta - 1) \cos \theta_1 \cos \theta_2 \\
&+ 3 \cos \theta \sin \theta [\cos \theta_1 \sin \theta_2 \cos(\phi - \phi_2) + \cos \theta_2 \sin \theta_1 \cos(\phi - \phi_1)] \\
&+ \sin \theta_1 \sin \theta_2 \left\{ \frac{3}{2} \sin^2 \theta [\cos(2\phi - \phi_1 - \phi_2) + \cos(\phi_2 - \phi_1)] - \cos(\phi_2 - \phi_1) \right\},
\end{aligned} \tag{4.94}$$

with $r^2 = (z_2 - z_1)^2 + \chi^2$ and $\sin \theta = \chi/r$.

The excess chemical potential is given by the functional derivative of Eq. (4.93):

$$\begin{aligned}
\mu_{dd}^{ex}(1) &= \frac{\delta \widehat{\mathcal{F}}_{dd}^{ex}}{\delta \rho(1)} = -\frac{m^2}{4\pi\epsilon_0} \int \rho(2) g_{MSA}(1, 2) \frac{D(1, 2)}{r^3} d(2) \\
&= -\frac{m^2}{4\pi\epsilon_0} \int_{-H}^H dz_2 \rho(z_2) \int_0^{2\pi} d\phi \int_0^\infty \chi d\chi \int_0^\pi \sin \theta_2 \alpha(z_2, \theta_2) d\theta_2 \\
&\times \int_0^{2\pi} d\phi_2 [1 + h_S(r) + h_\Delta(r)\Delta(1, 2) + h_D(r)D(1, 2)] \frac{D(1, 2)}{r^3}.
\end{aligned} \tag{4.95}$$

4.4.2 Behavior of the bulk DHS fluid

When the two walls move away to infinity, one obtains a homogeneous bulk fluid with constant density ρ_b in the presence of a uniform external field E_0 . The molecule distribution depends now only on the spatial orientation of the dipole, θ , such as

$$\rho(z, \theta) = \rho_b \alpha(\theta). \tag{4.96}$$

In the subsequent section, the dipole-dipole excess free energy Eq. (4.93) and the dipole-dipole excess chemical potential Eq. (4.95) are calculated in the homogeneous bulk fluid limit. These functional expressions of the state variables are the starting point for the determination of the DHS fluid density and the dipole orientation profile in the presence of an external electric field by use of equations (4.88) and (4.89), respectively.

The excess chemical potential can be determined either directly or indirectly using its definition as the functional derivative of the excess free energy. For completeness and to verify the consistency of the present model DFPT approach, both derivations are presented in detail in the appendix (§C.2.1). For the sake of simplicity, we show here only the principle steps of the direct derivation.

4.4.2.1 Dipole-dipole excess chemical potential of the homogeneous DHS fluid

The direct calculation of the orientation-dependent dipole-dipole excess chemical potential starts from Eq. (4.95). By setting $z_1 = 0$ and $z_2 = z$, Eq. (4.95) reads as

$$\begin{aligned}
\mu_{dd}^{ex}(\theta_1) &= -\frac{\rho_b m^2}{4\pi\epsilon_0} \int_{-H}^H dz \int_0^{2\pi} d\phi \int_0^\infty \chi d\chi \int_0^\pi \sin \theta_2 \alpha(\theta_2) d\theta_2 \int_0^{2\pi} d\phi_2 \frac{D(1, 2)}{r^3} \\
&\times [1 + h_S(r) + \Delta(1, 2)h_\Delta(r) + D(1, 2)h_D(r)]
\end{aligned} \tag{4.97}$$

The details of the calculation are given in the appendix (§C.2.1.2). The orientation-dependent dipole-dipole excess chemical potential can finally be written under the following form

$$\begin{aligned}\mu_{dd}^{ex}(\theta_1) &= \frac{8\pi\rho_b m^2 \alpha_1}{9\epsilon_0} \cos\theta_1 - \frac{\pi\rho_b m^2}{5\epsilon_0} K \left[\frac{40}{3}\alpha_0 + \frac{4}{15}\alpha_2 (3\cos^2\theta_1 - 1) \right] \\ &= \frac{\pi\rho_b m^2}{\epsilon_0} \left[-\frac{8}{3}K\alpha_0 + \frac{8}{9}\alpha_1 \cos\theta_1 - \frac{4}{75}K\alpha_2 (3\cos^2\theta_1 - 1) \right].\end{aligned}\quad (4.98)$$

The mean chemical potential due to the dipolar interactions is obtained by averaging over all the orientations

$$\begin{aligned}\mu_{dd}^{ex} &= \int \mu_{dd}^{ex}(\theta_1) \alpha(\omega_1) d\omega_1 = 2\pi \int_{-1}^1 \mu_{dd}^{ex}(\theta_1) \alpha(\cos\theta_1) d(\cos\theta_1) \\ &= \frac{2\pi^2 \rho_b m^2}{\epsilon_0} \left[-\frac{16}{3}K\alpha_0^2 + \frac{16}{27}\alpha_1^2 - \frac{16}{375}K\alpha_2^2 \right],\end{aligned}\quad (4.99)$$

which is in agreement with relation (C.33) in §C.2.1.1 of the appendix resulting from the functional derivation of the excess free energy.

4.4.2.2 Dipole moment orientation profile in a uniform electric field

For a bulk fluid submitted to a uniform electric field \mathbf{E}_0 , the coefficients α_k in the development of the dipole orientation distribution function $\alpha(\theta)$ in terms of Legendre polynomials can be rewritten by introducing the previous derived expression of $\mu_{dd}^{ex}(\theta)$ (4.98) in Eq. (4.92)

$$\alpha_k = \frac{2k+1}{4\pi} \frac{\int_{-1}^1 \exp \left\{ \beta \left[\frac{\pi\rho_b m^2}{\epsilon_0} \left(\frac{8}{3}K\alpha_0 - \frac{8}{9}\alpha_1 u + \frac{4}{75}K\alpha_2(3u^2 - 1) \right) + mE_0 u \right] \right\} P_k(u) du}{\int_{-1}^1 \exp \left\{ \beta \left[\frac{\pi\rho_b m^2}{\epsilon_0} \left(\frac{8}{3}K\alpha_0 - \frac{8}{9}\alpha_1 u + \frac{4}{75}K\alpha_2(3u^2 - 1) \right) + mE_0 u \right] \right\} du},\quad (4.100)$$

where $\cos\theta_1 = u$. After further simplification the above expression becomes

$$\alpha_k = \frac{2k+1}{4\pi} \frac{\int_{-1}^1 \exp \left\{ \beta \left[\frac{\pi\rho_b m^2}{\epsilon_0} \left(-\frac{8}{9}\alpha_1 u + \frac{4}{25}K\alpha_2 u^2 \right) + mE_0 u \right] \right\} P_k(u) du}{\int_{-1}^1 \exp \left\{ \beta \left[\frac{\pi\rho_b m^2}{\epsilon_0} \left(-\frac{8}{9}\alpha_1 u + \frac{4}{25}K\alpha_2 u^2 \right) + mE_0 u \right] \right\} du}.\quad (4.101)$$

Note that Eq. (4.101) verifies the condition $\alpha_0 = 1/(4\pi)$. Fig. 4.11 shows the orientation distribution of the dipoles in a bulk fluid submitted to different electric field strengths $E_0 = \Sigma/\epsilon_0$ generated by the surface charge densities $\pm\Sigma$ at the two walls. If $E_0 = 0$, as the first Legendre polynomial is $P_0(u) = 1$, it follows directly from Eq. (4.101) that $\alpha_1 = \alpha_2 = 0$ are solutions of Eq. (4.101) with $k \in \{1, 2\}$. All higher orders in α_k are also null. The dipole orientation distribution is independent of θ , being in agreement with an isotropic bulk fluid. Increasing $E_0 \neq 0$, the dipoles align along the electric field direction as expected.

4.4.2.3 Permittivity of a bulk DHS fluid submitted to a uniform electric field

In the case $\Sigma \neq 0$, the bulk DHS fluid is a dielectric polarized medium as the dipoles tend to align themselves along the field direction. The polarization of the DHS molecules is given by

$$P = \int_0^\pi m \cos(\theta) \rho(z, \theta) 2\pi \sin\theta d\theta = \frac{4\pi}{3} m \rho_b \alpha_1.\quad (4.102)$$

This dielectric polarization creates an internal electric field that reduces the overall field within the bulk DHS fluid. In the dielectric theory, if the polarization P is uniform, the internal electric

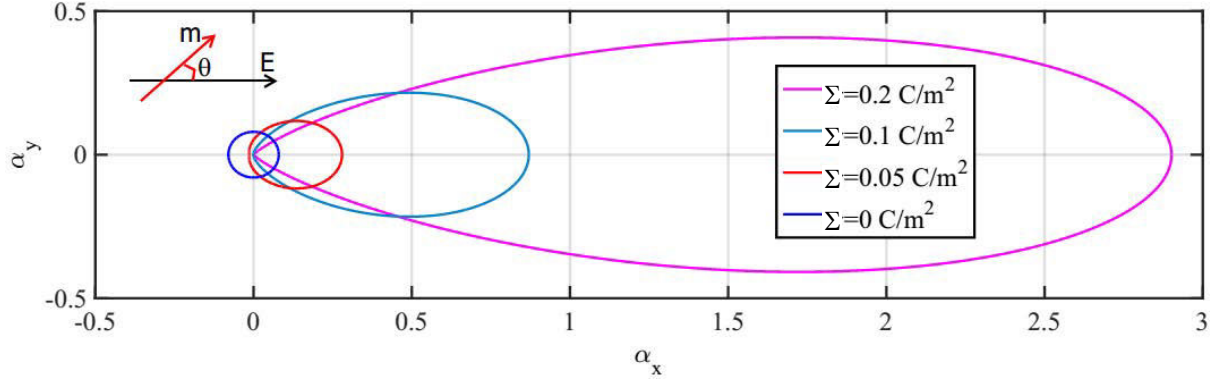


Figure 4.11: Dipole orientation profiles of a bulk fluid for different uniform electric fields: $E_0 = \Sigma/\epsilon_0$ and $\alpha(\theta) = \sqrt{\alpha_x^2 + \alpha_y^2}$.

field is straightforwardly calculated by adding the surface charges $\pm P$ on the boundaries of the medium. Therefore, the electric field within the bulk DHS fluid reads as

$$E = \frac{\Sigma - P}{\epsilon_0} = E_0 - \frac{P}{\epsilon_0}, \quad (4.103)$$

where E_0 is the electric field only driven by charges. Starting from the above relation, the relative permittivity ϵ of the medium can be calculated by the following expression

$$\begin{aligned} \epsilon\epsilon_0 E &= \epsilon_0 E + P \\ \epsilon\epsilon_0 \left(E_0 - \frac{P}{\epsilon_0}\right) &= \epsilon_0 \left(E_0 - \frac{P}{\epsilon_0}\right) + P = \epsilon_0 E_0. \end{aligned} \quad (4.104)$$

Hence

$$\epsilon = \frac{E_0}{E_0 - \frac{P}{\epsilon_0}} = \frac{E_0}{E_0 - \frac{4\pi}{3\epsilon_0} m \rho_b \alpha_1}. \quad (4.105)$$

In the MFA framework and at low electric field strength, the above relation reduces to the Clausius-Mossotti (CM) formula [102] (see Appendix §C.3)

$$\epsilon = \frac{1 + \frac{2}{9} \frac{\beta m^2 \rho_b}{\epsilon_0}}{1 - \frac{\beta m^2 \rho_b}{9\epsilon_0}} = \frac{1 + 2y}{1 - y}. \quad (4.106)$$

Fig. 4.12 illustrates the dependence of the permittivity of a bulk DHS fluid at a high density $\rho_b d^3 = 0.734$ and a low dipole moment strength $m^{*2} = \beta m^2 / (4\pi\epsilon_0 d^3) = 0.75$ as calculated by Eq. (4.105). This yields ϵ values between 1 and 11. As $y = 4\pi/9 \rho_b d^3 m^{*2}$, the Clausius-Mossotti formula (4.105) gives $\epsilon \simeq 11.0$. When the electric field E_0 increases, the quantity α_1/E_0 and therefore the relative permittivity ϵ decrease to tend towards 1 for high values of E_0 . For high dipolar interactions as in water ($m^{*2} \simeq 2$), taking into account the correlation effects (using the bulk values for the radial distribution functions) is not accurate enough to avoid the ‘‘Clausius-Mossotti catastrophe’’ and Eq. (4.105) is no longer valid.

4.4.3 Behavior of HS dipolar fluids confined between two walls

4.4.3.1 The dipole-dipole excess chemical potential

Now the case of an inhomogeneous situation is studied with the water solvent modeled as a DHS fluid confined between two planar hard walls located at $z = \pm H$. With the density profile

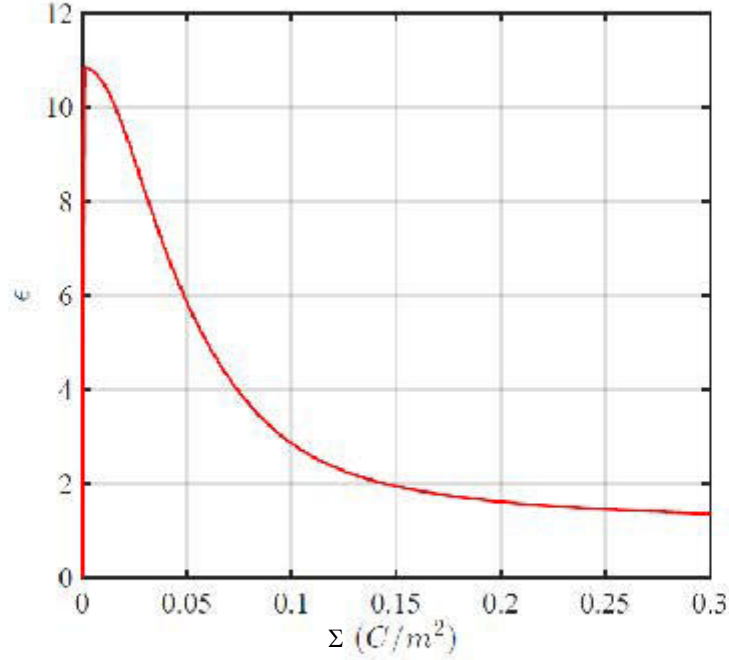


Figure 4.12: Evolution of the permittivity of a bulk DHS fluid submitted to an electric field $E_0 = \Sigma/\epsilon_0$, where Σ is the surface charge of the walls (bulk density $\rho_b d^3 = 0.734$ and reduced dipole moment strength $m^*2 = 0.75$).

expressed by Eq. (4.88) and the dipole distribution by Eq. (4.92), the dipole-dipole excess chemical potential μ_{dd}^{ex} is given by Eq. (4.95)

$$\begin{aligned} \mu_{dd}^{ex}(1) &= -\frac{m^2}{4\pi\epsilon_0} \int_{-H}^H dz_2 \rho(z_2) \int_0^{2\pi} d\phi \int_0^\infty \chi d\chi \int_0^\pi \alpha(z_2, \theta_2) \sin \theta_2 d\theta_2 \\ &\times \int_0^{2\pi} d\phi_2 [1 + h_S(r) + h_\Delta(r)\Delta(1, 2) + h_D(r)D(1, 2)] \frac{D(1, 2)}{r^3}. \end{aligned} \quad (4.107)$$

The resolution of the above expression plays the central role in determining the dipole orientation distribution Eq. (4.89) and the orientation-dependent density profile Eq. (4.85). The calculation is of the same type as that of the preceding section but a little more complicated in an inhomogeneous situation. The details are given in §C.2.2 of the appendix. Only the results are recalled here.

The excess chemical potential due to dipole-dipole interactions can be decomposed as

$$\mu_{dd}^{ex}(1) = \mu_{dd}^{ex}(1)|_S + \mu_{dd}^{ex}(1)|_\Delta + \mu_{dd}^{ex}(1)|_D \quad (4.108)$$

where

$$\mu_{dd}^{ex}(1)|_S = -\frac{2\pi m^2}{3\epsilon_0} \cos \theta_1 [(\rho\alpha_1) \otimes I_{h_S}](z_1), \quad (4.109)$$

$$\mu_{dd}^{ex}(1)|_\Delta = -\frac{\pi m^2}{4\epsilon_0} [J_{h_\Delta} \otimes I_{h_\Delta}](z_1), \quad (4.110)$$

$$\mu_{dd}^{ex}(1)|_D = -\frac{m^2}{4\epsilon_0} [\rho \otimes I_{h_D}^\rho + \rho\alpha_2 \otimes I_{h_D}^{\rho\alpha}](z_1) \quad (4.111)$$

$$\text{and } I_h(z) = \int_{|z|}^\infty \left(\frac{3z^2}{r^4} - \frac{1}{r^2} \right) h(r) dr \quad \text{for } h = h_S \text{ or } h_\Delta \quad (4.112)$$

$$\text{and } J_{h_\Delta}(z) = \rho(z_2) \left[\frac{4}{5} \alpha_2(z) \left(\cos^2 \theta_1 + \frac{1}{3} \right) + \frac{1}{\pi} \left(\cos^2 \theta_1 - \frac{1}{3} \right) \right]. \quad (4.113)$$

$$I_{h_D}^{\rho}(z) = \int_{|z|}^{\infty} dr \left[\frac{5}{3} - \frac{z^2}{r^2} + \cos^2 \theta_1 \left(\frac{3z^2}{r^2} - 1 \right) \right] \frac{h_D(r)}{r^2} \quad (4.114)$$

$$I_{h_D}^{\rho\alpha}(z) = -\pi \int_{|z|}^{\infty} dr \left[\frac{4}{3} - 8 \frac{z^2}{r^2} + \frac{36}{5} \frac{z^4}{r^4} + \cos^2 \theta_1 \left(-\frac{12}{5} + \frac{96}{5} \frac{z^2}{r^2} - \frac{108}{5} \frac{z^4}{r^4} \right) \right] \frac{h_D(r)}{r^2}. \quad (4.115)$$

4.4.3.2 Density and dipole orientation profiles in a uniform electric field

The orientation-dependent density profile of a DHS fluid confined between two plates Eq. (4.85) exerting a uniform electric field on the fluid, is rewritten as

$$\rho(z_1, \theta_1) = \frac{\rho_b}{4\pi} \exp \{ \beta [\mu_b^{ex} - \mu_{HS}^{ex}(\rho) - \mu_{dd}^{ex}(z_1, \theta_1) - V(\theta_1)] \}, \quad (4.116)$$

where the excess chemical potential of the bulk fluid in equilibrium with the one confined between the two plates μ_b^{ex} can be decomposed as

$$\mu_b^{ex} = \mu_{HS}^{ex}(\rho_b) + \mu_{dd}^{ex}(\rho_b), \quad (4.117)$$

where $\mu_{dd}^{ex}(\rho_b)$ is given by Eq. (4.99) with $\alpha_0 = 1/(4\pi)$ and $\alpha_1 = \alpha_2 = 0$ in the bulk limit if $E_0 = 0$ and the external potential reads as

$$V(\theta_1) = -mE_0 \cos \theta_1. \quad (4.118)$$

The spatial position dependent density profile is then obtained after integration of Eq. (4.116) over the solid angles θ_1 and ϕ_1 resulting in

$$\begin{aligned} \rho(z_1) &= \frac{\rho_b}{4\pi} \exp \{ \beta [\mu_b^{ex} - \mu_{HS}^{ex}(\rho)] \} \int_0^{2\pi} d\phi_1 \int_0^{\pi} d\theta_1 \sin \theta_1 \exp [-\beta (\mu_{dd}^{ex}(z_1, \theta_1) + V(z_1, \theta_1))] \\ &= \frac{\rho_b}{2} \exp \{ \beta [\mu_b^{ex} - \mu_{HS}^{ex}(\rho)] \} \int_{-1}^1 d(\cos \theta_1) \exp [-\beta (\mu_{dd}^{ex}(z_1, \theta_1) + V(z_1, \theta_1))]. \end{aligned} \quad (4.119)$$

In a similar manner as for the homogeneous DHS fluid, the coefficients $\alpha_k(z_1)$ of the Legendre development of the dipole orientation profile $\alpha(z_1, \theta_1)$ for the inhomogeneous case can be calculated by

$$\alpha_k(z_1) = \frac{2k+1}{4\pi} \frac{\int_{-1}^1 \exp [-\beta (\mu_{dd}^{ex}(z_1, \theta_1) + V(z_1, \theta_1))] P_k(\cos \theta_1) d(\cos \theta_1)}{\int_{-1}^1 \exp [-\beta (\mu_{dd}^{ex}(z_1, \theta_1) + V(z_1, \theta_1))] d(\cos \theta_1)}. \quad (4.120)$$

The dipole-dipole pressure in the bulk is finally calculated by

$$\begin{aligned} p_{dd}^b &= \rho_b \mu_{dd}^{ex} - f_{dd}^{ex} = \frac{16\pi^2 \rho_b^2 m^2}{3\epsilon_0} \left(-K\alpha_0^2 + \frac{\alpha_1^2}{9} - \frac{K}{125}\alpha_2^2 \right), \\ p_{dd}^* &= \beta d^3 \frac{16\pi^2 \rho_b^2 m^2}{3\epsilon_0} \left(-K\alpha_0^2 + \frac{\alpha_1^2}{9} - \frac{K}{125}\alpha_2^2 \right) \\ &= \frac{64\pi^3}{3} m^{*2} \rho_b^{*2} \left(-K\alpha_0^2 + \frac{\alpha_1^2}{9} - \frac{K}{125}\alpha_2^2 \right). \end{aligned} \quad (4.121)$$

The bulk pressure of a DHS fluid is then given by the sum of Eq. (2.105) and Eq. (4.121) leading to

$$p_b = p_b^{HS} + p_b^{dd} = k_B T \rho_b \frac{1 + \eta + \eta^2 - \eta^3}{(1 - \eta)^3}$$

$$+ \frac{16\pi^2 \rho_b^2 m^2}{3\epsilon_0} \left(-K\alpha_0^2 + \frac{\alpha_1^2}{9} - \frac{K}{125}\alpha_2^2 \right). \quad (4.122)$$

In the case $E_0 = 0$, $\alpha_0 = 1/(4\pi)$ and $\alpha_1 = \alpha_2 = 0$ in the bulk limit the above relation reduces to

$$p_b = k_B T \rho_b \frac{1 + \eta + \eta^2 - \eta^3}{(1 - \eta)^3} - \frac{\rho_b^2 m^2}{3\epsilon_0} K. \quad (4.123)$$

Similarly to the former case of a HS fluid confined between two hard walls in Chapter 2, the disjoining pressure of a confined DHS fluid in this configuration with $E_0 = 0$ is calculated by

$$\Pi = k_B T \rho(z = d/2) - p_b. \quad (4.124)$$

4.4.3.3 Application to the EDL

In the EDL description, the two plates exhibit an identical negative surface charge density, which generates an electric field $E_0 = 0$ between the two plates. Global electroneutrality will be ensured when adding ions into the interlayer space. Therefore, the external potential stems only from the finite particle size Eq. (2.98). As a numerical application, a DHS fluid confined between two neutral hard walls located at 0 and L is studied. According to existing MC data documented in the work of Tang et al [89], the parameter values are set to $L = 15d$, $\rho_b d^3 = 0.7$ and $m^{*2} = 2$. First, the spatial position-dependent density profile of the DHS fluid calculated with Eq. (4.119) along with MC results is presented on Fig. 4.13 in order to verify the accuracy of the present approach. The overall agreement between the present theory

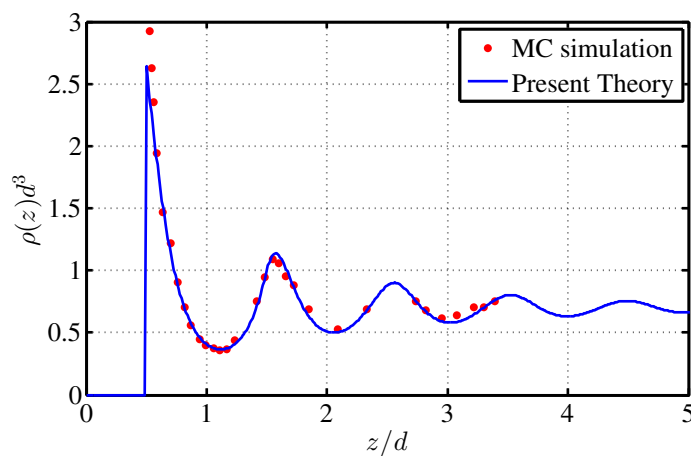


Figure 4.13: Density profile of a DHS fluid confined between two hard walls with $\rho_b d^3 = 0.7$ and $m^{*2} = 2$.

and the MC simulation is quite good. However, this approach underestimates the contact density by nearly 10%. This disagreement probably stems from the inaccurate approximation of the RDF in the vicinity of the walls [89] which is approximated by that of the corresponding bulk DHS fluid. Dipole-dipole correlations are characterized by the rotation capacity of the dipoles which is strongly influenced by its neighbors. Such interparticle correlation effects are represented by the dipole orientation distribution. Fig. 4.14 depicts a three-dimensional view of the dipole orientation profile $\alpha(z, \theta)$ of a confined DHS fluid in the same conditions as in Fig. 4.13. Obviously, the dipoles prefer to align parallel to the walls in the regions immediately adjacent to the walls and perpendicular to the walls in the next region. This kind of change in preferential orientation is periodic until reaching the uniform orientation behavior of dipoles at the center region of the two walls and the period is approximately one molecule diameter d . These conclusions are in good agreement with those of Tang et al. [89].

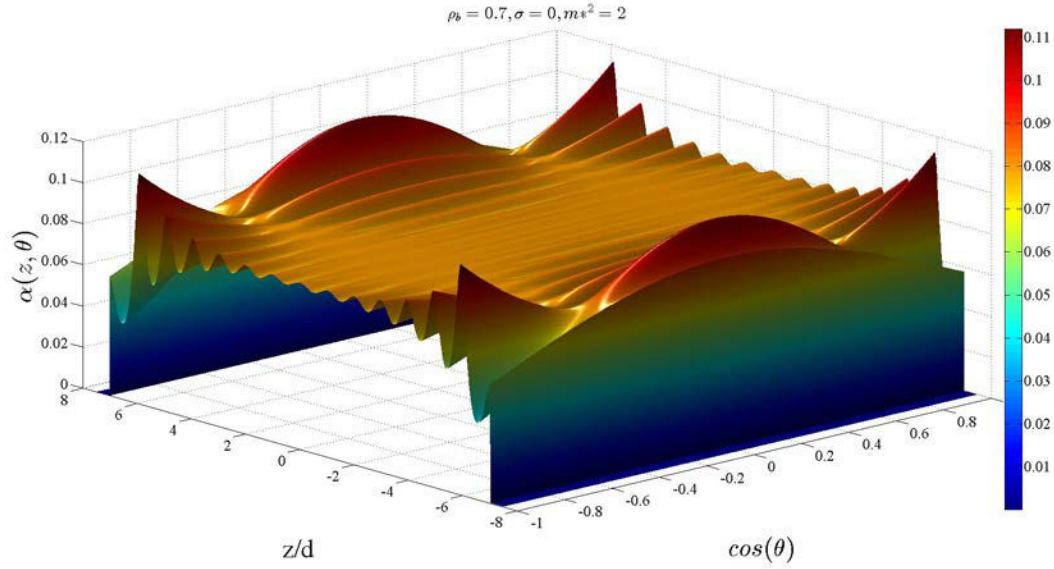


Figure 4.14: Dipole orientation distribution of the DHS fluid confined between two hard walls with $\rho_b d^3 = 0.7$, $m^* = 2$, $2H = 15d$.

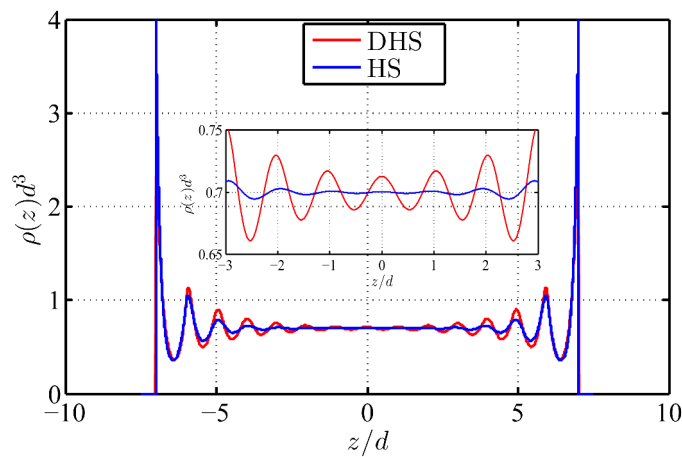


Figure 4.15: Density profile of a DHS fluid in comparison with that of the corresponding HS fluid: $\rho_b d^3 = 0.7$ and $m^* = 2$.

Fig. 4.15 shows dipole-dipole effects on the density profile in comparison with that of a simple HS fluid. The density distribution of the DHS fluid at this high bulk density has an oscillatory profile identical to that of the HS fluid. This reflects the dominant role of hard sphere exclusions. The attractive effects of dipole-dipole interaction reduce significantly the contact density in comparison with a simple HS fluid. In addition dipole correlations lead to a spatial layer organization of the molecules that is why the density profile of the DHS fluid is more oscillatory than that of the corresponding HS fluid. At small interplatelet distances

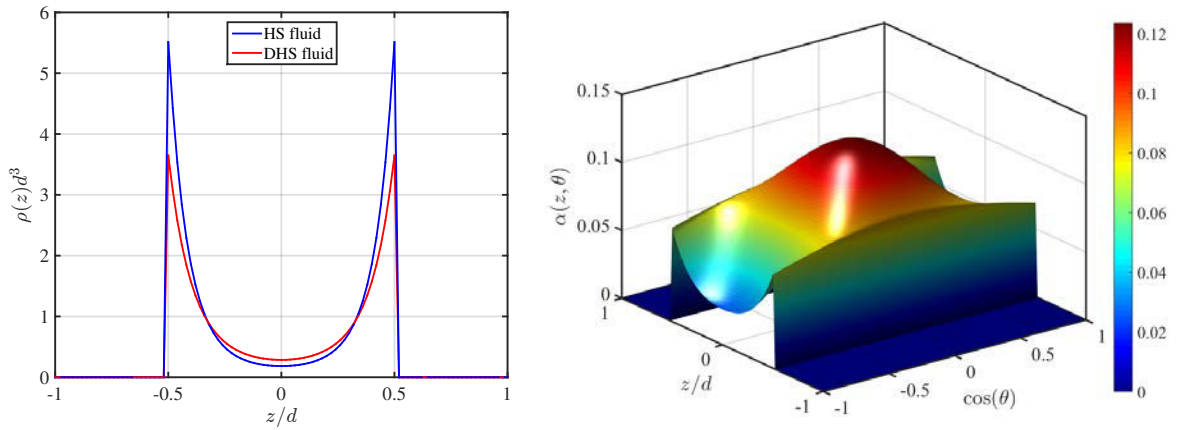
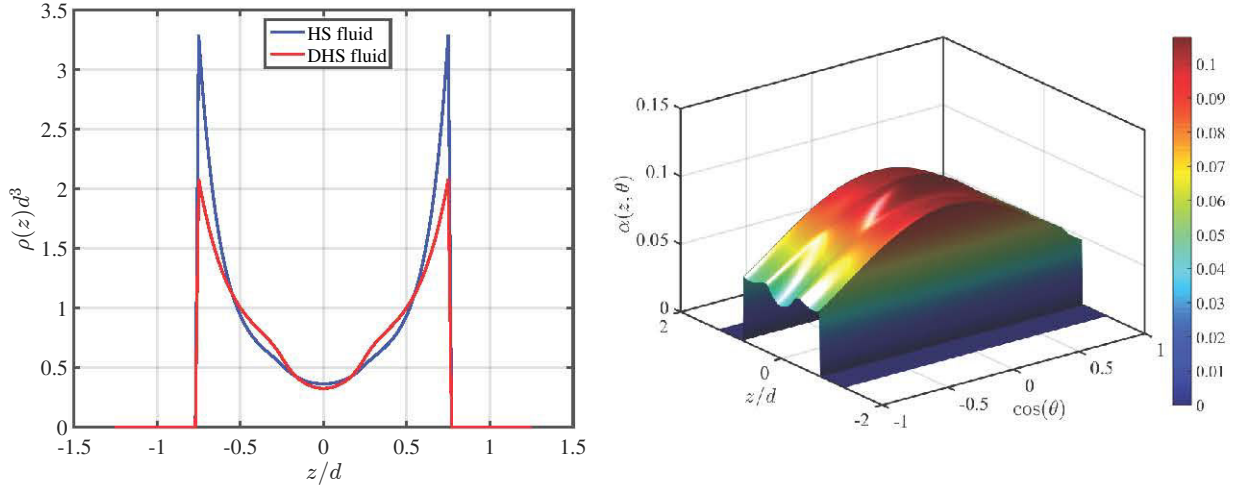
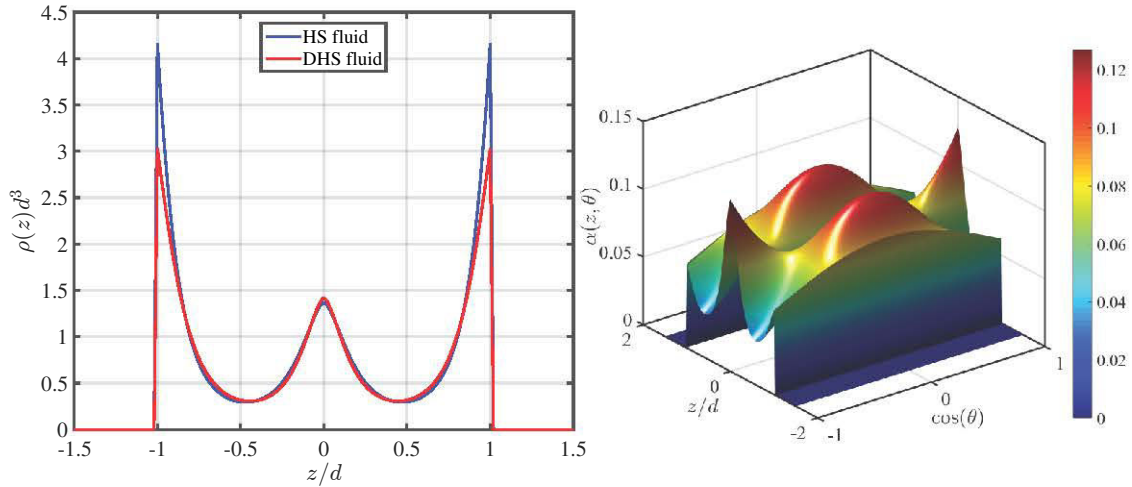


Figure 4.16: Density profiles of HS and DHS fluids ($2H = 2d$, $\rho_b d^3 = 0.7$ and $m^{*2} = 2$). The density profiles are depicted on the left and the dipole orientation distribution is presented on the right.

corresponding to the hydration behavior in the crystalline swelling regime of expansive clays, this model predicts discrete water layers similar to the former case of a HS fluid. If $2H = 2d$ (Fig. 4.16) the water molecules concentrate near the two walls in two layers. The orientation of the dipoles in these two layers is nearly uniform ($\alpha(z/d = \pm 0.5, \theta) = \alpha_0 = 1/(4\pi)$). In the middle of two walls there are very few water molecules with dipole moments orientated almost parallel to the walls. As shown in Fig. 4.17, $2H = 2.5d$ seems to be a transition configuration between the two states $2H = 2d$ and $2H = 3d$. In this case two layers adjacent to the walls can be observed as in the former case of $2H = 2d$, however in the middle between these two layers, some oscillations are observed on the density profile (left plot on Fig. 4.17). This leads to a significant change in the dipole orientation profile (right plot on Fig. 4.17), which differs completely from that of the former case. The dipoles in this case are orientated preferentially parallel to the walls at any spatial position in the interlayer space. If $2H = 3d$ as shown on Fig. 4.18, three layers of the water molecules separated by a distance of about one molecule diameter d can be observed. The dipole orientation of the water molecules in the two layers near the solid surfaces tend to be parallel to the walls. In the center layer, the behavior of the dipoles is completely different as they are orientated preferentially perpendicular to the walls.

Fig. 4.19 presents the disjoining pressure of the DHS fluid calculated with Eq. 4.124 for $\rho_b d^3 = 0.7$ and $m^{*2} = 2$ versus the separation distance between the walls in comparison with that of the corresponding HS fluid. It is obvious that the dipolar attractive forces reduce significantly the repulsive force of the simple HS fluid in the case of high bulk densities and intermediate dipole moment strength, especially at small separation distances. Similarly to the case of the corresponding HS fluid (see chapter 2), the disjoining pressure of a DHS fluid exhibits both repulsive and attractive parts where only the decreasing segments represent stable equilibrium configurations. This allows to explain the formation of discrete layers of the water molecules in the interlayer space in the crystalline swelling regime.

The final task is to find an appropriate dipole moment strength to obtain a reasonable bulk pressure $p_b = 10^5$ Pa as in the case of Lennard-Jones fluids presented in Chapter 3. With


 Figure 4.17: Same configuration as in Fig. 4.16 with $2H = 2.5d$.

 Figure 4.18: Same configuration as in Fig. 4.16 with $2H = 3d$.

the water molecule diameter $d = 2.8 \cdot 10^{-10} \text{m}$, the bulk water density $\rho_b d^3 = 0.7344$ and the temperature $T = 300 \text{K}$, the dipole moment strength m can be calculated from Eq. (4.123) as

$$p_b = k_B T \rho_b \frac{1 + \eta + \eta^2 - \eta^3}{(1 - \eta)^3} - \frac{\rho_b^2 m^2}{3\epsilon_0} K = 10^5. \quad (4.125)$$

The reduced dipole moment strength is found to be $m^{*2} = 4.68$ satisfying the bulk pressure criterion. However, with such a high dipolar moment, no solution can be found for the water density between the two walls. The failure is probably explained by the inaccuracy of the approximation of the radial distribution function of the inhomogeneous fluid by that of the corresponding bulk fluid, especially for high dipole moments [89].

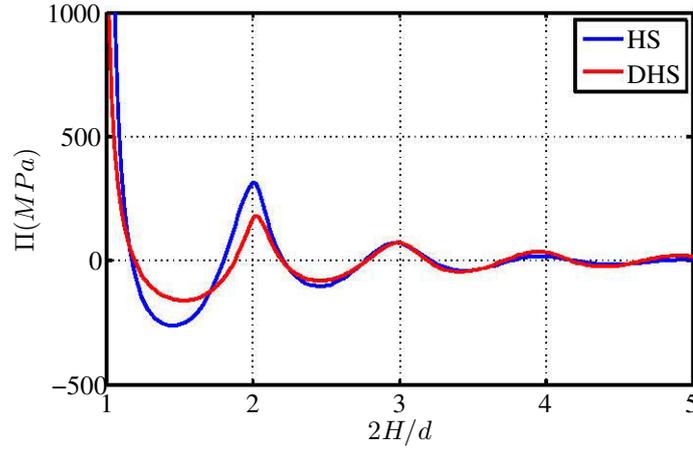


Figure 4.19: Disjoining pressure profile of the DHS fluid in comparison with that of the HS fluid: $\rho_b d^3 = 0.7$ and $m^{*2} = 2$.

4.5 Towards a “civilized” model of the Electrical Double Layer

With the aim of completing the Electric Double Layer (EDL) model, ions are now added to the water solvent. The electrolyte solution is modeled by a dipole-ion mixture. Ions are modeled as hard spheres with the charge concentrated at their center, water molecules are considered as hard spheres carrying a dipole moment at their center. The Van der Waals forces are modeled by dipole-dipole interactions accounting for Keesom forces and Lennard-Jones interactions accounting for Debye and London dispersion forces. Such a model is referred to as a “civilized” model [102].

4.5.1 Interaction potentials

The complexity of this fluid model in comparison with the former models discussed in this thesis stems from the electrical interactions between the fluid molecules. Therefore, we present here a brief summary of the electrical interactions between charges and dipoles.

Electric field and potential created by a charge

Consider a charge q_1 placed at \mathbf{r}_1 . At point \mathbf{r}_2 , it creates a potential $\Phi^{q_1}(\mathbf{r}_2)$ and an electric field $\mathbf{E}^{q_1}(\mathbf{r}_2)$ given by

$$\Phi^{q_1}(\mathbf{r}_2) = \frac{q_1}{4\pi\epsilon_0 r_{12}} \quad \mathbf{E}^{q_1}(\mathbf{r}_2) = -\nabla_{\mathbf{r}_2} \Phi^{q_1}(\mathbf{r}_2) = \frac{q_1}{4\pi\epsilon_0 r_{12}^3} \mathbf{r}_{12}, \quad (4.126)$$

with $\mathbf{r}_{12} = \mathbf{r}_2 - \mathbf{r}_1$ and $r_{12} = |\mathbf{r}_{12}|$.

Electric field and potential created by a dipole

Consider now a dipole \mathbf{m}_1 placed at \mathbf{r}_1 . It creates at point \mathbf{r}_2 a potential $\Phi^{d_1}(\mathbf{r}_2)$ and an electrical field $\mathbf{E}^{d_1}(\mathbf{r}_2)$ given by

$$\Phi^{d_1}(\mathbf{r}_2) = \frac{1}{4\pi\epsilon_0} \frac{\mathbf{m}_1 \cdot \mathbf{r}_{12}}{r_{12}^3} \quad \mathbf{E}^{d_1}(\mathbf{r}_2) = -\nabla_{\mathbf{r}_2} \Phi^{d_1}(\mathbf{r}_2) = \frac{1}{4\pi\epsilon_0} \left(3 \frac{\mathbf{m}_1 \cdot \mathbf{r}_{12}}{r_{12}^5} \mathbf{r}_{12} - \frac{\mathbf{m}_1}{r_{12}^3} \right). \quad (4.127)$$

Intermolecular potential

where ρ_{ib} is the total density of molecules i (irrespective of their orientation for the dipoles) in the bulk, μ_b^{HS} , μ_i^{LJ} and μ_i^{el} are respectively the excess chemical potential of hard spheres in the bulk, the excess chemical potential due to the Lennard-Jones potential and to electrical effects. These two last terms are determined in the next paragraphs.

4.5.2.1 Lennard-Jones term

In the mean field approximation, the excess free energy is given by

$$\mathcal{F}^{LJ}[\{\rho_i\}] = \frac{1}{2} \sum_{ij} \iint d(1)d(2) \rho_i(1) \rho_j(2) u_{ij}^{LJ}(|\mathbf{r}_1 - \mathbf{r}_2|) \Theta_H(r_{12} - d), \quad (4.132)$$

where $\Theta_H(r_{12} - d)$ recalls the hard sphere nature of the reference fluid. The corresponding excess chemical potential is obtained by the functional derivative of the above equation with respect to ρ_i

$$\mu_i^{LJ}(1) = \frac{\delta \mathcal{F}^{LJ}[\{\rho_i\}]}{\delta \rho_i(1)} = \sum_j \int d(2) \rho_j(2) u_{ij}^{LJ}(|\mathbf{r}_1 - \mathbf{r}_2|) \Theta_H(r_{12} - d). \quad (4.133)$$

This relation is applied to the case of a double layer using cylindrical coordinates. Taking advantage the translation invariance in the plane Oxy parallel to the plates, fix the point 1 \mathbf{r}_1 at the spatial position $(0, 0, z_1)$ and the point 2 (\mathbf{r}_2) at the position z_2 separated away from the Oz axis by a distance χ (see Fig. 4.10). This leads to

$$\begin{aligned} \mu_i^{LJ}(z_1) &= \sum_j \int_{-H}^H dz_2 \int_{\chi=0}^{\infty} 2\pi \chi d\chi \rho_j(z_2) u_{ij}^{LJ}(r_{12}) \Theta_H(r_{12} - d) \\ &= \sum_j \int_{-H}^H dz_2 \rho_j(z_2) \int_{\max(d, |z_2 - z_1|)}^{\infty} 2\pi r_{12} dr_{12} u_{ij}^{LJ}(r_{12}) \\ &= \sum_j \int_{-H}^H dz_2 \rho_j(z_2) v_{ij}^{LJ}(|z_2 - z_1|), \end{aligned} \quad (4.134)$$

with

$$v_{ij}^{LJ}(|z_2 - z_1|) = \int_{\max(d, |z_2 - z_1|)}^{\infty} 2\pi r_{12} dr_{12} u_{ij}^{LJ}(r_{12}). \quad (4.135)$$

4.5.2.2 Electrical term

The intrinsic excess free energy due to electrical effects is given by

$$\mathcal{F}^{el}[\{\rho_i\}] = \frac{1}{2} \sum_{ij \in \{d, +, -\}} \iint d(1) d(2) \rho_i(1) \rho_j(2) u_{ij}(1, 2) \Theta_H(r_{12} - d), \quad (4.136)$$

The total electrical excess free energy F^{el} is the sum of the intrinsic free energy \mathcal{F}^{el} and the effect of the charged plates giving rise to the external electrical field \mathbf{E}_{ext} and potential Φ_{ext}

$$F^{el}[\{\rho_i\}] = \mathcal{F}^{el}[\{\rho_i\}] + \sum_{i \in \{d, +, -\}} \int d(1) \rho_i(1) (q_i \Phi_{ext} - \mathbf{m}_i \cdot \mathbf{E}_{ext}), \quad (4.137)$$

where $m_{\pm} = 0$ and $q_d = 0$. The chemical potential is obtained by deriving the preceding expression

$$\mu_i^{el}(1) = \frac{\delta \mathcal{F}^{el}[\{\rho_i\}]}{\delta \rho_i(1)} + q_i \Phi_{ext} - \mathbf{m}_i \cdot \mathbf{E}_{ext}. \quad (4.138)$$

In the case of an EDL, Φ_{ext} is constant and \mathbf{E}_{ext} is null but the general case of different surface charges on the two external plates will be treated here. The electrical intrinsic excess chemical potential of the different species is achieved by deriving functionally the relation (4.136)

$$\begin{aligned} \frac{\delta \mathcal{F}^{el}}{\delta \rho_d(1)} &= \int d(2) \rho_d(2) u_{dd}(1, 2) \Theta_H(r_{12} - d) \\ &+ \sum_{i \in \{+, -\}} \int d\mathbf{r}_2 \rho_i(\mathbf{r}_2) u_{di}(1, 2) \Theta_H(r_{12} - d) \end{aligned} \quad (4.139)$$

$$\begin{aligned} \frac{\delta \mathcal{F}^{el}}{\delta \rho_{\pm}(\mathbf{r}_1)} = \frac{\delta \mathcal{F}^{el}}{\delta \rho_{\pm}(1)} &= \int d(2) \rho_d(2) u_{d\pm}(1, 2) \Theta_H(r_{12} - d) \\ &+ \sum_{i \in \{+, -\}} \int d\mathbf{r}_2 \rho_i(\mathbf{r}_2) u_{i\pm}(1, 2) \Theta_H(r_{12} - d), \end{aligned} \quad (4.140)$$

where $u_{ij}(1, 2)$ is the electrical interaction potential between the charge (or the dipole) i located at the position \mathbf{r}_1 (and with the dipole orientation $\boldsymbol{\omega}_1$ with the charge (or the dipole) j located at the position \mathbf{r}_2 (and with the dipole orientation $\boldsymbol{\omega}_2$. According to relation (4.128) with $i, j \in \{d, +, -\}$

$$\begin{aligned} u_{ij}(1, 2) &= -\mathbf{m}_i \cdot \mathbf{E}^{j2}(\mathbf{r}_1) + q_i \Phi^{j2}(\mathbf{r}_1) \\ &= -\mathbf{m}_j \cdot \mathbf{E}^{i1}(\mathbf{r}_2) + q_j \Phi^{i1}(\mathbf{r}_2). \end{aligned} \quad (4.141)$$

For dipoles, the combination of Eq. (4.139) with (4.141) yields

$$\begin{aligned} \frac{\delta \mathcal{F}^{el}}{\delta \rho_d(1)} &= \int d(2) \rho_d(2) u_{dd}(1, 2) \Theta_H(r_{12} - d) \\ &+ \sum_{i \in \{+, -\}} \int d\mathbf{r}_2 \rho_i(\mathbf{r}_2) u_{di}(1, 2) \Theta_H(r_{12} - d) \\ &= -\mathbf{m}_1 \cdot [\mathbf{E}_{dd}(1) + \mathbf{E}_{dq}(1)], \end{aligned} \quad (4.142)$$

with

$$\mathbf{E}_{dd}(1) = \int d(2) \rho_d(2) \mathbf{E}^{d2}(\mathbf{r}_1) \Theta_H(r_{12} - d), \quad (4.143)$$

$$\mathbf{E}_{dq}(1) = \sum_{i \in \{+, -\}} \int d\mathbf{r}_2 \rho_i(\mathbf{r}_2) \mathbf{E}^{i2}(\mathbf{r}_1) \Theta_H(r_{12} - d) \quad (4.144)$$

where $\mathbf{E}_{dd}(1)$ and $\mathbf{E}_{dq}(1)$ are respectively the electric field at the point \mathbf{r}_1 occupied by the dipole 1 due respectively to the dipoles and the ions in the solution.

For the ions Eq. (4.140) in combination with Eq. (4.141) gives

$$\begin{aligned} \frac{\delta \mathcal{F}^{el}}{\delta \rho_i(\mathbf{r}_1)} &= \int d(2) \rho_d(2) u_{id}(1, 2) \Theta_H(r_{12} - d) + \sum_{j \in \{+, -\}} \int d\mathbf{r}_2 \rho_j(\mathbf{r}_2) u_{ij}(1, 2) \Theta_H(r_{12} - d) \\ &= q_i [\Phi_{dq}(\mathbf{r}_1) + \Phi_{qq}(\mathbf{r}_1)], \end{aligned} \quad (4.145)$$

with

$$\Phi_{dq}(\mathbf{r}_1) = \int d(2) \rho_d(2) \Phi^{d2}(\mathbf{r}_1) \Theta_H(r_{12} - d), \quad (4.146)$$

$$\Phi_{qq}(\mathbf{r}_1) = \sum_{j \in \{+, -\}} \int d\mathbf{r}_2 \rho_j(\mathbf{r}_2) \Phi^{j2}(\mathbf{r}_1) \Theta_H(r_{12} - d). \quad (4.147)$$

where Φ_{dd} and Φ_{dq} are respectively the electric potential due to the dipoles and the ions in the solution.

The above results are now applied to the case of a electrical double layer with $-H < z < H$. The molecular densities are only dependent on z and the electric fields are now parallel to Oz . Taking advantage of translation invariance on the plane Oxy parallel to the plates, fix the point 1 (\mathbf{r}_1) at the spatial position $(0, 0, z_1)$ and the point 2 (\mathbf{r}_2) at the position z_2 separated away from the Oz axis by a distance χ . The vector $\mathbf{r}_{12}/r_{12} \cdot \mathbf{k}$ is $(z_2 - z_1)/r_{12}$ with $\mathbf{k} = (0, 0, 1)$. Averaging over the plane Oxy parallel to the plates, we obtain $\mathbf{m}_1 = m_1 \cos \theta_1 \mathbf{k}$ and $\mathbf{m}_2 = m_2 \cos \theta_2 \mathbf{k}$ with $d\omega_1 = 2\pi \sin \theta_1 d\theta_1$ and $d\omega_2 = 2\pi \sin \theta_2 d\theta_2$. The objective is to compute the field $E_{dd}(z_1)$ given by

$$\mathbf{E}_{dd}(z_1) = \int d\mathbf{r}_2 d\omega_2 \rho_d(\mathbf{r}_2, \omega_2) \frac{1}{4\pi \epsilon_0 r_{12}^3} \left[3 \frac{\mathbf{r}_{12}}{r_{12}} \left(\mathbf{m}_2 \cdot \frac{\mathbf{r}_{12}}{r_{12}} \right) - \mathbf{m}_2 \right] \Theta_H(r_{12} - d). \quad (4.148)$$

In cylindrical coordinates, the above equation can be rewritten as

$$E_{dd}(z_1) = \frac{m}{4\pi \epsilon_0} \int_{\theta_2=0}^{\pi} 2\pi \cos \theta_2 \sin \theta_2 d\theta_2 \int_{z_2=-H}^H dz_2 \rho(z_2, \theta_2) \times \int_{\chi=0}^{\infty} 2\pi \chi d\chi \frac{1}{r_{12}^3} \left[3 \frac{(z_2 - z_1)^2}{r_{12}^2} - 1 \right] \Theta_H(r_{12} - d), \quad (4.149)$$

where $r_{12} = \sqrt{(z_2 - z_1)^2 + \chi^2}$ with z_1 and z_2 being fixed, $2r_{12} dr_{12} = 2\chi d\chi$. It follows

$$\begin{aligned} & \int_{\chi=0}^{\infty} 2\pi \chi d\chi \frac{1}{r_{12}^3} \left[3 \frac{(z_2 - z_1)^2}{r_{12}^2} - 1 \right] \Theta_H(r_{12} - d) = \\ & 2\pi \int_{r_{12}=|z_2-z_1|}^{\infty} dr_{12} \left[3 \frac{(z_2 - z_1)^2}{r_{12}^4} - \frac{1}{r_{12}^2} \right] \Theta_H(r_{12} - d) = \\ & \begin{cases} 2\pi \left[-\frac{(z_2 - z_1)^2}{r_{12}^3} + \frac{1}{r_{12}} \right]_{|z_2-z_1|}^{+\infty} = 0 & \text{if } |z_2 - z_1| > d \\ 2\pi \left[-\frac{(z_2 - z_1)^2}{r_{12}^3} + \frac{1}{r_{12}} \right]_d^{+\infty} = 2\pi \left[\frac{(z_2 - z_1)^2}{d^3} - \frac{1}{d} \right] & \text{if } |z_2 - z_1| < d \end{cases} \quad (4.150) \\ & = 2\pi \left[\frac{(z_2 - z_1)^2}{d^3} - \frac{1}{d} \right] \Theta_H(d - |z_2 - z_1|). \end{aligned}$$

As a result, the electric field $E_{dd}(z_1)$ generated by the dipolar solvent particles reduces to

$$E_{dd}(z_1) = \frac{\pi m}{\epsilon_0} \int_{-H}^H dz_2 \int_0^{\pi} \cos \theta_2 \sin \theta_2 d\theta_2 \rho(z_2, \theta_2) \left[\frac{(z_2 - z_1)^2}{d^3} - \frac{1}{d} \right] \Theta_H(d - |z_2 - z_1|). \quad (4.151)$$

The polarization $P(z_1)$ is oriented along the Oz axis and given by

$$P(z_1) = m \int \cos \theta_1 \rho_d(z_1, \theta_1) d\omega_1 = 2\pi m \int_0^{\pi} d\theta_1 \cos \theta_1 \sin \theta_1 \rho_d(z_1, \theta_1). \quad (4.152)$$

This allows to write the electric field $E_{dd}(z_1)$ in the form

$$E_{dd}(z_1) = \frac{1}{2\epsilon_0} \int_{-H}^H dz_2 P(z_2) \left[\frac{(z_2 - z_1)^2}{d^3} - \frac{1}{d} \right] \Theta_H(d - |z_2 - z_1|). \quad (4.153)$$

The density profiles of the fluid constituents Eq. (4.131) can be now rewritten as

$$\rho_i(z, \theta) = \frac{\rho_{ib}}{4\pi} \exp \left\{ -\beta \left[\mu_i^{\text{HS}}[\rho] - \mu_i^{\text{HS}}(\rho_b) \right] \right\}$$

$$\begin{aligned}
 & + \sum_j \int_{\max(d, |z-z'|)}^{\infty} dz' \rho_j(z') v_{ij}^{\text{LJ}}(|z-z'|) - \mu_{ib}^{\text{LJ}}(\rho_b) + V_i^{\text{LJ} \text{ext}}(z) \\
 & + \left. q_i (\Phi_{qd} + \Phi_{qq} + \Phi_{ext}) - m_i \cos \theta (E_{dd} + E_{dq} + E_{ext}) - \mu_{ib}^{el} \right\}. \quad (4.154)
 \end{aligned}$$

The term $V_i^{\text{LJ} \text{ext}}(z)$ designates a Lennard-Jones-type interaction between the species i and the plates. The electrical contribution to the excess chemical potential of the bulk μ_{ib}^{el} is null for the ions (as the bulk potential is taken as the reference potential, i.e. Φ is the double layer potential) and the dipoles in the mean field approximation (see Eq. C.41 with $\alpha_1 = 0$). The electrical potential acting on the charges $\Phi = \Phi_{qd} + \Phi_{qq} + \Phi_{ext}$ which is the sum of the electrical potential due to the ions Φ_{qd} and the water molecules Φ_{qq} plus the external charges Φ_{ext} is classically identified as the macroscopic potential Φ solution of the Poisson equation (see §4.5.3). The electric field $E_{loc} = E_{dd} + E_{dq} + E_{ext}$ is the local field seen by the dipoles¹. It is the sum of the electric field $E_0 = E_{ext} + E_{dq}$ due to the external field and the charges in the solution. Therefore $E_{loc} = E_0 + E_{dd}$. The equation for the dipoles is then written as

$$\begin{aligned}
 \rho_d(z, \theta) = \rho_d(z) \alpha_d(z, \theta) = \frac{\rho_{db}}{4\pi} \exp \left\{ -\beta \left[\mu_d^{\text{HS}}[\rho] - \mu_d^{\text{HS}}(\rho_b) \right. \right. \\
 \left. \left. + \mu_d^{\text{LJ}}(z) - \mu_{db}^{\text{LJ}} + V_d^{\text{LJ} \text{ext}}(z) - m \cos \theta E_{loc} \right] \right\}. \quad (4.155)
 \end{aligned}$$

Using Eq. (4.116), integration of the above equation over the solid angle leads to

$$\begin{aligned}
 \rho_d(z) = 2\pi \int_0^\pi \rho_d(z, \theta) \sin \theta d\theta = \rho_d^b \exp \left\{ -\beta \left[\mu^{\text{HS}}[\rho] - \mu_b^{\text{HS}}(\rho_b) + \mu_d^{\text{LJ}}(z) - \mu_{db}^{\text{LJ}} + V_d^{\text{LJ} \text{ext}}(z) \right] \right\} \\
 \times \frac{\sinh[\beta m E_{loc}(z)]}{\beta m E_{loc}(z)}. \quad (4.156)
 \end{aligned}$$

The angular prefactor $\alpha(z, \theta)$ for the dipolar solvent obtained by dividing Eq. (4.155) by Eq. (4.156) leading to

$$\alpha(z, \theta) = \frac{1}{4\pi} \frac{\beta m E_{loc}(z)}{\sinh[\beta m E_{loc}(z)]} \exp[\beta m E_{loc}(z) \cos \theta], \quad (4.157)$$

where $\alpha(z, \theta)$ can be developed in terms of Legendre polynomials according to Eq. (4.90). Remember that $\alpha_0 = 1/4\pi$ and

$$\alpha_1(z) = \frac{3}{2} \int_{-1}^{+1} \alpha(z, \theta) P_1(\cos \theta) d \cos \theta = \frac{3}{2} \int_{-1}^{+1} \alpha(z, \theta) \cos \theta d \cos \theta. \quad (4.158)$$

Noting that

$$\int_{-1}^1 \exp(\beta m E x) x dx = \frac{2}{\beta m E} \left[\cosh(\beta m E) - \frac{\sinh(\beta m E)}{\beta m E} \right], \quad (4.159)$$

$\alpha_1(z)$ is given by

$$\alpha_1(z) = \frac{3}{4\pi} \left[\coth(\beta m E_{loc}(z)) - \frac{1}{\beta m E_{loc}(z)} \right]. \quad (4.160)$$

¹It should be noted that $\mathbf{E}^{d2}(\mathbf{r}_1) = -\nabla_{\mathbf{r}_1} \Phi^{d2}(\mathbf{r}_1)$ (see Eq. (4.143) and (4.146)), $\mathbf{E}^{\pm 2}(\mathbf{r}_1) = -\nabla_{\mathbf{r}_1} \Phi^{\pm 2}(\mathbf{r}_1)$ (see Eq. (4.144) and (4.147)) and $\mathbf{E}^{ext}(\mathbf{r}_1) = -\nabla_{\mathbf{r}_1} \Phi^{ext}(\mathbf{r}_1)$. But the operator $\nabla_{\mathbf{r}_1}$ does not commute with the integral sign as the densities ρ_i are discontinuous on the sphere $r_{12} = d$.

If the argument of the cotangent function is smaller than 1,

$$\coth x \simeq \frac{1}{x - x^3/3 + \mathcal{O}(x^5)} = \frac{1}{x} \left(1 + x^2/3 + \mathcal{O}(x^4)\right) = \frac{1}{x} + \frac{x}{3} + \mathcal{O}(x^3) \quad (4.161)$$

and therefore

$$\alpha_1(z) \simeq \frac{1}{4\pi} \beta m E_{loc}(z). \quad (4.162)$$

For ions, it comes

$$\rho_{\pm}(z) = \rho_{\pm}^b \exp \left\{ -\beta \left[\mu^{\text{HS}}[\rho] - \mu_{\pm}^{\text{HS}}(\rho_b) + \mu_{\pm}^{\text{LJ}}(z) - \mu_{\pm b}^{\text{LJ}} + V_{\pm}^{\text{LJ}}(z) + q_{\pm} \Phi(z) \right] \right\}. \quad (4.163)$$

If hard sphere and Lennard-Jones effects are neglected, the classical distribution is recovered as expected in the mean field approximation. The last step is to determine the local electric field $E_{loc}(z)$ and the electric potential $\Phi(z)$.

4.5.3 Poisson equation

The Poisson equation is written for a mixture of dipoles and ions in vacuum confined between two parallel plates placed at $z = \pm H$ and charged with a surface density Σ

$$\epsilon_0 \frac{d^2 \Phi}{dz^2} = - \sum_{i \in \{+, -\}} \rho_i q_i + \int d\omega m \cos \theta \frac{d\rho_d(z, \theta)}{dz} \quad (4.164)$$

$$= -Q_c(z) + \frac{dP}{dz}, \quad (4.165)$$

with $Q_c(z) = q_+ \rho_+(z) + q_- \rho_-(z)$ the local volume charge density and $P(z)$ the local density of polarization defined by the following relation

$$P(z) = \int_0^{\pi} m \cos \theta \rho_d(z, \theta) 2\pi \sin \theta d\theta = \frac{4\pi}{3} m \rho_d(z) \alpha_1(z), \quad (4.166)$$

where $\alpha_1(z)$ is solution of Eq. (4.160) ($\alpha_1 \simeq \beta m E_{loc}/(4\pi)$ as a first estimate given by Eq. (4.162)).

The limit conditions are written as

$$\begin{aligned} z = -H \quad -\epsilon_0 \frac{d\Phi(z)}{dz} &= \epsilon_0 E = \Sigma - P(z), \\ z = +H \quad -\epsilon_0 \frac{d\Phi(z)}{dz} &= \epsilon_0 E = -\Sigma - P(z). \end{aligned} \quad (4.167)$$

Considering the symmetry of the problem we can also use the condition that at $z = 0$, $E = -\epsilon_0 d\Phi/dz = 0$. It should be noted that the polarization is odd ($P(-z) = -P(z)$).

Performing a first integration for $0 \leq z \leq H$ we obtain (by symmetry $P(z=0) = 0$)

$$\epsilon_0 \frac{d\Phi}{dz} = - \int_0^z Q_c(z') dz' + P(z), \quad (4.168)$$

$$\text{or } E(z) = \underbrace{\frac{1}{\epsilon_0} \int_0^z Q_c(z') dz'}_{\text{field due to charges } E_0} - \underbrace{\frac{P(z)}{\epsilon_0}}_{\text{field due to dipoles}}. \quad (4.169)$$

A second integration provides

$$\Phi(z) = \Phi(0) + \frac{1}{\epsilon_0} \left[- \int_0^z dz' \int_0^{z'} Q_c(z'') dz'' + \int_0^z P(z) dz \right]$$

$$\begin{aligned}
 &= \Phi(0) + \frac{1}{\epsilon_0} \left\{ \left[-z' \int_0^{z'} Q_c(z'') dz'' \right]_{z'=0}^{z'=z} + \int_0^z z' Q_c(z') dz' + \int_0^z P(z) dz \right\} \\
 &= \Phi(0) + \frac{1}{\epsilon_0} \left[\int_0^z (z' - z) Q_c(z') dz' + \int_0^z P(z) dz \right].
 \end{aligned} \tag{4.170}$$

The local field E_{loc} can now be calculated starting from Eq. (4.103)

$$\begin{aligned}
 E(z) &= E_0(z) - \frac{P(z)}{\epsilon_0} \\
 E_{loc}(z) &= E_0(z) + E_{dd}(z) \\
 E_{loc}(z) &= E(z) + \frac{P(z)}{\epsilon_0} + E_{dd}(z).
 \end{aligned} \tag{4.171}$$

where $E_{dd}(z)$ is given by (see (4.153))

$$E_{dd}(z) = \frac{1}{2\epsilon_0} \int_{-H}^H dz' P(z') \left[\frac{(z' - z)^2}{d^3} - \frac{1}{d} \right] \Theta_H(d - |z' - z|). \tag{4.172}$$

If the polarization $P(z')$ is nearly uniform within $z - d < z' < z + d$, the above relation reduces to

$$E_{dd}(z) = \frac{P(z)}{2\epsilon_0} \int_{z-d}^{z+d} dz' \left[\frac{(z' - z)^2}{d^3} - \frac{1}{d} \right] = -\frac{2P(z)}{3\epsilon_0}, \tag{4.173}$$

and it follows

$$E_{loc}(z) = E(z) + \frac{P(z)}{3\epsilon_0}. \tag{4.174}$$

This relation is the well known Lorentz relation introduced in many classical textbooks [104].

The electric potential Φ is known to within an arbitrary constant which can be determined from the global electroneutrality condition of the system (plates + ionic fluid).

4.5.4 Results and discussions

In this section, we study a mixture of a dipolar solvent with a monovalent entirely dissociate salt confined between two identical negatively charged walls in order to predict qualitatively the behavior of the electrolyte solution in the crystalline swelling regime. The following parameters are chosen for the calculation: separation distance $2H = 4d$, dipole bulk density $\rho_d^b d^3 = 0.734$, water particle diameter $d = 2.8\text{\AA}$, reduced dipole moment $m^{*2} = 0.02$, electric surface charge density $\Sigma = -0.0135 \text{ C/m}^2$ and bulk ion concentration $c_b = 10^{-3} \text{ mol/L}$.

Fig. 4.20 presents the density distributions of ions. As the walls are negatively charged, the cations are strongly attracted by the walls, whereas the anions are excluded. Obviously, the density profiles of the two fluid components have the similar oscillatory behavior as that of a hard sphere fluid near a hard wall. This differs from the density profiles predicted in the case of a continuous solvent EDL model in which ion concentrations decrease or increase monotonously away from the plates. This difference originates from the finite size effects of the solvent particle which are stronger than electrical effects. The observation is also pronounced on the dipole density distribution (Fig. 4.21) which is almost coincided with that of the corresponding hard sphere fluid.

Fig. 4.22 shows the evolution of the different electric fields as well as the polarization in the EDL space. Due to the symmetry of the system, the polarization vanishes at the midplane and increases strongly close to the plates where the electric potential is high. However, the dipole-dipole electrical field E_{dd} , which is the average of the polarization over a distance of

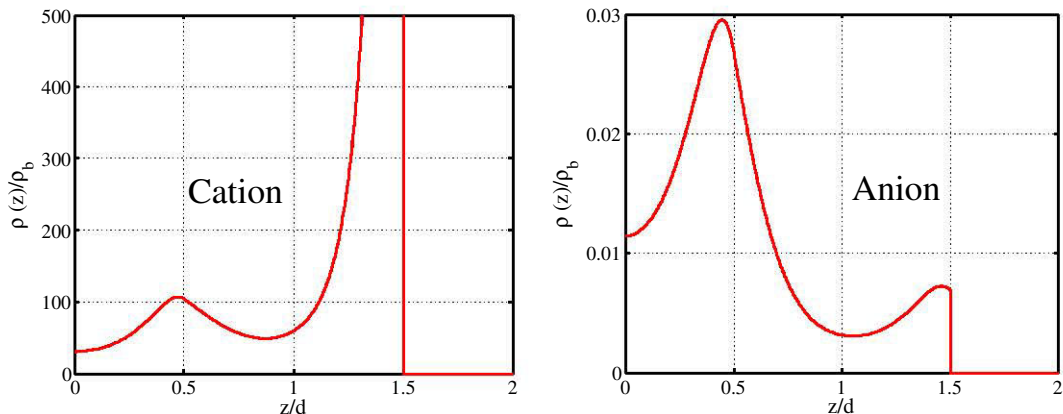


Figure 4.20: Density profiles of ions in the EDL space with $2H = 4d$, $\rho_d^b d^3 = 0.734$, $d = 2.8 \text{ \AA}$, $m^{*2} = 0.02$, $\Sigma = -0.0135 \text{ C/m}^2$ and $c_b = 10^{-3} \text{ mol/L}$.

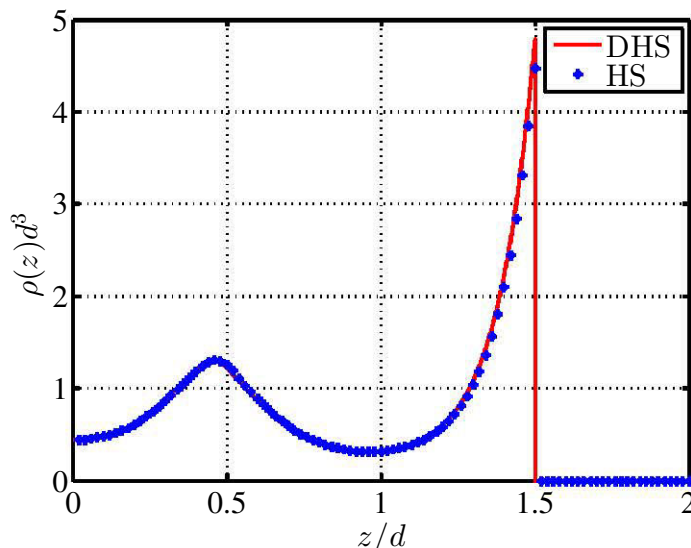


Figure 4.21: As in Fig. 4.20 for the dipole density profile and that of the corresponding hard sphere fluid.

a particle diameter, is almost uniform and negligible. Therefore the three electric fields E_0 , E_{loc} , $E(z)$ are almost identical in the center zone. In the vicinity of the plates, because of a strong increase of the polarization, the macroscopic electrical field $E(z)$ decreases significantly in comparison with the local field E_{loc} and the field due to charges E_0 . The decrease of the macroscopic electrical field would become very important when increasing slightly the dipole moment. This makes the macroscopic field E decreasing significantly near the plates. The “inverse” behavior of the macroscopic field when approaching the plates when increasing the dipole moment is absolutely impossible in the EDL space. This observation confirms the crucial role of correlation effects which are completely neglected in the present MFA approach.

4.6 Conclusion

This chapter accounts explicitly for the molecular and polar nature of the water solvent in an EDL using a dipolar hard sphere fluid. For studying such a fluid, first the MSA proposed by Wertheim [21] is presented in the case of a homogeneous fluid. The radial distribution function of a bulk DHS fluid calculated with MSA is then incorporated into the DFPT ap-

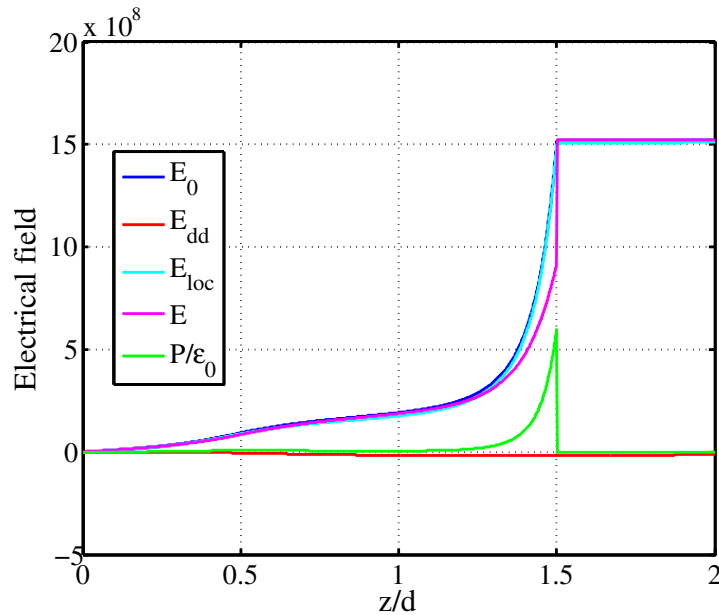


Figure 4.22: The evolution of the different electric fields in the EDL space.

proach presented in chapter 3 in order to represent the dipole-dipole correlation effects of the corresponding inhomogeneous fluid.

The numerical results show that the dipole-dipole interactions favor a spatial layer organization of the fluid molecules and reduce effectively the contact density of the fluid confined between two hard walls in comparison with the corresponding HS fluid. At small interplatelet distances corresponding to the crystalline swelling regime, the formation of fluid molecule layers is observed. The dipole orientation in the two layers immediately adjacent to the walls is nearly uniform as in the bulk limit whereas the dipole moments in the next layers prefer to be perpendicular to the walls while a few dipole moments located between two successive layers are almost parallel to the walls.

Dipole-dipole attractive interaction effects reduce significantly the disjoining pressure in comparison with that of the corresponding HS fluid. The oscillatory form for the disjoining pressure of a DHS fluid contributes effectively to explain the formation of discrete layers of water molecules in the low hydration regime. With a high water bulk density $\rho_b d^3 = 0.734$, a high value of dipole moment $m^*2 = 4.68$ is required to simulate reasonably the bulk water behavior. Such a high dipole moment leads to the inaccuracy of the MSA in approximation to describe the dipole-dipole correlation effects in an inhomogeneous DHS fluid, which is at the origin of the failure of the present approach.

Ions are finally added into the DHS water solvent as well as a negative surface charge of the platelets to complete the EDL description. The numerical results obtained by the present MFA approach shows an oscillatory form for the ions density profiles, which are very different from that predicted by a classical continuous solvent model. This is probably explained by the dominant role of hard sphere effects in comparison with electrical interaction effects. However, neglecting interparticle correlations in the framework of MFA makes inaccurate the prediction of the behavior of the EDL fluid especially in the cases of intermediate and high dipole moment values. Therefore, an exact calculation of the interparticle correlations within the electrolyte solution is necessary.

Appendix C

C.1 Legendre polynomials

- Definition

The Legendre polynomials are defined for any natural number n by:

$$\frac{d}{dx} \left[(1-x^2) \frac{dP_n(x)}{dx} \right] + n(n+1)P_n(x) = 0, \quad P_n(1) = 1 \quad (\text{C.1})$$

- First ten Legendre polynomials

$$\begin{aligned} P_0(x) &= 1 \\ P_1(x) &= x \\ P_2(x) &= \frac{1}{2}(3x^2 - 1) \\ P_3(x) &= \frac{1}{2}(5x^3 - 3x) \\ P_4(x) &= \frac{1}{8}(35x^4 - 30x^2 + 3) \\ P_5(x) &= \frac{1}{8}(63x^5 - 70x^3 + 15x) \\ P_6(x) &= \frac{1}{16}(231x^6 - 315x^4 + 105x^2 - 5) \\ P_7(x) &= \frac{1}{16}(429x^7 - 693x^5 + 315x^3 - 35x) \\ P_8(x) &= \frac{1}{128}(6435x^8 - 12012x^6 + 6930x^4 - 1260x^2 + 35) \\ P_9(x) &= \frac{1}{128}(12155x^9 - 25740x^7 + 18018x^5 - 4620x^3 + 315x) \\ P_{10}(x) &= \frac{1}{256}(46189x^{10} - 109395x^8 + 90090x^6 - 30030x^4 + 3465x^2 - 63) \end{aligned}$$

- Properties

$P_n(x)$ is an n th-degree polynomial. The polynomials for odd-values of n are odd and for even-values of n are even: $P_n(-x) = (-1)^n P_n(x)$.

- Scalar product

On the range $[-1, 1]$ Legendre polynomials are orthogonal with respect to the scalar product:

$$\langle P, Q \rangle = \int_{-1}^1 P(x) Q(x) dx \quad (\text{C.2})$$

$$\langle P_m, P_n \rangle = \int_{-1}^1 P_m(x) P_n(x) dx = 0 \quad \text{pour } m \neq n \quad (\text{C.3})$$

$$\|P_n\|^2 = \langle P_n, P_n \rangle = \frac{2}{2n+1} \quad (\text{C.4})$$

C.2 Calculation details in modeling dipolar hard sphere fluids

C.2.1 In the homogeneous bulk fluid

C.2.1.1 Calculation of the chemical potential from the excess free energy

The expression of the excess free energy due to dipole-dipole interactions per unit volume in a homogeneous DHS fluid given by Eq. (4.93) is rewritten below

$$\begin{aligned} \widehat{\mathcal{F}}_{dd}^{ex} &= -\frac{\rho_b^2 m^2}{8\pi\epsilon_0} \int_0^\pi \alpha(\theta_1) \sin \theta_1 d\theta_1 \int_0^{2\pi} d\phi_1 \int_{-\infty}^\infty dz \int_0^{2\pi} d\phi \int_0^\infty \chi d\chi \int_0^\pi \sin \theta_2 d\theta_2 \\ &\times \int_0^{2\pi} d\phi_2 \alpha(\theta_2) [1 + h_S(r_{12}) + h_\Delta(r_{12})\Delta(1,2) + h_D(r_{12})D(1,2)] \frac{D(1,2)}{r_{12}^3}. \end{aligned} \quad (\text{C.5})$$

Changing the integral variables, $r_{12} = r = \sqrt{z^2 + \chi^2}$, $\cos \theta = \frac{z}{r}$ and with z being fixed, $\chi d\chi = r dr$, it follows

$$\begin{aligned} \widehat{\mathcal{F}}_{dd}^{ex} &= -\frac{\rho_b^2 m^2}{8\pi\epsilon_0} \int_0^\pi \alpha(\theta_1) \sin \theta_1 d\theta_1 \int_0^{2\pi} d\phi_1 \int_{-\infty}^\infty dz \int_0^{2\pi} d\phi \int_{|z|}^\infty dr \int_0^\pi \sin \theta_2 d\theta_2 \\ &\times \int_0^{2\pi} d\phi_2 \alpha(\theta_2) [1 + h_S(r) + h_\Delta(r)\Delta(1,2) + h_D(r)D(1,2)] \frac{D(1,2)}{r^2}. \end{aligned} \quad (\text{C.6})$$

C.2.1.1.1 Calculation of the isotropic term in $D(1,2)$

The first two terms of Eq. (C.6) in $D(1,2)$ are

$$\begin{aligned} \widehat{\mathcal{F}}_{dd}^{ex}|_S &= -\frac{\rho_b^2 m^2}{8\pi\epsilon_0} \int_0^\pi \alpha(\theta_1) \sin \theta_1 d\theta_1 \int_0^{2\pi} d\phi_1 \int_{-\infty}^\infty dz \int_0^{2\pi} d\phi \int_{|z|}^\infty dr \int_0^\pi \sin \theta_2 d\theta_2 \\ &\times \int_0^{2\pi} d\phi_2 \alpha(\theta_2) [1 + h_S(r)] \frac{D(1,2)}{r^2} \end{aligned} \quad (\text{C.7})$$

The integration in ϕ , ϕ_1 and ϕ_2 is made using formal calculus and using the parity of the integral in z :

$$\begin{aligned} \widehat{\mathcal{F}}_{dd}^{ex}|_S &= -\frac{\rho_b^2 m^2}{4\pi\epsilon_0} \int_0^\pi \alpha(\theta_1) \sin \theta_1 d\theta_1 \int_0^\infty dz \int_{|z|}^\infty dr \int_0^\pi \alpha(\theta_2) \sin \theta_2 d\theta_2 \\ &\times 8\pi^3 \cos \theta_1 \cos \theta_2 (3 \cos^2 \theta - 1) \frac{[1 + h_S(r)]}{r^2}. \end{aligned} \quad (\text{C.8})$$

As $\cos \theta = \frac{z}{r}$ the following sub-integrals can be defined

$$\begin{aligned} I_{g_S} &= \int_0^\infty dz \int_{|z|}^\infty dr \left(3 \frac{z^2}{r^4} - \frac{1}{r^2} \right) (1 + h_S(r)) \\ I_{h_S} &= \int_0^\infty dz \int_{|z|}^\infty dr \left(3 \frac{z^2}{r^4} - \frac{1}{r^2} \right) h_S(r). \end{aligned} \quad (\text{C.9})$$

As

$$\int_0^\infty dz \int_z^\infty dr \left(3 \frac{z^2}{r^4} - \frac{1}{r^2} \right) = \int_0^\infty dz \left[\frac{1}{r} - \frac{z^2}{r^3} \right]_{r=z}^\infty = 0, \quad (\text{C.10})$$

$I_{g_S} = I_{h_S}$. The isotropic total correlation function $h_S(r)$ satisfies the following conditions: $h_S(r) = -1$ for $r < d$; the function is discontinuous at $r = d$ and tends to 0 at large values of r . I_{h_S} can thus be decomposed as

$$I_{h_S} = \underbrace{\int_0^d dz \int_z^d dr \left(-3\frac{z^2}{r^4} + \frac{1}{r^2} \right)}_A + \underbrace{\int_0^d dz \int_d^\infty dr \left(3\frac{z^2}{r^4} - \frac{1}{r^2} \right) h_S(r)}_B + \underbrace{\int_d^\infty dz \int_z^\infty dr \left(3\frac{z^2}{r^4} - \frac{1}{r^2} \right) h_S(r)}_C. \quad (\text{C.11})$$

The integration of the terms A and B follows directly

$$A = \int_0^d dz \int_z^d dr \left(-3\frac{z^2}{r^4} + \frac{1}{r^2} \right) = \int_0^d dz \left[\frac{z^2}{r^3} - \frac{1}{r} \right]_{r=z}^d = \int_0^d dz \left(\frac{z^2}{d^3} - \frac{1}{d} \right) = -\frac{2}{3}. \quad (\text{C.12})$$

$$B = \int_0^d dz \int_d^\infty dr \left(3\frac{z^2}{r^4} - \frac{1}{r^2} \right) h_S(r) = \int_d^\infty dr h_S(r) \left[\frac{z^3}{r^4} - \frac{z}{r^2} \right]_{z=0}^d = \int_d^\infty dr h_S(r) \left[\frac{d^3}{r^4} - \frac{d}{r^2} \right]. \quad (\text{C.13})$$

For C , an integration by parts is used with

$$\begin{cases} du = dz & \rightarrow u = z, \\ v(z) = \int_z^\infty dr \left(3\frac{z^2}{r^4} - \frac{1}{r^2} \right) h_S(r) & \rightarrow \frac{dv}{dz} = -\frac{2h_S(z)}{z^2} + 6z \int_z^\infty \frac{h_S(r)}{r^4} dr. \end{cases} \quad (\text{C.14})$$

It comes

$$C = \int_d^\infty dz \int_z^\infty dr \left(3\frac{z^2}{r^4} - \frac{1}{r^2} \right) h_S(r) = \left[z \int_z^\infty dr \left(3\frac{z^2}{r^4} - \frac{1}{r^2} \right) h_S(r) \right]_{z=d}^{z=\infty} + 2 \int_d^\infty \frac{h_S(r)}{r} dr - 6 \int_d^\infty z^2 dz \int_z^\infty \frac{h_S(r)}{r^4} dr, \quad (\text{C.15})$$

where the last term on the right hand side is

$$\begin{aligned} \int_d^\infty z^2 dz \int_z^\infty \frac{h_S(r)}{r^4} dr &= \left[\frac{z^3}{3} \int_z^\infty \frac{h_S(r)}{r^4} dr \right]_{z=d}^\infty + \int_d^\infty \frac{z^3}{3} \frac{h_S(z)}{z^4} dz \\ &= -\frac{d^3}{3} \int_d^\infty \frac{h_S(r)}{r^4} dr + \frac{1}{3} \int_d^\infty \frac{h_S(r)}{r} dr. \end{aligned} \quad (\text{C.16})$$

Hence, C reduces to

$$C = \int_d^\infty dr h_S(r) \left(\frac{d}{r^2} - \frac{d^3}{r^4} \right). \quad (\text{C.17})$$

Finally, the sub-integrals of Eq. (C.8) reduce to

$$I_{g_S} = I_{h_S} = A + B + C = -\frac{2}{3}. \quad (\text{C.18})$$

Substituting this result into Eq. (C.8), the isotropic part of the dipole-dipole excess free energy is rewritten as

$$\widehat{\mathcal{F}}_{dd}^{ex} \Big|_S = \frac{4\pi^2 \rho_b^2 m^2}{3\epsilon_0} \int_0^\pi \alpha(\theta_1) \cos \theta_1 \sin \theta_1 d\theta_1 \int_0^\pi \alpha(\theta_2) \cos \theta_2 \sin \theta_2 d\theta_2. \quad (\text{C.19})$$

With

$$\int_0^\pi \alpha(\theta) \cos \theta \sin \theta d\theta = \int_{-1}^1 \alpha(\theta) \cos \theta d(\cos \theta) = \frac{2}{3} \alpha_1, \quad (\text{C.20})$$

it comes finally

$$\boxed{\widehat{\mathcal{F}}_{dd}^{ex} \Big|_S = \frac{16\pi^2 \rho_b^2 m^2}{27\epsilon_0} \alpha_1^2}, \quad (\text{C.21})$$

which is the excess free energy contribution due to the dipole-dipole interactions obtained in the mean field approximation [102].

C.2.1.1.2 Calculation of the term in $\Delta(1,2)D(1,2)$

The second term of Eq. (C.6) in $\Delta(1,2)D(1,2)$ given by

$$\begin{aligned} \widehat{\mathcal{F}}_{dd}^{ex} \Big|_\Delta &= -\frac{\rho_b^2 m^2}{8\pi\epsilon_0} \int_0^\pi \alpha(\theta_1) \sin \theta_1 d\theta_1 \int_0^{2\pi} d\phi_1 \int_{-\infty}^\infty dz \int_0^{2\pi} d\phi \int_{|z|}^\infty dr \int_0^\pi \sin \theta_2 d\theta_2 \\ &\times \int_0^{2\pi} d\phi_2 \alpha(\theta_2) h_\Delta(r) \frac{\Delta(1,2)D(1,2)}{r^2} \\ &= -\frac{\rho_b^2 m^2}{4\pi\epsilon_0} \int_0^\pi \alpha(\theta_1) \sin \theta_1 d\theta_1 \int_0^\infty dz \int_z^\infty dr \int_0^\pi \alpha(\theta_2) \sin \theta_2 d\theta_2 \\ &\times h_\Delta(r) 2\pi^3 \frac{(3 \cos^2 \theta - 1)}{r^2} [\cos^2 \theta_1 + \cos^2 \theta_2 + 3 \cos^2 \theta_1 \cos^2 \theta_2 - 1], \quad (\text{C.22}) \end{aligned}$$

is solved in the same manner. Knowing that h_Δ vanishes for $r < d$, is discontinuous at $r = d$ and tends towards 0 for large values of r , we define the sub-integral

$$\begin{aligned} I_{h_\Delta} &= \int_0^\infty dz \int_z^\infty dr \left(3 \frac{z^2}{r^4} - \frac{1}{r^2} \right) h_\Delta(r) \\ &= \underbrace{\int_0^d dz \int_d^\infty dr \left(3 \frac{z^2}{r^4} - \frac{1}{r^2} \right) h_\Delta(r)}_A + \underbrace{\int_d^\infty dz \int_z^\infty dr \left(3 \frac{z^2}{r^4} - \frac{1}{r^2} \right) h_\Delta(r)}_B. \quad (\text{C.23}) \end{aligned}$$

The first integral term becomes

$$\begin{aligned} A &= \int_d^\infty h_\Delta(r) dr \int_0^d dz \left(3 \frac{z^2}{r^4} - \frac{1}{r^2} \right) = \int_d^\infty dr h_\Delta(r) \left[\frac{z^3}{r^4} - \frac{z}{r^2} \right]_{z=0}^d \\ &= \int_d^\infty dr h_\Delta(r) \left(\frac{d^3}{r^4} - \frac{d}{r^2} \right). \quad (\text{C.24}) \end{aligned}$$

The expression of B is analogous to Eq. (C.15) substituting h_S by h_Δ . Its solution is given by the relation (C.17) which corresponds to $-A$. It follows directly

$$\boxed{I_{h_\Delta} = 0 \longrightarrow \widehat{\mathcal{F}}_{dd}^{ex} \Big|_\Delta = 0} \quad (\text{C.25})$$

C.2.1.1.3 Calculation of the term in $D^2(1,2)$

The term in $D^2(1,2)$ of Eq. (C.6) is

$$\widehat{\mathcal{F}}_{dd}^{ex} \Big|_D = -\frac{\rho_b^2 m^2}{8\pi\epsilon_0} \int_0^\pi \alpha(\theta_1) \sin \theta_1 d\theta_1 \int_0^{2\pi} d\phi_1 \int_{-\infty}^\infty dz \int_0^{2\pi} d\phi \int_0^\infty \chi d\chi \int_0^\pi \alpha(\theta_2) \sin \theta_2 d\theta_2$$

$$\times \int_0^{2\pi} d\phi_2 h_D(r) \frac{D^2(1,2)}{r^3}. \quad (\text{C.26})$$

Changing the integral variables as $(z, \chi) \rightarrow (r, \theta)$, the Jacobian of the transformation is given by

$$\chi d\chi dz = r^2 dr \sin \theta d\theta, \quad (\text{C.27})$$

where θ varies from 0 to π and r from 0 to $+\infty$. It follows

$$\begin{aligned} \widehat{\mathcal{F}}_{dd}^{ex} \Big|_D &= -\frac{\rho_b^2 m^2}{8\pi\epsilon_0} \int_0^\pi \alpha(\theta_1) \sin \theta_1 d\theta_1 \int_0^{2\pi} d\phi_1 \int_0^\pi \alpha(\theta_2) \sin \theta_2 d\theta_2 \int_0^{2\pi} d\phi_2 \\ &\times \int_0^\pi \sin \theta d\theta \int_0^{2\pi} d\phi \int_0^\infty dr h_D(r) \frac{D^2(1,2)}{r} \\ &= -\frac{\rho_b^2 m^2}{8\pi\epsilon_0} \int_0^\pi \alpha(\theta_1) \sin \theta_1 d\theta_1 \int_0^\pi \alpha(\theta_2) \sin \theta_2 d\theta_2 \\ &\times \left[-\frac{8\pi^3}{5} (\cos^2 \theta_1 + \cos^2 \theta_2 - 3 \cos \theta_1 \cos \theta_2 - 7) \right] \int_0^\infty dr \frac{h_D(r)}{r}, \quad (\text{C.28}) \end{aligned}$$

where $\int_0^\infty dr \frac{h_D(r)}{r} = K$ according to Eq. (4.38). The dipole orientation distribution function, $\alpha(\theta)$, is decomposed in terms of the Legendre polynomial series as

$$\int_0^\pi \alpha(\theta_1) \sin \theta_1 d\theta_1 = \int_{-1}^1 \alpha(\theta_1) d(\cos \theta_1) = 2\alpha_0, \quad (\text{C.29})$$

$$\begin{aligned} \int_0^\pi \alpha(\theta_1) \cos^2 \theta_1 \sin \theta_1 d\theta_1 &= \int_{-1}^1 \alpha(\theta_1) \cos^2 \theta_1 d(\cos \theta_1) \\ &= \int_{-1}^1 \alpha(\theta_1) \frac{2P_2(\cos \theta_1) + P_0(\cos \theta_1)}{3} = \frac{2}{3}\alpha_0 + \frac{4}{15}\alpha_2. \quad (\text{C.30}) \end{aligned}$$

Hence, Eq. (C.28) reduces to

$$\widehat{\mathcal{F}}_{dd}^{ex} \Big|_D = \frac{\pi^2 \rho_b^2 m^2 K}{5\epsilon_0} \left(-\frac{80}{3}\alpha_0^2 - \frac{16}{75}\alpha_2^2 \right). \quad (\text{C.31})$$

In conclusion, the dipole-dipole excess free energy is

$$\widehat{\mathcal{F}}_{dd}^{ex} = \widehat{\mathcal{F}}_{dd}^{ex} \Big|_S + \widehat{\mathcal{F}}_{dd}^{ex} \Big|_\Delta + \widehat{\mathcal{F}}_{dd}^{ex} \Big|_D = \frac{16\pi^2 \rho_b^2 m^2}{3\epsilon_0} \left(-K\alpha_0^2 + \frac{\alpha_1^2}{9} - \frac{K}{125}\alpha_2^2 \right), \quad (\text{C.32})$$

where $\alpha_0 = 1/(4\pi)$. The first term in α_0^2 exists in the bulk without any externally applied field. The second term in α_1 is obtained in the MFA approach [102]. Consequently, the average excess chemical potential due to the dipole-dipole interaction is obtained by differentiating the preceding relation with respect to ρ_b

$$\mu_{dd}^{ex} = \frac{\partial \widehat{\mathcal{F}}_{dd}^{ex}}{\partial \rho_b} = \frac{32\pi^2 \rho_b m^2}{3\epsilon_0} \left(-K\alpha_0^2 + \frac{\alpha_1^2}{9} - \frac{K}{125}\alpha_2^2 \right). \quad (\text{C.33})$$

C.2.1.2 Direct calculation of the dipole-dipole excess chemical potential

The computation of the orientation-dependent dipole-dipole excess chemical potential starts from Eq. (4.97) rewritten below:

$$\mu_{dd}^{ex}(\theta_1) = -\frac{\rho_b m^2}{4\pi\epsilon_0} \int_{-H}^H dz \int_0^{2\pi} d\phi \int_0^\infty \chi d\chi \int_0^\pi \sin \theta_2 \alpha(\theta_2) d\theta_2 \int_0^{2\pi} d\phi_2 \frac{D(1,2)}{r^3}$$

$$\begin{aligned}
& \times [1 + h_S(r) + \Delta(1,2)h_\Delta(r) + D(1,2)h_D(r)] \\
& = -\frac{\rho_b m^2}{4\pi\epsilon_0} \int_{-H}^H dz \int_0^{2\pi} d\phi \int_{|z|}^\infty dr \int_0^\pi \sin\theta_2 \alpha(\theta_2) d\theta_2 \int_0^{2\pi} d\phi_2 \frac{D(1,2)}{r^2} \\
& \times [1 + h_S(r) + \Delta(1,2)h_\Delta(r) + D(1,2)h_D(r)] , \tag{C.34}
\end{aligned}$$

where the integral variables have been changed according to $(z, \chi) \rightarrow (z, r)$. First the integration is made over ϕ and ϕ_2 . As the result should be independent of ϕ_1 , an averaging over ϕ_1 as $\frac{1}{2\pi} \int_0^{2\pi} (\dots) d\phi_1$ is added to the above integral expression, which yields

$$\frac{1}{2\pi} \int_0^{2\pi} d\phi_1 \int_0^{2\pi} d\phi_2 \int_0^{2\pi} d\phi D(1,2) = 2\pi(3\cos^2\theta - 1) \cos\theta_1 \cos\theta_2, \tag{C.35}$$

$$\begin{aligned}
& \frac{1}{2\pi} \int_0^{2\pi} d\phi_1 \int_0^{2\pi} d\phi_2 \int_0^{2\pi} d\phi \Delta(1,2)D(1,2) = \frac{\pi}{2}(3\cos^2\theta - 1) \\
& \times (3\cos^2\theta_1 \cos^2\theta_2 + \cos^2\theta_1 + \cos^2\theta_2 - 1), \tag{C.36}
\end{aligned}$$

$$\begin{aligned}
& \frac{1}{2\pi} \int_0^{2\pi} d\phi_1 \int_0^{2\pi} d\phi_2 \int_0^{2\pi} d\phi D^2(1,2) = -\frac{\pi}{2} \left(5\cos^2\theta_1 + 5\cos^2\theta_2 + 12\cos^2\theta - 9\cos^4\theta - 5 \right. \\
& \left. - 9\cos^2\theta_1 \cos^2\theta_2 - 30\cos^2\theta_1 \cos^2\theta - 30\cos^2\theta_2 \cos^2\theta + 27\cos^2\theta_1 \cos^4\theta \right. \\
& \left. + 27\cos^2\theta_2 \cos^4\theta + 72\cos^2\theta_1 \cos^2\theta_2 \cos^2\theta - 81\cos^2\theta_1 \cos^2\theta_2 \cos^4\theta \right) \tag{C.37}
\end{aligned}$$

with $\cos\theta = \frac{z}{r}$, $H = \infty$ and $\rho(z) = \rho_b$, in the bulk DHS fluid. The calculation of Eq. (C.34) is analogous to that presented in section §C.2.1.1.

C.2.1.2.1 Calculation of the isotropic term

The two first isotropic terms of Eq. (C.34) are

$$\begin{aligned}
\mu_{dd}^{ex}|_S & = -\frac{2\pi\rho_b m^2}{\epsilon_0} \int_0^\infty dz \int_z^\infty dr \int_0^\pi \sin\theta_2 \alpha(\theta_2) d\theta_2 \frac{(3\cos^2\theta - 1) \cos\theta_1 \cos\theta_2}{r^2} g_S(r) \\
& = -\frac{2\pi\rho_b m^2}{\epsilon_0} \cos\theta_1 \int_0^\infty dz \int_z^\infty \left(3\frac{z^2}{r^4} - \frac{1}{r^2} \right) g_S(r) dr \int_0^\pi \sin\theta_2 \cos\theta_2 \alpha(\theta_2) d\theta_2, \tag{C.38}
\end{aligned}$$

which can be simplified by introducing

$$I_{g_S} = \int_0^\infty dz \int_z^\infty \left(3\frac{z^2}{r^4} - \frac{1}{r^2} \right) g_S(r) dr = -\frac{2}{3}, \tag{C.39}$$

$$J_S = \int_0^\pi \sin\theta_2 \cos\theta_2 \alpha(\theta_2) d\theta_2 = \frac{2}{3}\alpha_1. \tag{C.40}$$

$\mu_{dd}^{ex}|_S$ reduces then to

$$\boxed{\mu_{dd}^{ex}|_S = \frac{8\pi\rho_b m^2 \alpha_1}{9\epsilon_0} \cos\theta_1.} \tag{C.41}$$

C.2.1.2.2 Calculation of the term in $\Delta(1,2)D(1,2)$

The second term of Eq. (C.34) in $\Delta(1,2)D(1,2)$ is

$$\begin{aligned}
\mu_{dd}^{ex}|_\Delta & = -\frac{\pi\rho_b m^2}{2\epsilon_0} \int_0^\infty dz \int_0^\pi \sin\theta_2 \alpha(\theta_2) (3\cos^2\theta_1 \cos^2\theta_2 + \cos^2\theta_1 + \cos^2\theta_2 - 1) \\
& \times \int_z^\infty dr \frac{(3\cos^2\theta - 1)}{r^2} h_\Delta(r) = -\frac{\pi\rho_b m^2}{2\epsilon_0} I_{h_\Delta} J_{h_\Delta}, \tag{C.42}
\end{aligned}$$

where the sub-integrals are given by

$$I_{h_\Delta} = \int_0^\infty dz \int_z^\infty dr \left(\frac{3z^2}{r^4} - \frac{1}{r^2} \right) h_\Delta(r), \quad (\text{C.43})$$

$$\begin{aligned} J_{h_\Delta} &= \int_0^\pi \sin \theta_2 \alpha(\theta_2) (3 \cos^2 \theta_1 \cos^2 \theta_2 + \cos^2 \theta_1 + \cos^2 \theta_2 - 1) \\ &= \int_{-1}^1 2\alpha(\theta_2) \left[\left(\cos^2 \theta_1 + \frac{1}{3} \right) P_2(\cos \theta_2) + \left(\cos^2 \theta_1 - \frac{1}{3} \right) P_0(\cos \theta_2) \right] d(\cos \theta_2), \end{aligned} \quad (\text{C.44})$$

with $P_0(x) = 1$ and $P_2(x) = (3x^2 - 1)/2$. Note that $\|P_n\|^2 = 2/(2n + 1)$ and $\alpha_0 = 1/(4\pi)$, it comes

$$J_{h_\Delta} = \frac{4}{5} \alpha_2 \left(\cos^2 \theta_1 + \frac{1}{3} \right) + \frac{1}{\pi} \left(\cos^2 \theta_1 - \frac{1}{3} \right). \quad (\text{C.45})$$

Finally, with the relation Eq. (C.25), we obtain

$$\boxed{\mu_{dd}^{ex}|_\Delta = 0.} \quad (\text{C.46})$$

C.2.1.2.3 Calculation of the term in $D^2(1, 2)$

This term of Eq. (C.34) is given by

$$\mu_{dd}^{ex}|_D = -\frac{\rho_b m^2}{4\pi\epsilon_0} \int_{-\infty}^\infty dz \int_0^{2\pi} d\phi \int_0^\infty \chi d\chi \int_0^\pi \sin \theta_2 \alpha(\theta_2) d\theta_2 \int_0^{2\pi} \frac{D^2(1, 2)}{r^3} h_D(r). \quad (\text{C.47})$$

As before, after the integral variables change $(z, \chi) \rightarrow (r, \theta)$, it follows

$$\begin{aligned} \mu_{dd}^{ex}|_D &= -\frac{\rho_b m^2}{4\pi\epsilon_0} \int_0^\infty dr \int_0^\pi \sin \theta d\theta \int_0^{2\pi} d\phi \int_0^\pi \sin \theta_2 \alpha(\theta_2) d\theta_2 \int_0^{2\pi} \frac{D^2(1, 2)}{r} h_D(r) \\ &= -\frac{\pi \rho_b m^2}{5\epsilon_0} \int_{-1}^1 (3 \cos^2 \theta_1 \cos^2 \theta_2 - \cos^2 \theta_1 - \cos^2 \theta_2 + 7) \alpha(\theta_2) d(\cos \theta_2) \\ &\times \int_0^\infty \frac{h_D(r)}{r} dr. \end{aligned} \quad (\text{C.48})$$

Using the development of MSA for the DHS fluid with $K = \int_0^\infty h_D(r)/r dr$ and the decomposition of α in term of Legendre polynomial series

$$\begin{aligned} &\int_{-1}^1 (3 \cos^2 \theta_1 \cos^2 \theta_2 - \cos^2 \theta_1 - \cos^2 \theta_2 + 7) \alpha(\theta_2) d(\cos \theta_2) \\ &= \int_{-1}^1 \left[\cos^2 \theta_1 (3 \cos^2 \theta_2 - 1) - \frac{1}{3} (3 \cos^2 \theta_2 - 1) + \frac{20}{3} \right] \alpha(\theta_2) d(\cos \theta_2) \\ &= \int_{-1}^1 \left[\frac{2}{3} (3 \cos^2 \theta_1 - 1) P_2(\cos \theta_2) + \frac{20}{3} \right] \alpha(\theta_2) d(\cos \theta_2) \\ &= \frac{40}{3} \alpha_0 + \frac{4}{15} \alpha_2 (3 \cos^2 \theta_1 - 1), \end{aligned} \quad (\text{C.49})$$

leads to

$$\boxed{\mu_{dd}^{ex}|_D(\theta_1) = -\frac{\pi \rho_b m^2}{5\epsilon_0} K \left[\frac{40}{3} \alpha_0 + \frac{4}{15} \alpha_2 (3 \cos^2 \theta_1 - 1) \right].} \quad (\text{C.50})$$

Summing the contributions (C.41), (C.46) and (C.50), the dipole-dipole excess chemical potential is given by the following expression

$$\mu_{dd}^{ex}(\theta_1) = \mu_{dd}^{ex}|_S + \mu_{dd}^{ex}|_\Delta + \mu_{dd}^{ex}|_D$$

$$\begin{aligned}
&= \frac{8\pi\rho_b m^2 \alpha_1}{9\epsilon_0} \cos\theta_1 - \frac{\pi\rho_b m^2}{5\epsilon_0} K \left[\frac{40}{3}\alpha_0 + \frac{4}{15}\alpha_2 (3\cos^2\theta_1 - 1) \right] \\
&= \frac{\pi\rho_b m^2}{\epsilon_0} \left[-\frac{8}{3}K\alpha_0 + \frac{8}{9}\alpha_1 \cos\theta_1 - \frac{4}{75}K\alpha_2 (3\cos^2\theta_1 - 1) \right]. \quad (C.51)
\end{aligned}$$

The mean bulk chemical potential given by Eq. (C.33) is recovered by an integration over θ_1 (see Eq. (4.99)).

C.2.2 Dipole-dipole excess chemical potential of an inhomogeneous DHS fluid

The excess chemical potential due to dipole-dipole interactions of an inhomogeneous DHS fluid is given by Eq. (4.95)

$$\begin{aligned}
\mu_{dd}^{ex}(1) &= -\frac{m^2}{4\pi\epsilon_0} \int_{-H}^H dz_2 \rho(z_2) \int_0^{2\pi} d\phi \int_0^\infty \chi d\chi \int_0^\pi \alpha(z_2, \theta_2) \sin\theta_2 d\theta_2 \\
&\times \int_0^{2\pi} d\phi_2 [1 + h_S(r) + h_\Delta(r)\Delta(1, 2) + h_D(r)D(1, 2)] \frac{D(1, 2)}{r^3}. \quad (C.52)
\end{aligned}$$

C.2.2.1 Calculation of the term in $D(1, 2)$

The first two terms of Eq. (C.52) are rewritten by changing the integral variables as $r = \sqrt{(z_1 - z_2)^2 + \chi^2}$, $\cos\theta = \frac{|z_1 - z_2|}{r}$ and $\chi d\chi = r dr$

$$\begin{aligned}
\mu_{dd}^{ex}(1)|_S &= -\frac{m^2}{4\pi\epsilon_0} \int_{-H}^H dz_2 \rho(z_2) \int_0^{2\pi} d\phi \int_0^\infty \chi d\chi \int_0^\pi \alpha(z_2, \theta_2) \sin\theta_2 d\theta_2 \\
&\times \int_0^{2\pi} d\phi_2 [1 + h_S(r)] \frac{D(1, 2)}{r^3} \\
&= -\frac{m^2}{4\pi\epsilon_0} \int_{-H}^H dz_2 \rho(z_2) \int_0^{2\pi} d\phi \int_{|z_1 - z_2|}^\infty dr \int_0^\pi \alpha(z_2, \theta_2) \sin\theta_2 d\theta_2 \\
&\times \int_0^{2\pi} d\phi_2 g_S(r) \frac{D(1, 2)}{r^2}. \quad (C.53)
\end{aligned}$$

Since the final result is independent of ϕ_1 , it can be averaged over ϕ_1

$$\frac{1}{2\pi} \int_0^{2\pi} d\phi_1 \int_0^{2\pi} d\phi_2 \int_0^{2\pi} d\phi D(1, 2) = 4\pi^2 (3\cos^2\theta - 1) \cos\theta_1 \cos\theta_2. \quad (C.54)$$

Hence, it comes

$$\begin{aligned}
\mu_{dd}^{ex}(1)|_S &= -\frac{\pi m^2}{\epsilon_0} \int_{-H}^H dz_2 \rho(z_2) \int_0^\infty dr \int_0^\pi \alpha(z_2, \theta_2) \sin\theta_2 d\theta_2 \frac{(3\cos^2\theta - 1) \cos\theta_1 \cos\theta_2}{r^2} g_S(r) \\
&= -\frac{\pi m^2}{\epsilon_0} \cos\theta_1 \int_{-H}^H \rho(z_2) dz_2 \int_0^\pi \alpha(z_2, \theta_2) \sin\theta_2 \cos\theta_2 d\theta_2 \\
&\times \int_{|z_1 - z_2|}^\infty dr \left[3\frac{(z_1 - z_2)^2}{r^4} - \frac{1}{r^2} \right] g_S(r) \\
&= -\frac{2\pi m^2}{3\epsilon_0} \cos\theta_1 \int_{-H}^H \rho(z_2) \alpha_1(z_2) dz_2 \int_{|z_1 - z_2|}^\infty dr \left[3\frac{(z_1 - z_2)^2}{r^4} - \frac{1}{r^2} \right] g_S(r) \\
&= -\frac{2\pi m^2}{3\epsilon_0} \cos\theta_1 \int_{-\infty}^\infty \rho(z_2) \alpha_1(z_2) dz_2 \int_{|z_1 - z_2|}^\infty dr \left[3\frac{(z_1 - z_2)^2}{r^4} - \frac{1}{r^2} \right] g_S(r) \\
&= -\frac{2\pi m^2}{3\epsilon_0} \cos\theta_1 [(\rho\alpha_1) \otimes I_{h_S}](z_1), \quad (C.55)
\end{aligned}$$

where

$$I_{g_S}(z) = I_{h_S}(z) = \int_{|z|}^{\infty} \left(\frac{3z^2}{r^4} - \frac{1}{r^2} \right) g_S(r) dr = \int_{|z|}^{\infty} \left(\frac{3z^2}{r^4} - \frac{1}{r^2} \right) h_S(r) dr . \quad (\text{C.56})$$

C.2.2.2 Calculation of the term in $D(1,2)\Delta(1,2)$

The second term of Eq. (C.52) (in $D(1,2)\Delta(1,2)$) is

$$\begin{aligned} \mu_{dd}^{ex}(1)|_{\Delta} = & -\frac{m^2}{4\pi\epsilon_0} \int_{-H}^H dz_2 \rho(z_2) \int_0^{2\pi} d\phi \int_0^{\infty} dr \int_0^{\pi} \alpha(z_2, \theta_2) \sin \theta_2 d\theta_2 \\ & \times \int_0^{2\pi} d\phi_2 h_{\Delta}(r) \frac{\Delta(1,2)D(1,2)}{r^2} . \end{aligned} \quad (\text{C.57})$$

When averaging over ϕ_1

$$\begin{aligned} \frac{1}{2\pi} \int_0^{2\pi} d\phi_1 \int_0^{2\pi} d\phi_2 \int_0^{2\pi} d\phi \Delta(1,2)D(1,2) = & \pi^2(3 \cos^2 \theta - 1) \\ & \times (3 \cos^2 \theta_1 \cos^2 \theta_2 + \cos^2 \theta_1 + \cos^2 \theta_2 - 1) , \end{aligned} \quad (\text{C.58})$$

Eq. (C.57) becomes

$$\begin{aligned} \mu_{dd}^{ex}(1)|_{\Delta} = & -\frac{\pi m^2}{4\epsilon_0} \int_{-H}^H dz_2 \rho(z_2) \int_0^{\infty} dr \int_0^{\pi} \alpha(z_2, \theta_2) \sin \theta_2 (3 \cos^2 \theta_1 \cos^2 \theta_2 + \cos^2 \theta_1 \\ & + \cos^2 \theta_2 - 1) d\theta_2 h_{\Delta}(r) \frac{3 \cos^2 \theta - 1}{r^2} = -\frac{\pi m^2}{4\epsilon_0} [J_{h_{\Delta}} \otimes I_{h_{\Delta}}](z_1) , \end{aligned} \quad (\text{C.59})$$

with

$$\begin{aligned} I_{h_{\Delta}}(z_1 - z_2) &= \int_{|z_1 - z_2|}^{\infty} dr \left(3 \frac{(z_1 - z_2)^2}{r^4} - \frac{1}{r^2} \right) h_{\Delta}(r) \quad (\text{C.60}) \\ J_{h_{\Delta}}(z_2) &= \rho(z_2) \int_0^{\pi} \alpha(z_2, \theta_2) \sin \theta_2 (3 \cos^2 \theta_1 \cos^2 \theta_2 + \cos^2 \theta_1 + \cos^2 \theta_2 - 1) d\theta_2 \\ &= \rho(z_2) \left\{ \int_{-1}^1 2\alpha(z_2, \theta_2) \left[\left(\cos^2 \theta_1 + \frac{1}{3} \right) P_2(\cos \theta_2) \right. \right. \\ &\quad \left. \left. + \left(\cos^2 \theta_1 - \frac{1}{3} \right) P_0(\cos \theta_2) \right] d(\cos \theta_2) \right\} , \end{aligned} \quad (\text{C.61})$$

where $P_0(x) = 1$ and $P_2(x) = (3x^2 - 1)/2$ are the Legendre polynomials of order 0 and 2. With $\|P_n\|^2 = 2/(2n + 1)$ and $\alpha_0 = 1/(4\pi)$, the preceding integral expression reduces to

$$J_{h_{\Delta}}(z_2) = \rho(z_2) \left[\frac{4}{5} \alpha_2(z_2) \left(\cos^2 \theta_1 + \frac{1}{3} \right) + \frac{1}{\pi} \left(\cos^2 \theta_1 - \frac{1}{3} \right) \right] . \quad (\text{C.62})$$

C.2.2.3 Calculation of the term in $D^2(1,2)$

The last term of Eq. (C.52) is given by

$$\begin{aligned} \mu_{dd}^{ex}(1)|_D = & -\frac{m^2}{4\pi\epsilon_0} \int_{-H}^H dz_2 \rho(z_2) \int_0^{2\pi} d\phi \int_0^{\infty} \chi d\chi \int_0^{\pi} \alpha(z_2, \theta_2) \sin \theta_2 d\theta_2 \\ & \times \int_0^{2\pi} d\phi_2 \frac{h_D(r)}{r^3} D^2(1,2) . \end{aligned} \quad (\text{C.63})$$

Firstly, the integration over the solid angles gives

$$\frac{1}{2\pi} \int_0^{2\pi} d\phi_1 \int_0^{2\pi} d\phi_2 \int_0^{2\pi} d\phi D^2(1,2) = \pi^2(9 \cos^4 \theta - 5 \cos^2 \theta_1 - 5 \cos^2 \theta_2 - 12 \cos^2 \theta + 5)$$

$$\begin{aligned}
& +9 \cos^2 \theta_1 \cos^2 \theta_2 + 30 \cos^2 \theta \cos^2 \theta_1 + 30 \cos^2 \theta \cos^2 \theta_2 - 27 \cos^4 \theta \cos^2 \theta_1 - 27 \cos^4 \theta \cos^2 \theta_2 \\
& -72 \cos^2 \theta_1 \cos^2 \theta_2 \cos^2 \theta + 81 \cos^2 \theta_1 \cos^2 \theta_2 \cos^4 \theta) \\
& = \pi^2 \left[-\frac{5}{3} (3 \cos^2 \theta_2 - 1) + \frac{10}{3} + 3 \cos^2 \theta_1 (3 \cos^2 \theta_2 - 1) - 2 \cos^2 \theta_1 + 10 \cos^2 \theta (3 \cos^2 \theta_2 - 1) \right. \\
& \quad \left. - 2 \cos^2 \theta - 9 \cos^4 \theta (3 \cos^2 \theta_2 - 1) - 24 \cos^2 \theta_1 \cos^2 \theta (3 \cos^2 \theta_2 - 1) \right. \\
& \quad \left. + 6 \cos^2 \theta \cos^2 \theta_1 + 27 \cos^2 \theta_1 \cos^4 \theta (3 \cos^2 \theta_2 - 1) \right] \\
& = \pi^2 \left[2P_2(\cos \theta_2) \left(-\frac{5}{3} + 3 \cos^2 \theta_1 + 10 \cos^2 \theta - 9 \cos^4 \theta - 24 \cos^2 \theta_1 \cos^2 \theta + 27 \cos^2 \theta_1 \cos^4 \theta \right) \right. \\
& \quad \left. + \left(\frac{10}{3} - 2 \cos^2 \theta_1 - 2 \cos^2 \theta + 6 \cos^2 \theta \cos^2 \theta_1 \right) P_0(\cos \theta_2) \right]. \tag{C.64}
\end{aligned}$$

Consequently,

$$\begin{aligned}
& \frac{1}{2\pi} \int_0^{2\pi} d\phi_1 \int_0^{2\pi} d\phi_2 \int_0^{2\pi} d\phi D^2(1, 2) \int_0^\pi \alpha(z_2, \theta_2) \sin \theta_2 d\theta_2 \\
& = \pi^2 \left[\frac{4}{5} \alpha_2(z_2) \left(-\frac{5}{3} + 3 \cos^2 \theta_1 + 10 \cos^2 \theta - 9 \cos^4 \theta - 24 \cos^2 \theta_1 \cos^2 \theta + 27 \cos^2 \theta_1 \cos^4 \theta \right) \right. \\
& \quad \left. + 2\alpha_0 \left(\frac{10}{3} - 2 \cos^2 \theta_1 - 2 \cos^2 \theta + 6 \cos^2 \theta \cos^2 \theta_1 \right) \right] \\
& = 4\pi^2 \left[\left(-\frac{1}{3} \alpha_2(z_2) + \frac{3}{5} \cos^2 \theta_1 \alpha_2(z_2) + \frac{5}{3} \alpha_0 - \cos^2 \theta_1 \alpha_0 \right) \right. \\
& \quad \left. + \cos^2 \theta \left(2\alpha_2(z_2) - \frac{24}{5} \alpha_2(z_2) \cos^2 \theta_1 - \alpha_0 + 3\alpha_0 \cos^2 \theta_1 \right) \right. \\
& \quad \left. + \cos^4 \theta \left(-\frac{9}{5} \alpha_2(z_2) + \frac{27}{5} \cos^2 \theta_1 \alpha_2(z) \right) \right]. \tag{C.65}
\end{aligned}$$

The next step is to calculate the following integrals

$$I_{h_D}^{(0)}(z_1 - z_2) = \int_0^\infty \chi d\chi \frac{h_D(r)}{r^3} = \int_{|z_1 - z_2|}^\infty \frac{h_D(r)}{r^2} dr, \tag{C.66}$$

$$I_{h_D}^{(2)}(z_1 - z_2) = \int_0^\infty \chi d\chi \cos^2 \theta \frac{h_D(r)}{r^3} = (z_1 - z_2)^2 \int_{|z_1 - z_2|}^\infty \frac{h_D(r)}{r^4} dr, \tag{C.67}$$

$$I_{h_D}^{(4)}(z_1 - z_2) = \int_0^\infty \chi d\chi \cos^4 \theta \frac{h_D(r)}{r^3} = (z_1 - z_2)^4 \int_{|z_1 - z_2|}^\infty \frac{h_D(r)}{r^6} dr. \tag{C.68}$$

Finally, the expression of $\mu_{dd}^{ex}(1)|_D$ reduces to

$$\begin{aligned}
\mu_{dd}^{ex}(1)|_D & = -\frac{m^2 \pi}{\epsilon_0} \int_{-\infty}^\infty dz_2 \rho(z_2) \left\{ \alpha_2(z_2) \left[\left(-\frac{1}{3} + \frac{3}{5} \cos^2 \theta_1 \right) I_{h_D}^{(0)} + \left(2 - \frac{24}{5} \cos^2 \theta_1 \right) I_{h_D}^{(2)} \right. \right. \\
& \quad \left. \left. + \left(-\frac{9}{5} + \frac{27}{5} \cos^2 \theta_1 \right) I_{h_D}^{(4)} \right] + \left(\frac{5}{3} \alpha_0 - \alpha_0 \cos^2 \theta_1 \right) I_{h_D}^{(0)} + \left(-\alpha_0 + 3\alpha_0 \cos^2 \theta_1 \right) I_{h_D}^{(2)} \right\}. \tag{C.69}
\end{aligned}$$

Alternatively $\mu_{dd}^{ex}(1)|_D$ can be put in form of convolution integrals

$$\mu^{dd}|_D(z_1, \theta_1) = -\frac{m^2}{4\epsilon_0} \left[\rho \otimes I_{h_D}^\rho + \rho \alpha_2 \otimes I_{h_D}^{\rho\alpha} \right] \tag{C.70}$$

with

$$I_{h_D}^\rho(z) = \int_{|z|}^\infty dr \left[\frac{5}{3} - \frac{z^2}{r^2} + \cos^2 \theta_1 \left(\frac{3z^2}{r^2} - 1 \right) \right] \frac{h_D(r)}{r^2} \tag{C.71}$$

$$I_{h_D}^{\rho\alpha}(z) = -\pi \int_{|z|}^{\infty} dr \left[\frac{4}{3} - 8 \frac{z^2}{r^2} + \frac{36}{5} \frac{z^4}{r^4} + \cos^2 \theta_1 \left(-\frac{12}{5} + \frac{96}{5} \frac{z^2}{r^2} - \frac{108}{5} \frac{z^4}{r^4} \right) \right] \frac{h_D(r)}{r^2}. \quad (\text{C.72})$$

Finally the excess chemical potential due to dipole-dipole interactions is given by

$$\mu_{dd}^{ex}(1) = \mu_{dd}^{ex}(1)|_S + \mu_{dd}^{ex}(1)|_{\Delta} + \mu_{dd}^{ex}(1)|_D. \quad (\text{C.73})$$

C.3 Clausius-Mossotti formula

The Clausius-Mossotti formula for a bulk dipolar hard sphere fluid submitted to an electric field only driven by charges E_0 is easily derived starting from the exact relation Eq. (4.105)

$$\epsilon = \frac{E_0}{E_0 - \frac{P}{\epsilon_0}} = \frac{E_0}{E_0 - \frac{4\pi}{3\epsilon_0} \rho_b m \alpha_1}. \quad (\text{C.74})$$

In the mean field approximation and at low electric field strength, Eq. (4.160) reduces to

$$\alpha_1 \simeq \frac{\beta m E_{loc}}{4\pi}, \quad (\text{C.75})$$

where the local electric field acting on a dipole E_{loc} is given in the bulk case by the classical Lorentz relation (Eq. (4.174))

$$E_{loc} = E + \frac{P}{3\epsilon_0}, \quad (\text{C.76})$$

with $E = E_0 - P/\epsilon_0$ being the macroscopic electric field (driven by both charges and dipoles). Therefore

$$\begin{aligned} E_{loc} = E_0 - \frac{2P}{3\epsilon_0} &= E_0 - \frac{8\pi}{9\epsilon_0} \rho_b m \alpha_1 \\ &= E_0 - \frac{2\beta \rho_b m^2}{9\epsilon_0} E_{loc}. \end{aligned} \quad (\text{C.77})$$

The relative dielectric constant is then deduced from Eq. (C.74)

$$\epsilon = \frac{E_0}{E_0 - \frac{\beta \rho_b m^2}{3\epsilon_0} E_{loc}} = \frac{1 + 2y}{1 - y} \quad \text{with} \quad y = \frac{\beta \rho_b m^2}{9\epsilon_0}. \quad (\text{C.78})$$

Chapter 5

Modeling the hydro-mechanical behavior of unsaturated swelling clays

5.1 Introduction

After the detailed study of the nanoscale description of swelling clays presented in the previous chapters, this chapter is devoted to an application example to model the hydro-mechanical behavior during hydration at the observable macroscale starting from a description of the coupled physico-electrochemical phenomena at the nanoscopic clay platelet scale. The idea is to apply the three scale extension of Terzaghi's effective stress principle to unsaturated expansive clays that was rigorously derived by our group using micro-mechanical analyses [22] to numerically simulate macroscopic swelling pressure tests during hydration at fixed volume. This numerical application gave rise to an oral presentation at the "E-UNSAT2016" conference in Paris joint to a publication in the corresponding conference proceedings [34] which is essentially recovered in this chapter.

The numerical application refers to an experimental swelling pressure test of Imbert and Villar performed at the CIEMAT [11] on 50/50wt%¹ mixtures of pellets and powder of "FoCa" bentonite compacted at a dry density of 1.45 g/cm³. This reference experiment (called *MGR7* in [11]) has been performed with the pellets "RESEAL II" (initial water content 5%) and the powder "FoCa7" whose initial water content is 12%.

Fig.5.1 shows a schematic representation of the cylindrical oedometer cell (inner diameter 10 cm and height 5 cm) used for the hydration tests. The water infiltration is performed through the ceramic porous disc at the bottom by a deionized water column of 1m in height. The ceramic disc at the top being also porous so that the air inside the sample is at thermodynamic equilibrium with the surrounding air. The experiment consists in measuring the pressure that has to be applied on the upper disc (called "swelling pressure") in order to prevent sample deformation during water intake at constant temperature.

Fig.5.2 shows the evolution of the swelling pressure and the degree of saturation during the experiment. The saturation degree $S_w = 100\%$ corresponds to a final water content $\omega_f = 33.1 \pm 0.8\%$, the latter being defined as the ratio of fluid to solid mass $\omega = m_{water}/m_{solid}$. After an initial fast increase, the swelling pressure exhibits a temporary drop followed by a new increase until reaching a stationary value of the same magnitude as the first maximum. The final value at the fully saturated state, linked to the dry density, reaches values between 0.5 and 4 MPa. [105].

¹weight percent

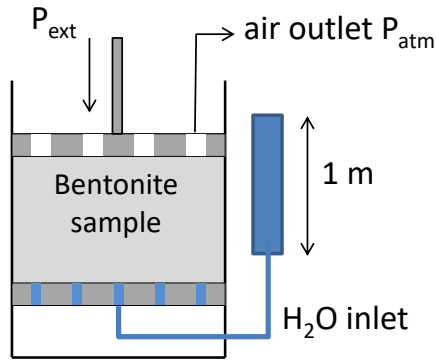


Figure 5.1: Experimental setup of the swelling pressure tests performed by Imbert and Villar [11].

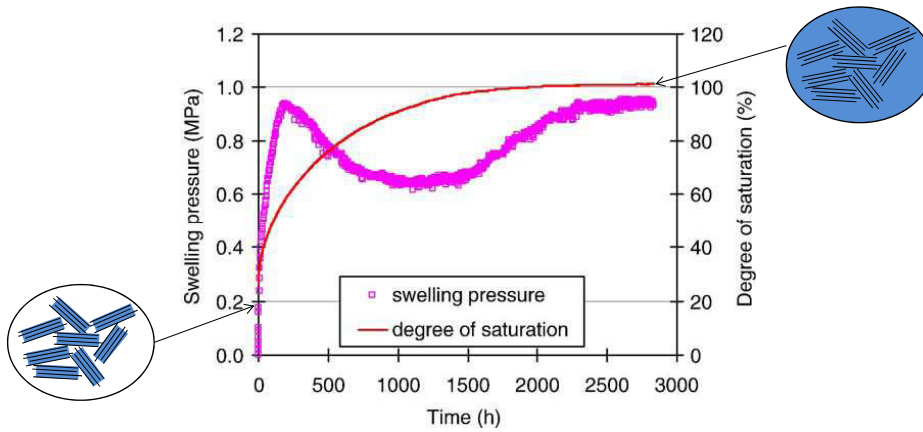


Figure 5.2: Evolution of the swelling pressure and the saturation degree during water infiltration of the pellets/bentonite powder mixture of the experiment MGR7 in [11].

Several modeling efforts have been undertaken to elucidate the physical phenomena underlying these observations [105, 106, 107, 108, 33, 22, 109]. The behavior is generally associated with the collapse of the microscopic solid structure when reaching the loading-collapse curve [105]. All these models are able to link the mechanical behavior to the capillary pressure drop during water uptake. However, to the best of our knowledge, they are all based on an empirical approach to account for micro- and nanoscopic contributions to the overall swelling pressure. In order to fill this gap between the local and overall hydro-mechanical behavior, we apply the multi-scale model of unsaturated expansive clays that was recently developed in our group [22] to numerically simulate the evolution of the swelling pressure during hydration.

The model derivation is based on the characteristic multi-scale structure of swelling clay minerals that is roughly presented in chapter 1 and recalled on Fig.5.3. According to this representation, swelling clays are porous media characterized by two porosity levels (referred to as nano- and micropores tied up to their size [110]) and three disparate length scales:

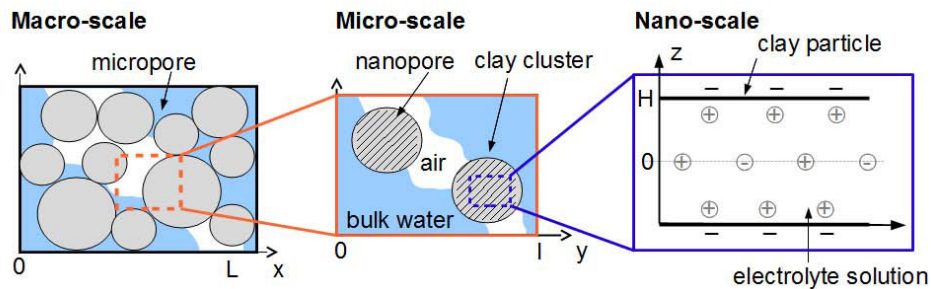


Figure 5.3: Multi-scale structure of swelling clays.

- At the nanoscale the medium is composed of incompressible linear-elastic clay platelets of constant surface charge $\Sigma < 0$. The platelets are separated by a nanoporous network saturated by a binary electrolyte solution. The monovalent ions in the aqueous solution are completely dissociated and distributed in the way to compensate the excess surface charge of the clay platelets resulting in the formation of a diffuse Electrical Double Layer (EDL) near the solid liquid interface. In the classical EDL approach considering the electrolyte solution as continuous and the ions as point charges, the force acting on the platelets, called disjoining pressure is of purely electrochemical nature. In this case, the disjoining pressure is purely repulsive and decreases monotonously for an increasing interlayer distance (cf. Fig.1.12).

As presented in the previous chapters and analyzed in more detail in this chapter, the nanoscale description can considerably be improved by considering the molecular nature of the electrolyte solution (water solvent + ions).

Among these different particle interactions (molecule size exclusion, dipolar and electrical effects), it is the finite size of the solvent molecules that is expected to dominate the swelling behavior at low hydration levels leading to the formation of discrete water layers in the interplatelet space. Therefore, as a first improvement of the nanoscale description of swelling clays, we consider the molecular nature of the water solvent only (as the ion concentration is negligible compared to that of water) by modeling it as a simple hard sphere fluid. As has been shown on Fig.2.7, this allows to reproduce an oscillatory shape of the disjoining pressure accounting for both, repulsion and attraction. Beyond the link between the physical phenomena at the different length scales and the resulting macroscopic hydro-mechanical behavior, this study aims at pointing out the limits of the classical EDL theory in modeling the disjoining pressure during hydration and to show the potential improvements that can be done on the nanoscale portrait. Note finally

that the present approach is straightforward to incorporate more sophisticated models including the dipolar nature of the water solvent as well as the presence of ions.

- At the intermediate microscale the platelets assemble to swollen clay aggregates (or particles) building the solid phase at that length scale. The particles are separated by a microporous network (free of EDL effects regarding their size) which is filled by a mixture of bulk water and air. Due to the meniscus between the air and the water phase, capillary pressure effects originate from that length scale.

Based on this representation of the local clay matrix it is thus possible to incorporate the coupling between (microscopic) capillary and (nanoscopic) disjoining pressure effects in the overall hydro-mechanical behavior over the entire water saturation range. The action of the capillary pressure is of repulsive nature tending to widen the micropores. The effect of the disjoining pressure at the particle scale however is opposite to that of the capillary pressure: pushing two adjacent platelets away from each other results in a swelling of the clay particles at the microscale. As will be shown in the following, the multi-scale model is able to provide further insight to the water transfer mechanism from the micro- to the nanoporous space and the linked evolution of the disjoining pressure during water infiltration.

This chapter is organized as follows. The detailed derivation being beyond the scope of this work, this chapter starts by presenting directly the final macroscopic model equations in an isotropic medium approximation. For more insight to the model derivation, we refer to [22]. Section 5.3 shows the application of the three-scale model to numerically simulate the oedometric water infiltration test of Imbert and Villar [11] starting with a presentation of the governing equations at the different hydration levels. The numerical results are finally analyzed in comparison to the experiment under consideration of the medium reorganization at the different local length scales.

5.2 Multi-scale model equations in an isotropic medium approximation

Starting from the formulation of the mechanical equilibrium at the local scales according to the geometric description presented in Fig.5.3, the total stress σ_T of the overall medium is obtained by periodic homogenization [30]. Neglecting shear stresses the total stress given by [22]

$$\sigma_T = \sigma_E \mathbf{I} - P_f^{eff} \mathbf{I} - \Pi_{eff} \mathbf{I}, \quad (5.1)$$

where \mathbf{I} designates the identity tensor is the sum of three terms: (i) an effective contact stress σ_E linked solely to the solid phase connectivity, (ii) an effective fluid pressure P_f^{eff} accounting for capillary pressure effects arising from the micropores and (iii) an effective disjoining pressure Π_{eff} strongly tied up with the action of the electrolyte solution on the clay platelets in the nanopores. In what follows, the different terms are explained in more detail.

5.2.1 Elastic contact stress

The present model approach considers elastic deformation only so that the effective contact stress $\sigma_E = tr(\sigma_E)/3$ is linked to the volumetric macroscopic strain $\epsilon = tr(\boldsymbol{\epsilon})$ by Hooke's law $\sigma_E = \tilde{K}\epsilon$, with \tilde{K} the macroscopic bulk modulus. Note that $\epsilon < 0$ in the case of compression.

For the determination of the macroscopic bulk modulus, we recall the classical definition of the macroscopic Biot coefficient α [111]

$$\alpha = 1 - \frac{\tilde{K}}{K_s}, \quad (5.2)$$

where K_s is the microscopic bulk modulus translating the rigidity of the clay particles. For an isotropic medium, the ratio $\frac{\tilde{K}}{K_s}$ can be estimated using self-consistent medium approximation according to [112]

$$\frac{\tilde{K}}{K_s} = 1 - \alpha = 1 - \frac{n_f}{1 - \frac{4\mu_s}{3K_s}}, \quad (5.3)$$

where μ_s designates the microscopic shear modulus of the solid phase (here the clay particles) and n_f the Eulerian inter-particle porosity defined as the ratio of the pore volume to the actual volume of the overall medium. It is recalled that $4\mu_s/3K_s = 2(1 - 2\nu_s)/(1 + \nu_s)$ allowing to express the above relation as a function of the Poisson coefficient of the clay particles ν_s which results in

$$\alpha = 1 - \frac{\tilde{K}}{K_s} = \frac{3n_f(1 - \nu_s)}{2(1 - 2\nu_s) + n_f(1 + \nu_s)}. \quad (5.4)$$

Note that K_s and ν_s are taken as parameters in this study.

5.2.2 Effective disjoining pressure

The effective disjoining pressure represents the macroscopic result of the nanoscopic disjoining pressure Π_d , which is given by [22]

$$\Pi_{eff} = (1 - \alpha)\Pi_d. \quad (5.5)$$

We may observe that α plays the role of a scaling factor accounting for the transmissibility of disjoining forces between adjacent clay particles. Using Eq.(5.4), Π_{eff} can be expressed as a function of the microporosity n_f and the Poisson coefficient of the solid phase at the microscale ν_s

$$\Pi_{eff} = \frac{2(1 - n_f)(1 - 2\nu_s)}{(1 + \nu_s)n_f + 2(1 - 2\nu_s)} \Pi_d. \quad (5.6)$$

From the above equation it is obvious that the model approach for the disjoining pressure Π_d at the nanoscale plays a crucial role in its contribution to the macroscopic behavior of the overall medium. As stated in chapter 1, the classical approach to express disjoining stresses is the EDL theory. One objective of the present study is to determine range of validity of the EDL for computing the disjoining pressure in swelling clays as well as its limits and the possible improvements that can be done by considering the molecular nature of the electrolyte solution.

We recall that in classical EDL theory Π_d is expressed as a function of ion concentration c_b and inter-platelet distance $2H$ using Poisson-Boltzmann (PB) equation [33]

$$\Pi_{d,PB}(c_b, H) = 2c_bRT [\cosh \bar{\varphi}_0(c_b, H) - 1], \quad \bar{\varphi}_0 = \frac{F\varphi_0(c_b, H)}{RT} \quad (5.7)$$

with $\varphi_0(c_b, H)$ the electric potential at the midplane between two adjacent platelets. As shown on Fig.1.12 the resulting disjoining pressure is purely repulsive and a decreasing function of the platelet distance. This approach is thus chosen for modeling Π_d in the osmotic swelling regime (large interplatelet distances) where disjoining forces might be driven by EDL effects.

At low water content (in the crystalline swelling regime) corresponding to the beginning of the experiment, solvation forces seem to play a major role in the swelling behavior at the platelet scale [12] resulting in a distribution of the density of water molecules that oscillates between maxima located at values $2H$ equal to nearly entire multiples of the molecule diameter $d_{H_2O} \approx 2.8 \text{ \AA}$ and minima lying on nearly odd entire multiples of the molecule half-diameter

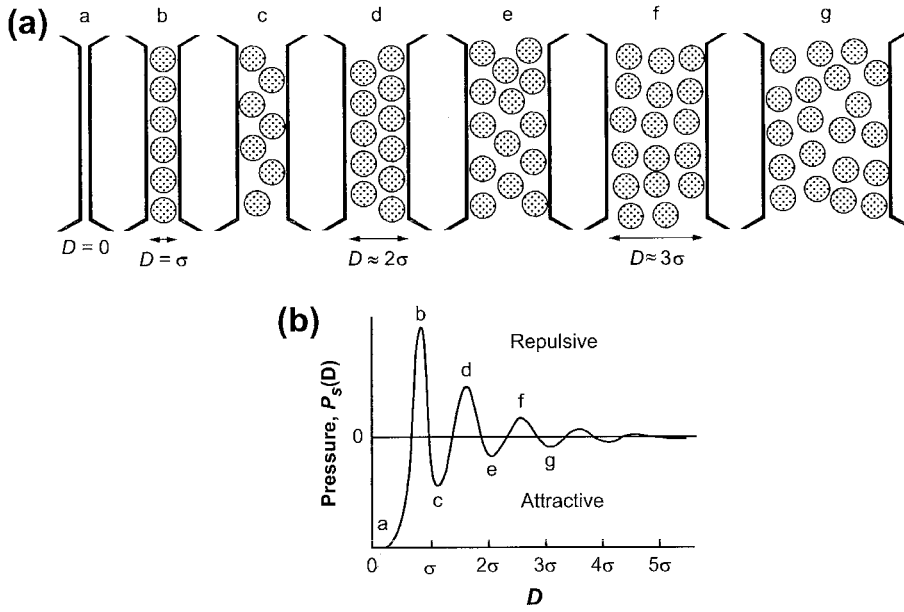


Figure 5.4: Distribution of (a) the water molecule density and (b) solvation pressure as a function of the interlayer space [12].

as shown on Fig.5.4a. The resulting solvation force (Fig.5.4b) exhibits as well an oscillatory shape allowing to account for repulsion and attraction which is not accounted for by classical EDL theory.

A simple approach to such a solvation force evolution is to model the electrolyte solution as a HS fluid (accounting for particle size effects of the solvent constituents) confined between two planar hard walls representing the clay platelets (Fig.2.3). Such a system has been discussed in chapter 2. We recall here directly the resulting expression of the disjoining pressure being a function of the interplatelet distance $2H$ Eq.(2.113)

$$\Pi_d(2H) = k_B T \rho(z = d/2, 2H) - P_{CS}(\rho_b), \quad (5.8)$$

where $\rho(z = d/2, 2H)$ is the particle density at the contact with the solid wall and $P_{CS}(\rho_b)$ is the Carnahan-Starling bulk pressure for a fluid of density ρ_b [44].

Fig.5.5 compares the profiles of the disjoining pressure obtained by PB theory ($c_b = 10^{-4}$ mol/l) and for a HS fluid ($\rho_b d^3 = 0.73$) as a function of the interplatelet distance normalized by the water molecule diameter $d = 2.8 \text{ \AA}$.

As expected, for a hard sphere fluid confined between two hard walls $\Pi_d(2H)$ has an oscillatory profile with maxima located at nearly entire multiples of particle diameter whose amplitude decreases rapidly with the platelet distance. Note that only the decreasing parts represent equilibrium states. In addition, the HS pressure reaches sensitively higher values at small interplatelet distances than the PB theory. It is thus obvious that the PB model has to be improved to predict the disjoining pressure for small interplatelet distances. The HS fluid model is chosen here in the crystalline swelling regime.

5.2.3 Equivalent fluid pressure

The equivalent fluid pressure is given by

$$P_f^{eff} = P_a - \chi^{eff} P_c, \quad (5.9)$$

with P_a the air pressure and P_c the capillary pressure defined as $P_c = P_a - P_w$ in such a way that $P_c > 0$. As the air is in equilibrium with the atmospheric pressure in the experiment, P_a

with k_B the Boltzmann constant. The density distribution of the bulk fluid ρ_b is expressed in terms of the bulk density ρ_b by Carnahan-Starling equation [17].

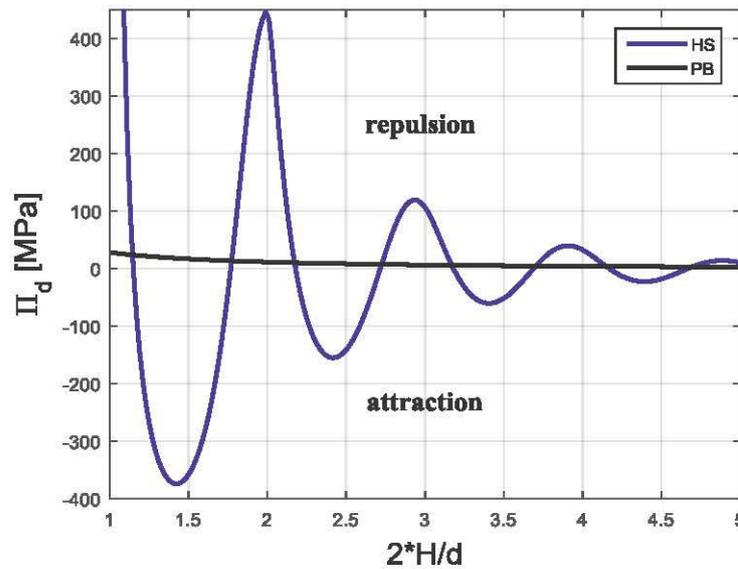


Figure 3. Disjoining pressure profiles of a PB fluid ($c_b=10^{-4}$ mol/l) and a HS fluid ($c_b=10^{-4}$ mol/l) as a function of normalized inter-platelet distance $2H/d$ ($d_{H_2O}=2.8\text{\AA}$).

Figure 3 compares the profiles of the disjoining pressure obtained by PB theory and for a HS fluid as a function of normalized inter-platelet distance $2H/d$. For the HS fluid, the water molecule diameter and normalized bulk concentration are set to $d_{H_2O}=2.8\text{\AA}$ and $\rho_b d^3=0.731$ (corresponding to a mass density $\rho_{H_2O}=10^3\text{kg/m}^3$). The HS fluid pressure allows to account for attraction ($\Pi_d < 0$) and repulsion ($\Pi_d > 0$), while PB is a purely repulsive decreasing function of the platelet distance. According to the expectations [14], the oscillatory profile of the HS fluid exhibits maxima at entire multiples of d whose amplitude decreases rapidly with the platelet distance. Note that only negative slope parts represent equilibrium positions. In addition, the HS law reaches somewhat higher values of the disjoining pressure at small distances than PB theory.

where χ ($0 \leq \chi \leq 1$) is the microscopic Bishop parameter. For capillary pressures higher than the water entering pressure P_c , the later can be expressed as a function of saturation, for example as [113]:

$$\chi(S_w) = \frac{P_c(S_w) + P_c^0}{P_c(S_w)}$$

Combination of Eqs. (5.4), (5.9) and (5.10) allows finally to express Π_d^f as a function of S_w^T and n_f parameters only, as follows:

5.2.4 Porosity

As shown in Fig. 5.3, the microscopic portrait of expansive clays consists of swollen clay particles separated by a porous network that is occupied by one or more bulk fluid phases. According to an Eulerian approach, the respective pore volume over the actual volume of the overall medium V , the microporosity is given by the ratio of the pore volume V_p to the total volume V . Assuming a stratified local arrangement, the nano-porosity is expressed by the inter-platelet distance according to $\phi = \frac{V_p}{V} = \frac{2H_s}{H+H_s}$, with $2H_s$ the platelet thickness. For an isotropic homogeneous distribution of the clusters, the two porosities are linked by a scalar version of the overall solid mass balance

$$(1-n_f)(1-\phi) = (1-\bar{n}_f)(1-\phi) \exp(-\varepsilon), \quad (8)$$

In the following, we will consider the different stages of the process, from the dry state to the fully hydrated state, and the numerical approximation of the pressure test results for powder/pellet systems presented in [113]. The ratio of the dry state to the hydrated state (100% swelling) is a measure of the deformation of the water content.

2.2.1 Initial

Initially, we consider the case of a dry sample (100% hydrated from the dry state) and the swelling pressure is zero. The initial application, the initial deformation is elastic stress $\sigma = 0$. Initially $P_{ext}^i = 0$ and it is assumed that the disjoining pressure is zero. As $w_1 = 0.8$, the swelling [18] fluid law in (7) this law, $2H$ which is constant platelet thickness porosity is $\phi^i = 0.8$. It is important to note that the disjoining pressure approximation fluid requires

the microporous space. For isotropic media, the variation of the Eulerian microporosity with respect to a strain free reference state at \bar{n}_f can be written as [22]

$$n_f - \bar{n}_f = (\alpha - n_f) \left[\epsilon + \frac{(1 - \chi)P_c}{K_s} - \frac{\Pi_d}{K_s} \right]. \quad (5.13)$$

Combination of the above equation with Eq. (5.4) allows to express n_f as a function of the macroscopic strain, the capillary and the disjoining pressure, parameterized by K_s and ν_s as follows

$$n_f - \bar{n}_f = \frac{n_f(1 - n_f)}{\frac{2(1 - 2\nu_s)}{1 + \nu_s} + n_f} \left[\epsilon + \frac{(1 - \chi)P_c}{K_s} - \frac{\Pi_d}{K_s} \right]. \quad (5.14)$$

For deformable media, it is generally more convenient to analyze the evolution of the porous space in terms of the Lagrangian porosity being defined with respect to the volume of the overall medium in the reference state \bar{V} , as $n_f^L = \frac{V_f^{micro}}{\bar{V}}$. Writing the actual volume of the medium as $V = \bar{V} + \Delta V$, the link with the Eulerian porosity is directly obtained

$$\begin{aligned} n_f^L &= \frac{V_f^{micro}}{V} \frac{V}{\bar{V}} = n_f \frac{\bar{V} + \Delta V}{\bar{V}} \\ &= n_f [1 + tr(\epsilon)] \\ &= n_f (1 + \epsilon). \end{aligned} \quad (5.15)$$

From the above equation it can easily be seen that in the absence of any deformation, both porosities are identical. The combination of the above equation with (5.13) yields then for the variation of the Lagrangian microporosity

$$\begin{aligned} n_f^L - \bar{n}_f &= n_f - \bar{n}_f + \epsilon n_f \\ &= \alpha \epsilon + \frac{\alpha - n_f}{K_s} [(1 - \chi)P_c - \Pi_d] \\ &= \alpha \epsilon + \beta [(1 - \chi)P_c - \Pi_d]. \end{aligned} \quad (5.16)$$

The above result is consistent with the classical Biot relation, with the coefficient β defined as

$$\beta = \frac{\alpha - n_f}{K_s} = \frac{(1 - \nu_s)(1 - n_f)n_f}{2(1 - 2\nu_s) + n_f(1 + \nu_s)} \frac{1}{K_s}. \quad (5.17)$$

In comparison to the saturated case, the fluid pressure contribution is accounted for by $(1 - \chi)P_c$ which is a function of the capillary pressure. In addition, the present multi-scale model allows to consider the impact of the disjoining pressure on the evolution of the porous space.

This last relation shows that a compression ($\epsilon < 0$) results in a decrease of the microporosity. P_c and Π_d being positive, a decrease of the capillary pressure (water uptake) results in a decrease of the microporous space and thus of n_f , while a decrease of the disjoining pressure should increase n_f which is in agreement with the expectations.

As in the microscopic case, the Eulerian nanoporosity is defined as the volumetric ratio of the interplatelet pores to the actual volume of a clay particle at the microscale

$$\langle \phi \rangle = \frac{V_f^{nano}}{V_s^{micro}}. \quad (5.18)$$

Note that the interplatelet distance is not necessarily uniform insight a clay particle. That is why the average value over the solid phase at the microscale is used, *i.e.* $\langle \phi \rangle^s = \frac{1}{V_s^{micro}} \int_{V_s^{micro}} \phi dV$.

Assuming a stratified nanoscopic structure consisting of a parallel arrangement of clay platelets of thickness $2H_s$ according to Fig. 5.3, $\langle \phi \rangle$ can be related to the interplatelet distance $2H$ according to

$$\langle \phi \rangle = \frac{H}{H + H_s}. \quad (5.19)$$

As shown in [22], the two porosities are linked to each other by an integral version of the overall solid mass balance, which can be written in its isotropic version as

$$(1 - n_f)(1 - \langle \phi \rangle^s) = (1 - \bar{n}_f)(1 - \langle \bar{\phi} \rangle^s) \exp(-\epsilon), \quad (5.20)$$

where the overbars refer again to a strain free reference state.

For the same reasons as before, for deformable media it might be more convenient to express the variation of the nanoporous space in the Lagrangian approach which defines the nanoporosity with respect to the particle volume at the reference state

$$\langle \phi^L \rangle = \frac{V_f^{nano}}{V_s^{micro}}. \quad (5.21)$$

The link with the Eulerian porosity is given by

$$\begin{aligned} \langle \phi^L \rangle &= \frac{V_f^{nano}}{V_s^{micro}} \times \frac{V_s^{micro}}{\bar{V}_s^{micro}} = \langle \phi \rangle \times \frac{V_s^{micro} + \Delta V_s^{micro}}{\bar{V}_s^{micro}} \\ &= \langle \phi \rangle (1 + \epsilon_s), \end{aligned} \quad (5.22)$$

with $\epsilon_s = \frac{\Delta V_s^{micro}}{\bar{V}_s^{micro}}$ the volumetric strain of a clay particle. The clay particle deformation ΔV_s^{micro} is defined as the sum of the variation of the porous space $\Delta V_f^{nano} = V_f^{nano} - \bar{V}_f^{nano}$ and the solid phase $\Delta V_s^{nano} = V_s^{nano} - \bar{V}_s^{nano}$ inside a particle. Assuming incompressible clay platelets ($\Delta V_s^{nano} = 0$), ϵ_s reduces to

$$\epsilon_s = \frac{\Delta V_f^{nano}}{\bar{V}_s^{micro}} = \frac{V_f^{nano} - \bar{V}_f^{nano}}{\bar{V}_s^{micro}} = \langle \phi^L \rangle - \langle \bar{\phi} \rangle. \quad (5.23)$$

Combination of the above equation with (5.22) allows to express the variation of the nanoporous space in the Eulerian approach as

$$\begin{aligned} \epsilon_s &= \langle \phi \rangle (1 + \epsilon_s) - \langle \bar{\phi} \rangle \\ &= \frac{\langle \phi \rangle - \langle \bar{\phi} \rangle}{1 - \langle \phi \rangle}. \end{aligned} \quad (5.24)$$

Defining the volumetric strain of the micropores as the variation of the Lagrangian micro-porosity $\epsilon_f = \frac{\Delta V_f^{micro}}{\bar{V}} = n_f^L - \bar{n}_f$ given by Eq.(5.16), in combination with Eq.(5.23) the overall strain can be rewritten as

$$\begin{aligned}
 \epsilon &= \frac{\Delta V_f}{\bar{V}} = \frac{\Delta V_f^{micro}}{\bar{V}} + \frac{\Delta V_f^{nano}}{\bar{V}} \\
 &= \frac{V_f^{micro} - \bar{V}_f^{micro}}{\bar{V}} + \frac{V_f^{nano} - \bar{V}_f^{nano}}{\bar{V}_s^{micro}} \frac{\bar{V}_s^{micro}}{\bar{V}} \\
 &= n_f^L - \bar{n}_f + \left[\langle \phi^L \rangle - \langle \bar{\phi} \rangle \right] \frac{\bar{V} - \bar{V}_f^{micro}}{\bar{V}} \\
 &= n_f^L - \bar{n}_f + \left[\langle \phi^L \rangle - \langle \bar{\phi} \rangle \right] (1 - \bar{n}_f) \\
 &= \epsilon_f + (1 - \bar{n}_f) \epsilon_s.
 \end{aligned} \tag{5.25}$$

The different terms of the total stress can thus all be expressed as functions of the nano- and micro-porosities. This means that the coupling between the different physical phenomena is made through these two porosity levels.

Note furthermore that these are exactly the inter- and intra-cluster porosities that allow to account for water transfer between the two porosity levels. As shown in the subsequent application, for a fixed sample volume, a decrease of the interparticle pores and therefore of n_f (due to a decrease of P_c during water infiltration, for example) is compensated by an increase of the interplatelet space and thus of $\langle \phi \rangle$ indicating a water transfer from the micro- to the nanopores. This increase of the separation distance between the clay platelets in turn results in a decrease of the disjoining pressure Π_d .

5.3 Application to an oedometric swelling pressure test

This section presents the governing equations used for the computation of the different stages of imbibition (the dry and the fully saturated states, along with intermediate saturations) during the oedometric swelling experiment shown in Figure.5.2. The swelling pressure is defined as P_{ext} the applied pressure to the upper disc to prevent volumetric strain. The total stress given by Eq.(5.1) is constant and equal to $-P_{ext}\mathbf{I}$. The assumptions underlying the computation according to the experimental data [11] are:

- At the initial state of the imbibition (denoted in the following by the superscript “i”), the water content of the sample is set to the mean value between the powder and the pellets $\omega^i \approx \frac{0.12 + 0.05}{2} = 0.085$ which corresponds to 1 to 2 water layers in the interplatelet pores [3]. The corresponding water saturation is $S_w^i = \omega^i / \omega^f = 0.26$ which is consistent with the experimental observations. For this saturation level, all water is assumed to be confined in the nanopores, while the micropores are only filled by air. The meniscus between the air and water should thus be located at the limit of the nanopores on the surface of the clusters as shown in Fig.5.2 implying that the microscopic Bishop coefficient is null, $\chi^i = 0$. This hypothesis agrees with a rough estimation of the pore diameter linked to the initial capillary pressure of about 200 MPa using Laplace equation $P_c = 2\gamma/R$. With the water/air surface tension $\gamma(298K) = 72 \times 10^{-3} \text{ N.m}$ the corresponding pore diameter is approximately $2R = 4\gamma/P_c \approx 2 \text{ nm}$ which is clearly superior to the nanopore diameter and justifies the assumption that the later is completely saturated.
- The final state of the imbibition (denoted by the superscript “f”) corresponds to the fully saturated state in the absence of any capillary pressure, i.e. $P_c^f = 0$.

5.3.1 Initial “dry state”

The initial state represents the reference state for this application, so that $n_f^i = \bar{n}_f$ and $\langle \phi \rangle = \phi^i = \bar{\phi}$. For the sake of simplicity, the brackets “ $\langle \cdot \rangle$ ” will be omitted in the notation of the average nanoporosity in the following. As sample deformation is prevented during water intake no overall elastic stress appears with respect to the initial state and $\sigma_E = 0$. Initially, there is no pressure applied to the cell $P_{ext}^i = 0$ and it follows from Eq.(5.1)

$$\begin{aligned}
 P_{ext} = 0, \sigma_E = 0 &\Rightarrow \Pi_{eff}^i = -P_f^{eff,i} \\
 (5.9) &\Rightarrow \Pi_{eff}^i = -\left(P_a - \chi^{eff,i} P_c^i\right) . \\
 P_a \approx 0 &\Rightarrow \Pi_{eff}^i \approx \chi^{eff,i} P_c^i
 \end{aligned} \tag{5.26}$$

In combination with Eqs. (5.5) and (5.10), it comes

$$\begin{aligned}
 (1 - \alpha^i) \Pi_d^i &= \left[1 - (1 - \chi^i) \alpha^i\right] P_c^i = (1 - \alpha^i) P_c^i \\
 &\Rightarrow \Pi_d^i(\phi^i) = P_c^i(S_w^i) = 200 \text{ MPa} ,
 \end{aligned} \tag{5.27}$$

which means that the initial high capillary pressure is completely compensated by the disjoining pressure.

Assuming crystalline swelling at the beginning of the experiment the disjoining pressure is computed by the hard sphere fluid law (5.8) which allows to estimate the interplatelet distance corresponding to the initial capillary pressure value as

$$\Pi_{d,HS}(H^i) = P_c^i = 200 \text{ MPa} \xrightarrow{(5.8)} 2H^i = 3.12 \text{ \AA} . \tag{5.28}$$

This corresponds to 1-2 water layers which is consistent with the assumption of crystalline swelling [3]. The corresponding nanoporosity is estimated using Eq.(5.19) by assuming a platelet thickness $2H_s = 1\text{nm}$

$$\phi^i = \bar{\phi} = \frac{H^i}{H^i + H_s} = 0.24 . \tag{5.29}$$

In order to show the improvement of the HS law compared to the PB law in computing the disjoining pressure at the initial state, Fig.5.6 compares the disjoining pressure curves obtained with a classical PB approach (5.7) for $c_b = 10^{-4}$ mol/l (fixed value for the rest of chapter) with that obtained with a HS fluid law (5.8). The figure shows also the disjoining pressure value at the initial state of imbibition and the corresponding interplatelet distance estimated from relation Eq.(5.8). It can easily be seen that at small interplatelet distances, the disjoining pressure values predicted by the HS fluid law are significantly higher than those predicted by the PB law. It is thus obvious that the disjoining pressure estimated with the PB theory is not able to compensate the high initial capillary pressure. This confirms again the need to take into account the solvation forces for computing the disjoining pressure at the beginning of the imbibition experiment. Even if modeling the electrolyte solution by a simple HS fluid is a very simplistic approach which requires further improvement (including ionic and dipolar interactions as presented in the previous chapters), this approach represents a clear improvement of the nanoscale description at low hydration levels where the solvation forces dominate the EDL effects.

For the estimation of the microporosity at the initial state n_f^i we introduce:

- the dry density $\rho_{ss} = m_s^{nano}/V_s^{nano} = 2670 \text{ kg/m}^3$ [115], with m_s^{nano} the mass of the solid phase in a clay particle;

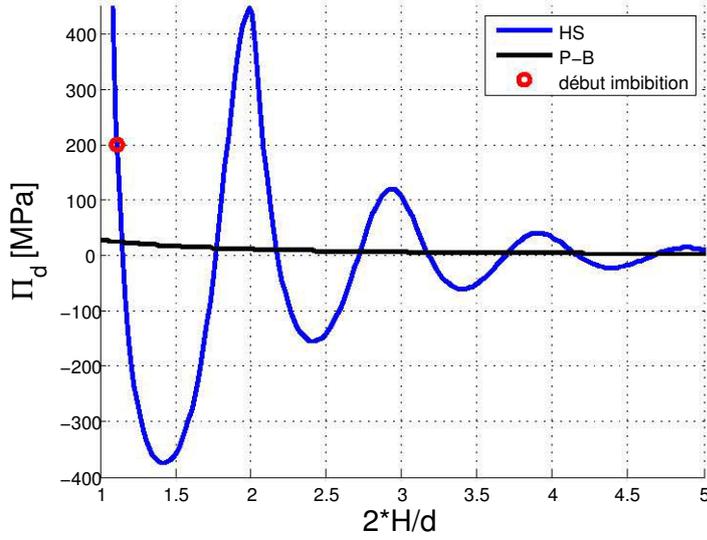


Figure 5.6: Disjoining pressure profiles obtained with a PB law Eq.(5.7) for $c_b = 10^{-4}$ mol/l and with a HS fluid Eq.(5.8). The red point indicates the value at the initial state of the imbibition experiment equal to the capillary pressure.

- all water being located in the nanopores, the initial water content is defined as the mass ratio of water to the solid phase inside a particle $\omega_i = m_{H_2O}^{nano}/m_s^{nano} = 0.085$;
- the dry density of the sample $\rho_{dry} = m_s^{micro}/V = 1.45$ g/cm³, with m_s^{micro} the mass of the solid phase at the microscale.

It follows

$$\begin{aligned}
 \frac{\rho_{dry}}{\rho_{ss}(1-\phi)} &= \frac{m_s^{micro}}{V} \frac{V_s^{nano}}{m_s^{nano}} \frac{V_s^{micro}}{V_s^{nano}} \\
 &= \frac{V_s^{nano}}{V} \frac{m_s^{nano} + m_{H_2O}^{nano}}{m_s^{nano}} = (1 - n_f^i)(1 + \omega^i) \\
 \Rightarrow n_f^i &= \bar{n}_f = 1 - \frac{\rho_{dry}}{\rho_{ss}(1-\phi^i)(1 + \omega^i)} = 0.39
 \end{aligned} \tag{5.30}$$

5.3.2 Final fully saturated state

At the final state the medium is completely saturated ($S_w^f = 1$), the capillary pressure vanishes and from Eq.(5.9) it follows that the fluid pressure contribution becomes negligible $P_f^{eff,f} = P_a \approx 0$. From the mechanical equilibrium Eq.(5.1), it can be concluded that the external swelling pressure reaches its maximum value which is entirely ensured by disjoining pressure effects

$$\begin{aligned}
 \sigma_E = 0, P_f^{eff,f} = 0 &\Rightarrow P_{ext}^f = \Pi_{eff}^f = (1 - \alpha^f) \Pi_d^f(H^f) \\
 &= \frac{2(1 - n_f^f)(1 - 2\nu_s)}{(1 + \nu_s)n_f^f + 2(1 - 2\nu_s)} \Pi_d^f(H^f),
 \end{aligned} \tag{5.31}$$

where $\Pi_d^f(H^f)$ is a function of the interplatelet distance at the final state H^f . At full saturation it seems reasonable to assume osmotic swelling and the disjoining pressure is consequently given by PB theory Eq.(5.7).

The values of the porosities depend on chosen approach, Eulerian or Lagrangian. As macroscopic deformation is prevented ($\epsilon = 0$), it comes directly from Eq. (5.15) that the Eulerian

and the Lagrangian microporosities are identical. The volumetric strain of the microporous space is thus given by

$$\begin{aligned}\epsilon_f^f &= n_f^f - \bar{n}_f = n_f^{L,f} - \bar{n}_f \\ &= \frac{\alpha^f - n_f^f}{K_s} \Pi_d^f = \beta^f \Pi_d^f.\end{aligned}\quad (5.32)$$

As the nanoporosity is defined with respect to volume of the solid phase at the microscale, even without any effective medium deformation, the clay particles are free to shrink or swell during water imbibition. The Eulerian and the Lagrangian nanoporosities differ from each other. The Eulerian nanoporosity at the final state is directly obtained by application of Eq. (5.20)

$$\phi^f = 1 - \frac{(1 - \bar{n}_f)(1 - \bar{\phi})}{1 - n_f^f}.\quad (5.33)$$

The corresponding Lagrangian nanoporosity can be expressed by insertion of $\epsilon = 0$ in Eq. (5.25), which results in

$$\phi^L = \bar{\phi} - \frac{n_f^L - \bar{n}_f}{1 - \bar{n}_f}.\quad (5.34)$$

Alternatively, by the use of Eq. (5.23) in combination with the above equation, the volumetric strain of the clay particles with respect to the reference configuration can be expressed as

$$\epsilon_s^f = \phi^L - \bar{\phi} = \frac{\bar{n}_f - n_f^L}{1 - \bar{n}_f}.\quad (5.35)$$

From this last relation, it can be seen that in the absence any macroscopic deformation, a decrease in the microporous space is compensated by a swelling of the clay particles, whereas an increase of the interparticle space induces a shrinkage of the solid phase at the microscale.

5.3.3 Intermediate saturations

At intermediate saturations we chose a representation of the overall medium by a division into two parts as shown schematically on Fig.5.7: a fully saturated part of height $x + \Delta$ at the bottom and a part of height $L - x - \Delta$ at the top being at the initial saturation, where L denotes the sample height and Δ the local macroscopic deformation due to the different saturations of both parts. Note that this might not correspond to the real configuration. But as no information is given about the advancement of the water front during water infiltration, this representation has the advantage that it does not require to define microscopic saturation and capillary pressure which can differ from their macroscopic values.

As the sample diameter is fixed, the volumetric fractions of both parts are given by the ratio of their respective height to the sample height

$$\begin{aligned}\text{Bottom part: } \theta_b &= \frac{x + \Delta}{L}; \\ \text{Top part: } \theta_t &= \frac{L - x - \Delta}{L} = 1 - \frac{x + \Delta}{L} = 1 - \theta_b.\end{aligned}\quad (5.36)$$

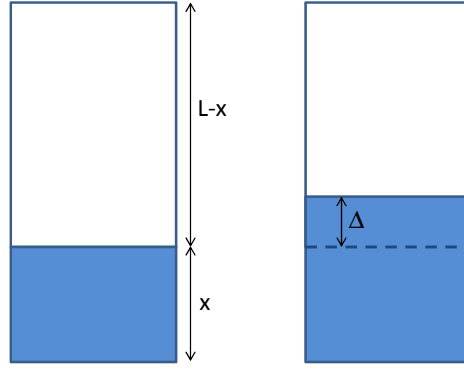


Figure 5.7: Representation of the sample at intermediate saturations as composed of two parts: the bottom being fully saturated and the top at the initial saturation. The overall saturation is obtained by the volume ratio of the two parts. On the left: configuration without local deformation; on the right: with local deformation Δ due to different water contents

The overall saturation is thus given by mean value over both parts weighted by their respective volume fraction as

$$S_w^T = \theta_b + (1 - \theta_b)S_w^i, \quad (5.37)$$

with $S_w^i = \omega^i/\omega^f = 0.26$. The local vertical strains $\epsilon_i = \{0, 0, \epsilon_i\}$ read as

$$\epsilon_b = \frac{\Delta}{x} \quad \text{and} \quad \epsilon_t = -\frac{\Delta}{L-x}, \quad (5.38)$$

where the coupling with the saturation is made via the overall water saturation (5.37). The corresponding oedometric elastic pressures are given by

$$\sigma_E^{b/t} = \widetilde{M}^{b/t} \epsilon_{b/t}, \quad (5.39)$$

with $\widetilde{M}^{b/t} = \widetilde{K}^{b/t} + \frac{4}{3}\mu^{b/t}$ the oedometric bulk modulus. Using Eq.(5.4) in combination with the relation $\mu = \frac{3(1-2\nu)\widetilde{K}}{2(1+\nu)}$ for the Lamé parameter μ assuming a constant value for the macroscopic Poisson ratio ν , the oedometric bulk modulus is linked to the microporosity $n_f^{b/t}$ via the Biot coefficient as follows

$$\widetilde{M}^{b/t} = \frac{3(1-\nu)}{1+\nu} K_s \left(1 - \alpha(n_f^{b/t})\right). \quad (5.40)$$

As the system is assumed at mechanical equilibrium, the total pressure of each part corresponds to the external swelling pressure P_{ext} . The bottom part being completely saturated, the capillary pressure is nul and $P_f^{eff,b} = P_a \approx 0$, whereas at the top part we have the initial configuration of hydration ($S_w^t = S_w^i$). This means that all water is confined in the nanopores and consequently $\chi^t = 0$ and $P_c^t = P_c^i = \Pi_d^i = 200$ MPa. The equivalent fluid pressure in this part is obtained by a combination of Eq.(5.9) and Eq.(5.10) which gives $P_f^{eff,t} = P_a - \chi_t^{eff} P_c^i = P_a - [1 - (1 - \chi^t)\alpha^t] P_c^i = P_a - [1 - \alpha(n_f^t)] \Pi_d^i$. As a result, the respective vertical components of the total pressure can be written as

$$\text{Bottom part:} \quad -P_{ext}(S_w^T) = -P_f^{eff,b} + \sigma_E^b - \Pi_{eff}^b$$

$$\begin{aligned}
&= -P_a + \widetilde{M}^b(n_f^b)\epsilon_b - \left[1 - \alpha(n_f^b)\right] \Pi_d(H^b) \\
&= -P_a + \left[1 - \alpha(n_f^b)\right] \left[\frac{3(1-\nu)}{1+\nu} K_s \epsilon_b - \Pi_d(H^b)\right] \\
&= -P_a + \frac{2(1-n_f^b)(1-2\nu_s)}{(1+\nu_s)n_f^b + 2(1-2\nu_s)} \left[\frac{3(1-\nu)}{1+\nu} K_s \frac{\Delta}{x} - \Pi_d(H^b)\right]
\end{aligned} \tag{5.41}$$

$$\begin{aligned}
\text{Top part: } -P_{ext}(S_w^T) &= -P_f^{eff,t} + \sigma_E^t - \Pi_{eff}^t \\
&= -\left\{P_a - \left[1 - \alpha(n_f^t)\right] P_c^i\right\} + \widetilde{M}^s(n_f^t)\epsilon_s - \left[1 - \alpha(n_f^t)\right] \Pi_d(H^t) \\
&= -P_a + \widetilde{M}^t(n_f^t)\epsilon_t + \left[1 - \alpha(n_f^t)\right] \left[\Pi_d^i - \Pi_d(H^t)\right] \\
&= -P_a + \left[1 - \alpha(n_f^t)\right] \left[\frac{3(1-\nu)}{1+\nu} K_s \epsilon_t + \Pi_d^i - \Pi_d(H^t)\right] \\
&= -P_a + \frac{2(1-n_f^t)(1-2\nu_s)}{(1+\nu_s)n_f^t + 2(1-2\nu_s)} \\
&\times \left[-\frac{3(1-\nu)}{1+\nu} K_s \frac{\Delta}{L-x} + \Pi_d^i - \Pi_d(H^t)\right].
\end{aligned} \tag{5.42}$$

Note that in the completely saturated bottom part Π_d is computed by PB law (5.7), whereas in the top part it is determined by the HS fluid law (5.8). In a similar way, the respective Eulerian microporosities are obtained from Eq.(5.13) which yields

$$\begin{aligned}
n_f^b &= \bar{n}_f + \left(\alpha(n_f^b) - n_f^b\right) \left[\epsilon_b - \frac{\Pi_d(\phi^b)}{K_s}\right] \\
&= \bar{n}_f + \frac{n_f^b(1-n_f^b)}{2(1-2\nu_s) + n_f^b} \left[\frac{\Delta}{x} - \frac{\Pi_d(\phi^b)}{K_s}\right]
\end{aligned} \tag{5.43}$$

and

$$\begin{aligned}
n_f^t &= \bar{n}_f + \left(\alpha(n_f^t) - n_f^t\right) \left[\epsilon_t + \frac{\Pi_d^i - \Pi_d(\phi^t)}{K_s}\right] \\
&= \bar{n}_f + \frac{n_f^t(1-n_f^t)}{2(1-2\nu_s) + n_f^t} \left[-\frac{\Delta}{L-x} + \frac{\Pi_d^i - \Pi_d(\phi^t)}{K_s}\right].
\end{aligned} \tag{5.44}$$

Contrarily to the fully saturated state where macroscopic strain is prevented (note that in this case, the sample is entirely composed of the bottom part), at intermediate saturations, the Eulerian and Lagrangian microporosities differ from each other due to the presence of local strains in each part. Their respective values can be expressed from Eq. (5.16) as follows

$$\begin{aligned}
n_f^{L,b} &= \bar{n}_f + \alpha(n_f^b)\epsilon_b - \beta^b \Pi_d(\phi^b) \\
&= \bar{n}_f + \frac{3n_f^b(1-\nu_s)}{2(1-2\nu_s) + n_f^b(1+\nu_s)} \frac{\Delta}{x} - \frac{\alpha(n_f^b) - n_f^b}{K_s} \Pi_d(\phi^b)
\end{aligned} \tag{5.45}$$

and

$$n_f^{L,t} = \bar{n}_f + \alpha(n_f^t)\epsilon_t + \beta^t \left[\Pi_d^i - \Pi_d(\phi^t)\right]$$

$$= \bar{n}_f - \frac{3n_f^t(1-\nu_s)}{2(1-2\nu_s) + n_f^t(1+\nu_s)} \frac{\Delta}{L-x} + \frac{n_f^t(1-n_f^t)}{\frac{2(1-2\nu_s)}{1+\nu_s} + n_f^t} \frac{\Pi_d^i - \Pi_d(\phi^t)}{K_s}. \quad (5.46)$$

The Eulerian nanoporosities are expressed from the mass conservation of the solid phase Eq.(5.20) which simplify in the limit of small deformations to

$$\begin{aligned} (1-n_f^b)(1-\phi^b) &= (1-\bar{n}_f)(1-\bar{\phi}) \exp(-\epsilon_b) \\ &= (1-\bar{n}_f)(1-\bar{\phi}) \frac{x}{x+\Delta}, \end{aligned} \quad (5.47)$$

and

$$\begin{aligned} (1-n_f^t)(1-\phi^t) &= (1-\bar{n}_f)(1-\bar{\phi}) \exp(-\epsilon_t) \\ &= (1-\bar{n}_f)(1-\bar{\phi}) \frac{L-x}{L-x-\Delta}. \end{aligned} \quad (5.48)$$

To derive the above expressions we adopted an approximation of the elementary deformation de as a function of the elementary variation of the sample height dl as follows $de = \frac{dl}{l}$. Integration of this equation results in

$$[\epsilon]_0^{\epsilon_b} = [\ln l]_x^{x+\Delta} \longrightarrow \epsilon_b = \ln \frac{x+\Delta}{x}, \quad (5.49)$$

and

$$[\epsilon]_0^{\epsilon_t} = [\ln l]_{L-x}^{L-x-\Delta} \longrightarrow \epsilon_t = \ln \frac{L-x-\Delta}{L-x}. \quad (5.50)$$

In the same way as for the fully saturated state, the corresponding Lagrangian nanoporosities are obtained by insertion of Eqs. (5.45) and (5.46) in Eq. (5.25), which results in

$$\begin{aligned} \phi^{L,b} &= \bar{\phi} + \frac{\epsilon_b - n_f^{L,b} + \bar{n}_f}{1-\bar{n}_f} \\ &= \bar{\phi} + \frac{[1-\alpha(n_f^b)]\epsilon_b + \beta^b \Pi_d(\phi^b)}{1-\bar{n}_f}. \end{aligned} \quad (5.51)$$

and

$$\begin{aligned} \phi^{L,t} &= \bar{\phi} + \frac{\epsilon_t - n_f^{L,t} + \bar{n}_f}{1-\bar{n}_f} \\ &= \bar{\phi} + \frac{[1-\alpha(n_f^t)]\epsilon_t + \beta^t [\Pi_d^i - \Pi_d(\phi^t)]}{1-\bar{n}_f}. \end{aligned} \quad (5.52)$$

Replacing α and β by their respective explicit expressions (5.4) and (5.17), it comes

$$\phi^{L,b} = \bar{\phi} + \frac{1-n_f^b}{1-\bar{n}_f} \times \frac{2(1-2\nu_s) \frac{\Delta}{x} + (1-\nu_s) n_f^b \frac{\Pi_d(\phi^b)}{K_s}}{2(1-2\nu_s) + n_f^b(1+\nu_s)}. \quad (5.53)$$

and

$$\phi^{L,t} = \bar{\phi} - \frac{1 - n_f^t}{1 - \bar{n}_f} \times \frac{2(1 - 2\nu_s) \frac{\Delta}{L - x} - (1 - \nu_s) n_f^t \frac{\Pi_d^i - \Pi_d(\phi^t)}{K_s}}{2(1 - 2\nu_s) + n_f^t(1 + \nu_s)}. \quad (5.54)$$

Alternatively, by the use of Eq. (5.23) in combination with the above equations, the volumetric strain of the clay particles with respect to the reference configuration can be expressed as

$$\begin{aligned} \epsilon_s^b &= \frac{[1 - \alpha(n_f^b)] \epsilon_b + \beta^b \Pi_d(\phi^b)}{1 - \bar{n}_f} \\ &= \frac{1 - n_f^b}{1 - \bar{n}_f} \times \frac{2(1 - 2\nu_s) \frac{\Delta}{x} + (1 - \nu_s) n_f^b \frac{\Pi_d(\phi^b)}{K_s}}{2(1 - 2\nu_s) + n_f^b(1 + \nu_s)}, \end{aligned} \quad (5.55)$$

and

$$\begin{aligned} \epsilon_s^t &= \frac{[1 - \alpha(n_f^t)] \epsilon_t + \beta^t [\Pi_d^i - \Pi_d(\phi^t)]}{1 - \bar{n}_f} \\ &= -\frac{1 - n_f^t}{1 - \bar{n}_f} \times \frac{2(1 - 2\nu_s) \frac{\Delta}{L - x} - (1 - \nu_s) n_f^t \frac{\Pi_d^i - \Pi_d(\phi^t)}{K_s}}{2(1 - 2\nu_s) + n_f^t(1 + \nu_s)}. \end{aligned} \quad (5.56)$$

This results in a system of 6 unknowns $\{P_{ext}, x \text{ (or } \Delta), n_f^{b/t}, \phi^{b/t}\}$ depending on the overall water saturation S_w^T parameterized by K_s , ν and ν_s .

5.4 Results and discussion

This section depicts the numerical results of the simulation of the swelling pressure during hydration and the related evolution of the microscopic properties giving further insight to the local rearrangement. As the present approach has a purely qualitative character, without any loss of generality, we impose the Poisson ratio of the clusters being fixed and equal to that at the macroscale $\nu = \nu_s = 0.25$. The numerical results are analyzed in terms of K_s playing the role of a scaling parameter accounting for the transmissibility between nanoscopic disjoining and microscopic capillary effects. If it is not mentioned otherwise K_s is set to 5 MPa allowing to obtain values of the swelling pressure nearby the experimental results, at least for moderately high saturations [34].

5.4.1 Swelling and disjoining pressure

To start, remind that according to the model approach presented in the previous section the overall medium is considered to be composed of two parts, a fully saturated bottom part and a top part remaining at the initial saturation level. The overall saturation S_w^T is then given by the mean value of both parts weighted by their respective volume ratio according to Eq. (5.37). The initial state of saturation corresponds thus to the medium consisting only of the top part ($S_w^T = S_w^i = 26\%$). As developed in section 5.3.1, we assume crystalline swelling in this part. Consequently, even at intermediate states the disjoining pressure in the top part Π_d^t is approached by the HS fluid law of Eq.(5.8). Inversely, the final state corresponds to the medium

consisting only of the bottom part ($S_w^T = 1$) being at full saturation. According to data in literature [24], the interlayer space is filled by three or more water layers which is consistent with osmotic swelling. As stated in section 5.3.2 the disjoining pressure in this part Π_d^b is thus calculated with the PB law of Eq.(5.7).

In what follows, we show our numerical results of the evolution of the overall effective pressure, commonly designated as “swelling pressure”, as a function of the overall saturation degree. A comparison with the evolution of its nanoscopic counterpart which is the disjoining pressure allows to conclude about the contribution of the later to the overall swelling behavior.

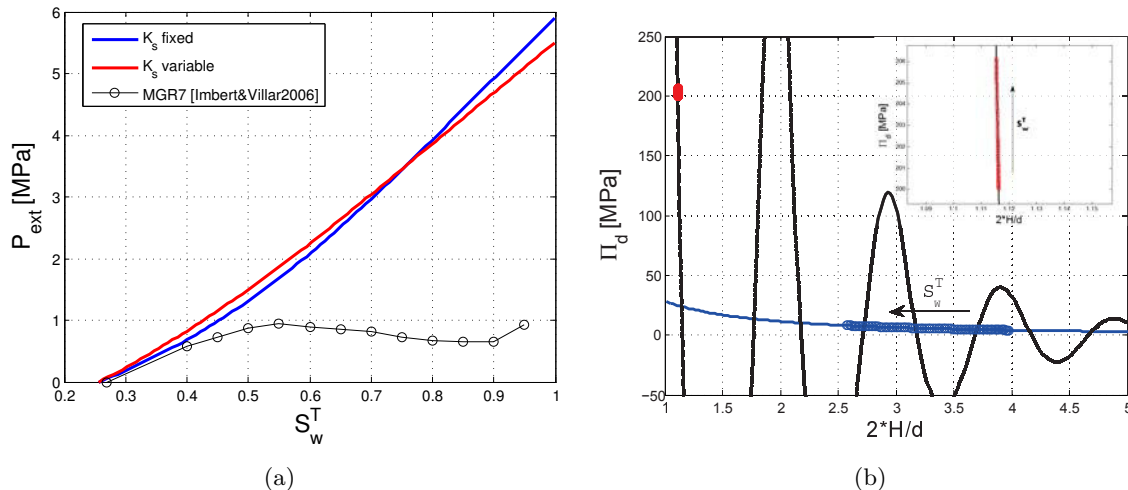


Figure 5.8: (a) Numerical results of the swelling pressure as a function of the overall saturation of the medium and comparison to the experimental data from [11]; (b) Disjoining pressure in the bottom (saturated \rightarrow PB law) and in the top part (initial state \rightarrow HS law). The curves are obtained with with $K_s = 5$ MPa.

The blue curve in Fig.5.8(a) shows the external swelling pressure P_{ext} obtained with the present three-scale model as a function of the overall medium saturation for the microscopic clay particle bulk modulus set to $K_s = 5$ MPa. The numerical results are compared to the experimental values taken from [11] and represented by black circles in this figure.

In agreement with the experimental results, P_{ext} increases with the overall saturation. Owing to the separation of the different contributions (contact stress, capillary pressure and disjoining forces) to the total swelling pressure in Eq.(5.1), the model indicates that this behavior is rather due to the collapse of the capillary pressure in the micropores than to an increase of the disjoining pressure in the nanopores.

As shown on Fig.5.8(b), Π_d decreases during water infiltration. The red dots correspond to the top part of the sample being at the initial saturation where Π_d is computed by a HS law Eq.(5.8), whereas the blue dots correspond to the bottom part being at full saturation where Π_d is estimated using PB theory Eq.(5.7). It can be seen that with increasing saturation, Π_d increases in the top part (inset in Fig. 5.8(b)), while it decreases in the bottom part. At full saturation the medium being entirely composed by the bottom part so that capillary pressure vanishes. As a consequence, the external pressure is completely determined by the disjoining pressure which is calculated by classical EDL theory. It is worth noting that the interplatelet distance estimated with the PB law at full saturation corresponds to about 3 water layers in the nanopores which is in agreement with the expectations [24].

However, Figure.5.8(a) highlights also the limits of the present model. After a good agreement at low saturations, the numerical values clearly exceed the experimental ones. Furthermore, after a first increase, the experiment swelling pressure decreases before increasing again.

Such behavior is confirmed by many experimental and modeling studies for different clay types [11, 105]. It is generally explained by the collapse of the solid matrix when reaching the loading-collapse (LC) line in the context of elasto-plastic deformation corresponding to a restructuring of solid structure at the microscopic scale [105].

In order to account for this local reorganization, we propose here a first simplistic approach which includes swelling at the nanoscopic clay platelet scale within the rigidity of a microscopic clay particle. As a consequence, instead of imposing a fixed value for the microscopic rigidity, K_s is related to the nanoporosity as follows

$$K_s(S_w^T) = K_s^i \frac{\phi^i}{\phi(S_w^T)}, \quad (5.57)$$

where $K_s^i = 5$ MPa is the microscopic compressibility at the initial state. This law does not aim to quantitatively represent the evolution of microscopic rigidity, but it allows to capture qualitatively the impact of the variation of the nanostructure on the rigidity of the clay clusters. Thus, The latter should become softer when the interplatelet space increases.

The swelling pressure obtained by the simulations with K_s evolving according to Eq. (5.57) is shown by the red curve in Fig.5.8(a). It can be seen that for an overall saturation up to 70%, the values of P_{ext} are slightly higher than those obtained with a constant K_s . A possible explanation might be that the major part of the medium in this case is composed by the dry top part which is compressed by the swelling of the saturated bottom part (Fig. 5.10). The overall medium becomes thus more rigid thereby resulting a more important swelling pressure. When the saturation further increases, the compression of the top part reduces which results in a decrease of K_s in this part. In addition, the major part of the medium is now saturated with an interlayer spacing higher than at the initial state. The overall medium softens and the swelling pressure is lower than for K_s fixed at 5 MPa throughout the experiment. This simplified approach allows to reduce the value of the swelling pressure at full saturation (of about 6.5% in this application example), but the reduction is not sufficient to recover the experimental observations nor to reproduce its temporary drop. More efforts have to be done to correctly account for plastic deformation. The following analyses are thus realized with fixed values of K_s .

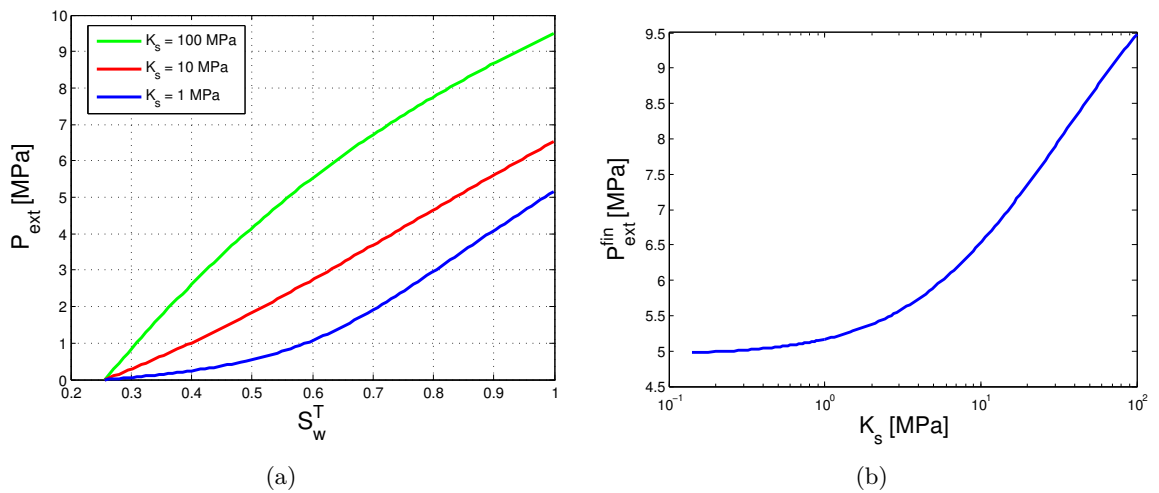


Figure 5.9: (a) External pressure as a function of the total saturation of the medium for different values of K_s . (b) Evolution of the swelling pressure at the final (saturated) state as a function of the microscopic bulk modulus K_s .

To further investigate the impact of microscopic rigidity on the swelling pressure Fig.5.9(a) depicts the evolution of P_{ext} during water intake for different values of K_s taken between 0.5

MPa and 100 MPa. For high values of K_s , steep increase of P_{ext} is observed at low saturation levels which attenuates at high saturations. In contrast, for low values of K_s , the external pressure increases rather at high saturation levels. The swelling pressure at the final state of hydration decreases when the bulk modulus of clay clusters K_s decreases. Nevertheless even with very low values ($K_s = 1$ MPa), the external pressure is still significantly higher than experimental values. In order to test if the present model allows to recover the experimental values at full saturation, Fig.5.9(b) shows the evolution of the final swelling pressure P_{ext}^f as a function of K_s . Although a decrease of P_{ext}^f is observed when K_s decreases, the multi-scale model clearly overestimates the swelling pressure at full saturation. Moreover, these values of K_s are significantly lower than the values of the effective bulk modulus documented in literature lying commonly between 10 and 50 GPa [116, 117]. Despite these apparent limits of the present model approach, two important conclusions can be drawn:

- To obtain external swelling pressures in the MPa regime, K_s has to be of the same order of magnitude which is significantly lower than the values of the overall bulk modulus documented in the literature.
- We remind that due to the separation of the different contributions to the overall stress, K_s is only tied up to the connectivity of the clay platelets inside a particle. Thus regarding these low values of K_s we conclude that the overall rigidity of the medium might not be ensured by the connectivity of the solid phase, but it is explained by the action of the disjoining pressure acting on the clay platelets in the nanopores.

5.4.2 Deformation and porosities

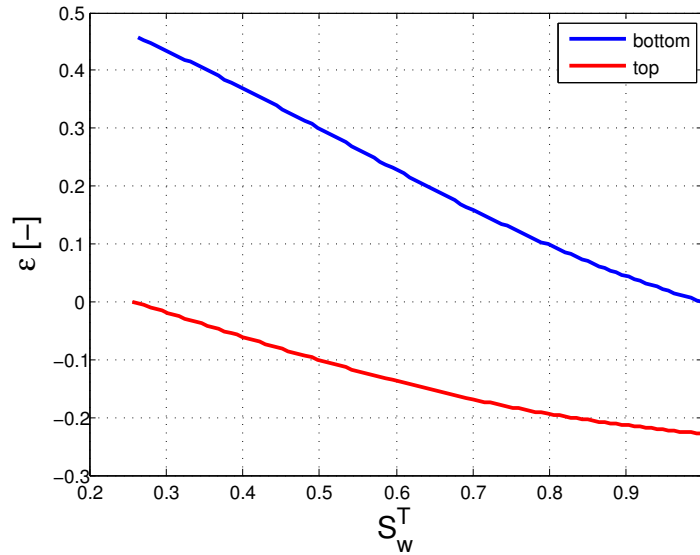


Figure 5.10: Deformation in the bottom (at full saturation) and top (at initial saturation) parts as a function of the total saturation of the medium for $K_s = 5$ MPa.

As highlighted in section 5.3.3, even if the overall sample deformation is prevented, local volumetric strain can appear as a consequence of the difference in the saturation degree inside the sample. The evolution of the respective vertical deformation in the two parts of the medium with the overall saturation is illustrated in Fig.5.10. According to the expectation, the fully saturated bottom part swells, whereas the top part (at the initial state) is compressed. Gradually, as hydration goes on, the swelling of the bottom part decreases down to zero at the final state. This is logical as the volume of the oedometric cell is fixed and at the final state

the entire medium is composed of the bottom part. The top part is continuously compressed during hydration.

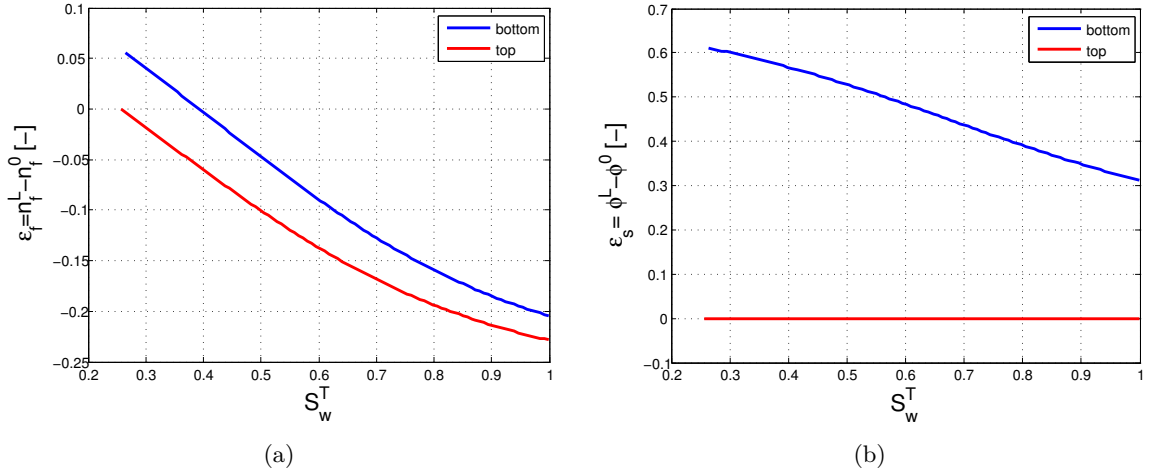


Figure 5.11: Volumetric strain of (a) the micropores and (b) the clay particles in the bottom (saturated) and top (initial state) parts as a function of the total saturation of the medium for $K_s = 5$ MPa.

Figure.5.11 allows to get a better insight to the repartition of the deformation in the two parts between the variation of the microscopic fluid and solid phases. (Figure.5.11(a) presents the evolution of the volumetric strain in the micropores which is defined as the variation of the Lagrangian microporosity according to Eq. (5.16) with the overall saturation. Similarly, Fig.5.11(b) depicts the corresponding evolution of the clay particle strain which is given by the variation of the Lagrangian nanoporosity according to Eq.(5.23).

These graphs point out that the swelling of the bottom part is mainly due to the increase of the interplatelet space. As shown by the blue line in Fig. 5.11(a) after a slight increase at low hydration degrees, the microporous space is continuously compressed with increasing water intake. This behavior is consistent the reduction and final collapse of the capillary pressure at full saturation as stated in literature [105]. Consequently, water is transferred from the micro- to the nanopores thereby increasing the interlayer space which is in agreement with a positive strain of the clay particles as shown by the blue line in Fig.5.11(b). According to the numerical results, after a steep increase at the beginning of hydration the nanoporosity in the bottom part decreases during infiltration but remains always higher than its value in the initial reference state. This behavior might be explained by the fixed overall sample volume which limits the swelling. A different swelling behavior of the clay particles might be observed for free hydration.

In the top part the micro- and nanoporosities decrease during water infiltration as shown by the red lines in Fig. 5.11(a) and 5.11(b), respectively. The numerical results indicate that the compression of this part is mainly due to the decrease of the microporous space. The clay particles are only slightly compressed. In the present model approach this is due to the fact that the interplatelet distance is limited by the divergence of the disjoining pressure of the HS fluid law at a separation distance of one water molecule diameter (cf. Fig.5.5). Nevertheless, note that even if the present HS fluid law might overestimate the minimum interplatelet distance to one water layer, the limitation of the compression of the nanopores is consistent with the intercalation of hydrated cations to compensate the surface charge of the clay platelets [13]. The compression of the clay particles would have been certainly be more pronounced if the nanopores were initially filled by at two water layers.

Note finally that the variation of the nanoporosities with S_w^T in both parts is at the origin of the respective evolution of the disjoining pressure as depicted in Fig.5.8(b). For completion

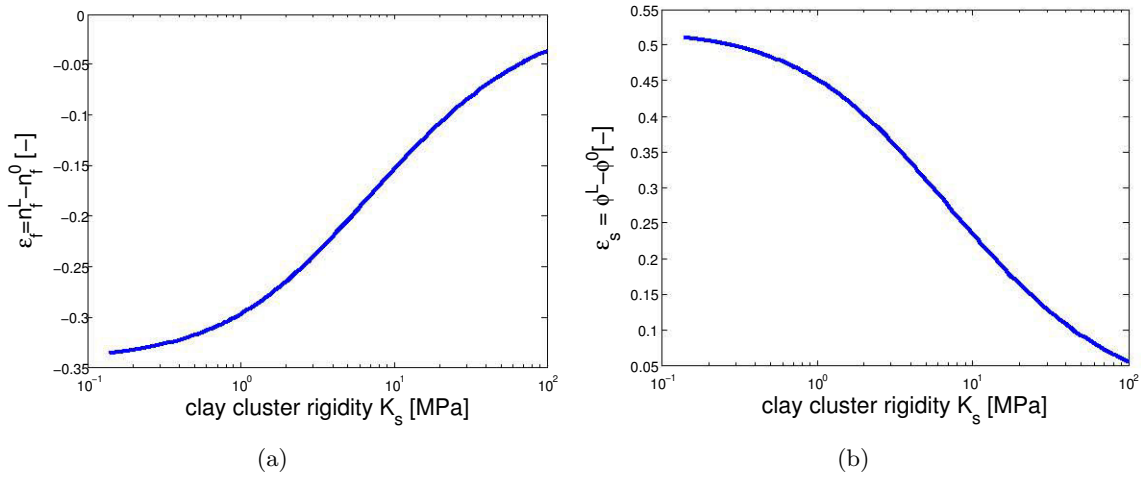


Figure 5.12: Volumetric strain of (a) the micropores and (b) the clay particles at the fully saturated state as a function of the microscopic bulk modulus K_s .

of the above analysis, Fig.5.12 depicts the volumetric strain of (a) the micropores ϵ_f^f and (b) the clay particles ϵ_s^f at the fully saturated state as a function of the microscopic bulk modulus K_s . As overall sample deformation is prevented, the Eulerian and Lagrangian microporosities are identical and ϵ_f^f is computed with Eq.(5.32).

In agreement with the collapse of the capillary pressure in the micropores at full saturation [106], the numerical results show a reduction of the microporosity between the initial dry and the final saturated state (Fig.5.12(a)).

As macroscopic strain is prevented, the decrease in the inter-particle space is compensated by an increase of the inter-platelet space as shown on Fig. 5.12(a). This confirms that even in the absence of macroscopic strain the clay particles can swell. At a consequence, the Lagrangian and Eulerian nanoporosities do not coincide and ϵ_s^f is given by the difference between the Lagrangian nanoporosity between the initial and the final state according to Eq.(5.35).

The curves on Fig.5.12 confirm thus the ability of the multi-scale model in capturing the water transfer from the micro-to the nanopores during hydration. As can be seen furthermore on these graphs, such evolution of the porous space is more pronounced for a soft solid matrix being characterized by low values of K_s .

Note finally that the increase of the nanoporosity is at the origin of the significant reduction of the disjoining pressure during water as depicted on Fig.5.13.

5.5 Conclusion

The multi-scale version of Terzaghi’s effective stress principle for unsaturated expansive clays accounting for electro-chemo-hydro-mechanical coupling at different length-scales [22] is applied to numerically simulate swelling pressure tests at constant volume. The comparison between our numerical results and experimental data performed at the CIEMAT highlight the ability of our model in discriminating between the respective contributions of microscopic capillary pressure and nanoscopic disjoining forces to the overall swelling pressure. The main conclusions are:

- The model is able to capture water transfer from the microscopic inter-particle to the nanoscopic inter-platelet pores during hydration. As a consequence, the increase of the swelling pressure observed in the experimental data and confirmed by our numerical computations can be explained as the result of two phenomena: the high capillary pressure at the initial low saturation level is completely compensated by the disjoining pressure. With

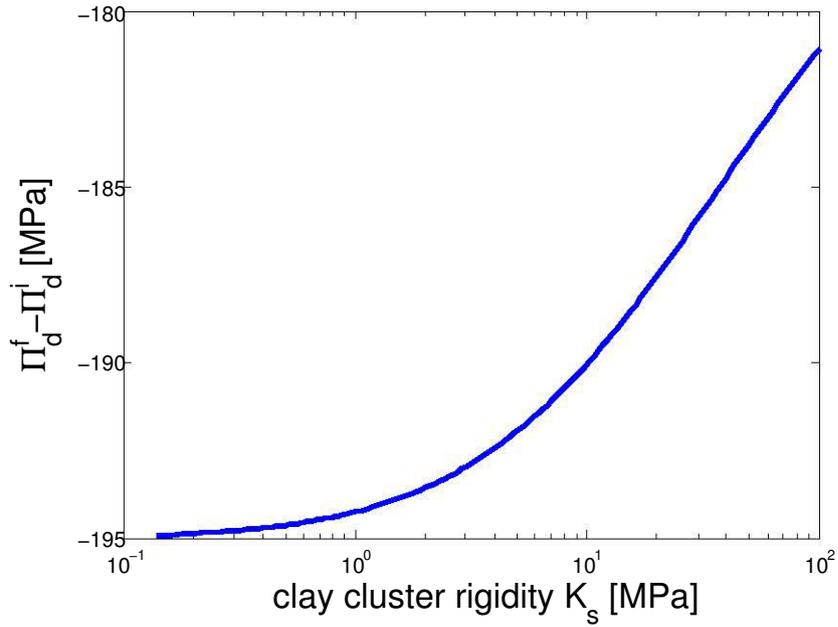


Figure 5.13: Variation of the disjoining pressure between the initial ($S_w^i = 0.26$) and the final fully saturated state as a function of the microscopic bulk modulus K_s .

increasing saturation, water is continuously transferred from the micro- to the nanopores resulting in a decrease of the microscopic inter-particle pores and a swelling of the clay particles. At full saturation when capillary pressure vanishes the swelling pressure corresponds to the effective disjoining pressure with a somewhat lower magnitude compared to its initial value due to a higher inter-platelet distance within the clay agglomerates at the nano-scale.

- The classical PB theory remains valid at high saturation levels in the osmotic swelling regime where swelling is driven by EDL effects. However, for low hydration, in the crystalline swelling regime the molecular character of the electrolyte solution has to be taken into account for accurately modeling the disjoining pressure at small inter-platelet distances. By selecting a nanoscopic description of a simple HS fluid confined between two planar hard walls the disjoining pressure has been computed using classical DFT. Notwithstanding the simplicity of our approach it leads to an improvement of the nanoscopic description, particularly at low hydration levels.
- In the present model approach, the microscopic bulk modulus is only linked to the solid phase connectivity inside the clay clusters and plays the role of a scaling parameter between disjoining and capillary effects. The numerical results show that in order to obtain swelling pressures in the MPa regime, K_s has to be of the same order of magnitude, which is significantly lower than the values of the overall bulk modulus typically found in the literature. We conclude that the overall rigidity of the medium may thus be ensured by nanoscopic disjoining forces.

Some shortcomings still persist such as the overestimation of the swelling pressure and the inability in reproducing the temporary drop of the swelling pressure during water intake. Such behavior is generally explained by a rearrangement of the clay particles in the frame of elastoplastic deformation which is not accounted in the present model approach the latter assuming only elastic deformation. Being an important aspect to be included in the multiscale model, this is however out of the scope of this thesis.

Conclusion and future work

This thesis presents some possible improvements for modeling the nanoscale portrait of swelling clays by considering the water solvent as a fluid of individual molecules in order to account for both their finite size and polar nature. The objective is to recover existing experimental evidences and computational results obtained with molecular dynamic models such as the presence of discrete water layers at low hydration, the evolution of the swelling pressure during water intake ... Through chapters 2 to 4 different phenomena of increasing complexity are successively considered in the Electrical Double Layer description, such as the molecule size and polar nature of the water solvent inducing interparticle correlation effects. Finally, the presence of ions is included to arrive at the so-called "civilized" model of EDL.

In a first step presented in Chapter 2, the finite size of the water molecules is considered by representing the EDL as a simple hard sphere fluid confined between two planar hard walls. Such a fluid is a fundamental reference system in statistical mechanics commonly treated by the Fundamental Measure Theory (FMT). This theory is known as the most powerful toolbox for studying (mixtures of) one-component homogeneous and inhomogeneous hard sphere fluids primarily thanks to its easy implementation and very good performance especially at low and intermediate bulk densities. At low hydration, that is at small interplatelet distances of a few molecular diameters, the electrolyte solution can be modeled in a first approach as a HS fluid confined between two hard walls. The resulting density profiles obtained with FMT show an oscillatory behavior which is in agreement with an arrangement of the fluid molecules in the interplatelet space in discrete layers at low hydration. Varying the distance between the two parallel plates leads to an oscillatory behavior of the disjoining pressure (being defined as the pressure acting on the plates to keep them at a fixed distance) which allows to account for attraction or repulsion. Solely the decreasing parts of the disjoining pressure with increasing separation distance represent mechanically stable configurations, which is consistent with the experimentally observed formation of discrete water layers at low hydration. However, when modeling the electrolyte solution as a simple HS fluid, the fluid pressure values obtained at small interplatelet distances or in the bulk limit are unrealistically high. Therefore, an interparticle attractive potential has to be added to the purely repulsive HS potential in order to remedy this shortcoming.

In chapter 3, the water solvent is modeled as a Lennard-Jones (LJ) fluid which exhibits both repulsive and attractive parts in its intermolecular potential. The LJ fluid presents a convenient approach to account for the polar nature of the water solvent as it averages the different types of dipolar interactions. In several former studies the density profiles of different inhomogeneous LJ fluids have been accurately calculated by using a very accurate Density-Functional Perturbation Theory (DFPT) in which interparticle correlations are included through the computation of the Radial Distribution Function. An application of this approach for modeling an electrolyte solution in the case of a low LJ interaction strength ($\beta\epsilon = 0.7407$) predicts oscillatory density profiles for both the solvent and ions, which is similar to the results obtained when modeling the solvent as a simple HS fluid. A more realistic approach for the water solvent consists in imposing a high interaction strength $\beta\epsilon = 1.077$ to produce a reasonable bulk pressures (of the order of 10^5 Pa). However, in this case the simulations show that almost no water molecules are present in the EDL space because they are strongly attracted by the bulk water.

Chapter 4 tries to improve the LJ solvent model by taking explicitly into account the orientation of the molecule dipoles through a DFPT approach. For the sake of simplicity, dipole-dipole correlation effects of the inhomogeneous Dipolar Hard Sphere (DHS) fluid are approximated by those of the corresponding homogeneous bulk fluid. The numerical results confirm again the formation of discrete molecule layers in the crystalline swelling regime and gives in addition the dipole orientation profile over the interplatelet space. For high dipole moments, the disjoining pressure of the DHS fluid is significantly reduced in comparison with that of the corresponding HS fluid and reasonable bulk pressures can be recovered. However, the computation of interparticle correlations of the inhomogeneous DHS fluid by those of the corresponding bulk DHS fluid is no longer realistic in the case of high dipole moments, which is at the origin of the failure of the present DHS model approach. To remedy this shortcoming the behavior of an electrolyte solution is finally studied in the framework of the Mean Field Approximation for a DHS fluid of a low dipole moment. The corresponding numerical simulations result in oscillatory density profiles of the fluid components even for ions.

An application example is presented in chapter 5 by incorporation of the improved description at the nanoscale developed in this work into the three-scale model for unsaturated clayey soils developed by Mainka et al. [22] to simulate the swelling pressure evolution of a clay sample during hydration at constant volume. The numerical results obtained with this double porosity model allow to capture the contributions of the microscopic capillary pressure and nanoscopic disjoining forces to the overall swelling pressure. It can be shown that their evolution is a consequence of the water transfer from the micro- to the nanopores during water uptake. As a first qualitative improvement of the nanoscale portrait for crystalline swelling, the electrolyte solution is modeled as a simple HS fluid confined between two planar hard walls. PB theory is assumed to remain valid at high hydration (osmotic swelling). This leads to a significant improvement of the swelling pressure computation, especially at low hydration level. Obviously some shortcomings still persist, such as the inability of the present model in accounting for elasto-plastic deformation.

In conclusion, this work contributes to improve existing nanoscale models of expansive clayey soils by accounting for the molecular nature of the water solvent. The obtained results exhibit the dominant role of the molecular character of the electrolyte solution which is then incorporated into a three-scale model obtained in the framework of periodic homogenization in order to numerically simulate the hydromechanical behavior of swelling clays during oedometric hydration tests. The comparison between the numerical results and experimental data confirms that a better description of the mechanical behavior at the macroscale stems partially from improvements of the nanoscale model.

While this thesis has proposed an improvement of the nanoscopic description of expansive clayey soils, some opportunities for extending the scope of this work are suggested below.

- Wertheim's result for the dielectric constant calculated with MSA is obviously much better than that of the two classical formula of Clausius-Mossotti and Onsager. However, the MSA is not able to produce the dielectric constant of water ($\epsilon = 80$). Some existing more sophisticated closures could be investigated.
- To complete the "civilized" model of the electrolyte solution, dipole-dipole correlation effects of the inhomogeneous DHS fluid have to be calculated accurately for the case of water with high density and dipole moment values. This is actually a very difficult task, but it should be undertaken.
- Regarding the application to simulate swelling pressure tests, a rearrangement of the clay particles in the frame of elasto-plastic deformations has to be incorporated into the three-scale model in order to correctly recover the evolution of the swelling pressure over the entire saturation range.

Résumé en français

**Taking into account the solvent discontinuous nature
in the mechanical modeling of swelling clays**

**Prise en compte du caractère discontinu du solvant
dans la modélisation mécanique des argiles gonflantes**

LES argiles hydratées gonflantes se rencontrent dans maints aspects de la vie allant des activités agricoles à la protection de l'environnement et des procédés industriels au génie civil. Elles sont utilisées par exemple comme barrières pour éviter la dispersion des polluants dans l'environnement ou pour la gestion des déchets y compris les déchets radioactifs de haute activité. Une caractéristique importante est leur comportement de contraction-gonflement qui peut être gênant car il est capable de provoquer la dégradation voire l'effondrement des structures (bâtiments, ponts, routes, tunnels. . .) construites sur des sites en argile gonflante. Dans l'industrie pétrolière, la stabilité des forages dans les schistes riches en argile dépend fortement de leur capacité de gonflement. La résolution de ces problèmes nécessite donc une compréhension approfondie des phénomènes physiques qui sous-tendent le comportement des sols argileux expansifs.

L'objectif de cette thèse est l'amélioration à l'échelle nanométrique des modèles d'argiles gonflantes en considérant le fluide dans l'espace interfoliaire composé d'eau comme solvant et d'ions – cations compensateurs pour assurer l'électroneutralité globale et anions – non plus comme un milieu continu mais comme un milieu discontinu sous forme de molécules individuelles afin de tenir compte à la fois de leur taille finie, de la nature dipolaire de l'eau et des effets de corrélation entre les molécules. Cette thèse s'insère dans une série de travaux visant à construire, par changement d'échelle, un modèle d'argiles gonflantes pour le génie civil fondé sur une description aussi précise que possible de la physique à l'échelle du nanomètre.

Chapitre 1 – Introduction à la modélisation des argiles gonflantes

Le premier chapitre rappelle quelques notions de base sur les smectites qui constituent la principale composante minérale des argiles expansives. Une caractéristique essentielle pour pouvoir modéliser par changement d'échelle le comportement des sols argileux à l'échelle macroscopique de l'ingénieur en génie civil est d'adopter une représentation géométrique de complexité raisonnable. Les argiles expansives présentent en effet toute une hiérarchie d'échelles avec, au moins, trois échelles de longueurs caractéristiques distinctes (nano, micro et macro) et deux niveaux de porosité (nanopores et micropores) [15].

À une échelle de longueur de l'ordre du nanomètre, elles sont composées d'un assemblage de couches de phyllosilicate chargées électriquement appelées feuillets. Leur charge négative vient de substitutions isomorphes de cations structuraux de valence supérieure par d'autres de valence inférieure et aussi de la présence de défauts dans le réseau cristallin de la smectite. Les feuillets d'argile sont séparés par un réseau nanoporeux saturé par une solution aqueuse d'électrolyte. La charge de surface négative des feuillets attire les cations de la solution d'électrolyte afin d'assurer l'électronéutralité globale du système (phases solide et liquide). En raison de cette attraction, la concentration des cations au voisinage de la surface d'argile dépasse celle de la solution d'équilibre loin de celle-ci appelée *bulk*. Les cations chargés positivement forment ensemble avec les feuillets d'argile chargés négativement une double couche électrique (EDL ou *Electrical Double Layer*) diffuse. La longueur caractéristique de l'EDL est la longueur de Debye $\mathcal{O}(10^{-9}$ m) qui donne la longueur sur laquelle les particules chargées interagissent. À l'échelle microscopique intermédiaire de longueur caractéristique $\mathcal{O}(10^{-6}$ m), les feuillets argileux se rassemblent pour former des paquets qui constituent la phase solide à cette échelle de longueur. Ces derniers sont séparés par un réseau de micropores remplis soit par de l'eau pure, soit par un mélange d'eau et d'air dans le cas non saturé. Du fait de leur taille, les micropores sont totalement exempts d'effets EDL.

Ce travail se concentre sur les effets mécaniques engendrés par une telle situation et plus particulièrement sur la pression de gonflement qui est l'équivalent macroscopique de la pression de disjonction à l'échelle des feuillets. La pression de disjonction est définie comme l'excès de pression vis-à-vis de la pression du *bulk* pour maintenir la distance interfoliaire à une valeur fixée tandis que la pression de gonflement est l'excès de pression, toujours par rapport au *bulk* (avec une pression de liquide éventuellement négative dans le cas non saturé), pour maintenir un échantillon à volume fixé.

Sur la base de cette configuration locale, le but est de faire des prédictions sur le comportement mécanique de ces milieux à l'échelle macroscopique observable. Une technique rigoureuse pour mettre à niveau les phénomènes électrochimiques hydromécaniques couplés qui se produisent aux petites échelles à l'échelle macroscopique observable est l'homogénéisation périodique [16]. C'est pourquoi cette procédure est utilisée dans le cadre de cette thèse de doctorat pour dériver les lois constitutives macroscopiques qui sont pertinentes pour les ingénieurs en génie civil. Dans ce cadre, étudier les phénomènes qui se produisent aux échelles locales et plus précisément à l'échelle nanométrique joue un rôle crucial comme brique élémentaire dans la modélisation des argiles expansives.

L'approche classique pour modéliser les phénomènes physiques se produisant à l'échelle nanométrique est la théorie de la double couche électrique, initialement proposée séparément par Gouy et Chapman [17], dans laquelle le solvant (eau) est considéré comme un diélectrique continu et les ions comme des charges ponctuelles. La pression de disjonction est la répulsion résultant des effets combinés de l'attraction électrostatique entre la charge de surface négative des feuillets d'argile et le nuage cationique dissous de la solution d'électrolyte et le rôle prédominant de la pression osmotique. Elle peut être obtenue en résolvant le problème classique de Poisson-Boltzmann (PB). Malgré sa simplicité, cette approche est capable de décrire quantitativement le comportement de la double couche électrique pour des ions monovalents à des

niveaux d'hydratation élevés, dans le régime dit de *gonflement osmotique* [18]. Même dans ce régime *osmotique*, un des défauts du modèle de PB est de prédire seulement un gonflement alors que pour des cations plurivalents des comportements plus complexes sont observés. Une modélisation plus sophistiquée toujours avec un solvant continu mais avec des ions de taille finie et en prenant en compte les effets de corrélation entre les ions permet de bien rendre compte de ce phénomène [20, 35].

Le cas du *gonflement cristallin* aux faibles hydratations et donc avec des distances interfoliaires de la taille des molécules d'eau est infiniment plus délicat à décrire. Doivent être prises en compte non seulement les interactions entre les ions et les parois des feuillettes mais également les forces d'hydratation entre le solvant dipolaire (eau) et ces parois. Le présent travail va tenter de poursuivre cette tâche en augmentant progressivement la sophistication de la description.

Chapitre 2 – Introduction à la Théorie de la Fonctionnelle de densité (DFT) et application aux fluides de sphères dures

Dans une première étape, seule la taille finie des molécules d'eau va être prise en compte en ne considérant que le solvant, ce dernier étant représenté comme fluide simple de sphères dures (HS pour *Hard Spheres*). L'approche peut être jugée très élémentaire mais le fluide de sphères dures est une référence fondamentale dans le cadre du développement de modèles plus sophistiqués issus de la mécanique statistique.

La modélisation d'un fluide de sphères dures va utiliser la théorie fondamentale de la mesure (FMT pour *Fundamental Measure Theory*). Cette théorie est connue comme l'outil le plus puissant pour étudier analytiquement un fluide homogène constitué de sphères dures ou d'un mélange de sphères dures. Ses bases théoriques et sa mise en œuvre sont décrites au chapitre 2. Ses performances sont excellentes comparées aux simulations moléculaires surtout aux densités moléculaires faibles ou intermédiaires.

A basse hydratation, c'est-à-dire pour de faibles distances interfoliaires de l'ordre de quelques diamètres moléculaires, une première approche de modélisation considère le fluide interfoliaire comme un fluide HS confiné entre deux parois dures planes parallèles. Les profils de densité obtenus avec la théorie fondamentale de la mesure montrent un comportement oscillatoire en accord avec un agencement des molécules fluides en couches discrètes dans l'espace interfoliaire.

La variation de la distance entre les deux plaques parallèles conduit à un comportement oscillatoire de la pression de disjonction qui permet de rendre compte de l'attraction ou de la répulsion. Seules les distances interfoliaires où la pression de disjonction est décroissante quand la distance entre les plaques augmente sont des configurations mécaniquement stables. Ceci est cohérent avec l'observation expérimentale qui montre que le remplissage de l'espace interfoliaire se fait par des couches d'eau discrètes à faible hydratation. Cependant, la modélisation par un fluide de sphères dures entraîne de grandes valeurs de la pression exercée par le fluide sur le solide pour de petites distances interfoliaires qui sont irréalistes. Un potentiel attractif interparticulaire doit nécessairement être ajouté au potentiel de sphères dures purement répulsif afin de remédier à cette lacune.

Chapitre 3 – Fluide de Lennard-Jones

Dans le chapitre 3, l'eau est modélisée comme un fluide de Lennard-Jones (LJ) avec un potentiel intermoléculaire composé de deux termes variant en r^{-6} et r^{-12} respectivement. De ce fait, ce potentiel est répulsif aux faibles distances de séparation et attractif aux longues distances de séparation. Le fluide de Lennard-Jones est une alternative simple pour prendre en compte la nature polaire de l'eau car pour les trois types d'interactions dipolaires (Keesom, Debye, London), le potentiel attractif aux grandes distances de séparation r a un comportement en r^{-6} analogue au potentiel LJ de type 6-12.

Dans un premier temps, les profils de densité pour différents fluides LJ confinés entre deux plaques parallèles ont été calculés par une approche perturbative de la théorie de la fonctionnelle de densité (DFPT) à partir du modèle de sphères dures dans laquelle les corrélations interparticulaires sont incluses par l'intermédiaire de la fonction de distribution radiale (RDF pour *Radial Distribution Function*). Cette dernière est calculée pour la situation inhomogène du fluide confiné entre deux plaques au moyen de la résolution de l'équation d'Ornstein-Zernike. Elle est complétée par une fermeture incluant une fonction *bridge* tirée de la littérature pour le cas des fluides LJ. La résolution est effectuée dans l'espace de Hankel en r , la coordonnée z perpendiculaire aux plaques jouant un rôle de paramètre. Les résultats obtenus par cette méthode sont en excellent accord avec les simulations par dynamique moléculaire dans les mêmes conditions expérimentales.

Cette approche est ensuite utilisée pour simuler le fonctionnement d'une double couche électrique en ajoutant aux potentiels de sphères dures et de Lennard-Jones le potentiel de Coulomb pour les ions (toutes les molécules sont supposées avoir le même diamètre). Dans le cas d'un faible potentiel d'interaction de type LJ des profils de densité oscillatoires sont observés pour le solvant et les ions, ce qui est similaire aux résultats obtenus lors de la modélisation avec un fluide de sphères dures. Une approche plus réaliste pour l'eau consisterait à augmenter le potentiel d'interaction afin d'obtenir des pressions dans le *bulk* plus raisonnables (de l'ordre de 10^5 Pa). Cependant, dans ce cas, les simulations montrent que l'eau liquide ne pénètre plus dans l'espace interfoliaire (même avec des potentiels d'interaction eau-paroi élevés).

Chapitre 4 – Fluide de sphères dures dipolaire

Le chapitre 4 tente d'améliorer le modèle de LJ pour le solvant en prenant explicitement en compte le caractère dipolaire des molécules du solvant en supposant que, pour l'eau, les interactions de type Keesom sont dominantes. Chaque molécule est alors une sphère dure dotée en son centre d'un moment dipolaire fixe pouvant s'orienter en fonction du champ électrique local d'où la dénomination fluide de sphères dures dipolaire (DHS pour *Dipolar Hard Sphere*). Des travaux récents de Olesky et al. [100, 101, 102, 103] suggèrent que la prise en compte des corrélations entre molécules pourrait être la clef pour améliorer la description des fluides dipolaires. La méthode perturbative du paragraphe précédent (DFPT) est donc reprise. L'approche de Wertheim est utilisée pour calculer la fonction de distribution radiale dans le *bulk* [21]. Pour alléger les calculs des effets de corrélation dipôle-dipôle autant que possible, la RDF du fluide en situation inhomogène entre deux plaques a été approchée par celle du fluide homogène du *bulk*. Les résultats numériques confirment à nouveau la formation de couches de molécules discrètes dans le régime du gonflement cristallin et donnent en outre le profil d'orientation des dipôles dans l'espace interfoliaire. Pour des faibles moments dipolaires, la pression de disjonction du fluide DHS est significativement réduite par rapport à celle du fluide HS correspondant et des valeurs de pression raisonnables peuvent être récupérées. Cependant, le calcul des corrélations interparticulaires du fluide DHS inhomogène à partir de la RDF du fluide DHS homogène en équilibre ne permet pas d'atteindre une valeur de la constante diélectrique du solvant dans le cas des moments dipolaires élevés. Ceci est sans doute à l'origine de la défaillance du modèle DHS dans l'approche actuelle.

Les bases d'un modèle dit "civilisé" sont ensuite développées avec l'eau se comportant comme un fluide DHS et les ions comme des sphères dures complétées par un potentiel de Coulomb. Vu la très faible amélioration des performances du modèle due à la prise en compte des corrélations intermoléculaires, une approche de type champ moyen a été privilégiée. Un exemple numérique de résolution est fourni pour un cas de faible moment dipolaire du solvant.

Chapitre 5 – Modélisation du comportement hydromécanique des argiles gonflantes non saturées

Le chapitre 5 est un retour aux échelles macroscopiques du génie civil. Les modèles plus sophistiqués à la nanoéchelle développés dans ce travail sont incorporés dans le modèle à trois échelles pour les sols argileux insaturés développé par Mainka et al. [22]. La situation étudiée est l'évolution de la pression de gonflement d'un échantillon d'argile pendant l'hydratation à volume constant bien documentée par Imbert and Villar [11].

Les résultats numériques obtenus par nos simulations à l'aide de ce modèle à double porosité permettent de saisir la contribution simultanée de la pression capillaire microscopique et des forces de disjonction nanoscopiques à la pression globale de gonflement. On peut montrer que leur évolution est une conséquence du transfert d'eau des micropores aux nanopores lors de l'hydratation. Comme première amélioration qualitative du portrait à l'échelle nanométrique pour le gonflement cristallin, la solution d'électrolyte est modélisée comme un simple fluide de sphères dures confiné entre deux parois rigides planes. La théorie de Poisson-Boltzmann est supposée rester valable à forte hydratation dans le cas du gonflement osmotique. Ceci conduit à une amélioration significative du calcul de la pression de gonflement, en particulier aux faibles niveaux d'hydratation. De toute évidence, des imperfections persistent, comme l'incapacité du modèle à trois échelles à décrire les déformations irréversibles subies par les empilements microscopiques des feuillets que les modèles classiques de génie civil traduisent dans le langage des transformations élasto-plastiques.

Conclusion

Ce travail a analysé les possibilités ainsi que les difficultés liées à une description détaillée des phénomènes à l'échelle moléculaire entre les feuillets de smectites avec comme objectif ultime (à terme) une modélisation rigoureuse des argiles fondées sur un processus de changement d'échelle. Pour pouvoir procéder avec efficacité au changement d'échelle, des modèles simplifiés doivent être construits sans renoncer à une représentation pertinente de la physique à l'échelle nanométrique.

La prise en compte du caractère dipolaire de l'eau caractérisée par un moment dipolaire élevé reste un véritable défi. D'une part, des fermetures pour le *bulk* plus sophistiquées que le modèle de Wertheim existent et mériteraient d'être étudiées. D'autre part, la prise en compte des corrélations entre les molécules dans le cas du fluide inhomogène est très exigeante et semble ne pas pouvoir se satisfaire de l'utilisation des fonctions de distributions radiales du fluide dans le *bulk* en équilibre correspondant.

Pour simuler les tests de pression de gonflement, une autre difficulté fondamentale et de nature complètement différente est liée au réarrangement des particules d'argile dans le cadre des déformations élasto-plastiques qui devrait être incorporé dans le modèle à trois échelles si l'on souhaite récupérer correctement l'évolution de la pression de gonflement sur toute la plage de saturation.

En espérant que ce travail puisse contribuer à faire avancer les idées pour atteindre cet objectif un peu idéal de disposer d'un modèle d'argiles gonflantes fondé sur une description physique pertinente des phénomènes à la nanoéchelle et propagé vers les échelles macroscopiques du génie civil par un changement d'échelle!

Bibliography

- [1] Kenichi Soga and JK Mitchell. Fundamentals of soil behavior. *Wiley. Third Edition. ISBN*, 10:0–471, 2005.
- [2] J Likos William. Measurement of crystalline swelling in expansive clay. *Geotechnical Testing Journal*, 27(6):540–546, 2004.
- [3] Laurent J et al. Michot. Water organisation at the solid–aqueous solution interface. *Comptes Rendus Geoscience*, 334(9):611–631, 2002.
- [4] RK Taylor and TJ Smith. The engineering geology of clay minerals; swelling, shrinking and mudrock breakdown. *Clay Minerals*, 21(3):235–260, 1986.
- [5] Yang Song, Catherine A Davy, David Troadec, A-M Blanchenet, Frédéric Skoczylas, Jean Talandier, and Jean-Charles Robinet. Multi-scale pore structure of COx claystone: towards the prediction of fluid transport. *Marine and Petroleum Geology*, 65:63–82, 2015.
- [6] RD Groot, NM Faber, and JP Van der Eerden. Hard sphere fluids near a hard wall and a hard cylinder. *Molecular Physics*, 62(4):861–874, 1987.
- [7] Loup Verlet. Computer “experiments” on classical fluids. ii. equilibrium correlation functions. *Physical Review*, 165(1):201, 1968.
- [8] James F Lutsko. Density functional theory of inhomogeneous liquids. II. A fundamental measure approach. *The Journal of chemical physics*, 128(18):184711, 2008.
- [9] JG Powles, G Rickayzen, and ML Williams. The density profile of a fluid confined to a slit. *Molecular Physics*, 64(1):33–41, 1988.
- [10] IK Snook and W Van Megen. Solvation forces in simple dense fluids. I. *The Journal of Chemical Physics*, 72(5):2907–2913, 1980.
- [11] Christophe Imbert and M Victoria Villar. Hydro-mechanical response of a bentonite pellets/powder mixture upon infiltration. *Applied Clay Science*, 32(3):197–209, 2006.
- [12] Jacob N Israelachvili. *Intermolecular and surface forces: revised third edition*. Academic press, 2011.
- [13] M Önal. Physicochemical properties of bentonites: an overview. *Communications de la Faculté des Sciences de l’Université d’Ankara Series B*, 52:7–21, 2006.
- [14] IE Odom. Smectite clay minerals: properties and uses. *Philosophical Transactions of the Royal Society of London A: Mathematical, Physical and Engineering Sciences*, 311(1517):391–409, 1984.
- [15] Márcio A Murad and Christian Moyne. A dual-porosity model for ionic solute transport in expansive clays. *Computational Geosciences*, 12(1):47–82, 2008.

- [16] Christian Moyne and Márcio A Murad. Electro-chemo-mechanical couplings in swelling clays derived from a micro/macro-homogenization procedure. *International Journal of Solids and Structures*, 39(25):6159–6190, 2002.
- [17] H Van Olphen and Pa Ho Hsu. An introduction to clay colloid chemistry. *Soil Science*, 126(1):59, 1978.
- [18] Philip F Low. Structural component of the swelling pressure of clays. *Langmuir*, 3(1):18–25, 1987.
- [19] S Lamperski, CW Outhwaite, and LB Bhuiyan. A modified Poisson-Boltzmann analysis of the solvent primitive model electrical double layer. *Molecular Physics*, 87(5):1049–1061, 1996.
- [20] TD Le, C Moyne, MA Murad, and SA Lima. A two-scale non-local model of swelling porous media incorporating ion size correlation effects. *Journal of the Mechanics and Physics of Solids*, 61(12):2493–2521, 2013.
- [21] MS Wertheim. Exact solution of the mean spherical model for fluids of hard spheres with permanent electric dipole moments. *The Journal of Chemical Physics*, 55(9):4291–4298, 1971.
- [22] Julia Mainka, Marcio A Murad, Christian Moyne, and Sidarta A Lima. A modified effective stress principle for unsaturated swelling clays derived from microstructure. *Vadose Zone Journal*, 13(5), 2014.
- [23] Eric Ferrage. *Etude expérimentale de l'hydratation des smectites par simulation des raies 00 de diffraction des rayons X. Implications pour l'étude d'une perturbation thermique sur la minéralogie de l'argilite du site Meuse-Haute Marne*. PhD thesis, Thesis Grenoble I, 2004.
- [24] Eric Ferrage, Bruno Lanson, Laurent J Michot, and Jean-Louis Robert. Hydration properties and interlayer organization of water and ions in synthetic Na-smectite with tetrahedral layer charge. part 1. results from X-ray diffraction profile modeling. *The Journal of Physical Chemistry C*, 114(10):4515–4526, 2010.
- [25] Fritz T Madsen and Max Müller-Vonmoos. The swelling behaviour of clays. *Applied Clay Science*, 4(2):143–156, 1989.
- [26] H Van Olphen. *An introduction to clay colloid chemistry, for clay technologists, geologists, and soil scientists*. Wiley, 1977. 2nd edition.
- [27] Wilmer Olivares and Donald A McQuarrie. Interaction between electrical double layers. *The Journal of Physical Chemistry*, 84(8):863–867, 1980.
- [28] Frederick George Donnan. The theory of membrane equilibria. *Chemical Reviews*, 1(1):73–90, 1924.
- [29] BF Bohor and Randall E Hughes. Scanning electron microscopy of clays and clay minerals. *Clays and Clay Minerals*, 19(1), 1971.
- [30] JL Auriault. Behavior of porous saturated deformable media. *Geomaterials-In Constitutive Equations and Modeling*, Elsevier, New York, pages 311–328, 1990.
- [31] Christian Moyne and Márcio Murad. Macroscopic behavior of swelling porous media derived from micromechanical analysis. *Transport in Porous Media*, 50(1-2):127–151, 2003.

-
- [32] Christian Moyne and Márcio A Murad. A two-scale model for coupled electro-chemo-mechanical phenomena and Onsager's reciprocity relations in expansive clays: II Computational validation. *Transport in Porous Media*, 63(1):13–56, 2006.
- [33] Christian Moyne and Márcio A Murad. A two-scale model for coupled electro-chemo-mechanical phenomena and Onsager's reciprocity relations in expansive clays: I Homogenization analysis. *Transport in Porous Media*, 62(3):333–380, 2006.
- [34] Julia Mainka, Marcio A Murad, Van Duy Tran, Tien Dung Le, and Christian Moyne. Application of a multi-scale form of terzaghi's effective stress principle for unsaturated expansive clays to simulate hydro-mechanical behavior during hydration. In *3rd European Conference on Unsaturated Soils (E-UNSAT)*, Paris 12-14 September 2016.
- [35] Tien Dung Le. *Mécanique et transport dans les milieux poreux déformables: prise en compte des corrélations ion-ion et application aux argiles smectiques*. PhD thesis, Université de Lorraine, 2013.
- [36] Eric Ferrage, Boris A Sakharov, Laurent J Michot, Alfred Delville, Allan Bauer, Bruno Lanson, Sylvain Grangeon, Gilles Frapper, Mónica Jiménez-Ruiz, and Gabriel J Cuello. Hydration properties and interlayer organization of water and ions in synthetic Na-smectite with tetrahedral layer charge. part 2. toward a precise coupling between molecular simulations and diffraction data. *The Journal of Physical Chemistry C*, 115(5):1867–1881, 2011.
- [37] Randall T Cygan, Jian-Jie Liang, and Andrey G Kalinichev. Molecular models of hydroxide, oxyhydroxide, and clay phases and the development of a general force field. *The Journal of Physical Chemistry B*, 108(4):1255–1266, 2004.
- [38] A Delville. Toward a detailed molecular analysis of the long-range swelling gap of charged rigid lamellae dispersed in water. *The Journal of Physical Chemistry C*, 116(1):818–825, 2011.
- [39] A Delville. Beyond the diffuse layer theory: A molecular analysis of the structural, dynamical, and mechanical properties of charged solid/liquid interfaces. *The Journal of Physical Chemistry C*, 117(28):14558–14569, 2013.
- [40] HJC Berendsen, JR Grigera, and TP Straatsma. The missing term in effective pair potentials. *Journal of Physical Chemistry*, 91(24):6269–6271, 1987.
- [41] DA McQuarrie. *Statistical mechanics*. University Science Books, 2000.
- [42] Yaakov Rosenfeld. Free-energy model for the inhomogeneous hard-sphere fluid mixture and density-functional theory of freezing. *Physical Review Letters*, 63(9):980, 1989.
- [43] R Evans. The nature of the liquid-vapour interface and other topics in the statistical mechanics of non-uniform, classical fluids. *Advances in Physics*, 28(2):143–200, 1979.
- [44] Jean-Pierre Hansen and Ian R McDonald. *Theory of simple liquids, Fourth Edition*. Elsevier, 2013.
- [45] Douglas Henderson. *Fundamentals of inhomogeneous fluids*. CRC Press, 1992.
- [46] Terrell L Hill. *Statistical mechanics: principles and selected applications*. Courier Corporation, 2013.
- [47] LS Ornstein and F Zernike. Accidental deviations of density and opalescence at the critical point of a single substance. *Proc. Akad. Sci.(Amsterdam)*, 17:793, 1914.

- [48] Jean-Marc Bomont. Recent advances in the field of integral equation theories: bridge functions and applications to classical fluids. *Advances in Chemical Physics*, 139:1–84, 2008.
- [49] MS Wertheim. Exact solution of the Percus-Yevick integral equation for hard spheres. *Physical Review Letters*, 10(8):321, 1963.
- [50] JL Lebowitz and JK Percus. Mean spherical model for lattice gases with extended hard cores and continuum fluids. *Physical Review*, 144(1):251, 1966.
- [51] Eduardo Waisman and Joel L Lebowitz. Mean spherical model integral equation for charged hard spheres I. Method of solution. *The Journal of Chemical Physics*, 56(6):3086–3093, 1972.
- [52] Eduardo Waisman and Joel L Lebowitz. Mean spherical model integral equation for charged hard spheres. II. Results. *The Journal of Chemical Physics*, 56(6):3093–3099, 1972.
- [53] Niharendu Choudhury and Swapan K Ghosh. Integral equation theory of Lennard-Jones fluids: A modified Verlet bridge function approach. *The Journal of Chemical Physics*, 116(19):8517–8522, 2002.
- [54] Loup Verlet. Integral equations for classical fluids: I. The hard sphere case. *Molecular Physics*, 41(1):183–190, 1980.
- [55] GA Martynov and GN Sarkisov. Exact equations and the theory of liquids. V. *Molecular Physics*, 49(6):1495–1504, 1983.
- [56] Donald E Sullivan. Statistical mechanics of a nonuniform fluid with long-range attractions. *Physical Review A*, 25(3):1669, 1982.
- [57] Robert Evans. Density functionals in the theory of nonuniform fluids. *Fundamentals of Inhomogeneous Fluids*, 1:85–176, 1992.
- [58] Shiqi Zhou and JR Solana. Progress in the perturbation approach in fluid and fluid-related theories. *Chemical Reviews*, 109(6):2829–2858, 2009.
- [59] Yaakov Rosenfeld, Dominique Levesque, and Jean-Jacques Weis. Free-energy model for the inhomogeneous hard-sphere fluid mixture: Triplet and higher-order direct correlation functions in dense fluids. *The Journal of Chemical Physics*, 92(11):6818–6832, 1990.
- [60] E Kierlik and ML Rosinberg. Density-functional theory for inhomogeneous fluids: adsorption of binary mixtures. *Physical Review A*, 44(8):5025, 1991.
- [61] S Phan, E Kierlik, ML Rosinberg, B Bildstein, and G Kahl. Equivalence of two free-energy models for the inhomogeneous hard-sphere fluid. *Physical Review E*, 48(1):618, 1993.
- [62] José A Cuesta and Yuri Martínez-Ratón. Fundamental measure theory for mixtures of parallel hard cubes. I. General formalism. *The Journal of Chemical Physics*, 107(16):6379–6389, 1997.
- [63] R Roth, R Evans, A Lang, and G Kahl. Fundamental measure theory for hard-sphere mixtures revisited: the White Bear version. *Journal of Physics: Condensed Matter*, 14(46):12063, 2002.
- [64] Roland Roth. Fundamental measure theory for hard-sphere mixtures: a review. *Journal of Physics: Condensed Matter*, 22(6):063102, 2010.

-
- [65] Howard Reiss, HL Frisch, E Helfand, and JL Lebowitz. Aspects of the statistical thermodynamics of real fluids. *The Journal of Chemical Physics*, 32(1):119–124, 1960.
- [66] E Kierlik and ML Rosinberg. Free-energy density functional for the inhomogeneous hard-sphere fluid: application to interfacial adsorption. *Physical Review A*, 42(6):3382, 1990.
- [67] R Roth and S Dietrich. Binary hard-sphere fluids near a hard wall. *Physical Review E*, 62(5):6926, 2000.
- [68] JL Lebowitz. Exact solution of generalized Percus-Yevick equation for a mixture of hard spheres. *Physical Review*, 133(4A):A895, 1964.
- [69] Norman F Carnahan and Kenneth E Starling. Equation of state for nonattracting rigid spheres. *The Journal of Chemical Physics*, 51(2):635–636, 1969.
- [70] Hendrik Hansen-Goos and Roland Roth. A new generalization of the Carnahan-Starling equation of state to additive mixtures of hard spheres. *The Journal of Chemical Physics*, 124(15):154506, 2006.
- [71] Hendrik Hansen-Goos and Roland Roth. Density functional theory for hard-sphere mixtures: the White Bear version mark II. *Journal of Physics: Condensed Matter*, 18(37):8413, 2006.
- [72] Zixiang Tang, LE Scriven, and HT Davis. Density-functional perturbation theory of inhomogeneous simple fluids. *The Journal of Chemical Physics*, 95(4):2659–2668, 1991.
- [73] John Alan Barker and Douglas Henderson. What is “liquid”? Understanding the states of matter. *Reviews of Modern Physics*, 48(4):587, 1976.
- [74] John D Weeks, David Chandler, and Hans C Andersen. Role of repulsive forces in determining the equilibrium structure of simple liquids. *The Journal of Chemical Physics*, 54(12):5237–5247, 1971.
- [75] Bo Qiao Lu, R Evans, and MM Telo da Gama. The form of the density profile at a liquid-gas interface: Dependence on the intermolecular potential. *Molecular Physics*, 55(6):1319–1338, 1985.
- [76] Loup Verlet and Jean-Jacques Weis. Equilibrium theory of simple liquids. *Physical Review A*, 5(2):939, 1972.
- [77] Zhou Shi-Qi. Augmented Kierlik - Rosinberg fundamental measure functional and extension of fundamental measure functional to inhomogeneous non-hard sphere fluids. *Communications in Theoretical Physics*, 54(6):1023, 2010.
- [78] Der-Ming Duh and ADJ Haymet. Integral equation theory for uncharged liquids: The Lennard-Jones fluid and the bridge function. *The Journal of Chemical Physics*, 103(7):2625–2633, 1995.
- [79] Der-Ming Duh and Douglas Henderson. Integral equation theory for Lennard-Jones fluids: the bridge function and applications to pure fluids and mixtures. *The Journal of Chemical Physics*, 104(17):6742–6754, 1996.
- [80] Lloyd L Lee. Constructing a new closure theory based on the third-order Ornstein-Zernike equation and a study of the adsorption of simple fluids. *The Journal of Chemical Physics*, 135(20):204706, 2011.

- [81] Michael Plischke and Douglas Henderson. Density profiles and pair correlation functions of lennard-jones fluids near a hard wall. *The Journal of Chemical Physics*, 84(5):2846–2852, 1986.
- [82] Roland Kjellander and Sten Sarman. A study of anisotropic pair distribution theories for lennard-jones fluids in narrow slits: Part I. Density profiles and surface interactions. *Molecular Physics*, 70(2):215–237, 1990.
- [83] Roland Kjellander and Sten Sarman. A study of anisotropic pair distribution theories for Lennard-Jones fluids in narrow slits. part II. Pair correlations and solvation forces. *Molecular Physics*, 74(3):665–688, 1991.
- [84] Yiping Tang and Jianzhong Wu. Modeling inhomogeneous van der Waals fluids using an analytical direct correlation function. *Physical Review E*, 70(1):011201, 2004.
- [85] Yang-Xin Yu. A novel weighted density functional theory for adsorption, fluid-solid interfacial tension, and disjoining properties of simple liquid films on planar solid surfaces. *The Journal of Chemical Physics*, 131(2):024704, 2009.
- [86] William A Steele. The physical interaction of gases with crystalline solids: I. Gas-solid energies and properties of isolated adsorbed atoms. *Surface Science*, 36(1):317–352, 1973.
- [87] Yiping Tang and Jianzhong Wu. A density-functional theory for bulk and inhomogeneous Lennard-Jones fluids from the energy route. *The Journal of Chemical Physics*, 119(14):7388–7397, 2003.
- [88] B Smit. Phase diagrams of Lennard-Jones fluids. *The Journal of chemical physics*, 96(11):8639–8640, 1992.
- [89] Zixiang Tang, LE Scriven, and HT Davis. Structure of a dipolar hard sphere fluid near a neutral hard wall. *The Journal of Chemical Physics*, 96(6):4639–4645, 1992.
- [90] Chandra N Patra and Swapan K Ghosh. A nonlocal density functional theory of electric double layer: Symmetric electrolytes. *The Journal of Chemical Physics*, 100(7):5219–5229, 1994.
- [91] F Lado. Numerical Fourier transforms in one, two, and three dimensions for liquid state calculations. *Journal of Computational Physics*, 8(3):417–433, 1971.
- [92] Milton Abramowitz, Irene A Stegun, et al. Handbook of mathematical functions. *Applied Mathematics Series*, 55:62, 1966.
- [93] CG Gray and KE Gubbins. *Theory of molecular fluids, Volume 1: Fundamentals Clarendon*. Oxford, 1984.
- [94] GN Patey. An integral equation theory for the dense dipolar hard-sphere fluid. *Molecular Physics*, 34(2):427–440, 1977.
- [95] D Henderson. Some simple results for the properties of polar fluids. *arXiv preprint arXiv:1202.4247*, 2012.
- [96] J. S. Høye, J. L. Lebowitz, and G. Stell. Generalized mean spherical approximations for polar and ionic fluids. *Journal of Chemical Physics*, 61(8):3253–3260, 1974.
- [97] Herbert Fröhlich. *Theory of dielectrics*. Clarendon Press, 1949.
- [98] John G Kirkwood. The dielectric polarization of polar liquids. *The Journal of Chemical Physics*, 7(10):911–919, 1939.

-
- [99] Mónica Valiskó and Dezso Boda. Dielectric constant of the polarizable dipolar hard sphere fluid studied by Monte Carlo simulation and theories. *Condensed Matter Phys*, 8(2):357–376, 2005.
- [100] Anna Oleksy and Jean-Pierre Hansen. Towards a microscopic theory of wetting by ionic solutions. I. surfaces properties of the semi-primitive model. *Molecular Physics*, 104(18):2871–2883, 2006.
- [101] Anna Oleksy and Jean-Pierre Hansen. Microscopic density functional theory of wetting and drying of a solid substrate by an explicit solvent model of ionic solutions. *Molecular Physics*, 107(23-24):2609–2624, 2009.
- [102] Anna Oleksy and Jean-Pierre Hansen. Wetting of a solid substrate by a “civilized” model of ionic solutions. *The Journal of Chemical Physics*, 132(20):204702, 2010.
- [103] Anna Oleksy and Jean-Pierre Hansen. Wetting and drying scenarios of ionic solutions. *Molecular Physics*, 109(7-10):1275–1288, 20011.
- [104] Charles Kittel. Introduction to solid state physics. 2005. ISBN 047141526X, 2005.
- [105] A Gens, B Vallejan, M Sanchez, C Imbert, MV Villar, and M Van Geet. Hydromechanical behaviour of a heterogeneous compacted soil: experimental observations and modelling. *Geotechnique*, 61(5):367–386, 2011.
- [106] A Gens and EE Alonso. A framework for the behavior of unsaturated expansive clays. *Canadian Geotechnical Journal*, 29(6):1013–1032, 1992.
- [107] EE Alonso, J Vaunat, and A Gens. Modelling the mechanical behaviour of expansive clays. *Engineering Geology*, 54(1–2):173–183, 1999.
- [108] M Sanchez, A Gens, LD Guimaraes, and S Olivella. A double structure generalized plasticity model for expansive materials. *International Journal for Numerical and Analytical Methods in Geomechanics*, 29(8):751–787, 2005.
- [109] E Alonso, A Gens, and A Josa. A constitutive model for partially saturated soils. *Geotechnique*, 40(3):405–430, 1990.
- [110] Antonio Lloret Morancho, Marıa Victoria Villar, M Sanchez, Antonio Gens Sole, Xavier Pintado Llurba, and Eduardo Alonso Perez de Agreda. Mechanical behaviour of heavily compacted bentonite under high suction changes. *Geotechnique*, 53(3):27–40, 2003.
- [111] M Biot and D Willis. The theory of consolidation. *J. Appl Elastic Coefficients of the Mech*, 24:594–601, 1957.
- [112] Jean-Louis Auriault, Claude Boutin, and Christian Geindreau. *Homogenization of coupled phenomena in heterogenous media*, volume 149. John Wiley & Sons, 2010.
- [113] Abel Carlos Jacinto, Marıa Victoria Villar, Roberto Gomez-Espina, and Alberto Ledesma. Adaptation of the van Genuchten expression to the effects of temperature and density for compacted bentonites. *Applied Clay Science*, 42(3):575–582, 2009.
- [114] Jean-Michel Pereira, Henry Wong, Philippe Dubujet, and Patrick Dangla. Adaptation of existing behaviour models to unsaturated states: Application to CJS model. *International Journal for Numerical and Analytical Methods in Geomechanics*, 29(11):1127–1155, 2005.
- [115] A-M. Tang. Experimental characterisation of engineered clay barrier in nuclear waste disposals. In *Applied Unsaturated Soil Mechanics*, MUSE School, Paris, May (2006).

Bibliography

- [116] Brian E Hornby, Larry M Schwartz, and John A Hudson. Anisotropic effective-medium modeling of the elastic properties of shales. *Geophysics*, 59(10):1570–1583, 1994.
- [117] Colin M Sayers. The effect of anisotropy on the Young’s moduli and Poisson’s ratios of shales. *Geophysical Prospecting*, 61(2):416–426, 2013.

Taking into account of the discontinuous nature of the solvent in the mechanical modeling of swelling clays

This work aims at improving the nanoscale description of expansive clayey soils using the Density Functional Theory (DFT). Water is no longer considered as a continuous solvent but as a fluid of individual polar molecules in order to recover existing experimental and modeling results such as the presence of discrete water layers in the interplatelet space or the variation of the disjoining pressure with the interplatelet distance at low hydration level. Different physical phenomena of increasing complexity are successively considered. The finite size of the water molecules is firstly taken into account by modeling water as a Hard Sphere fluid using the Fundamental Measure Theory. The polar nature of the water solvent is then implicitly taken into account through a Lennard-Jones potential averaging the different types of Van der Waals interactions. Next the polar nature of the solvent is explicitly modeled by considering water as a Dipolar Hard Sphere fluid. These two fluid models are studied in the framework of the Density Functional Perturbation Theory in which correlation effects between the fluid molecules are incorporated. Ions are finally added in order to complete the Electrical Double Layer description at the nanoscale. With the objective of an application to civil engineering, the improved expression of the disjoining pressure at the nanoscale is included in a modified form of Terzaghi's effective stress principle for unsaturated expansive clays recently developed by our group in order to numerically simulate the hydro-mechanical behavior of expansive clays during water uptake.

Keywords: *swelling clay, porous media, electrical double layer, discontinuous solvent, disjoining pressure, interparticle correlations*

Prise en compte du caractère discontinu du solvant dans la modélisation mécanique des argiles gonflantes

Ce travail vise à améliorer la description à l'échelle du nanomètre des sols argileux expansifs en utilisant la théorie de la fonctionnelle de densité (DFT). L'eau n'est plus considérée comme un solvant continu mais comme un fluide de molécules polaires individuelles. L'objectif est de reproduire les résultats issus de l'expérience ou de la modélisation numérique tels que la présence de couches d'eau discrètes dans l'espace interfolaire ou la variation de la pression de disjonction avec la distance interfolaire dans le régime de gonflement cristallin. Différents phénomènes physiques de complexité croissante sont successivement étudiés. La taille finie des molécules d'eau est tout d'abord prise en compte en modélisant l'eau comme un fluide de sphères dures traité par la théorie fondamentale de la mesure. La nature polaire du solvant est ensuite implicitement considérée en utilisant un potentiel intermoléculaire de Lennard-Jones pour reproduire les différents types d'interactions de Van der Waals. La nature dipolaire de l'eau est ensuite explicitement modélisée par un fluide dipolaire de sphères dures. Ces deux derniers modèles utilisent une approche perturbative de la théorie de la fonctionnelle de densité dans laquelle les effets de corrélation entre les molécules du fluide sont incorporés. Les ions sont finalement ajoutés afin de compléter la description de la double couche électrique. En vue d'une application au génie civil, l'expression améliorée de la pression de disjonction à l'échelle nanométrique est incluse dans une forme modifiée du principe de Terzaghi appliqué aux argiles expansives non-saturées récemment développée dans notre groupe afin de simuler numériquement le comportement hydro-mécanique des argiles gonflantes lors d'essais d'infiltration d'eau.

Mot-clés: *argiles gonflantes, milieux poreux, double couche électrique, solvant discontinu, pression de disjonction, corrélations intermoléculaires*